Max-Planck-Institut für Metallforschung
Stuttgart

The strength limits of ultra-thin copper films

Guillaume Wiederhirn

Dissertation
an der
Universität Stuttgart

Bericht Nr. 199
Juli 2007

The Strength Limits Of Ultra-Thin Copper Films

Von der Fakultät für Chemie der Universität Stuttgart
zur Erlangung der Würde eines Doktors der
Naturwissenschaften (Dr. rer. nat.) genehmigte Abhandlung

Vorgelegt von

Guillaume Wiederhirn

aus Colmar, Frankreich

Hauptberichter:	Prof. Dr. phil. Eduard Arzt
Mitberichter:	Prof. Dr. rer. nat. Gerhard Dehm
Tag der mündlichen Prüfung:	02.07.2007

Institut für Metallkunde der Universität Stuttgart
und
Max-Planck-Institut für Metallforschung Stuttgart

Stuttgart, Juli 2007

Meinen Eltern

"Des chercheurs qui cherchent, on en trouve, mais
des chercheurs qui trouvent, on en cherche."

Charles de Gaulle

Guillaume Wiederhirn

THE STRENGTH LIMITS OF ULTRA-THIN COPPER FILMS

Max Planck Institute for Metals Research and
Institute of Physical Metallurgy, University of Stuttgart, 2007
212 pages, 97 figures, 15 tables

Abstract

Elucidating size effects in ultra-thin films is essential to ensure the performance and reliability of MEMS and electronic devices. In this dissertation, the influence of a capping layer on the mechanical behavior of copper (Cu) films was analyzed. Passivation is expected to shut down surface diffusion and thus to alter the contributions of dislocation- and diffusion-based plasticity in thin films.

Experiments were carried out on 25 nm to 2 µm thick Cu films magnetron-sputtered onto amorphous-silicon nitride coated silicon (111) substrates. These films were capped with 10 nm of aluminum oxide or silicon nitride passivation without breaking vacuum either directly after Cu deposition or after a 500 °C anneal. The evolution of thermal stresses in these films was investigated mainly by the substrate curvature method between -160 °C and 500 °C.

Negligible differences were detected for the silicon nitride vs. the aluminum oxide passivated Cu films. The processing parameters associated with the passivation deposition also had no noticeable effect on the stress-temperature behavior of the Cu. However, the thermomechanical behavior of passivated Cu films strongly depended on the Cu film thickness. For films in the micrometer range, the influence of the passivation layer was not significant, which suggests that the Cu deformed mainly by dislocation plasticity. However, diffusional creep plays an increasing role with decreasing film thickness since it becomes increasingly difficult to nucleate dislocations in smaller grains. Size effects were investigated by plotting the stress at room temperature after thermal cycling as a function of the inverse film thickness. Between 2 µm and 200 nm, the room temperature stress was inversely proportional to the film thickness. The passivation exerted a strong effect on Cu films thinner than 100 nm by effectively shutting down surface diffusion mechanisms. Since dislocation processes were also shut off in these ultra-thin films, they exhibited purely elastic behavior in the measured temperature range. Their lack of plasticity was confirmed by *in-situ* TEM analysis, which revealed the presence of sessile parallel glide dislocations during thermal cycling. The stress plateau reported for films thinner than 100 nm was attributed to the fact that the thermal strain applied was insufficient to induce yielding. The highest stress value of 1.7 GPa measured at -150 °C is therefore a lower limit for the actual flow stress since even at this high stress the films remained elastic.

Guillaume Wiederhirn

DIE FESTIGKEITSGRENZE VON ULTRA-DÜNNEN KUPFERSCHICHTEN

Max-Planck-Institut für Metallforschung und
Institut für Metallkunde, Universität Stuttgart, 2007
212 Seiten, 97 Abbildungen, 15 Tabellen

Kurzzusammenfassung

Ein verbessertes Verständnis von Größeneffekten in ultra-dünnen Metallschichten ist zwingend erforderlich, um die Leistung und Zuverlässigkeit von MEMS und elektronischen Geräten gewährleisten zu können. In dieser Doktorarbeit wurde der Einfluss einer Deckschicht auf das mechanische Verhalten dünner Kupferschichten (Cu) untersucht. Durch eine Passivierungsschicht sollte Oberflächendiffusion unterbunden werden und somit die Beiträge zur Plastizität durch versetzungsbasierte und diffusionsbasierte Mechanismen in dünnen Schichten verändert werden.

Experimente wurden an Cu-Schichten mit Schichtdicken zwischen 25 nm und 2 µm durchgeführt. Die Schichten wurden mittels Hochleistungskathodenzerstäuben (Magnetron-Sputtern) im Ultrahochvakuum auf mit amorphem Siliziumnitrid beschichteten (111) Silizium-Substraten abgeschieden. Ohne Unterbrechung des Vakuums wurden die Schichten mit einer 10 nm dicken Aluminiumoxid- oder Siliziumnitrid-Passivierungschicht bedeckt, entweder direkt nach der Cu-Abscheidung oder nach anschließendem Auslagern bei 500 °C. Die Entwicklung von thermischen Spannungen in den Cu-Schichten wurde hauptsächlich mittels der Substrat-Krümmungsmethode zwischen -160 °C und 500 °C untersucht.

Dabei wurden nur unbedeutende Unterschiede zwischen den mit Siliziumnitrid und den mit Aluminiumoxid passivierten Cu-Schichten festgestellt. Die Herstellungsparameter, die mit der Passivierungsabscheidungstemperatur in Zusammenhang stehen, hatten auch keinen erkennbaren Einfluss auf das Spannungs-Temperatur-Verhalten der Cu-Schichten. Im Gegensatz dazu besteht eine starke Abhängigkeit des thermomechanischen Verhaltens passivierter Cu-Schichten von der jeweiligen Cu-Schichtdicke. Für Schichten im Mikrometerbereich ist der Einfluss der Passivierungsschicht nicht bedeutend, was darauf hinweist, dass die Verformung hauptsächlich auf Versetzungsplastizität beruht. Mit abnehmender Cu-Schichtdicke jedoch spielt Diffusionskriechen eine zunehmende Rolle, aufgrund der zunehmenden Schwierigkeit, Versetzungen in kleinen Körnern zu erzeugen. Größeneffekte wurden durch Auftragung der Spannung bei Raumtemperatur nach der thermischen Zyklierung gegen die reziproke Schichtdicke untersucht. Zwischen 2 µm und 200 nm ist die Raumtemperaturspannung umgekehrt proportional zur Schichtdicke. Auf Cu-Schichten dünner als 100 nm übt die Passivierung einen starken Einfluss aus, indem sie Oberflächendiffusionsmechanismen effektiv unterbindet. Da Versetzungsprozesse in diesen ultra-dünnen Schichten ebenso unterbunden sind, weisen diese Cu-Schichten im gemessenen Temperaturbereich ein reines elastisches Verhalten auf. Das Fehlen von Plastizität in diesen Filmen wurde mittels *in-situ* TEM Analyse bestätigt, bei der parallele Gleitversetzungen festgestellt wurden, die während der thermischen Zyklierung unbeweglich blieben. Das für Schichten dünner als 100 nm auftretende Spannungsplateau ist darauf zurückzuführen, dass die angelegte thermische Dehnung nicht ausreicht, um Fliessen zu erreichen. Der bei -150 °C gemessene höchste Spannungswert von 1.7 GPa stellt deswegen eine untere Grenze für die tatsächliche Fliessspannung dar, da die Schichten auch bei dieser hohen Spannung elastisch blieben.

DANKSAGUNG

Die vorliegende Arbeit wurde in der Zeit zwischen Januar 2004 und April 2007 in der Abteilung von Herrn Prof. Dr. Eduard Arzt am Max-Planck-Institut für Metallforschung in Stuttgart angefertigt.

Herrn Prof. Dr. Eduard Arzt danke ich für die Aufnahme in seine Arbeitsgruppe und die Möglichkeit, diese spannende Arbeit in seiner Abteilung durchzuführen. Wertvolle Anregungen und Diskussionen mit ihm haben ganz wesentlich zum Gelingen dieser Arbeit beigetragen. Besonders geschätzt habe ich sein wiederholtes Vertrauen in mich.

Bei Herrn Prof. Dr. Gerhard Dehm möchte ich mich für die freundliche Übernahme des Mitberichts bedanken.

Ich möchte mich bei allen meinen Betreuern bedanken, die den Zug dieser Arbeit verlassen haben, oder die später eingestiegen sind.

Dem „Erfinder" meines Arbeitsthemas, Herrn Prof. Dr. John Balk, danke ich für die anfängliche Betreuung meiner Arbeit. In den 6 Monaten, in denen er mich betreut hat, durfte ich viel von ihm lernen. Er hat mir die Bedienung des Transmissionselektronenmikroskops beigebracht und dabei wertvolle Tipps gegeben. Seine Lebensphilosophie („If it's not worth doing, it's not worth doing well") hat mich weiterhin während der ganzen Doktorarbeit begleitet.

Meinem zweiten Betreuer Herrn Prof. Dr. Gerhard Dehm danke ich, dass er nach seinem Weggang aus Stuttgart immer noch für Fragen zur Verfügung stand. Augrund seiner ruhigen und liebevollen Führungsart ist er Vorbild für mich geworden.

Meiner dritten Betreuerin Frau Dr. Julie Nucci möchte ich herzlich danken, dass sie die Arbeit in der letzten Phase mit sehr viel Engagement betreut hat. Auch nach ihrem Umzug in die USA hat sie sich ungezwungen weiter eingesetzt. Ihre hilfreichen

Kommentare haben diese Arbeit wesentlich verbessert. Sehr dankbar bin ich für ihre Hilfe beim Strukturieren der Arbeit: bewundernswert war ihr Einsatz in dieser Novembernacht.

Vielen Dank auch an meinen letzten Betreuer Herrn Dr. Gunther Richter. Die volle wissenschaftliche Freiheit, die er mir gelassen hat, habe ich sehr genossen. Nichts desto Trotz war er stets bereit, mir zuzuhören, mich zu motivieren oder zu trösten.

Ich bedanke mich bei der International Max Planck Research School for Advanced Materials für die finanzielle Unterstützung, besonders bei Herrn Dr. Hans-Georg Libuda, der mich in vielen Punkten unterstützt hat.

Ohne verschiedene Serviceeinrichtungen und Techniker wäre diese Arbeit nicht möglich gewesen.

Herzlichen Dank an das Dünnschichtlabor für die Herstellung der Schichten. Besonders involviert waren die Herren Dr. Thomas Wagner, Gerhard Adam, Dr. Gunther Richter sowie Frau Ilse Lakemeyer.

Die mikroskopische Untersuchung der Schichten war ein wichtiger Teil dieser Arbeit. Vielen Dank hierbei an das Zentrum für Elektronenmikroskopie und Herrn Dr. Peter van Aken, dass ich die Transmissionselektronenmikroskope benutzen durfte. Herrn Peter Kopold und Herrn Kersten Hahn danke ich besonders für die fantastische Betreuung der Geräte. Frau Birgit Heiland hat mir liebevoll die Kunst des FIB-Mikroskops beigebracht und schöne TEM-Lamellen präpariert. Frau Natascha Sauer stand mir ebenfalls bei Fragen der TEM Präparation immer mit Rat und Tat zur Seite. Mit Frau Dr. Ulrike Wegst durfte ich die Feinheiten der REM-Bedienung lernen. Herr Dr. Gerrit Huber hat die schönen AFM Bilder dieser Arbeit aufgenommen.

Mit Hilfe von Herrn Dr. Hans-Peter Lamparter, Herrn Dr. Udo Welzel und Frau Martina Dudek konnten Röntgenuntersuchungen in der ZWE „Röntgenbeugung“ durchgeführt werden. Vielen Dank!

Für die prompte Durchführung meiner Aufträge oder einfach für kompetente Beratung gilt ein besonderer Dank: der Feinmechanischen Werkstatt, dem Tieftemperatur-Service, der Metallographischen Schule, der TEM-Präparationsgruppe vom Zentrum für Elektronenmikroskopie und der Glasbläserei.

Was wäre unsere Gruppe ohne unsere Sekretärin? Herzlichen Dank an Frau Jutta Hess für Ihre Effizienz und Nettigkeit.

Viele Experimente in dieser Arbeit hätten ohne die Hilfe von folgenden Personen nicht durchgeführt werden können:

Vielen Dank an Herrn Andreas Schneider und Herrn Dr. Thomas Wübben für die Unterstützung beim Aufbau der Kühlanlage und bei der Durchführung der Kühlexperimente. Mit ihrem unermüdlichen Rumbasteln haben sie die „Rose-TTE“ zum Laufen gebracht!

Herr Yener Kuru von der Abteilung von Herrn Prof. Dr. Mittemeijer hat röntgenographische Spannungsmessungen für mich durchgeführt. Ich danke ihm für seine Hilfsbereitschaft und sehr angenehme Art.

Bei allen Arbeitskollegen möchte ich mich für die tolle Arbeitsatmosphäre bedanken. Mit ihnen konnte ich viele interessante und bereichernde Diskussionen durchführen. Insbesondere möchte ich Frau Dr. Linda Sauter erwähnen, die immer zur Verfügung stand, um mir zu helfen, meine experimentellen oder theoretischen Probleme zu lösen. Danke auch für die netten philosophischen Gespräche!

Auch wenn es bei den Experimenten nicht geklappt hat, gab es immer einen Grund sich zu freuen zur Arbeit zu gehen: alle meine wundervollen Freunde, die ich dort kennen gelernt habe. Danke für Eure Freundschaft!

Ich mag mir nicht vorstellen, wie es gewesen wäre, mein Büro – und damit die Hälfte meines Lebens – mit jemand anderem zu teilen. Ich hatte die genialsten Bürokollegen, die man sich nur erträumen kann! Vielen Dank Gerrit! Nach der ersten Minute, in der du das Büro mit deiner Sprudelkiste betreten hast, wusste ich, dass wir uns verstehen würden. Ich glaube, wir haben gemeinsam einen Maßstab erschaffen, wie man gleichzeitig arbeiten und Spaß haben kann. Dass wir darüber hinaus Freunde geworden sind, erfreut mich besonders. Mit Shravanthi konnte ich die tolle Erfahrung mit Gerrit fortsetzen… aber diesmal auf Englisch!

Während der Arbeit habe ich nicht nur viel Wissenschaftliches gelernt, sondern auch viel Menschliches. Dank der Amerikaner, die unsere Gruppe bereichert haben, sind meine Klischees über USA zerplatzt.

Ein „Danke“ ist zu wenig für alles, was sie für mich gemacht hat. Petra war in der Zeit der Arbeit in jeder Hinsicht immer für mich da, um mir zuzuhören und mir zu helfen. Von ihrer ansteckenden Lebensfreude werde ich hoffentlich nie heilen!

Viele Freunde und Bekannte außerhalb des Instituts haben mein Leben in Stuttgart aufgepeppt. Ohne meine Franzosen-Klicke wäre ich nach meiner Diplomarbeit vielleicht nicht in Deutschland geblieben. Merci beaucoup Claire, Vincent, Lucie et Eva! Sans vous, Stuttgart aurait été un peu plus gris.

Danke auch an meine langjährigen Freunde, die Verständnis dafür hatten, dass ich mich in den letzten drei Jahren nicht viel gemeldet habe.

Meiner Familie, die mich immer wieder ermutigt hat, gilt mein herzlicher Dank. Meine Schwester Valérie, der ich „alles nachmache“, war immer ein Vorbild für mich. Die Herausforderung, besser als sie zu sein, hat sicherlich zum Gelingen meines Studiums beigetragen! Meinen Eltern danke ich, dass sie mich während meines Studiums und der Promotion in jeglicher Hinsicht immer unterstützt haben. Ich bin unheimlich glücklich solche tollen Eltern zu haben!

SYMBOLS AND ABBREVIATIONS

SYMBOLS

a	lattice parameter [m]
b	Burgers vector length [m]
b	distance between atoms in the slip direction [m]
C_{ij}	single crystal elastic stiffnesses [N/m²]
d	interplanar spacing [m]
d	grain size [m]
d^0	strain-free interplanar spacing [m]
d_{med}	median grain size [m]
d_{aver}	average grain size [m]
E	Young's modulus [N/m²]
h	thickness [m]
K	numerical constant [-]
k_B	Boltzmann constant [J/K]
k_{HP}	Hall-Petch constant [N/m$^{3/2}$]
M	biaxial elastic modulus [N/m²]
N_f	film normal
N_p	glide plane normal

n	exponential factor [-]
q	slope of the thermoelastic part of stress-temperature curves [$N \cdot m^{-2} \cdot K^{-1}$]
R	correlation factor of a linear regression [-]
R_{ref}	radius of curvature of the uncoated wafer [m]
R_{meas}	radius of curvature of the coated wafer [m]
S_d	size of a dislocation source [m]
S_{ij}	single crystal elastic compliances [m^2/N]
s	Schmid factor [-]
T	temperature [K]
T_0	temperature at which a film is free of thermal strain [K]
T_M	melting temperature [K]
T_S	substrate temperature during deposition [K]
$\dot{T}$	heating/cooling rate [K/s]
t	time [min]
x	displacement [m]
W_{gb}	energy of the misfit dislocations at the grain boundaries [J]
W_i	energy of the misfit dislocations at the film/substrate interface [J]
α	thermal expansion coefficient [K^{-1}]
α	numerical constant in the source model [-]
β_{gb}	cut-off radius of the dislocations stress fields at the grain boundary [-]
β_p	cut-off radius of the dislocations stress fields at the film/passivation layer interface [-]
β_s	cut-off radius of the dislocations stress fields at the film/substrate interface [-]
$\Delta\alpha$	difference in CTEs between film and substrate [K^{-1}]
ΔF	activation energy for obstacle controlled dislocation glide [J]
γ_s	surface free energy [J/m^2]
γ_i	interfacial free energy [J/m^2]
ε	strain [-]
$\varepsilon_{elastic}$	elastic strain [-]
$\varepsilon_{thermal}$	thermal strain [-]

$\dot{\varepsilon}_{plastic}$	plastic strain rate [s^{-1}]
$\dot{\varepsilon}_0$	pre-exponential factor for obstacle controlled dislocation glide [s^{-1}]
θ	incident angle for X-rays [°]
λ	angle between the film normal and the Burgers vector [°]
μ	shear modulus [N/m²]
ν	Poisson's ratio [-]
σ	stress [Pa]
σ_{50}	film stress at 50 °C after cycling [N/m²]
σ_0	friction stress in the Hall-Petch relationship [N/m²]
σ_{max}	theoretical strength [N/m²]
σ_y	yield stress [N/m²]
τ	shear stress [N/m²]
τ_{max}	theoretical shear stress [N/m²]
$\hat{\tau}$	athermal flow stress [N/m²]
φ	rotation angle in XRD [°]
ϕ	angle between the glide plane normal and the film normal [°]
ψ	inclination angle in XRD [°]
ψ^*	strain-free inclination angle in XRD [°]

ABBREVIATIONS

Symbol suffixes

f	film
p	passivation layer
s	substrate

General

AES	Auger Electron Spectroscopy
AFM	Atomic Force Microscope
BF	Bright Field

CTE	Thermal Expansion Coefficient
DF	Dark Field
EDX	Energy Dispersive X-ray Spectrometry
FIB	Focused Ion Beam
RT	Room Temperature
SAD	Selected Area Diffraction
SEM	Scanning Electron Microscope
TEM	Transmission Electron Microscope
UHV	Ultra-High Vacuum
UTS	Ultimate Tensile Strength
XPS	X-ray Photoelectron Spectroscopy
XRD	X-Ray Diffraction

Materials

Al	Aluminum
Al_xO_y	Aluminum oxide
Cu	Copper
Si	Silicon
SiO_x	Silicon oxide
Si_xN_y	Silicon nitride

Samples

CuR	Unpassivated as-deposited Cu films
CuA	Unpassivated Cu films annealed at 500 °C (from this study)
CuAB	Unpassivated Cu films annealed at 500 °C (from Balk)
CuAlO	Cu films passivated with Al_xO_y
CuSiN	Cu films passivated with Si_xN_y
CuSiN/RR	Si_xN_y deposited after Cu deposition at room temperature
CuSiN/AA	Si_xN_y deposited at 500 °C after Cu annealing at 500 °C
CuSiN/AR	Si_xN_y deposited at room temperature after Cu annealing at 500 °C
B1 or B2	Batch 1 or Batch 2

INDEX

Index *1*

Chapter 1 Introduction *7*

Chapter 2 Literature Review And Compilation *11*

2.1 Introduction **11**

2.2 Theoretical strength of metals **12**

2.3 Deformation mechanisms in thin films **16**

2.3.1 Dislocation plasticity 16

2.3.2 Diffusion-driven plasticity 22

2.4 Mechanics of passivated thin films **25**

2.4.1 Plasticity models 25

2.4.2 Studies of passivated films in literature 26

2.5 Compilation of the literature **29**

2.6 Summary of the literature and motivation of the study **35**

Chapter 3 Thin film systems *39*

3.1 Introduction **39**

3.2 Passivated Cu films **40**

3.2.1 Cu deposition 40

3.2.2 Aluminum oxide passivated Cu films 41

3.2.3 Silicon nitride passivated Cu films 41

3.2.4 Back side passivation 42

3.2.5 Summary 43

3.3 Unpassivated Cu films **44**

3.4 Additional samples **45**

Chapter 4 Experimental methods *47*

4.1 Introduction **47**

4.2 Microstructural characterization **48**

4.2.1 Microscopic techniques 48

4.2.2 Quantitative microstructural analysis 51

4.2.3 X-ray diffraction measurements 52

4.2.4 Surface analysis 52

4.3 Stress measurement **52**

4.3.1 Wafer curvature technique 52

4.3.2 X-ray diffraction 55

4.4 Dislocation behavior **56**

Chapter 5 Microstructural Characterization *59*

5.1 Introduction **59**

5.2 Results **60**

5.2.1 Microstructure of the Al_xO_y passivated Cu films 60

5.2.2 Microstructure of the Si_xN_y passivated Cu films of type CuSiN/AR 68

5.2.3 Microstructure of the Si_xN_y passivated Cu films of type CuSiN/AA 70

5.2.4 Microstructure of the Si_xN_y passivated Cu films of type CuSiN/RR 72

5.2.5 Microstructure of unpassivated Cu films (type CuR and CuA) 78

5.3 Discussion **79**

5.3.1 UHV-sputtered Cu films ... 79
5.3.2 Microstructure of the passivation layers ... 82
5.3.3 Pores in the CuSiN/AR/B1 films ... 83
5.3.4 Hillocks in the CuSiN/AA films thinner than 200 nm ... 83

5.4 Summary ... 86

Chapter 6 Effect Of Surface Passivation On The Mechanical Behavior Of Cu Thin Films ... 87

6.1 Introduction ... 87

6.2 Stress measurements ... 88

6.2.1 Stress-temperature curves for the Al_xO_y passivated Cu films ... 89
6.2.2 Stress-temperature curves for the Si_xN_y passivated Cu films (type CuSiN/AR) ... 94
6.2.3 Stress-temperature curves for the unpassivated annealed Cu films ... 97
6.2.4 Hysteresis of the stress-temperature curves ... 98
6.2.5 Stress at 50 °C ... 99

6.3 Dislocations ... 100

6.3.1 Dislocations in thicker films ... 100
6.3.2 Dislocations in thinner films ... 102
6.3.3 *In-situ* TEM experiment ... 104

6.4 Discussion ... 106

6.4.1 Accuracy of the stress measurement ... 106
6.4.2 Elastic properties of the films ... 106
6.4.3 Passivation effects on the thermomechanical behavior ... 108
6.4.4 Simulation of the stress-temperature curves based on dislocation glide ... 113
6.4.5 Pores as fast diffusion paths ... 116
6.4.6 Comparison of the oxide and nitride passivation layers ... 117
6.4.7 Stress at 50 °C ... 119

6.5 Summary and motivation for chapters 7 and 8 ... 127

Chapter 7 Effect Of Passivation Deposition Temperature On The Mechanical Behavior Of Cu Thin Films ... 129

7.1 Introduction and motivation ... 129

7.2 Stress measurements ... 130

7.2.1 Stress-temperature behavior 130
7.2.2 Stress at 40 °C and 50 °C 133

7.3 Dislocation behavior 135

7.4 Discussion 136

7.4.1 Stress-temperature behavior 136
7.4.2 Stress at 40 °C and 50 °C 137

7.5 Summary 140

Chapter 8 Low Temperature Behavior Of Cu Thin Films: The Stress Plateau As a Measurement Artifact? 143

8.1 Introduction and motivation 143

8.2 Experimental procedure 144

8.2.1 Wafer curvature cooling experiments 145
8.2.2 X-ray diffraction cooling experiments 147

8.3 Results 148

8.3.1 Low temperature stress evolution in unpassivated films 148
8.3.2 Low temperature stress evolution in passivated films 149
8.3.3 Thermal expansion coefficient at low temperatures 155

8.4 Discussion 156

8.4.1 Wafer curvature vs. XRD 156
8.4.2 Effect of passivation and annealing on the film properties 157
8.4.3 Stress behavior at low temperatures 158

8.5 Summary 162

Chapter 9 Summary And Conclusions 165

Chapter 10 Appendix 169

10.1 List of the literature data plotted in the masterplot 170

10.2 Correction of stresses measured with substrate curvature in passivated films 184

10.3 XPS analysis of the films 188

10.3.1 XPS spectra of a 10 nm thick Si_xN_y layer 188

10.3.2 XPS spectra of the 100 nm thick CuSiN/AR/B1 film 189
10.3.3 XPS spectra of the 25 nm thick CuSiN/RR film 190

10.4 Plotted stress values 191

10.5 Code for the simulation of thermally activated dislocation glide 192

10.6 Influence of the passivation layer thickness 193

10.7 Stress-temperature curves reproducibility for films of different batches 194

10.8 Contribution of this study to the field 195

Chapter 11 Deutsche Zusammenfassung 197

11.1 Einleitung 197

11.2 Experimente 198

11.3 Ergebnisse und Diskussion 199

Chapter 12 References 205

CHAPTER 1

INTRODUCTION

Since the appearance of mankind on earth, many human and technological revolutions have been triggered by man's increasing ability to master metals[1]. After using stone tools for millions of years in the Stone Age, prehistory came to an end when our ancestors first began making tools from hammered copper ore in the fourth millennium BC. The Copper Age, in which man first started using metals, is considered to be the first technological revolution. Over the course of the next one thousand of years copper tools and jewelry became widespread and revolutionized man's way of life. The Bronze Age and modern metallurgy began by 2500 BC with the discovery of alloying and the development of enduring metallurgical techniques including melting, forging or casting. The Iron Age began by 1000 years BC with the invention of the bloomery, a furnace and forge in which wrought iron in the form of blooms is made directly from the ore. Much more efficient tools could now be fabricated and this era is followed by a

ceaseless extension of metallurgical know-how. The continual improvement of processing techniques and specifically the invention of the blast furnace in the Middle Age gave rise to the iron industry. Later, progress in metallurgy made mass production of iron possible. This led to the introduction of steam power fuelled by coal and of powered machinery characteristic of the second big revolution of mankind: the industrial revolution of the 19th century. Many improvements including the Bessemer process for steel manufacturing contributed to the increasing role of metals in modern society. During the 20th century, the creation of powerful analytical tools such as electron microscopes enabled the scientific research that revealed how a materials' microstructure is correlated to its measured properties. This accumulation of knowledge supported the rise of computer technology with the development of integrated circuits, which was the prerequisite for the revolution we are currently experiencing. The exponentially-increasing demand for powerful microelectronic devices requires constant device miniaturization to improve speed and performance. As feature sizes decrease to the nanoscale, scientists today are overwhelmed with new questions. Down to which dimensions are bulk properties preserved? When are dimensions small enough that bulk properties no longer exist and how does the material actually behave? How can science exploit these novel and sometimes exceptional properties? The answers to these questions are key to the success of the nanotechnology revolution. In this context, this dissertation aims humbly at improving our insight into size effects on the mechanical properties of thin metal films.

The race toward ever-smaller scales is intimately related to thin film technology. Thin metal films are especially critical in microelectronics, where they are used as interconnect metallization. Figure 1.1 shows a cross-sectional micrograph of the interconnect wiring of an integrated circuit chip processed with the recent Intel® 65 nm manufacturing technology. Due to the difference in thermal expansion coefficients (CTE) between the metal films and the surrounding materials, thermal stresses arise during manufacturing and in operation. These stresses can trigger film delamination, cracking, and lead to device failure. A solid understanding of the mechanical properties of thin films is therefore essential to ensure the performance, reliability, and lifetime of thin film devices.

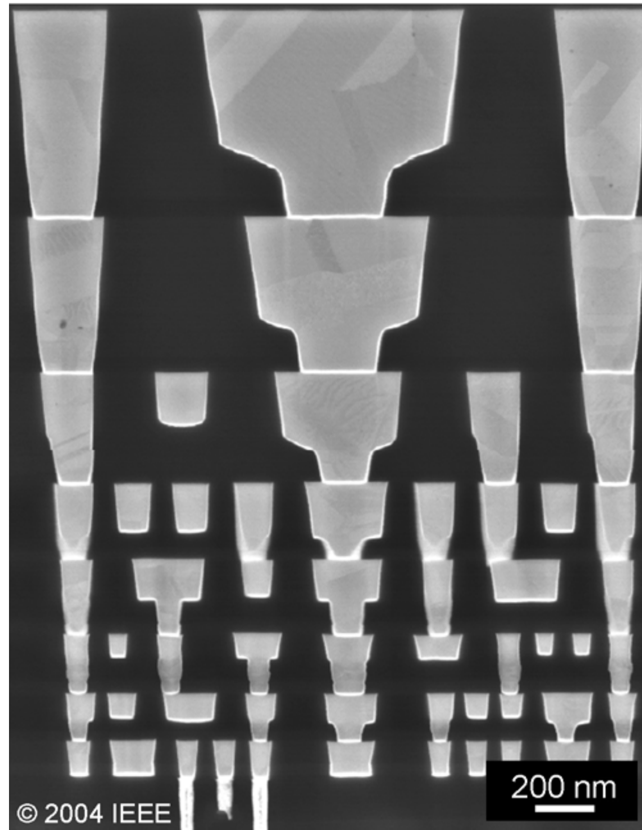

Figure 1.1: Cross-sectional image of the interconnect wiring of an integrated circuit processed with the 65 nm technology by Intel®. Eight layers of Cu metallization are visible. The features are reaching sizes down to about 100 nm. Authorized reproduction from [2].

Comprehending and optimizing the mechanical properties of thin films is not only a fundamental challenge for technological applications, but is also a beloved topic in materials research. The academic interest in this field is due to size effects. The mechanical properties of geometrically and/or microstructurally constrained materials, such as thin films, indeed differ greatly from the bulk properties. The most surprising feature is that thin films show much higher flow stresses compared to their bulk counterparts. However, thin film plasticity is complex, depending on many parameters such as film thickness, grain size, and nature of the interfaces. Despite a large number of studies in this field, further research is still necessary to understand the exact mechanisms accounting for size effects.

Thermal stresses arising in thin films can be relaxed by dislocation and/or diffusive processes. A free film surface, which geometrically constrains dislocation motion[3] and is a dominant diffusion path[4], plays a crucial role in thin film deformation. Suppressing

surface diffusion in thin films is expected to alter the contributions of dislocation- and diffusion-based plasticity, and thus is likely to clarify their role during deformation. Thin films can be effectively passivated through the deposition of a carefully selected material onto their surface. An extensive amount of work was done to characterize the mechanical behavior of passivated films down to the sub-micrometer regime. However, only very limited experimental data was collected for nanoscale films with thicknesses below 100 nm.

The present work contributes this body of knowledge through the study of passivated copper (Cu) films on substrates with thicknesses ranging from 25 nm to 2 µm. Cu was first investigated as an alternative to aluminum (Al) metallization in the early 1990s and has been extensively studied since its industrial incorporation as an interconnect metallization in 1998 (see Figure 1.1). Since Cu rapidly diffuses into silicon (Si), where it poisons device performance, Cu metallization always requires encapsulation by thin diffusion barriers to keep it from reaching the Si. In addition, thick dielectric layers are deposited as interlevel dielectrics or as passivation layers around Cu lines. It thus appears critical to understand how the mechanical properties of Cu films are affected by surface passivation, both for industrial applications and fundamental knowledge.

Three main topics will be addressed in this study. First, the effect of a passivation layer on the film deformation mechanisms will be investigated. Second, the importance of the processing parameters during passivation will be examined. Finally, the interesting film behavior at liquid nitrogen temperatures measured using a unique wafer curvature cooling setup will be described. All these aspects will shed new light on the deformation mechanics of micron- and nanosized metallic materials.

CHAPTER 2

LITERATURE REVIEW AND COMPILATION

2.1 Introduction

Compared to their bulk counterparts, thin metal films exhibit much higher flow stresses. Over past 20 years, many studies on a variety of materials have been carried out to understand this size effect[5]. Two principal reasons for this strengthening effect were reported: constrained plasticity due to the film thickness[3] and microstructural constraints within the film, such as grain boundaries[6,7]. Diffusion at elevated temperature also plays an important role in thin film stress evolution. In this chapter, the main experimental and theoretical advances in thin film thermomechanical behavior will be summarized. First, a short review of the principal models estimating the theoretical strength of metals is provided as a reference point to better understand flow

stress values. In a second part, the current understanding of the field is described. A third section is specifically dedicated to an extensive evaluation of the literature regarding the mechanical behavior of passivated films. The main experimental results are compiled into a single "masterplot" and discussed. The uncertainties and questions brought to light by the "masterplot" motivate this dissertation.

2.2 Theoretical strength of metals

To better comprehend the flow stress values discussed in the literature review and reported in this dissertation, it is necessary to understand where these film stress values lie compared to the maximum theoretical strength a metal can sustain. This strength was estimated with different models.

Frenkel (1926) produced the simplest calculation of the theoretical shear stress, τ_{max}, of a crystal[8]. In this estimate, a crystal is subjected to a simple shear mode of deformation. He considered the shearing of two neighboring planes of atoms past each other, in the direction of shear, as shown in Figure 2.1(a).

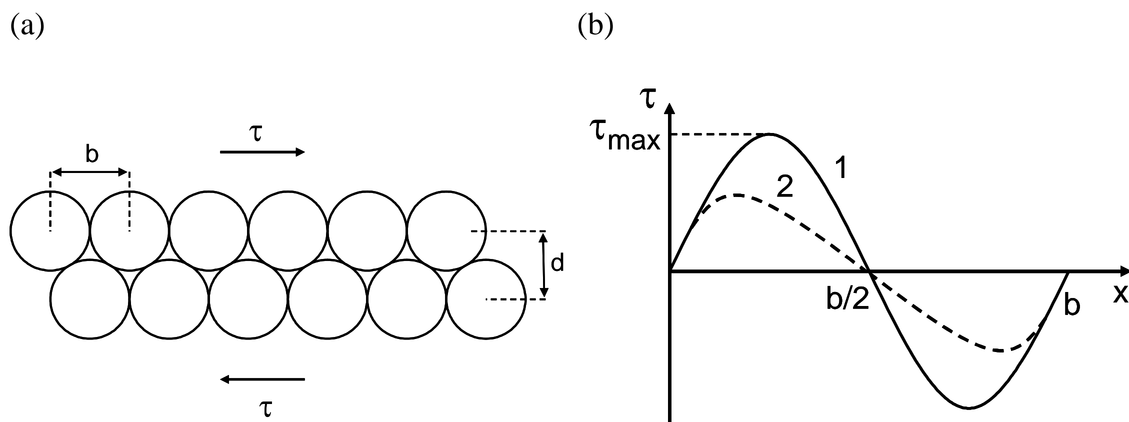

Figure 2.1: Estimation of the theoretical shear strength of a crystal. (a) Sketch representing the shearing of two atomic rows of atoms. (b) Applied shear stress τ as a function of the relative displacement x approximated with a sinusoidal function in Frenkel's model[8] (1) and with a more realistic function (2) as proposed by Orowan[9].

In this model, the crystal is homogeneously strained and the planes are assumed to be undistorted by the imposed shear. The planes are spaced with a distance *d* and the atoms along the slip direction with a distance *b*. The shear stress, τ, to shear the upper plane over the lower one over a distance *x* can be modeled by a sinusoidal function as shown by the curve (1) in Figure 2.1(b):

$$\tau = K \sin\frac{2\pi x}{b} \tag{2.1}$$

The constant *K* is determined by the condition that the initial slope must agree with the shear modulus, μ, of the material.

According to Hooke's law, for small *x*:

$$\tau = \mu\frac{x}{d} \tag{2.2}$$

In addition, close to the origin we have:

$$\tau = K\frac{2\pi x}{b} \tag{2.3}$$

A combination of Equations (2.2) and (2.3) gives following expression for *K*:

$$K = \frac{\mu b}{2\pi d} \tag{2.4}$$

The shear stress, τ, finally is:

$$\tau = \frac{\mu b}{2\pi d}\sin\frac{2\pi x}{b} \tag{2.5}$$

The maximum stress at which the lattice becomes mechanically unstable and slip should take place occurs for $x = \frac{b}{4}$ and hence:

$$\tau_{max} = \frac{\mu b}{2\pi d} \tag{2.6}$$

In a rough approximation, $b \cong d$. Thus,

$$\tau_{max} \cong \frac{1}{2\pi}\mu \tag{2.7}$$

Despite the simplicity of Frenkel's approach, it has nevertheless been subjected to various criticisms. The sinusoidal relation in the above calculation is controversial. Orowan[9] first pointed out that Frenkel's model overestimates the theoretical shear strength and that a more realistic law for the forces between atoms should be taken. Frenkel's model takes no account of possible configurations of mechanical stability the lattice may pass through while sheared. The shear stress-displacement curve should oscillate with a smaller period than the atom distance *b*, as shown schematically in curve (2) Figure 2.1(b).

Mackenzie (1949)[10] took this aspect into account in a refinement of Frenkel's model. He derived the expression of the variation of potential energy between two neighboring planes, *U(x)*, from equation (2.5), knowing that:

$$\tau = \frac{\partial U(x)}{\partial x} \tag{2.8}$$

U(x), which represents the stored elastic strain energy of the crystal per unit area of shear plane, is then:

$$U(x) = \frac{\mu b^2}{4\pi^2 d}\left(1 - \cos\frac{2\pi x}{b}\right) \tag{2.9}$$

He recognized in this equation the first two terms of a Fourier series for *U(x)* and

proposed to take into account the higher order terms in the series to get a better approximation of the energy. He deduced the coefficients of the other terms from general considerations about interatomic forces and stability positions in the sheared lattice. In the case of a face-centered cubic metal, he showed that the theoretical shear strength can be calculated with:

$$\tau_{max} \cong \frac{1}{30}\mu \tag{2.10}$$

This value is said to be the lowest limit of the theoretical shear strength. A detailed description of the mathematics of Mackenzie's approach is to be read in [11].

Bragg and Lomer came to the same conclusion as Mackenzie with bubble raft studies[12,13]. They simulated a perfect Cu crystal by adjusting the bubble size in their raft so that the elastic interactions between the soap bubbles were comparable to that between Cu atoms. The critical strain to initiate shear in the bubble raft corresponded to a shear strength of $\mu/30$.

Later attempts to estimate the theoretical shear strength focused on finding a realistic expression for the energy, *U(x)*, and are presented in a review paper of Macmillan[14].

Following the previously described models, numerical values of the theoretical shear strength were calculated for Cu. In addition, the theoretical strength, σ_{max}, was calculated according to:

$$\sigma_{max} = \frac{\tau_{max}}{s} \tag{2.11}$$

where s is the Schmid factor.

Table 2.1 provides an overview over the different models and values obtained.

Table 2.1: Expressions and numerical values of the theoretical shear stress of Cu following calculations of Frenkel and Mackenzie. The calculation required use of following constants: μ_{Cu} = 42.1 GPa[15] and s = 0.27 for a (111)-textured face-centered cubic film under biaxial stress.

Model	Theoretical shear strength τ_{max}		Theoretical strength σ_{max}
	Expression	Value for Cu [GPa]	Value for Cu [GPa]
Frenkel	$\tau_{max} \cong \frac{1}{2\pi}\mu$	6.7	24.8
Mackenzie	$\tau_{max} \cong \frac{1}{30}\mu$	1.4	5.2

A value of 5.2 GPa will be assumed for the theoretical strength of Cu for this dissertation, since it was determined with the most realistic model. This high value for the theoretical strength is obviously to be contrasted with the experimentally measured yield stresses for e.g. bulk Cu. Values between 30 and 100 MPa are indeed found, depending on the cold working and annealing conditions of the measured specimens[16]. This difference is explained by the presence of defects in real crystal structures. In particular, dislocations reduce the plastic flow stress to well below that of the ideal shear strength.

2.3 Deformation mechanisms in thin films

As found in many studies, film strength increases with decreasing dimension, i.e. film thickness and/or grain size (e.g. [17,18]). Models and simulations of deformation for a thin film with a free surface based on dislocation plasticity and diffusion are described in this section and compared with experimental results.

2.3.1 Dislocation plasticity

Dislocation motion is one of the controlling mechanisms in thin film plasticity. Models based on dislocation confinement in the film, on grain boundaries acting as dislocation

barriers or on lack of mobile dislocations were derived.

In a single-crystalline thin film, dislocation motion is confined within the film due to its finite thickness. Following a study carried out by Freund[19] on the stability of misfit dislocations in epitaxial films, Nix[3] developed a model accounting for film thickness effects due to the presence of interfaces. He considered the channeling of a single dislocation in a single-crystalline thin film on a substrate under biaxial compression. Since the dislocation is confined in the film, a misfit dislocation segment will be deposited near the film/substrate interface as the threading dislocation glides on its slip plane. Figure 2.2 shows a sketch illustrating the Nix-Freund model.

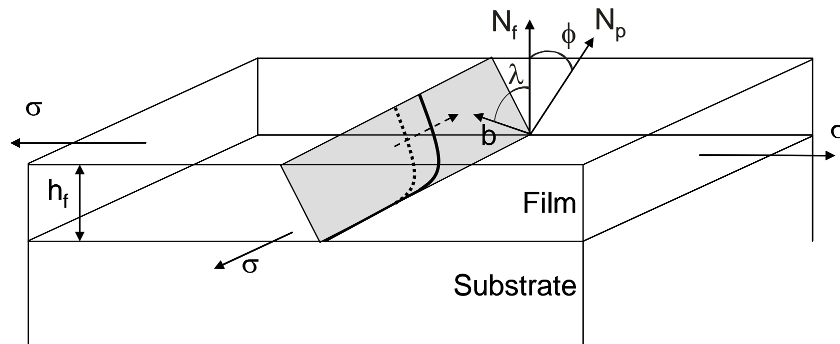

Figure 2.2: Sketch illustrating the Nix-Freund model. A threading dislocation moves in a thin film on a substrate under a biaxial stress σ on an inclined plane and deposits a misfit dislocation segment at the film/substrate interface.

By making an energy balance between the energy release due to dislocation motion and the stored line energy of the misfit dislocation, Nix derived the following equation expressing the stress needed to move the dislocation:

$$\sigma_{Nix} = \frac{\sin\phi}{\cos\phi\cos\lambda} \frac{b\,\mu_{eff}}{2\pi(1-\nu_f)\,h_f} \tag{2.12}$$

The quantity μ_{eff} can be interpreted as an effective shear modulus and shows a weak dependence on film thickness:

$$\mu_{eff} = \frac{\mu_f \mu_s}{\mu_f + \mu_s} \ln\left(\frac{\beta_s h_f}{b}\right) \tag{2.13}$$

where ϕ and λ are the angles between the glide plane normal N_p and the film normal N_f, and between the film normal and the Burgers vector b, respectively. ν_f is the Poisson's ratio of the film, h_f and h_s the thicknesses of the film and the substrate, respectively. μ_f is the shear modulus of the film and μ_s the shear modulus of the substrate. β_s is a numerical constant defining the cut-off radius of the stress fields of the dislocations at the substrate interface. The most remarkable feature of Nix-Freund model is that, at first approximation, it predicts a strong dependence of the film strength on the film thickness, varying approximately linearly with the inverse of the film thickness h_f^{-1}.

The validity of Nix-Freund model was confirmed experimentally with flow stress measurements of epitaxial Cu and Al films on single-crystalline Al_2O_3 substrates[20-22]. Moreover, as predicted by the model, threading dislocations with misfit segments at the interface were observed with *in-situ* transmission electron microscopy (TEM) in these Cu[22,23] and Al films[20,21,24]. However, polycrystalline Cu and Al films on Si with amorphous SiO_x and Si_xN_y interlayers and polycrystalline Cu films on Al_2O_3 show significantly higher stresses than predicted by the Nix-Freund model, but still depend linearly on the inverse of the film thickness[22,23,25]. During *in-situ* TEM studies of these films, the film/substrate interface was observed to act as a dislocation sink and no stable misfit segments were found[20,22,26-28]. One of the reasons why the Nix-Freund model underestimates the flow stresses of polycrystalline films is that it does not take into account obstacles to dislocation motion, such as interactions with grain boundaries or with other dislocations.

Thompson extended the Nix-Freund model to take the grain size contribution on the flow stress into account[6,7]. It is indeed found that thin films have small grain sizes (in the order of the film thickness), which makes it necessary to consider grain size strengthening. In this model, Thompson additionally considers that misfit segments are laid down at the grain boundaries (Figure 2.3).

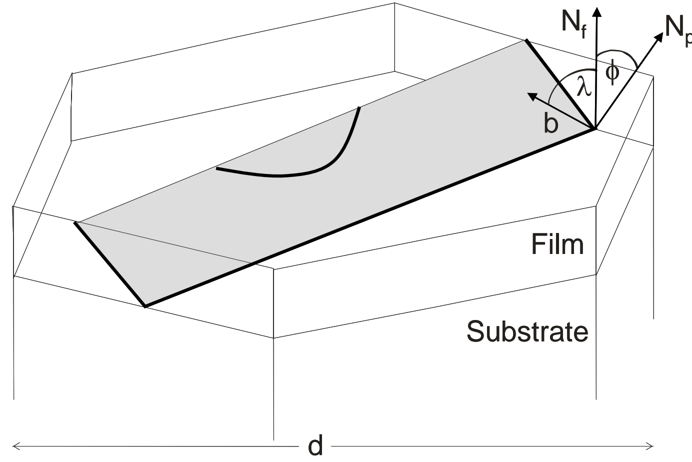

Figure 2.3: Sketch of a dislocation moving through a grain with misfit segments deposited at the grain boundaries and at the film/substrate interface, according to Thompson model.

He assumes that the energy required to deposit these segments is similar to the energy of the interfacial dislocation segments. The flow stress is then given by the following expression:

$$\sigma_{Thompson} = \frac{\sin\phi}{b\,\cos\phi\,\cos\lambda}\left(\frac{W_i}{h_f} + \frac{2W_{gb}}{d\,\sin\phi}\right) \tag{2.14}$$

where d is the grain size, W_i the energy of the misfit dislocations at the film/substrate interface, with an expression similar to the one used in the Nix-Freund model:

$$W_i = \frac{b^2}{4\pi(1-\nu_f)}\,\frac{\mu_f\mu_s}{\mu_f+\mu_s}\ln\left(\frac{\beta_s h_f}{b}\right) \tag{2.15}$$

and W_{gb} the energy of the misfit dislocations at the grain boundaries:

$$W_{gb} = \frac{b^2\mu_f}{4\pi(1-\nu_f)}\,\ln\left(\frac{\beta_{gb} d}{b}\right) \tag{2.16}$$

where β_{gb} is a constant describing the cut-off radius of the dislocation at the grain boundary. According to the above equations, the flow stress of the film increases both with decreasing film thickness and with decreasing grain size.

Such a dependency was reported by Venkatraman *et al.* for polycrystalline Al films[17]. With substrate curvature measurements, they showed that, at constant grain size, the room temperature yield stress varies linearly with the reciprocal film thickness. Both the film thickness and grain size contributions need to be taken into account to predict the stress values.

A similar study was carried out for polycrystalline Cu films with thicknesses of 600 nm and 1 µm by Keller *et al.*[18]. The flow stress was shown to be proportional to the inverse square root of the grain size *d*. This type of dependence is known for bulk metallic materials and was described by Hall and Petch[29,30]. They predicted that yield stress should increase with decreasing grain size following the relationship:

$$\sigma_y = \sigma_0 + k_{HP}\, d^{-\frac{1}{2}} \tag{2.17}$$

where σ_y is the yield stress, σ_0 the friction stress representing the resistance of the crystal lattice to dislocation movement and k_{HP} the locking parameter measuring the relative hardening contribution of the grain boundaries. However, in Keller's study, the measured Hall-Petch coefficient, k_{HP}, was about three times larger than that of bulk Cu.

To properly model the experimental results, one should add to the film thickness and grain size contributions the dislocation interactions, which also represent a microstructural constraint on dislocation motion. For the Cu films of Keller *et al.*, the dislocation density determined with X-ray diffraction (XRD) was shown to increase with decreasing film thickness. Qualitative agreement between measurements and models could be achieved by taking dislocation interactions into account[18].

Nix theoretically analyzed strengthening effects due to obstacle dislocations[31]. A moving threading dislocation may be repelled from a misfit dislocation already present at one interface. A strength increase of a factor of about 2.6 is predicted for a 1 µm thick film. However, this approach remains incomplete since no attractive interaction between dislocations was considered.

Simulations of dislocation interactions were also carried out[32-37]. In these studies, discrete dislocation dynamics within a two-dimensional framework was used to

simulate strain-hardening. Pant *et al.* predicted a flow stress increase due to the interaction between two dislocations, which was nevertheless smaller than for the Nix approach[33,34]. Furthermore, Nicola *et al.* proposed an explanation for size effects in thin films that assumes a hard boundary layer at the film/substrate interface is formed. The width of the boundary layer, which arises from dislocation pile-ups at the interface, does not scale with film thickness[36]. This was observed with TEM by Xiang *et al*. for free-standing electroplated Cu films[38]. However, the necessity to perform three-dimensional simulations to describe thin film behavior was pointed out. Moreover, strain hardening cannot account for higher flow stresses in ultra-thin films, since TEM observations of polycrystalline Cu films revealed a decrease of dislocation density with decreasing film thickness between 400 and 100 nm[22].

Until now, only models based on dislocation glide were reported. Von Blanckenhagen *et al.* developed a model to account for the flow stress increase with decreasing film thickness based on dislocation nucleation[39-42]. Their three-dimensional simulations of thin film plasticity suggested that the ability to activate dislocation sources might control plastic yielding in thin films. The flow stress in the film can be related to the size of a dislocation source, S_d, by following Orowan-type equation[39,40]:

$$\sigma_{Source} = \frac{1}{s}\frac{\mu_f b}{2\pi}\frac{1}{S_d}\ln\left(\frac{\alpha S_d}{b}\right) \qquad (2.18)$$

where α is a numerical constant.

In a free-standing film, the stress for repeated activation of the source was shown to be minimized when its size is equal to one third of the smaller of film thickness or grain size. For $d > h_f$, the source size is:

$$S_d = \frac{h_f}{3} \qquad (2.19)$$

The combination of Equations (2.18) and (2.19) gives the following expression for the film yield stress according to this model, called the source model:

$$\sigma_{Source} = \frac{1}{s}\frac{3\mu_f\, b}{2\pi}\frac{1}{h_f}\ln\left(\frac{\alpha\, h_f}{3b}\right) \tag{2.20}$$

This expression is similar to that of the Nix-Freund model, showing the same dependency on the inverse of the film thickness, but with about three times larger stress values. With this model, the flow stress values are reasonably well predicted for polycrystalline Cu films thicker than 400 nm[43]. In thinner films, the stress becomes independent of film thickness[25], as will be discussed now. However, there is no experimental verification of this model available yet.

2.3.2 Diffusion-driven plasticity

Compared to bulk materials, thin films exhibit a higher volume fraction of grain boundaries and interfaces, which represent fast diffusion pathways. Diffusion is therefore more likely to be a dominant deformation mechanism for thin films at high temperatures than for bulk materials. In particular, stress relaxation by diffusional creep can occur. Many attempts were made to simulate the stress-temperature behavior of thin films with bulk constitutive equations for creep deformation[44-47]. These calculations were based on power-law creep, power-law breakdown, or diffusional creep. However, they did not take into account the specific thin film geometry. Whereas creep mechanisms are often controlled by grain-boundary diffusion in bulk materials[48,49], surface and interfacial diffusion must also be considered in the case of thin polycrystalline films on substrates, due to their high interface to volume ratio. For a well-bonded film such as Al, it is reasonable to assume that diffusion along the film/substrate interface is much smaller than at the free surface. Jackson and Li proposed that diffusional relaxation of a film would relax material near the surface but not near the substrate[50]. Thouless formulated this problem mathematically, implicitly allowing the grains to slide freely on the substrate[51]. This model was improved by Gao *et al.*, who provided the first rigorous mathematical analysis of grain boundary diffusional creep constrained by a substrate in a film with a free surface[52]. In this model,

no sliding or diffusion along the film/substrate interface was allowed. Only diffusion at grain boundaries and at the film surface can occur. Surface diffusion was considered to be too fast to be rate controlling, and the effect of grain boundary grooving was neglected. At elevated temperatures, for a film under tension, atoms can diffuse from the surface into the grain boundaries and accumulate there, forming a grain boundary wedge (Figure 2.4). The wedge was modeled as an array of climbing edge dislocations. The stress distribution around a relaxed grain boundary resembles that of a mode I crack, exhibiting an inverse square-root stress singularity near the wedge tip at the film/substrate interface. The stress field is inhomogeneous both in the film plane and in the direction normal to the film plane and enhances dislocation plasticity processes in the film. Due to this singularity, shear stresses act also on planes parallel to the film/substrate interface, even if they are, under a homogeneous biaxial stress state, free of shear stresses.

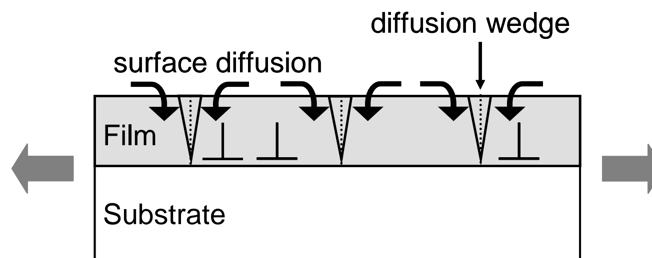

Figure 2.4: Sketch illustrating Gao's model of constrained diffusional creep[52]. At high temperatures, in a film under tensile stress, atoms diffuse from the surface into the grain boundaries where they form diffusion wedges. These wedges represent stress singularities and enhance dislocation plasticity processes.

This type of dislocation motion was observed by Balk *et al.* in polycrystalline Cu thin films thinner than 400 nm during *in-situ* TEM thermal cycling experiments[25,43,53-55]. Dislocation glide occurred on (111) planes parallel to the film/substrate interface. These dislocations were absorbed by the grain boundaries upon heating and were emitted upon cooling. An example of so-called "parallel glide dislocations" observed in a 270 nm thick Cu film is shown Figure 2.5 after thermal cycling.

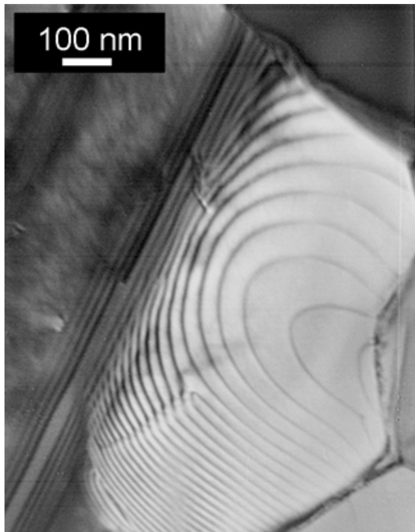

Figure 2.5: TEM image of parallel glide dislocations observed in a (111)-oriented grain in a 270 nm thick Cu film. Figure by courtesy of T. J. Balk[56].

A detailed analysis of dislocation densities and plastic strain showed that parallel glide dislocations accounted for most of the plastic deformation in ultra-thin films. The density of threading dislocations was also observed to decrease with decreasing film thickness; the activation energy of these dislocations being supposedly too high in ultra-thin films. In summary, the change of deformation mechanism for films thinner than 400 nm can be explained by constrained diffusional creep. Moreover, in the same thickness range, the flow stress no longer depends on the film thickness[25]. Thus, the origin of the stress plateau was attributed to the presence of parallel glide dislocations in the ultra-thin films. Due to their nature, their activation is supposed to be equally difficult in all the ultra-thin films, becoming thickness-independent.

Simulations of stress-temperature curves based on constrained diffusional creep were carried out by Weiss *et al.*[57-59]. Thermally activated dislocation glide was also included in the model. The simulated curves showed a good qualitative agreement with experimental data. Thus, stress relaxation at high temperature could be clearly attributed to constrained diffusional creep. A different approach by Bühler *et al.* could also reproduce the behavior at elevated temperatures[60]. They included a threshold stress for the onset of constrained diffusional creep, motivated by discrete dislocation dynamics simulations.

2.4 Mechanics of passivated thin films

Until now, the review was limited to models and experimental results for thin films with a free surface and revealed the predominant role of surface diffusion. Passivating the film surface is expected to suppress surface diffusion. Following the argument of Jackson and Li[50] stipulating that mass transport is negligible at the film/substrate interface, it is indeed reasonable to assume that a well-bonded surface passivation resist diffusional flow. The suppression of surface diffusion is therefore expected to change dramatically the mechanical behavior of the films. In this section, the influence of passivation is treated following the concepts of the different plasticity models. The main results of experimental and theoretical studies of passivated films will also be provided.

2.4.1 Plasticity models

The Nix-Freund model also applies to passivated films[3]. For the case of a non-shearable passivation, a dislocation dipole is created in the film as the dislocation moves. Misfit dislocations are deposited at both the film/substrate and the film/passivation interface, as schematically shown in Figure 2.6.

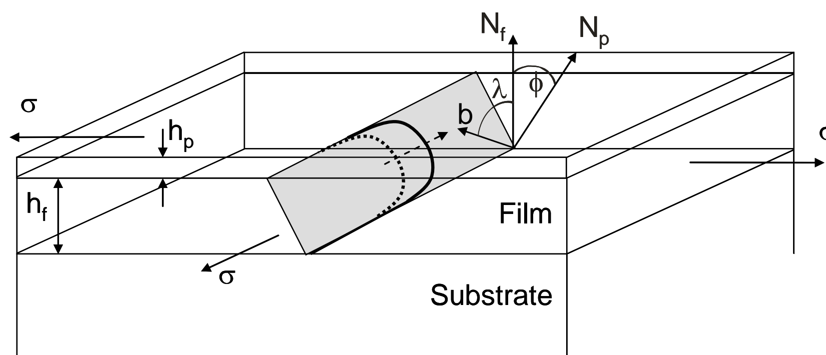

Figure 2.6: Schematic illustrating the Nix-Freund model in a passivated film. The dislocation threading through the film deposits a misfit segment at both the film/substrate and the film/passivation layer interface.

Following this approach, a passivation term is added to the expression of the effective shear modulus, μ_{eff}, given in Equation (2.13):

$$\mu_{eff} = \frac{\mu_f \mu_s}{\mu_f + \mu_s} \ln\left(\frac{\beta_s h_f}{b}\right) + \frac{\mu_f \mu_p}{\mu_f + \mu_p} \ln\left(\frac{\beta_p h_p}{b}\right) \tag{2.21}$$

with the index p referring to the passivation layer. From this equation, it appears that the Nix-Freund model predicts higher yield stresses for passivated films compared to unpassivated films.

In the extension of his model, Nix incorporated strain hardening effects in passivated films[31]. A threading dislocation moving through the film is forced to squeeze in between the two dislocations that comprise the misfit dipole obstacle. For a 1 µm thick film, the film stress is predicted to be 4.4 higher than for an unpassivated film without dislocation obstacles. This is to be compared to the stress increase of 2.6 obtained for unpassivated films.

The source model can also be applied to a passivated film with an optimal source size, S_d, four times smaller than the film thickness[40,41]:

$$S_d = \frac{h_f}{4} \tag{2.22}$$

2.4.2 Studies of passivated films in literature

A number of experimental data on the mechanical behavior of passivated films can be found in the literature. Both naturally and artificially passivated metal films were studied with different techniques (wafer curvature, tensile testing, bulge testing). Al films, for which the presence of a strong, adherent native oxide serves as a "natural" passivation, have been extensively examined. Compared to Cu, Al films exhibit a different stress-temperature behavior[17,46,61]. In particular, fine-grained Al films are able to sustain biaxial stresses of several hundred MPa at temperatures as high as 400 °C[17]. This behavior was attributed to the passivation layer, which inhibits diffusional deformation and causes the plastic deformation to be dominated by dislocation

processes within the grains. Like for unpassivated Cu films, a linear dependency of the flow stress upon the inverse of the film thickness was observed for Al polycrystalline films thicker than 400 nm. For films with thicknesses between 100 and 400 nm, a stress plateau was reported[22].

Many studies were conducted on artificially passivated films. As for Al, a particular thermomechanical behavior was reported for passivated Cu films[18,38,45,46,62-69]. Vinci *et al.* investigated the influence of different passivation layers (Ta or Si_3N_4) on the mechanical properties of Cu films with thicknesses ranging from 200 nm to 1.2 µm thick[45,62,63]. The observed behavior was independent of both the passivation layer nature and thickness. Following the classical mechanism theoretically described by Gibbs[49], Vinci pointed out that a film with a columnar grain structure under biaxial stress requires atomic transport between the film surface and grain boundaries for diffusional creep to occur. The inhibition of surface diffusion could hence suppress diffusional creep in a thin film without affecting the power-law creep processes. The same argument was used by Thouless *et al.* and Keller *et al.* to account for the behavior of passivated Cu films[18,46]. Indeed, the stress at 600 °C of 450 nm to 1 µm thick Cu films passivated with 50 nm Si_xN_y was shown to increase by an order of magnitude compared to unpassivated films[18]. Moreover, a linear dependence of the flow stresses at room temperature with the inverse of the film thickness was found. The high stress values could be explained by superimposing the Nix-Freund model, grain size strengthening and strain hardening. An anomalous thermomechanical behavior was reported in passivated Cu film exposed to air before passivation with Si_xN_y in several studies[64,67,70-72]. An increase in compressive stress at elevated temperatures was observed after the film stress had been at a constant level near zero over a certain temperature range. The weakening of the film adhesion due to the exposure of the interface to oxygen is a possible explanation. Compared to unpassivated films, a significant increase of the flow stress is reported by Xiang *et al.* for 800 nm to 10 µm thick free-standing electroplated Cu films passivated with Ti on both sides of the membrane[38]. The flow stress was also proportional to the inverse of the film thickness. SiO_x-passivated 40 to 400 nm thick Cu films analyzed with wafer curvature by Shen *et al.* are the thinnest films available in literature[66,68,69]. Very high room temperature stresses reaching 1 GPa are explained by a strong strain hardening.

Alloyed Cu films were also studied and shown to behave like passivated films. Weiss *et al.* examined 500 nm to 1 µm thick Cu-1% Al alloyed films produced under ultra-high vacuum conditions and compared their stress-temperature behavior to pure Cu films prepared under the same conditions[57-59]. The unpassivated films showed stress relaxation at high temperatures which could be clearly attributed to diffusional creep whereas this stress relaxation was absent in the Cu-1% Al films. In these films, Al supposedly segregated and oxidized at the surface producing a self-passivating effect.

Several studies on other metals corroborate the trends detailed for Al and passivated Cu films. Kobrinsky and Thompson studied both bare and passivated polycrystalline Ag films on Si substrates with thicknesses ranging from 0.2 to 1.2 µm[73]. They noticed that the flow stress in the passivated films increased with decreasing film thickness. For bare films, the flow stress increased with decreasing film thickness between 1.2 µm and 0.5 µm but then decreased with further decrease in film thickness. Also noble metals were studied. Leung *et al.* [74-76] measured the stresses of bare and passivated Au films with thicknesses ranging from 0.2 to 2.5 µm with wafer curvature. The stress-temperature curves of passivated films could be described based on dislocation plasticity and the yield stresses were inversely proportional to the film thickness.

Lots of effort was put into simulating the stress-temperature behavior of passivated films. Flinn *et al.* first described the general shape of stress-temperature curves of Al films using a law for thermally-activated dislocation glide[77]. The same mechanism was invoked by Thouless *et al.* for passivated noble metal films[46] and by Weiss *et al.* to describe the behavior of a 500 nm thick Cu-1% Al film[59]. However, this model failed to describe some features of the curves including the observed compressive stress plateau between 300 and 500 °C upon heating. Shen improved this model by incorporating kinematic strain hardening[66,68,69]. With this model, the stress-temperature behavior of passivated Cu films[66,68,69] and passivated Au films[76] could be predicted in a satisfactory way. Nevertheless, it is based on debatable assumptions: the yield stress is assumed to decline linearly with temperature and the work hardening is taken constant with increasing strain. Moreover, it has substantial latitude in fit, with three variables to empirically fit the model to the data.

Only very few TEM studies of passivated films are to be found in literature. Balk *et al.*

examined a 200 nm thick self-passivated Cu-1% Al film. In contrast to an equally thick unpassivated Cu film, in which parallel glide dislocations dominate, only threading dislocation motion was observed[25,55]. Jawarani *et al.* carried out *in-situ* TEM studies of a 600 nm Al-1% Cu film passivated with phosphor-silicate-glass and silicon nitride[78]. Both edge and screw dislocations were found to have caused slip on inclined (111) planes and multiple slip (two or more sets of intersecting slip traces) was frequently observed. Microstructural investigations showed that grain size and encapsulation are the major contributions to the strength of a thin film with a given thickness. Additional strengthening was provided by interactions between dislocations on multiple slip systems.

2.5 Compilation of the literature

As highlighted in the literature review, a substantial body of experimental work was undertaken to better understand the mechanical behavior of several thin metal films, including free-standing films and those deposited on substrates, with and without passivation. This huge amount of data makes it difficult to have a global vision on the field. Before beginning with experiments, the initial work of this dissertation was to compile and distill a subset of the literature data. This was essential to truly understand the field, to identify the unresolved features and to bring to light the remaining challenges.

Studies in which several film thicknesses were compared are included for Ag, Al, Au and Cu films. The collected data is presented in Figure 2.7 where the normalized film stress is plotted vs. the film thickness h_f. The stress values were normalized with respect to the shear moduli of the different materials: μ_{Ag} = 26.4 GPa, μ_{Al} = 25.4 GPa, μ_{Cu} = 42.1 GPa (from [15]) and μ_{Au} = 27.6 GPa (calculated from E_{Au} = 78.5 GPa and ν_{Au} = 0.42[79]).

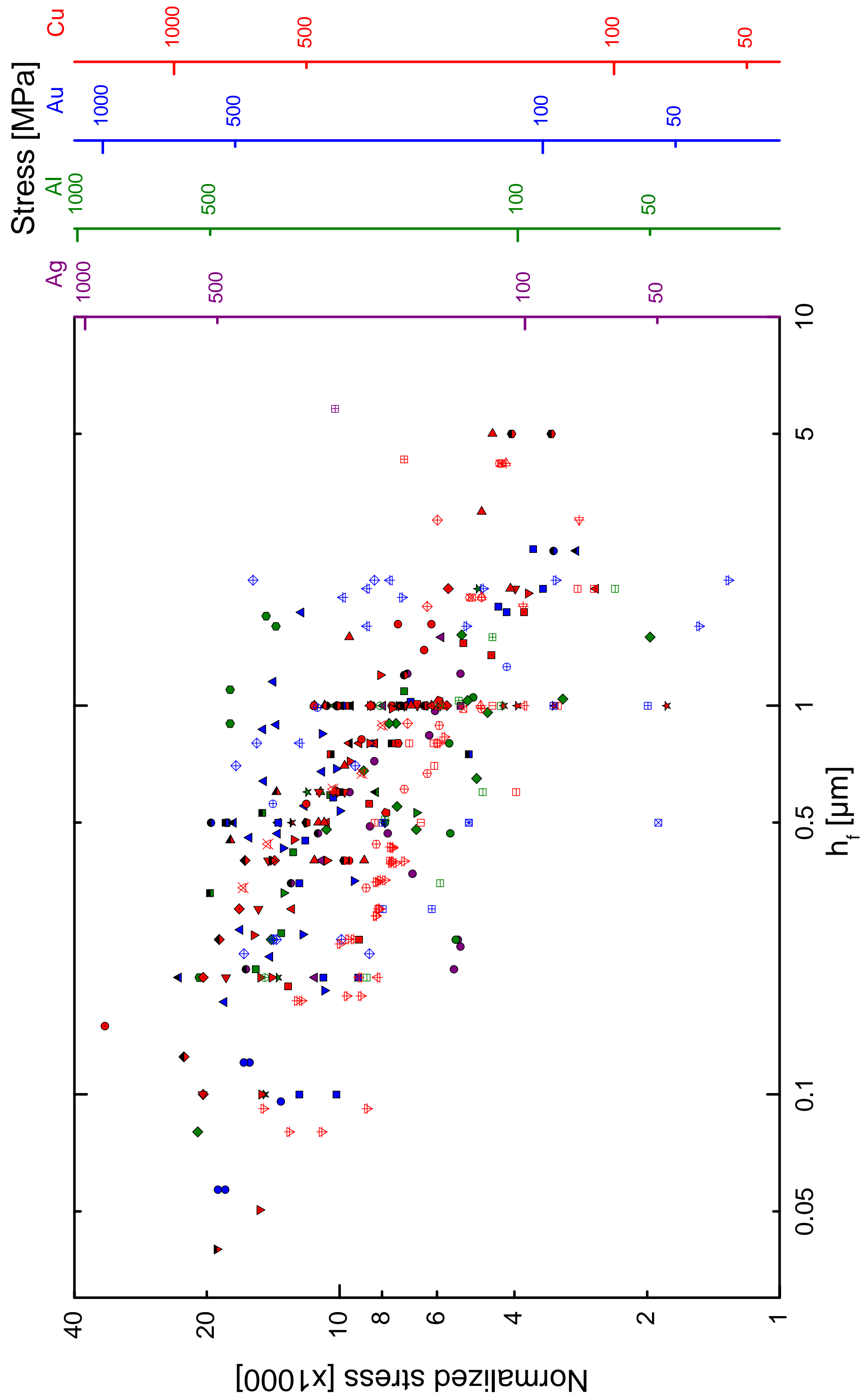

Stress [MPa]
Cu
1000
500
100
50
Au
1000
500
100
50
Al
1000
500
100
50
Ag
1000
500
100
50
Normalized stress [x1000]
40
20
10
8
6
4
2
1
h_f [μm]
0.05
0.1
0.5
1
5
10

Bare films on substrates

Data set	Ref.
Ag96 Thouless	46
Ag98 Kobrinsky	73
Ag03 Schwaiger	80
Al86 Doerner	82,83
Al89 Korhonen	84
Al90 Venkatraman	85
Al91Paszkiet	81
Al92 Venkatraman	17,83
Al96 Thouless	46
Al97 Jawarani	78
Al99 Macionczyk	83,86
Al01 Dehm	21,22,87
Au00 Leung	75,76
Au06 Sauter1	88
Au06 Sauter2	88
Au06 Sauter3	88
Cu91 Flinn	90
Cu93 Thouless	44
Cu93 Vinci	62
Cu95 Vinci	45
Cu96 Thouless	46
Cu98 Keller	18,47
Cu99 Hommel	89
Cu01 Hommel1	83,91
Cu01 Hommel2	83,91
Cu00 Weihnacht	94
Cu00 Spolenak1	96
Cu00 Spolenak2	96
Cu00 Weiss	57,59
Cu03 Balk	25,56
Cu04 Schmidt1	101,102
Cu04 Schmidt2	101,102
Cu04 Edongué	23
Cu06 Gan	4

Epitaxial films

Data set	Ref.
Al01E Dehm	20-22
Cu04E Edongué	23

Passivated epitaxial films

Data set	Ref.
Cu04EP Edongué	23

Passivated films on substrates

Data set	Ref.
Ag96P Thouless	46
Ag98P Kobrinsky	73
Al91P Paszkiet	81
Al96P Thouless	46
Al97P Jawarani	78
Au00P Leung1	75
Au00P Leung2	74
Au00P Leung3	76
Cu93P Vinci	62
Cu95P Vinci	45
Cu96P Thouless	46
Cu98P Shen	66
Cu03P Shen1	68,69
Cu03P Shen2	68,69
Cu98P Keller	18
Cu99P Hommel	89
Cu00P Weiss	57,59
Cu02P Shu	71
Cu03P Shu	72
Cu02P Vinci	70
Cu06P Gan	4

Free-standing films

Data set	Ref.
Ag00F Huang	92
Al03F Son	93
Al04F Espinosa	95
Au02F Espinosa	95,97-99
Au03F Son	93
Au03F Emery1	100
Au03F Emery2	100
Au03F Emery3	103
Cu00F Huang	92
Cu04F Xiang	104
Cu04F Espinosa	95
Cu05F Onuseit	105
Cu06F Xiang1	106
Cu06F Xiang2	106
Cu06F Xiang3	107
Cu06F Xiang4	107

Passivated free-standing films

Data set	Ref.
Au02FP Espinosa	98
Cu04FP Xiang	104
Cu06FP Xiang1	107
Cu06FP Xiang2	107

Figure 2.7: “Masterplot” of the room temperature stress normalized with respect to the shear moduli vs. film thickness for Ag, Al, Au and Cu thin films. The axes on the right give the stress values for the different materials.

It is important to keep in mind that the films were deposited with different techniques (sputtering, e-beam evaporation, electroplating, etc…) and under different conditions, which can strongly influence their mechanical properties. Differences in high temperature stress behavior between Cu films deposited under high vacuum[18] and ultra-high vacuum[59] conditions clearly illustrate this difficulty. Moreover, different measurement techniques were employed. The substrate curvature technique was used for most films on substrates. However, data from X-ray diffraction techniques is also included. For free-standing films, the stress was measured with bulge testing or deflection tests. The definitions of the flow stress are as diverse as the measurement methods. For techniques based on thermal cycling, the flow stress is considered to be the room temperature stress after thermal cycling. This is however in several cases not a valid assumption, as will be shown in the course of this dissertation. For methods like microtensile or bulge testing, in which the stress is determined as a function of strain, the flow stress is defined as the stress at strains between 0.1 and 0.5%.

For all the compiled literature data, a precise description of the film preparation conditions and the employed measurement methods together with the stress values is provided in the appendix (section 10.1). Each thin film material is represented with a different color: violet for Ag, green for Al, blue for Au and red for Cu. Different categories of films can be distinguished: bare polycrystalline films on substrates (full single-colored symbols), passivated polycrystalline films on substrates (half black-half colored symbols), bare epitaxial films on substrates (empty horizontally-crossed symbols), passivated epitaxial films on substrates (empty vertically-crossed symbols), bare free-standing films (empty symbols with a + sign) and passivated free-standing films (empty symbols with a × sign). Please note that for some films, the grain size is smaller than the film thickness and is therefore expected to be the controlling parameter. A plot of the stress as a function of grain size for these films would be more appropriate. However, this could not be achieved since grain size data was only available for a very limited number of studies. The grain size values found in literature are given in the appendix (section 10.1), too.

Several features are striking on this plot. The thickness of the studied films ranged from 40 nm to 5 µm, with the largest amount of data for 1 µm thick films. Only very few

stress values are available for films thinner than 100 nm. Globally, the data scatter is large, especially for free-standing films. However, the stress values lie within the same range for all the materials. Overall, the stress visibly increases with decreasing film thickness. This trend seems to stop for films thinner than 400 nm, for which the stress seems to stagnate and form a plateau.

Figure 2.8, which only includes Cu thin film data, more clearly reveals the principal trends of the masterplot. In addition, stress values of other confined systems in which size effects were reported – namely nanocrystalline (nc) Cu[108] and Cu whiskers[109] – are plotted as a function of the grain size and the whisker diameter, respectively. The theoretical strength limit of Cu calculated with Mackenzie's model and yield stress values measured for bulk Cu are marked on the graph as well. In order to see how good the models described earlier in this section fit the experimental data, the stress values predicted by the Nix-Freund model and by the source model calculated for unpassivated Cu films are also presented on the plot.

Again, the stress appears to increase linearly with decreasing film thickness, before entering in a saturation regime for films thinner than 400 nm. Although the source model is in better agreement than the Nix-Freund model, both models underestimate the stress level and fail to predict the experimentally observed stress plateau regime.

Although nanocrystalline Cu typically has grain sizes smaller than the thickness of the thin films, it exhibits lower stresses. This proves that the geometry specific to thin films plays a more considerable role in plasticity than their small grain sizes. Cu whiskers of a given diameter exhibit much higher stresses than thin films of the same thickness. These stresses are the highest reported in this review and the closest to the theoretical strength limit, peaking at about 3 GPa for a whisker of 1.2 μm diameter. In this case, it is no longer exclusively the confined geometry which determines the deformation mechanism, but also the defect density. The whiskers were indeed almost devoid of defects[109].

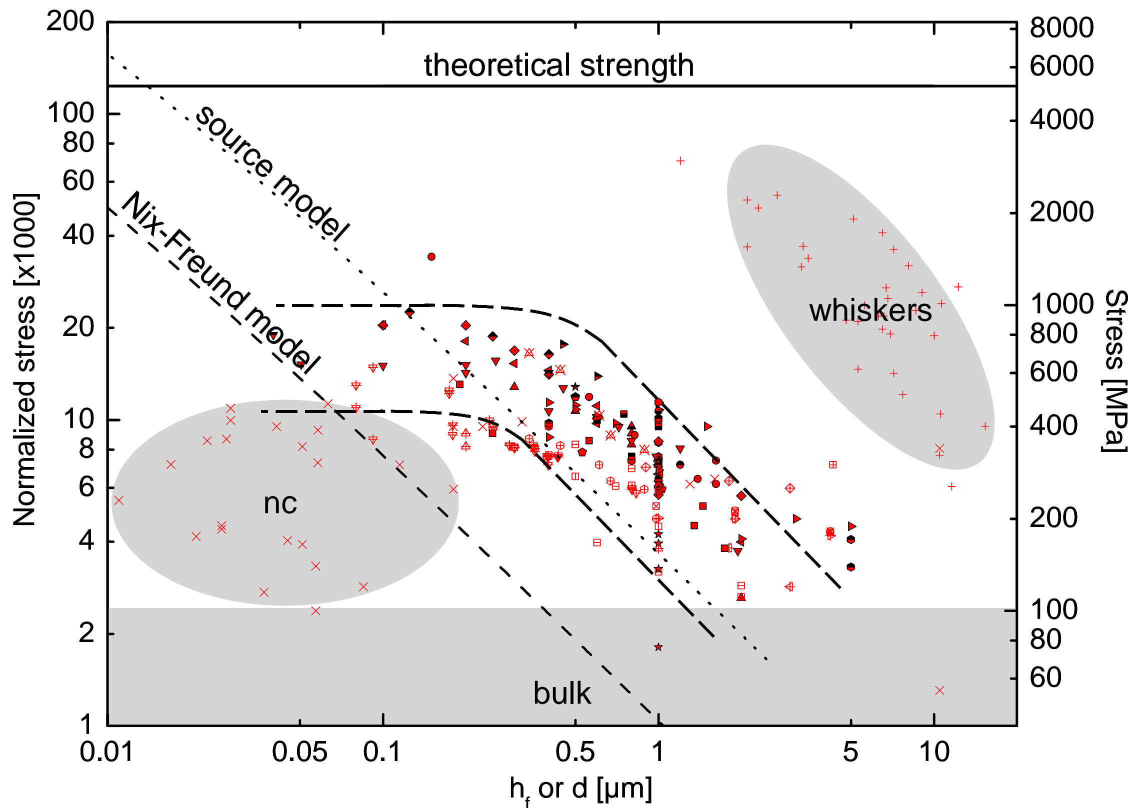

Figure 2.8: Compilation of the literature data available for Cu thin films plotted together with data of nanocrystalline Cu (× symbols)[108] and Cu whiskers (+ symbols)[109]. The rest of the legend is provided in Figure 2.7. The main trend in the stress evolution is highlighted with two thick dotted lines. The theoretical strength and the bulk stress level are also shown, as well as the stress values predicted by the Nix-Freund model and the source model for unpassivated Cu films. The thin dashed line represents the prediction of Nix-Freund model calculated with Equations (2.12) and (2.13) using the following values: $\sin\phi / \cos\phi \cos\lambda = 3.17$ for a (111)-textured film, $b = 2.56$ Å, $\beta_s = 1.7$, $\mu_f = 42.1$ GPa, $\mu_s = 63.7$ GPa and $\nu_f = 0.34$. The thin dotted line corresponds to the predictions of the source model calculated with Equation (2.20) using the following constants: $\alpha = 2.5$, $b = 2.56$ Å, $\mu_f = 42.1$ GPa and $s = 0.27$.

The masterplot shown in Figure 2.7 is re-plotted in Figure 2.9 to focus on passivated films by using bigger symbols for this data. From this plot, it appears that the stress for passivated films generally lies above the stresses for unpassivated films, as already described in this chapter. The most striking feature is the lack of data for films thinner than 400 nm.

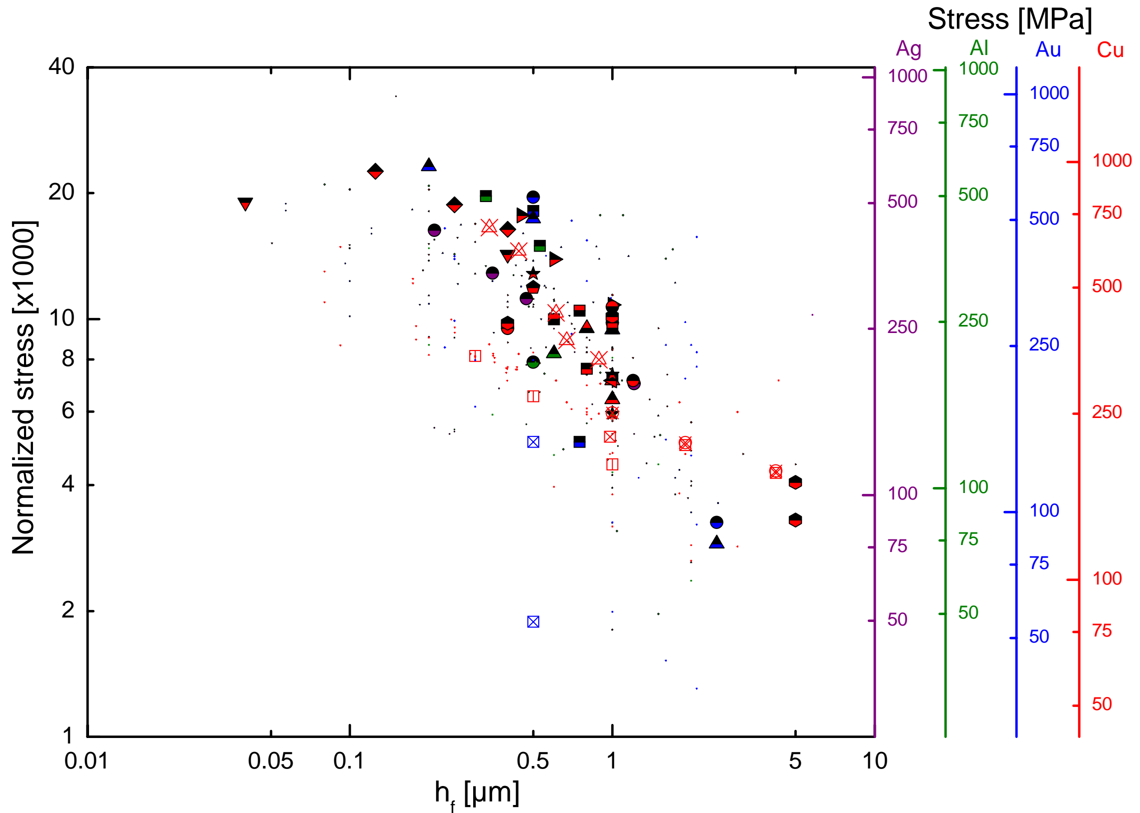

Figure 2.9: Compilation of the literature data for the Ag, Al, Au and Cu films, with focus on the data collected for passivated films.

2.6 Summary of the literature and motivation of the study

The thermomechanical behavior of thin films has been studied extensively in the last 15 years and the exact mechanisms accounting for the unexpected thin film yield stresses were investigated both theoretically and experimentally. To describe the size effect in thin film plasticity, several models were developed, based on constraints on dislocation motion or limited dislocation nucleation. Despite the large amount of work, many aspects are not fully understood.

Thin film plasticity was shown to be controlled by both dislocation glide and diffusion. Study of passivated films confirmed the prominent role of diffusional creep in the stress relaxation of unpassivated films. Passivating a thin film suppressed surface diffusion and hence inhibited grain boundary diffusional creep. However, the literature

compilation indicated that only limited information about thermal stresses of passivated films thinner than 400 nm is available. For unpassivated Cu films lying in this thickness range, the flow stress was revealed to be film thickness-independent[25]. As an explanation for this stress plateau, a change of dislocation mechanism with dislocations gliding parallel to the film/substrate interface and thus becoming thickness-insensitive was proposed. The formation of parallel glide dislocations was attributed to constrained diffusional creep, in which atoms diffuse from the surface into the grain boundaries. One could speculate that suppressing constrained diffusional creep through passivation layer deposition could suppress parallel glide dislocation generation and likewise the flow stress plateau for ultra-thin films. The aim of this study is therefore to extend the knowledge of stress behavior to passivated films thinner than 400 nm and explore this speculation. The study of these films will resolve the interplay between the stress plateau, parallel glide dislocations, and constrained diffusional creep to yield an improved understanding of the origin of the plateau for unpassivated films.

Several aspects of passivation will be addressed in this work. First, we will study the influence of a passivation layer on the stress-temperature evolution of ultra-thin films. Earlier studies found increased strengths at both room and elevated temperatures for passivated films in the sub-micrometer regime. However, it may be different for ultra-thin films in which different deformation mechanisms are likely to be active. Moreover, the influence of the passivation layer nature will be investigated. The lack of TEM dislocation studies for passivated films will also be remedied. This study will indeed provide the first comprehensive TEM study of passivated films, including *in-situ* experiments. The influence of the preparation route on the mechanical properties of passivated films will also be addressed. Certain dislocation-based deformation mechanisms were indeed shown to rely on diffusive mechanisms. Changing the passivation temperature may therefore make it possible to artificially freeze certain dislocation types in the film, and thereby control the dominant deformation mechanisms. Finally, the behavior of passivated films will also be examined for the first time at low temperatures, where diffusion plays a negligible role.

To clarify these points, Cu thin films passivated with aluminum oxide (Al_xO_y) and silicon nitride (Si_xN_y) were prepared and examined. The choice of Cu was motivated

both by its technological relevance since its industrial incorporation as an interconnect metallization in 1998 and by the wide range of data available. Al_xO_y was chosen as a passivation layer to provide a direct comparison with the Cu-1% Al self-passivated films prepared by Weiss *et al.* [57,59]. Si_xN_y is a well-known passivation material used in many studies and devices for its effectiveness as a diffusion barrier[110].

CHAPTER 3

THIN FILM SYSTEMS

3.1 Introduction

In this work, the influence of surface diffusion on the deformation mechanisms of ultra-thin Cu films will be investigated. In order to address this issue as exhaustively as possible, the study of several Cu thin film systems is necessary. The main parameters varied were the film thickness, the passivation material, and the deposition conditions. In particular, aluminum oxide (Al_xO_y) and silicon nitride (Si_xN_y) passivation layers were compared. This section will be dedicated to the precise description of the thin film systems and their preparation routes.

3.2 Passivated Cu films

The layer stacking sequence of the prepared passivated films is presented in Figure 3.1.

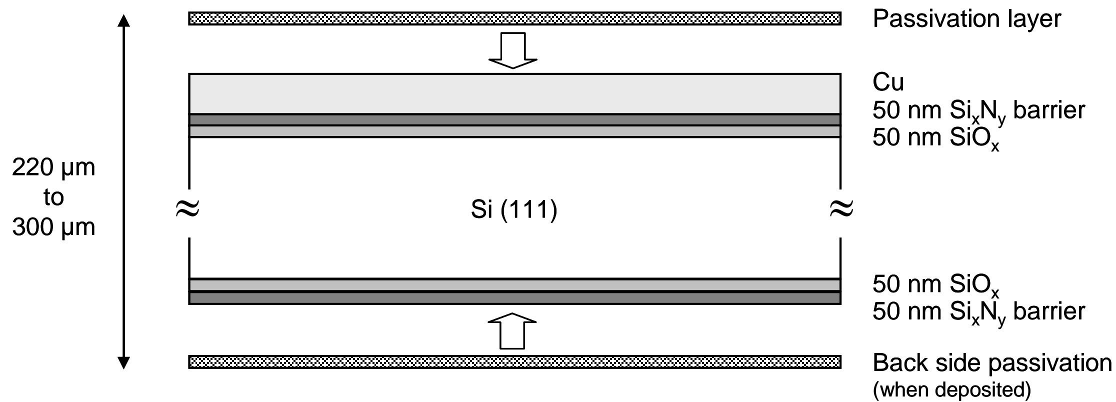

Figure 3.1: Schematic cross section of the prepared passivated film systems.

3.2.1 Cu deposition

The preparation of the Cu films was common to all the systems and was carried out as follows. The Cu films were deposited on (111) Si wafers by DC magnetron sputtering under ultra-high vacuum (UHV) conditions with a base pressure of about 10^{-8} Pa (DCA Intruments). The two inch diameter, 220 to 300 µm thick, (111) Si substrates were coated during fabrication on the front and back side with nominally 50 nm thick amorphous thermal silicon oxide (SiO_x) followed by a 50 nm thick amorphous silicon nitride (Si_xN_y) layer deposited to prevent Cu-Si interdiffusion (Crystec GmbH). After cleaning the substrates in the deposition chamber with argon-ion bombardment (200 eV, 2 minutes), Cu films with thicknesses varying between 25 nm and 2 µm, with an emphasis on films less than 200 nm thick, were deposited at room temperature. Argon was used as a sputter gas under a pressure of $2.5 \cdot 10^{-1}$ Pa. The sputtering rates ranged from 0.1 to 0.5 nm/s. In order to obtain a homogeneous film thickness, the substrates were rotated during deposition at 100 rev/min.

3.2.2 Aluminum oxide passivated Cu films

The Cu films were annealed at 500 °C in UHV with a base pressure of about 10^{-8} Pa for 1 hour directly after deposition without breaking the vacuum to stabilize the microstructure. For passivation, the Cu films were cooled down to room temperature before depositing a 10 nm thick aluminum film. The samples were heated again to 500 °C under an O_2 partial pressure of 10^{-3} Pa for 2 minutes to oxidize the aluminum film. In the rest of the work, this type of films are abbreviated **CuAlO** (referring to **Cu** films passivated with **Al**uminum **O**xide).

3.2.3 Silicon nitride passivated Cu films

The passivation of the Cu films with a silicon nitride film was performed following three different preparation routes (Figure 3.2). Two batches of these films – noted **B1** and **B2** – were prepared with one year in-between. These films are abridged **CuSiN** (referring to **Cu** films passivated with **Si**licon **N**itride).

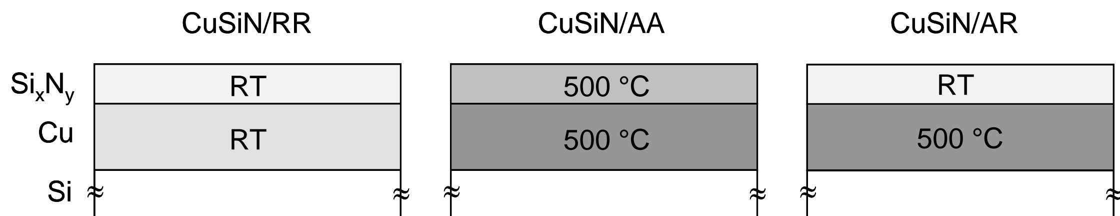

Figure 3.2: Sketch representing the preparation conditions of the three types of Si_xN_y passivated films. RT stands for room temperature. For the Cu film, the indicated temperature corresponds to its annealing temperature. For the Si_xN_y film, it corresponds to its deposition temperature.

Passivation at room temperature without annealing

For these films, a 10 thick Si_xN_y film was reactively sputtered using a Si target and nitrogen gas with a partial pressure of $3.2 \cdot 10^{-2}$ Pa directly after Cu deposition at room temperature, without breaking vacuum and without any heat treatment to alter the Cu microstructure prior to passivation. Argon was used as a sputter gas under a pressure of $2.5 \cdot 10^{-1}$ Pa. In addition, a 100 nm thick Cu film was passivated with a 50 nm thick Si_xN_y layer following this same procedure. These films are noted **CuSiN/RR** (R stands for the **R**oom temperature deposition of the Cu film – first character – and of the passivation

layer – second character).

Passivation at the annealing temperature

In this film system, the Cu films were annealed for 1 hour at 500 °C, before a 10 nm thick Si_xN_y layer was sputtered under the same conditions as mentioned above at the annealing temperature. A 100 nm Cu film passivated with 50 nm Si_xN_y was also prepared. The abbreviation of this type of film is **CuSiN/AA** (A stands for the **A**nnealing of the Cu film and the passivation deposition at the **A**nnealing temperature).

Passivation at room temperature after annealing

Finally, in the last preparation route, the room temperature deposited Cu films were annealed for 1 hour at 500 °C, cooled back down to room temperature, and then a 10 nm thick Si_xN_y film was deposited under the same conditions as mentioned above. They are noted **CuSiN/AR** (A stands for the **A**nnealing of the Cu film and R for the Si_xN_y deposition at **R**oom temperature).

3.2.4 Back side passivation

The film stress was measured with the wafer curvature method described in details in section 4.3.1. In the case of passivated films, it is necessary to subtract out the influence of the capping layer from the total film stress. This is achieved by depositing a passivation layer on the back side of the samples, which is referred to as "back side passivation". The stress in the capping layer is then mechanically canceled out by the back side film. This approach, which was experimentally verified, is discussed in detail in the appendix (section 10.2). No back side passivation was deposited for the CuAlO films with the exception of the 100 nm film, for which 10 nm of Al were deposited and oxidized on the back side of the substrate after 2 wafer curvature thermal cycles. For all the CuSiN films, a 10 nm thick Si_xN_y layer was sputtered on the back side of the wafer using the same procedure as for the capping layer i.e. either at room temperature or at 500 °C. The 100 nm thick Cu films were back side passivated after two stress-temperature cycles in the wafer curvature apparatus. The films passivated with a 50 nm thick Si_xN_y layer were back side passivated with a layer of the same thickness. This step

was generally carried out prior to Cu deposition except for the films passivated at room temperature after annealing (type CuSiN/AR). In this case, the Si_xN_y layer of the back side of the wafer was deposited in a final step, to avoid premature thermal cycling during the Cu film annealing.

3.2.5 Summary

The preparation characteristics of the studied passivated films are summarized in Table 3.1.

Table 3.1: Preparation characteristics of the studied passivated films.

	CuAlO	CuSiN/RR		CuSiN/AA		CuSiN/AR	
		B1	B2	B1	B2	B1	B2
Cu film							
Thickness [nm]	25 40 50 100 200 400 600 1000 2000	25 50 100 200 600 2000	30 75 100	50 100 200 600	30 50 75 100	25 50 100 200 600	30 50 75 100
Deposition temperature	RT	RT		RT		RT	
Annealing	1h at 500 °C	No		1h at 500 °C		1h at 500 °C	
Passivation layer	Al_xO_y	Si_xN_y		Si_xN_y		Si_xN_y	
Thickness [nm]	10	10 / 50		10 / 50		10	
Deposition temperature	Al at RT	RT		500 °C		RT	
Additional heat treatment	heated and oxidized at 500 °C	No		No		No	
Back side passivation	100 nm thick film	Yes		Yes		Yes	

RT: Room Temperature

3.3 Unpassivated Cu films

In this work, a comparison of the mechanical properties of the passivated films with unpassivated films was necessary to account for the effect of passivation. However, the measurement of the stress-temperature behavior of unpassivated Cu films was not the main focus of the present study since such films have already been studied over a broad film thickness range by Balk[25,53-55]. These Cu films, whose thickness varies between 30 nm and 2 μm were prepared and measured at the Max Planck Institute for Metals Research using the same wafer curvature system as was used for these studies. Balk magnetron sputtered Cu films onto amorphous-Si_xN_y coated (100) Si wafers in ultra-high vacuum at room temperature and then annealed them for 1 hour at 500 °C. These samples are abbreviated **CuAB** (for **A**nnealed **Cu** films from **B**alk). However, since the films were deposited in a different sputtering system, their microstructure could differ from that of our Cu films before passivation. To verify that these films can be used as a comparison, unpassivated Cu films were also deposited in this study. Both annealed (noted **CuA**) and non-annealed (noted **CuR**) films were prepared according to the previously described procedure. The preparation characteristics of the studied unpassivated films are summarized in Table 3.2.

Table 3.2: Preparation characteristics of the studied unpassivated films.

	CuAB	CuR	CuA
Thickness [nm]	30, 50, 100, 200, 270, 400, 500, 600, 800, 1000, 2000	100	100, 600
Deposition temperature	RT	RT	RT
Annealing	1h at 500 °C	No	1h at 500 °C

RT: Room Temperature

3.4 Additional samples

The passivation layers were also deposited directly on Si wafers, without a Cu layer, to serve as reference samples. A 10 nm thick Al_xO_y layer was prepared following the procedure described above. Si_xN_y films with thicknesses of 10 and 50 nm were also sputtered at room temperature. Since the wafers were used for wafer curvature stress measurements, all the films were deposited simultaneously on about (1x1) cm² substrates for microstructural studies and TEM sample preparation.

CHAPTER 4

EXPERIMENTAL METHODS

4.1 Introduction

Throughout the work, many experimental methods were used to study the different thin films systems presented in chapter 3. This chapter aims at describing the standard techniques and apparatus employed to characterize and mechanically test the thin films. A first part will be dedicated to the film microstructure characterization using microscopic and analytical techniques. It will be followed in a second part by an overview of stress measurement techniques. Finally, a description of the *in-situ* transmission electron microscopy setup used to observe dislocation behavior will be provided.

4.2 Microstructural characterization

4.2.1 Microscopic techniques

Several microscopic techniques were used to characterize the microstructure of the studied thin film systems and especially their surface morphology before and after thermal cycling. These studies were carried out on the (1x1) cm^2 sample pieces sputtered along with the 2 inch wafers.

Scanning Electron Microscope (SEM)

The film surfaces were imaged with a field emission Scanning Electron Microscope (SEM) (Leo 1530 VP, Carl Zeiss). The electron accelerating voltage was varied between 5 and 15 kV. The samples could be tilted up to 45° towards the electron beam. The images were recorded using a secondary electron detector located in the column and a backscattered electron detector. The low energetic secondary electrons that result from inelastic processes and originate within a few nanometers from the sample surface effectively reveal the surface topography. Imaging with backscattered electrons, which are generated from much deeper in the sample, reveals information regarding the sample composition and crystallography.

Focused Ion Beam (FIB) microscope

A focused ion beam (FIB) microscope (FEI 200, 30 keV gallium beam) was used to characterize the grain size, the topography (grooves, pores, hillocks) and the texture of the films. The working principle of a FIB is similar to that of a scanning electron microscope, except that in this technique, the sample is scanned with a focused beam of high-energy gallium ions instead of electrons. The number of secondary electrons reaching the detector depends on the channeling probability of the gallium ions in the grains, which results in a strong orientation contrast. Grains with an open crystallographic orientation with respect to the incident ion beam appear dark in the image. Indeed, for these grains, the number of secondary electrons emitted close to the surface is small since the ion beam penetrates deep into the solid. Imaging was achieved with beam currents between 70 and 150 pA. Identical spots on the samples were

recorded and compared at three tilt angles between 0 and 45° to properly reveal all the Cu grains and determine an accurate grain size and grain size distribution, as described in section 4.2.2. The high momentum of the primary gallium ions was used to sputter away the passivation layer in order to reveal the underlying Cu microstructure. Cross sectional views were also made by sputter-etching a square hole into the film with a 1000 pA ion beam and then tilting the specimen by 45°. Some of the cross sectional images were recorded in a FEI Nova Nanolab dual beam microscope which has both an electron and an ion beam.

Atomic Force Microscope (AFM)

An atomic force microscope (AFM) (NanoWizard AFM, JPK Instruments) was used to obtain information about the surface topology. Images of surfaces varying between 1 µm² and 10 µm² were acquired in the "contact" imaging mode. In this mode, the hard-sphere repulsion force between the cantilever and the surface is kept constant during scanning by maintaining a constant deflection. The data processing was carried out with JPK Image Processing software. The image cross section mode of this software was used to determine the size and height of the imaged surface particles.

Conventional Transmission Electron Microscope (TEM)

Two conventional transmission electron microscopes were employed in the study. A JEOL JEM 2000 FX TEM operated at 200 kV was used to investigate both the microstructure and the dislocation behavior in the films thinner than 200 nm. Thicker films were investigated in a JEOL JEM 4000 EX microscope operated at 400 kV. Prior to TEM analysis, plan-view and cross-sectional specimens were prepared. The TEM specimens have to be thin enough to achieve electron transparency and at the same time maintain mechanical stability. These conditions result in a complex and time-consuming preparation procedure.

The plan-view specimens were prepared using a procedure described by Strecker *et al.*[111]. A 3 mm disc, corresponding to that of the TEM specimen holder, was cut out of the sample using an ultrasonic disc cutter (Gatan Ultrasonic Disc Cutter, Gatan). After mechanical thinning, the disc was ground from the Si side down to approximately

80 μm, and then dimpled (Gatan Dimpler Grinder, Model 656, Gatan) from the same side down to about 30 μm. The remaining Si was selectively etched away with a solution of HNO_3:HF:CH_3COOH (2:1:1). The Si_xN_y film on the wafer stops the etching and thus leaves the Cu film intact. A schematic of the preparation procedure is provided in Figure 4.1. For Cu films thicker than 400 nm, it was necessary to thin the Cu film. This was performed with low angle ion milling (incident angle: 6°, voltage: 3.3 kV; Gatan Precision Ion Polishing System, Gatan) on the passivated side until electron transparency was reached.

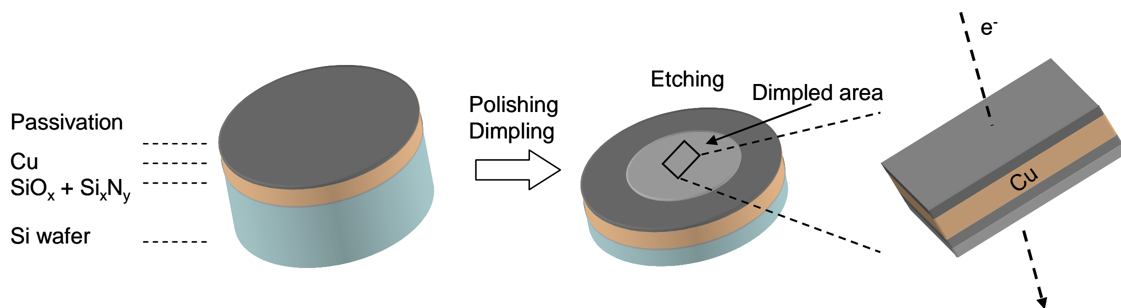

Figure 4.1: Schematic of the principal preparation steps of a plan-view TEM specimen.

The cross sections were prepared following two different procedures. For the CuAlO films, a metallographic procedure was employed. Two pieces of the Cu-coated samples (3 mm wide and 1 cm long) were glued together with the passivated sides facing each other (G1 Epoxy Kit, Gatan). The glue was hardened in a furnace at 130 °C for about 30 minutes. Two pieces of trapezoidal-shaped Si were then glued on both sides of the sandwich obtained, so that the total height of the stack reached about 3 mm (Figure 4.2). A 500 nm thick slice was cut off using a diamond saw. This slice was ground and polished on one side. The other side was ground to 80 μm. Finally, it was dimpled and ion-milled to reach electron transparency.

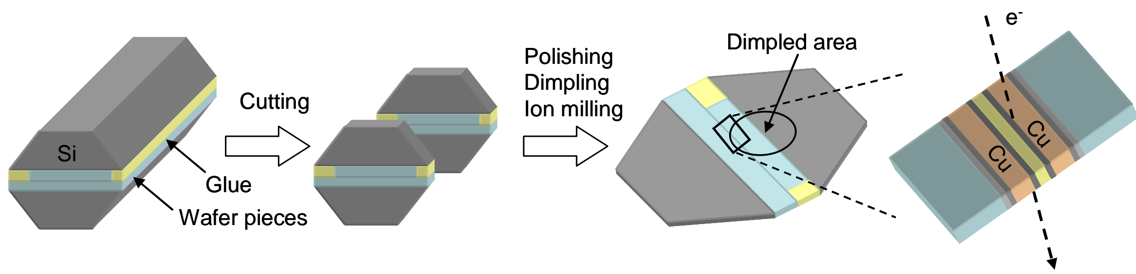

Figure 4.2: Schematic of the main preparation steps of a cross-sectional TEM sample.

The CuSiN cross-sectional TEM specimens were prepared by ion milling with a FIB microscope. A thin electron transparent lamella was cut out of the sample and transferred onto a Cu grid with a micro-manipulator. A precise description of this method can be found in [112].

High Resolution Transmission Electron Microscope (HRTEM)

The interface Cu/Si_xN_y passivation of the CuSiN films was analyzed on cross-sectional specimens with a JEOL ARM 1250 high resolution transmission electron microscope, operated at 1.25 MV. Details about this microscope are found in [113].

4.2.2 Quantitative microstructural analysis

To determine Cu grain size and grain size distributions, SEM, FIB or TEM images were analyzed following the same procedure. The grain boundaries seen on a reference image were drawn on a transparency foil. Images of the identical area taken at different tilt angles, and thus different grain contrasts, revealed boundaries not visible in the reference image. Twin boundaries, characterized by straight lines, were not considered. A digitized image of the transparency foil was created using a digital camera or a scanner and subsequently analyzed with a computer program (Quantimet 500, Carl Zeiss). The grain size determined is the equivalent circular grain diameter calculated from the effective grain circumference. Between 100 and 300 grains were evaluated per film. The principal error on the grain size emerges from the drawing step, since it is often difficult to clearly distinguish the boundaries. To estimate the error, a single image was analyzed by two different operators. A relative error of 10% seems to be a reasonable value. The same method was employed to analyze hillock densities.

4.2.3 X-ray diffraction measurements

θ-2θ scans were recorded between $2\theta = 10°$ and 140° using the Cu-K_{α} radiation (Philips MRD and Siemens D5000). The angular resolution was of 0.04° and the dwell time varied between 1 and 5s. To determine the film texture, (111)-pole figures were also recorded using the 2θ angle of the (111)-oriented Cu grains from the θ-2θ scans.

4.2.4 Surface analysis

After Cu deposition or passivation, some films were kept in vacuum and directly analyzed with X-ray Photoelectron Spectroscopy (XPS) and Auger Electron Spectroscopy (AES) (Specs). With these techniques, it was possible to analyze the impurities on the film surface and to verify if the passivation layer is continuous. Some films were also analyzed after exposure to air. An Energy Dispersive X-ray (EDX) spectrometer (Ge detector, Noran Instruments) mounted in the JEOL 2000 FX TEM was used to determine the elemental composition at the interface Cu film/passivation layer.

4.3 Stress measurement

4.3.1 Wafer curvature technique

The thermomechanical film behavior was measured as a function of temperature by the wafer curvature technique. Due to the mismatch between the coefficients of thermal expansion (CTE) of the substrate and the film, a biaxial stress evolves in the film during thermal cycling, which in turn induces a change in the wafer curvature. Since the substrate is much thicker than the film and deforms purely elastically, the film stress σ_f can be calculated from the substrate curvature using the equation derived by Stoney[114]:

$$\sigma_f = \frac{M_s h_s^2}{6h_f}\left(\frac{1}{R_{meas}} - \frac{1}{R_{ref}}\right) \tag{4.1}$$

where M_s is the biaxial modulus of the substrate, h_s is the substrate thickness and h_f is the film thickness. R_{meas} and R_{ref} are the radii of curvature of the coated and uncoated wafers, respectively. Indeed, since uncoated wafers are not perfectly flat, the initial radii of curvature R_{ref} of the wafers were measured prior to film deposition. For (111)-oriented Si wafers, $M_{Si(111)}$ = 229.1 GPa was calculated from the Si single crystal elastic constants[79].

The substrate curvature is measured with a laser-scanning method in a furnace (ROSE I) in which a He-Ne laser is scanned across the wafer with a rotating mirror placed in the focal plane of a lens with 1 m focal length. Since parallel incident beams reflected by a curved surface are no longer parallel, the curvature of the wafer is determined from the position of the reflected laser spot on a position-sensitive photo cell. A 2 inch wafer was positioned on a tripod consisting of three NiCr/Ni thermocouples in the middle of the furnace. To avoid sample oxidation, the furnace was purged with nitrogen before and during thermal cycling. Additionally, a tantalum foil was placed in the furnace to getter residual oxygen. More details about the experimental setup are to be found in [18].

The films were cycled several times between room temperature and 500 °C. Some films were also cycled to 600 or 700 °C. The heating rate was 6 K/min whereas the cooling rate was controlled by the nitrogen flow and could only be kept at 6 K/min down to 100 °C; below 100 °C, it dropped to 4 K/min.

Identical experimental conditions were achieved for the measurement of the unpassivated films from Balk (type CuAB) used in this work as a comparison: same apparatus, temperature range and heating and cooling slopes.

A precise analysis of the experimental error of the film stress measurement was carried out. According to Equation (4.1) and considering the substrate biaxial Young’s modulus as a constant, the error $\Delta\sigma_f$ of the film stress can be estimated with:

$$\Delta\sigma_f = \left|\frac{\partial\sigma_f}{\partial h_s}\right| \cdot \Delta h_s + \left|\frac{\partial\sigma_f}{\partial h_f}\right| \cdot \Delta h_f + \left|\frac{\partial\sigma_f}{\partial\left(\frac{1}{R_{meas}} - \frac{1}{R_{ref}}\right)}\right| \cdot \Delta\left(\frac{1}{R_{meas}} - \frac{1}{R_{ref}}\right) \tag{4.2}$$

A further development of Equation (4.2) leads to following expression:

$$\Delta\sigma_f = |\sigma_f| \cdot 2\frac{\Delta h_s}{h_s} + |\sigma_f| \cdot \frac{\Delta h_f}{h_f} + \frac{M_s h_s^2}{6h_f} \cdot \left|\frac{1}{R_{meas}}\right| \cdot \left|\frac{\Delta R_{meas}}{R_{meas}}\right| + \frac{M_s h_s^2}{6h_f} \cdot \left|\frac{1}{R_{ref}}\right| \cdot \left|\frac{\Delta R_{ref}}{R_{ref}}\right| \tag{4.3}$$

where Δh_s is the uncertainty of the substrate thickness, Δh_f the uncertainty of the film thickness and ΔR_{ref} and ΔR_{meas} the errors of the curvature measurements for the uncoated and the coated substrates, respectively.

The substrate thickness was measured with a digital dial indicator (Millitast 1085, Mahr) providing a resolution of ± 1 µm. Over the entire 2 inch wafer, the thickness varied at maximum ± 3 µm. For a 220 µm thick wafer, the relative error on the thickness is then of about 1.5%. To estimate the error of the film thickness, TEM cross-sectional specimens of different samples were prepared and analyzed. The real thickness was measured and compared with the nominal value. The maximal encountered error was of 3.5%.

The error of the curvature measurement mainly emerges from the positioning accuracy of the wafer in the apparatus. Indeed, due to the non-uniformity of the curvature of the wafers, the measured radius of curvature can differ drastically depending on the position of the line along which it is measured. To quantify the influence of the positioning of the wafer, different wafers, coated or uncoated, were measured several times after changing their position with respect to the laser scanning line. The measurement error for the radius of curvature was estimated to be about 5%. Since this positioning problem originates mainly in the non-uniform curvature of the uncoated silicon wafer, it is therefore possible to simplify the error estimation by assuming an error of the reference measurement $\Delta R_{ref} / R_{ref}$ of 10% and an error of the coated wafer measurement $\Delta R_{meas} / R_{meas}$ of 0%. All the other measurement errors inherent to the laser scanning

system are negligible compared to this error.

Plugging these numbers into Equation (4.3), the error of the stress measurement is given by:

$$\Delta\sigma_f = 0.05\left|\sigma_f\right| + 0.1\frac{M_s}{6h_f}\cdot h_s^2\cdot\left|\frac{1}{R_{ref}}\right| \tag{4.4}$$

According to this equation, the error decreases with increasing radius of curvature of the substrate. This seems reasonable. Indeed, for a flat wafer with a high radius of curvature, the reference curvature subtracted from the measured one (see Equation (4.1)) is small and the error due to its non-uniformity minimally impacts the film stress error. Depending on the sample, stress errors ranged from 5% to 30%, typically being of about 15%.

4.3.2 X-ray diffraction

As discussed above, the measurement error for absolute film stress values can be important. This issue becomes even more serious for the thinnest films for which the error is bigger, since the stress values are higher. To verify the accuracy of the stress values obtained with wafer curvature, the room temperature stress of several films was determined with X-ray diffraction in the (1x1) cm² as-deposited samples, prepared along with the wafers. X-ray diffraction stress measurements were performed using a Bruker D8 Discover diffractometer operating in parallel-beam geometry equipped with a rotating-anode Cu X-ray source (Bruker TXS), a collimating X-ray mirror (Xenocs)[115] and a scintillation counter. Residual stresses in the Cu film were determined with the $\sin^2\psi$ method, described in details in [116]. θ-2θ scans are recorded for the Cu (111) reflection between 41.5° and 45° at two inclination angles, $\psi = 0°$ and $\psi = 70.54°$. Pearson VII functions were fitted to each reflection by using the software Profit 1.0 (Philips) in order to determine peak parameters such as peak maximum position, shape parameter, integral breadth, Voigt parameter and peak asymmetry parameter[117]. The (111) interplanar spacings, d_ψ, determined out of the peak angle with Bragg's law for each ψ angle, were then plotted as a function of $\sin^2\psi$. The measured strain, ε_ψ, depends

on the interplanar spacing, d_ψ:

$$\varepsilon_\psi = \frac{d_\psi - d_0}{d_0} \tag{4.5}$$

where d_0 is the strain-free interplanar spacing.

Due to the strong and sharp (111) fiber texture typical for Cu films, the crystallite group method (CGM) can be employed. In this method, all crystallites that have the same orientation are considered as a single crystal. Measured strain and stress in the film are related with following formula:

$$\varepsilon_\psi = \left[2S_{12} + \frac{2}{3}S_0 + \frac{1}{2}S_{44}\sin^2\psi\right]\sigma_f \tag{4.6}$$

with $S_0 = S_{11} - S_{12} - \frac{S_{44}}{2}$ (4.7)

S_{11}, S_{12} and S_{44} are the single crystal elastic compliances. Equation (4.6) is valid if plane stress condition is met and the sample has a rotationally symmetric biaxial stress state ($\sigma_{11} = \sigma_{22} = \sigma$ and $\sigma_{12} = \sigma_{23} = \sigma_{13} = \sigma_{33} = 0$)[118]. The strain-free inclination angle, ψ^*, is calculated with Equation (4.6) for $\varepsilon_\psi = 0$. The associated strain-free interplanar distance, d_0, is determined on the d_ψ vs. $\sin^2\psi$ plot. Using Equation (4.5), the strain, ε_ψ, is finally plotted vs. $\sin^2\psi$. The stress, σ_f, can be deduced from the slope of the obtained straight line with Equation (4.6).

4.4 Dislocation behavior

The dislocation behavior was studied by TEM. A precise description of TEM dislocation characterization is found in Williams and Carter[119]. Dislocations and other structural defects cause lattice distortions, e.g. by bending the crystal planes, as well as

displacements of atoms from their sites in the perfect crystal. These distortions alter the local diffraction conditions and therefore cause contrast in conventional TEM. For practical dislocation analysis, a two beam condition is required. To achieve this diffraction condition, the sample is tilted until two bright spots appear on a selected area diffraction (SAD) pattern: the primary beam and one Bragg reflection. Both Bright-Field (BF) and Dark-Field (DF) imaging modes were used. A BF image is formed using the central spot of the diffraction pattern, which contains the incident electrons. An objective aperture is used to block all other beams from reaching the imaging system. Areas of strongly diffracting materials, such as dislocations, therefore appear dark in a BF image. A DF image is formed when the objective aperture is positioned to allow only the diffracted beam to reach the imaging system. Thus, only crystal structures diffracting into the spot chosen with the aperture (i.e. having a particular plane spacing in the chosen orientation) appear bright in the image.

In-situ TEM experiments were conducted to study the dislocation mobility and interactions in the films. Both plan-view and cross-sectional TEM specimens were studied. During *in-situ* experiments, the specimens were thermally cycled between room temperature and 500 °C using a double tilt heating holder (Gatan) regulated with a controller (SmartSet Hot Stage Controller, Gatan). The heating rate was about 20 K/min whereas the cooling rate was maximum 15 K/min. A dwell time of about 15 minutes at 500 °C was necessary for dislocation analysis. Thermal cycling was performed under a pressure of about $5 \cdot 10^{-5}$ Pa, as required for TEM imaging. In these experiments, the films deform in a similar way as during a wafer curvature thermal cycling. It is therefore possible to correlate the observed dislocation movements with the stress evolution in the films.

CHAPTER 5

MICROSTRUCTURAL CHARACTERIZATION

5.1 Introduction

The mechanical properties of the films studied cannot be fully understood and explained without microstructural data. Since this study encompasses film systems consisting of different materials prepared under different experimental conditions (chapter 3), it is therefore expected that they will exhibit different microstructures. In this chapter, a detailed description and analysis of the main microstructural features of the films is provided. Particular attention will be devoted to the Cu/passivation layer interface.

5.2 Results

5.2.1 Microstructure of the Al_xO_y passivated Cu films

The microstructure of the Cu films annealed for 1 hour at 500 °C and passivated with 10 nm Al_xO_y (type CuAlO) was investigated before thermal cycling with focused ion beam, scanning electron and transmission electron microscopy.

The FIB microscope was used to analyze films thicker than 100 nm. The passivation layer was first sputtered away with a beam current of 1000 pA for a few seconds. Subsequently, the microstructure of the Cu films was imaged using secondary electrons. The observed Cu microstructure in as-deposited films is shown in Figure 5.1 for film thicknesses of 100 nm (a) and 1 µm (b). All films are polycrystalline, with a large number of twinned grains. Grooves are visible at some grain boundaries for the thicker films.

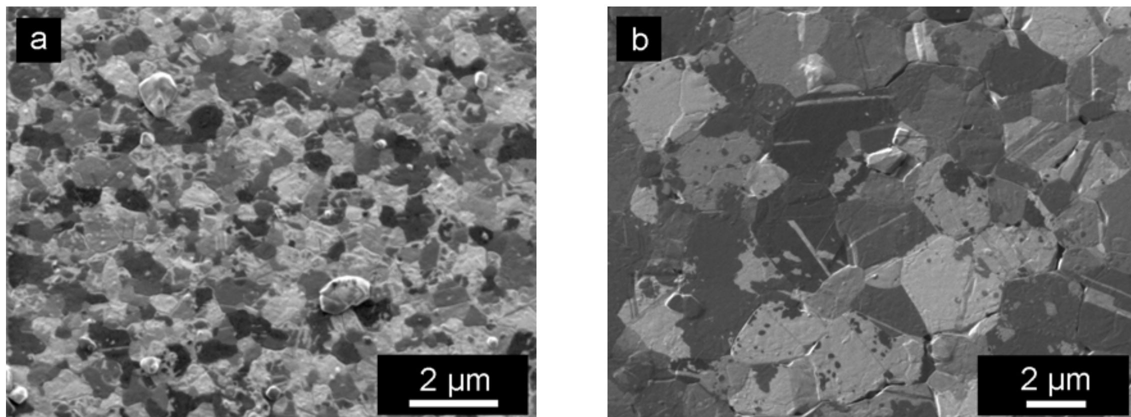

Figure 5.1: FIB micrographs of 100 nm (a) and 1 µm (b) thick Cu films passivated with 10 nm Al_xO_y. The passivation was removed with the ion beam before imaging. Samples were tilted at angles of 30° (a) and 25° (b). Twins and grooved grain boundaries are visible.

In Figure 5.2, a FIB micrograph of a 2 µm thick film in which a trench was sputter-etched reveals mostly columnar grains.

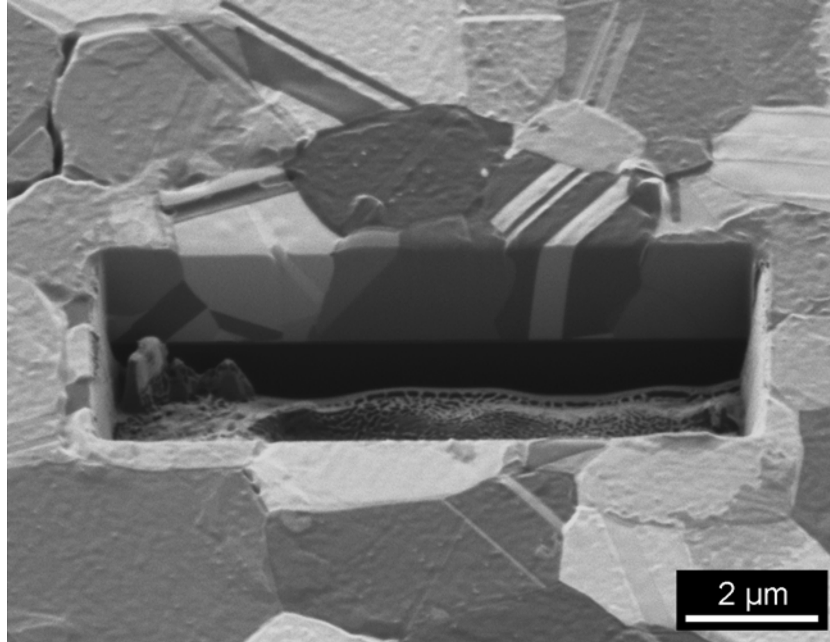

Figure 5.2: FIB micrograph of the 2 µm thick CuAlO film. The tilt angle of the sample is 45°. Columnar twinned grains are visible on the side wall of the sputter-etched trench. Smaller, non-columnar grains are also visible. The Si substrate appears black.

The Cu grain size was analyzed based on FIB micrographs, except for the 100 and 200 nm thick films for which TEM micrographs were used. The small grains characteristic of very thin films were indeed hard to resolve accurately with FIB microscopy. The grain size of the 25 and 50 nm thick films could not be determined since the TEM micrographs taken could not be analyzed. The grain size distributions for all the measured films are shown in Figure 5.3. The approximate linearity of the curves indicates a lognormal distribution for all film thicknesses.

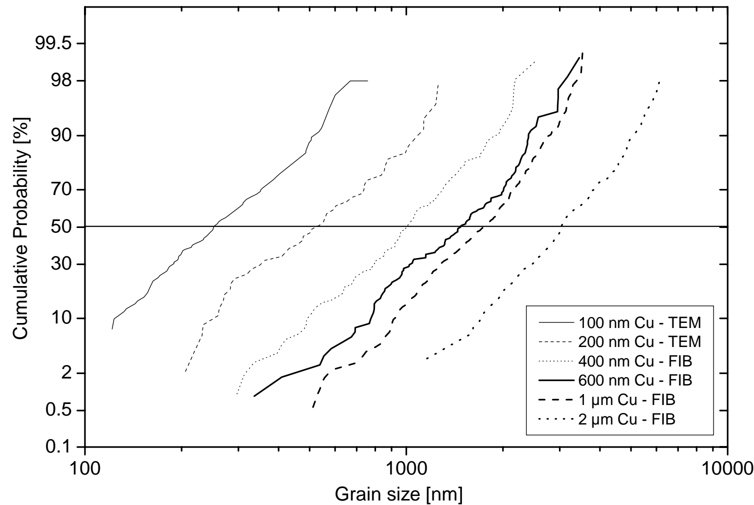

Figure 5.3: Grain size distributions for the different CuAlO films. The roughly linear plot indicates lognormal grain size distributions. The legend specifies the type of micrographs on which the analysis was based.

Two parameters representative of the distribution were determined and are summarized in Table 5.1: the median grain size, d_{med}, and the average grain size, d_{av}.

Table 5.1: Grain size data for the as-deposited CuAlO films. In these films, Cu was annealed for 1 hour at 500 °C before passivation at room temperature.

Film thickness h_f [nm]	Median grain size d_{med} [nm]	Average grain size d_{av} [nm]	Aspect ratio d_{med}/h_f
100	251	299	2.5
200	509	599	2.5
400	996	1113	2.5
600	1472	1581	2.5
1000	1729	1805	1.7
2000	3033	3283	1.5

The average grain size is higher than the median grain size, because it is affected by the extreme values of the distribution curves. The median value, which does not take into account these extremes, better represents the actual grain size. It will be used in the rest of the work as the grain size, *d*. The aspect ratio between median grain size and film thickness is of 2.5 for films thinner than 600 nm and of about 1.6 for thicker films. The dependency between the median grain size and the film thickness is evaluated on the plot in Figure 5.4. The grain size clearly increases with increasing film thickness.

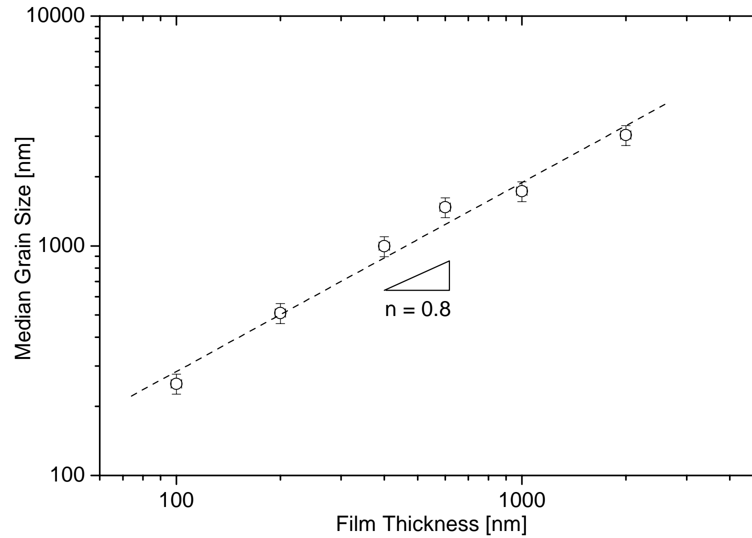

Figure 5.4: Power-law plot of the median grain size as a function of film thickness for the CuAlO films. The grain size clearly increases with increasing film thickness.

Films thinner than 100 nm were studied with scanning electron and transmission electron microscopy. All the ultra-thin films, including the 25 nm thick film, are continuous. Figure 5.5 shows an SEM (a) and a TEM (b) micrograph of the 50 nm thick film.

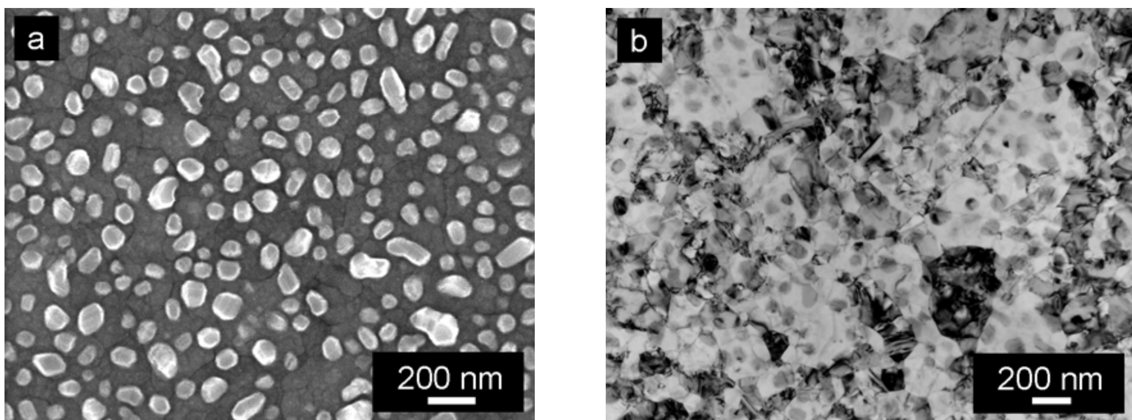

Figure 5.5: SEM (a) and TEM (b) micrographs of the 50 nm thick CuAlO film. Many particles are dispersed over the Cu film. Cu grain boundaries are also visible.

Numerous particles dispersed over the Cu film are visible. On the TEM micrograph, one can distinguish many ~100 nm large spots by their contrast, which most likely correspond to the particles on the film surface as revealed by SEM. Surfaces of all films thinner than 100 nm show similar features.

The passivation layer could be precisely observed on cross sectional TEM images which are shown in Figure 5.6 for the 100 nm (a), 200 nm (b) and 1 µm (c) thick films. The Cu films exhibit a columnar grain structure. The thickest films are also mostly columnar, but exhibit a small fraction of non-columnar grains with horizontal grain boundaries. Two particles are lying on the Cu surface in Figure (a). The passivation layer on top of the Cu film is visible in Figures (b) and (c).

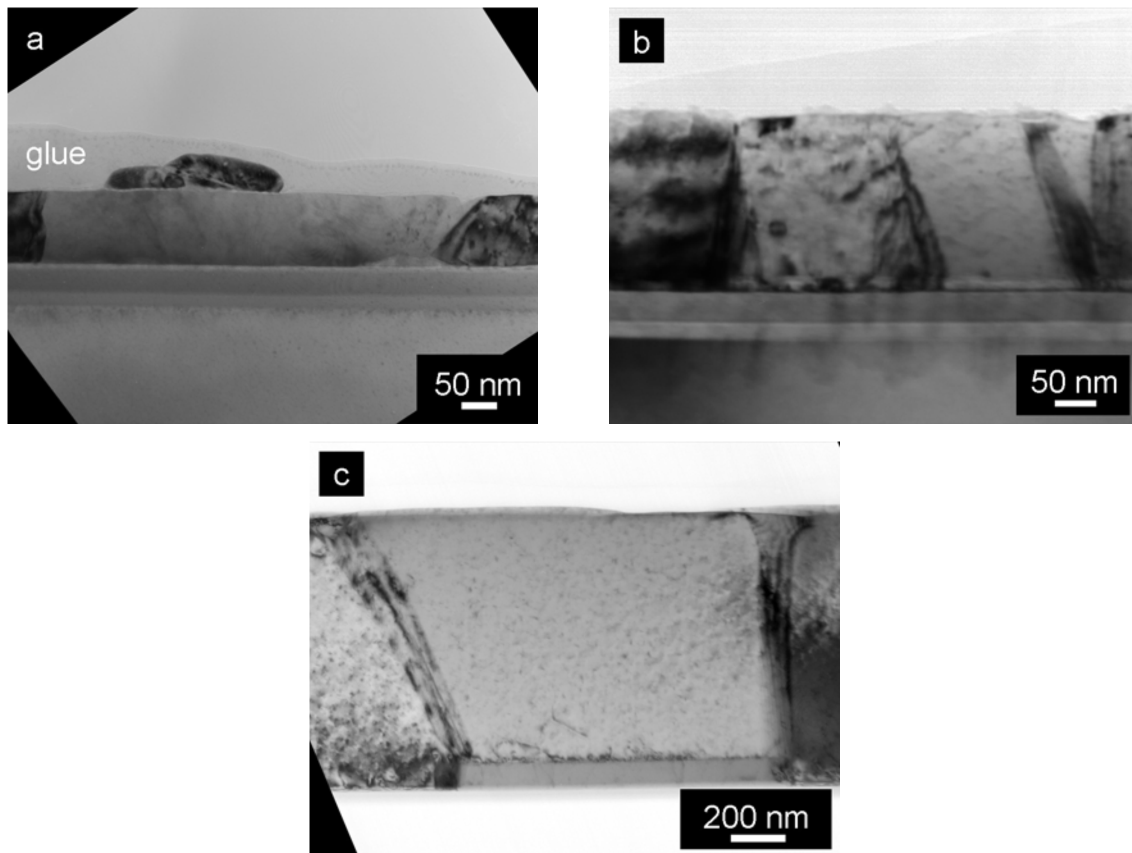

Figure 5.6: Cross sectional TEM images of (a) 100 nm, (b) 200 nm and (c) 1 µm thick Cu films passivated with 10 nm Al_xO_y. On all the micrographs, the Si substrate is on the bottom. The grains are mostly columnar, except for the 1 µm film where one horizontal grain boundary close to the film/substrate interface is visible (c). For the 100 nm thick film (a), two particles are lying on top of the Cu film. The grey contrast observed around these particles is caused by the glue used for TEM sample preparation. The black dots in the grains are artifacts of ion-milling.

In Figure 5.7, the layer sequence is visible for the 100 nm thick film. A thin Al_xO_y film completely covers the Cu surface. Moreover, an ~150 nm wide, 20 nm high particle is lying on top of the Cu film. EDX studies of the particle in the TEM revealed the

presence of Al. It was, however, not possible to determine whether it is Al or Al_xO_y since the EDX resolution limit was reached.

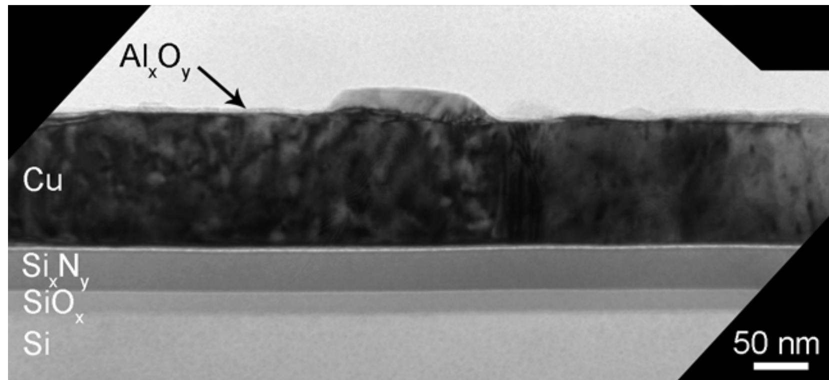

Figure 5.7: Cross sectional TEM image of the 100 nm thick CuAlO film. The layer sequence is clearly visible. The passivation layer consists of both a very thin layer covering the Cu surface films and higher islands.

A precise analysis of the thickness of the passivation film covering the Cu surface was performed on the TEM micrograph Figure 5.7. It yielded an average value of 5 ± 1 nm. Similar thicknesses were also measured on the other micrographs in Figure 5.6. The thickness of the interlayers were also measured and are on average 22 ± 1 nm for SiO_x and 39 ± 1 nm for Si_xN_y. These layers are thinner than expected from the nominal values furnished by the wafer producer (50 nm for each layer).

To get more information about the diameter and height of the particles dispersed over the film surface, AFM studies were performed (Figure 5.8). As already indicated by TEM observations, the surface of the 100 nm thick Cu film (a) is rough. The particles of the passivation layer are about 100 to 200 nm wide and 30 nm high. For the 1 µm thick film (b), the roughness is much smaller. The particles on the Cu surface are flatter (about 10 nm high). Some very small particles (about 30 nm wide and 5 nm high) are also located at the grooved grain boundary.

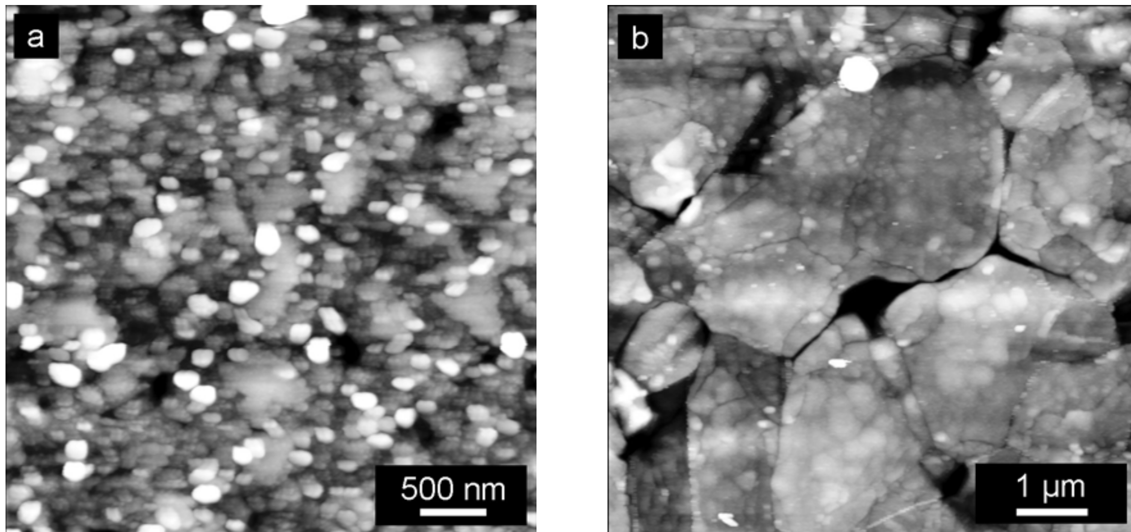

Figure 5.8: AFM micrographs of the 100 nm (a) and 1 µm (b) thick CuAlO films. The height scale is of 31.6 nm for (a) and 55.1 nm for (b). The roughness is large for the 100 nm film covered with 100 to 200 nm wide and 30 nm high particles whereas it is much smaller for the 1 µm film on which the particles are flatter.

X-ray diffraction studies were carried out to characterize the crystallographic orientation of the films. Figure 5.9 shows θ-2θ scans of the 400 nm and 2 µm thick films. All diffraction peaks stem from Si (of the substrate) and Cu. No peaks from Al or Al_xO_y are visible. This is most likely due to the low thickness of the passivation layer which prevents the formation of peaks higher than the background noise level. Cu appears exclusively in its (111) crystallographic orientation for the thinner film. Two main peaks for $\theta = 43.4°$ and 95.2°, which correspond to the (111) and (222) Cu reflexes are visible. The peak for $\theta = 50.6°$ reveals a small amount of (100)-oriented Cu grains in the 2 µm thick film. The Si (111) peak at $\theta = 28.5°$ is also detected, since the X-rays are not fully attenuated by the Cu films.

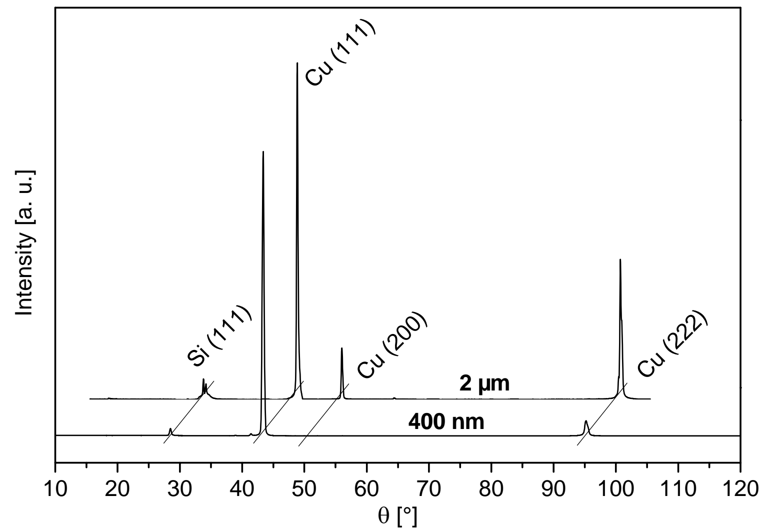

Figure 5.9: X-ray θ-2θ scans of the 400 nm and 2 µm thick CuAlO films. The scan of the 2 µm thick film is slightly shifted for clarity. The films are strongly (111) textured. The presence of (100)-oriented Cu grains in the 2 µm thick film is also revealed. The underlying Si substrate is visible in the scan, too. Al or Al_xO_y could not be detected.

All analyzed films reveal a strong and sharp (111) texture, as illustrated by the (111) pole figure of the 1 µm thick film in Figure 5.10. The central peak at $\psi = 0°$ and the continuous diffraction ring at $\psi = 70.5°$ together with the results of the θ-2θ scans indicate that the Cu grains grew with the (111) planes parallel to the substrate with a random in-plane orientation.

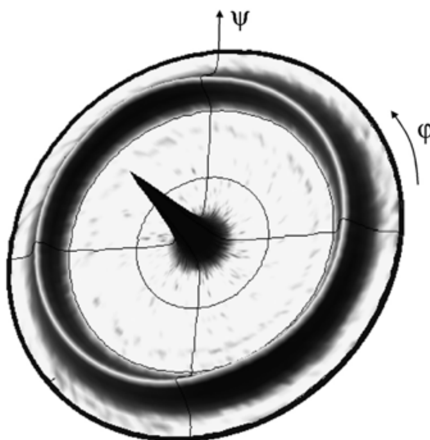

Figure 5.10: (111) pole figure of the 1 µm thick CuAlO film measured between $\psi = -90°$ and $\psi = +90°$. The narrow central (111) Cu peak indicates a strong (111) texture.

5.2.2 Microstructure of the Si_xN_y passivated Cu films of type CuSiN/AR

The microstructure of the Cu films annealed at 500 °C for 1 hour and then passivated at room temperature with 10 nm Si_xN_y (type CuSiN/AR) is discussed here. Two different batches of these samples (B1 and B2) were prepared and show different features.

All the films have a Cu structure similar to that of the CuAlO films with columnar grains and a (111)-texture. Due to these similarities, no grain size analysis was carried out. However, the passivation layer is different: it is much smoother than for the CuAlO films, since no surface topology is visible in the SEM.

The 25 nm thick film from batch 1 was not used for mechanical measurements since only about 50% of its substrate surface is covered by the film. However, the 30 nm thick film from batch 2 is continuous.

The main difference between the 2 prepared batches is the porosity. The films from batch 1 have many pores and marked grain boundary grooves, as visible on the SEM images of the 100 nm (a) and the 600 nm (b) thick Cu films in Figure 5.11.

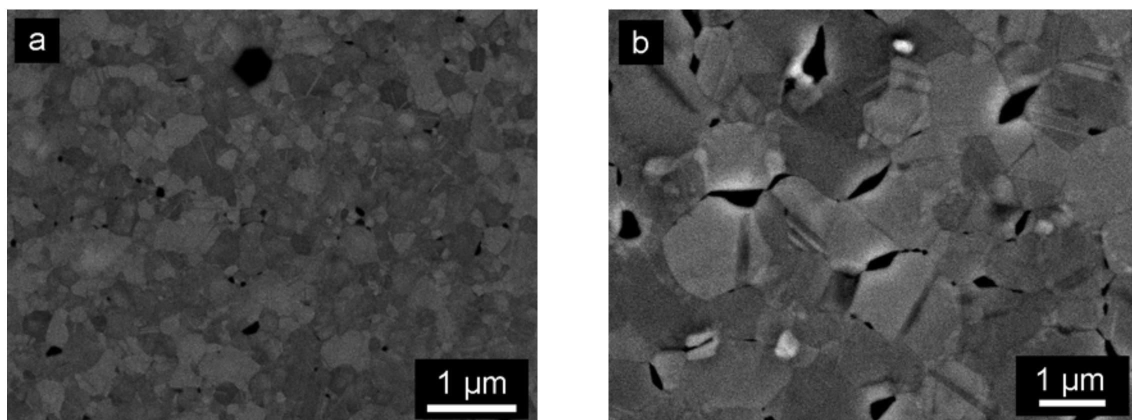

Figure 5.11: SEM images of the 100 nm (a) and 600 nm (b) thick CuSiN/AR/B1 films. Many pores and grain boundary grooves are visible.

The pores were characterized in the FIB microscope. Figure 5.12 shows a cross sectional cut through a pore from the 100 nm thick film of batch 1. The pore clearly reaches the film/substrate interface. The columnar grain structure is also visible.

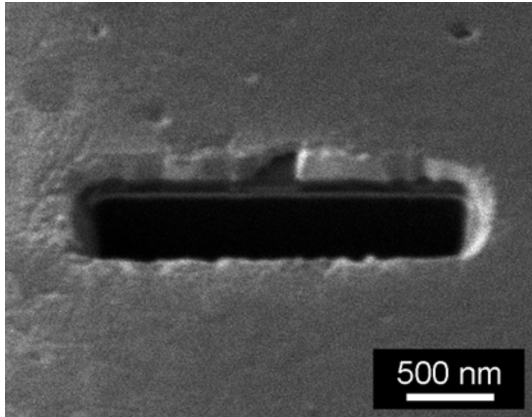

Figure 5.12: FIB micrograph of the 100 nm thick CuSiN/AR/B1 film. The tilt angle of the sample is 45°. A trench was sputter-etched through a pore, which clearly reaches the film/substrate interface.

With a porous Cu film, the capping layer can obviously not passivate the complete film surface. This is confirmed by XPS measurements of the 100 nm thick film from batch 1 presented in Figure 5.13. In addition to the peaks characteristic for Si_xN_y, a Cu peak is visible in the spectrum. O and C peaks are also detected due to the exposure of the film to air before characterization. The detailed spectra for the different peaks are given in the appendix (section 10.3) together with an XPS study of a 10 nm thick Si_xN_y layer.

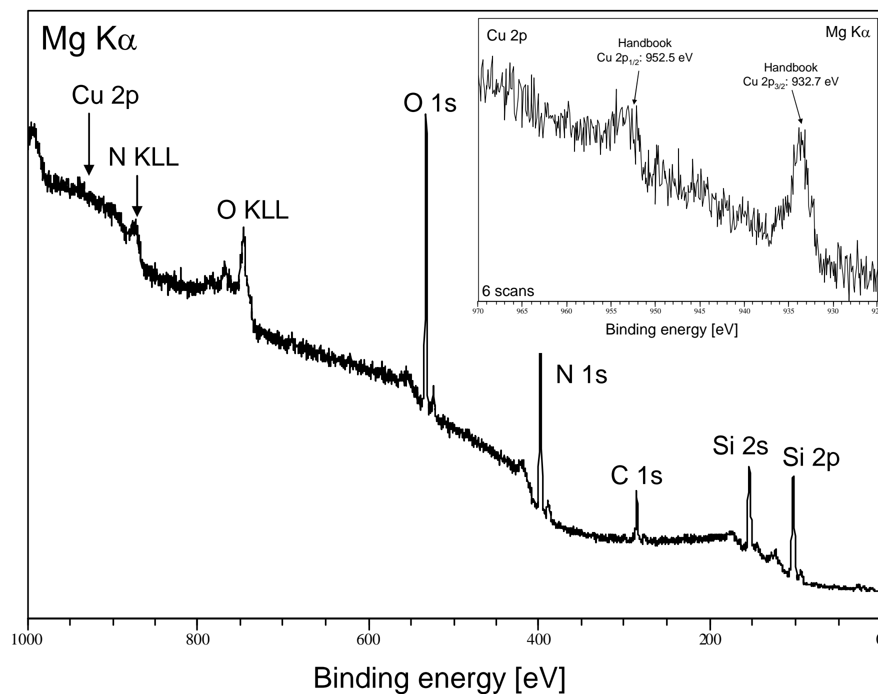

Figure 5.13: XPS spectrum of the 100 nm CuSiN/AR/B1 film. The inset shows the detailed spectrum of the Cu peaks.

No pores were observed in the Cu films from batch 2. This is shown in Figure 5.14, a SEM image of the 100 nm thick film from batch 2. The grain size is clearly the same as for the 100 nm film from batch 1 (shown in Figure 5.11(a) with the same scale bar).

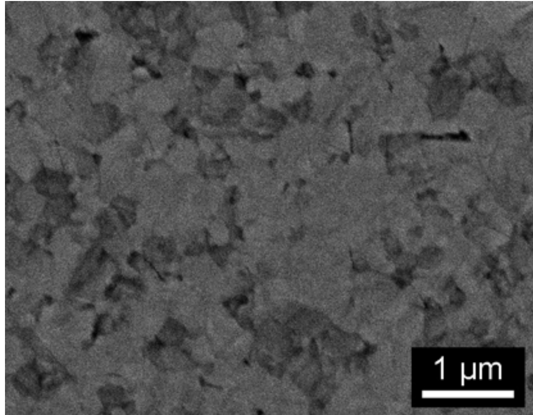

Figure 5.14: SEM image of the 100 nm thick CuSiN/AR/B2 film, showing a continuous Cu layer.

5.2.3 Microstructure of the Si_xN_y passivated Cu films of type CuSiN/AA

The microstructure of the Cu films annealed at 500 °C for 1 hour and passivated at this temperature with 10 nm Si_xN_y (type CuSiN/AA) was studied. As for the CuSiN/AR films, two batches of samples were prepared. They had identical microstructures, so that no distinction will be made between them in the rest of the work.

The microstructure observed for the CuSiN/AA films is illustrated with SEM and TEM micrographs of the 100 and 600 nm thick films in Figure 5.15 and Figure 5.16. The Cu structure is identical to that of the CuSiN/AR films, with columnar grains and a strong (111)-texture, so that no Cu grain size analysis was performed. However, annealing produced hillocks on the surface of the films thinner than 200 nm. Again, the passivation layer is not visible.

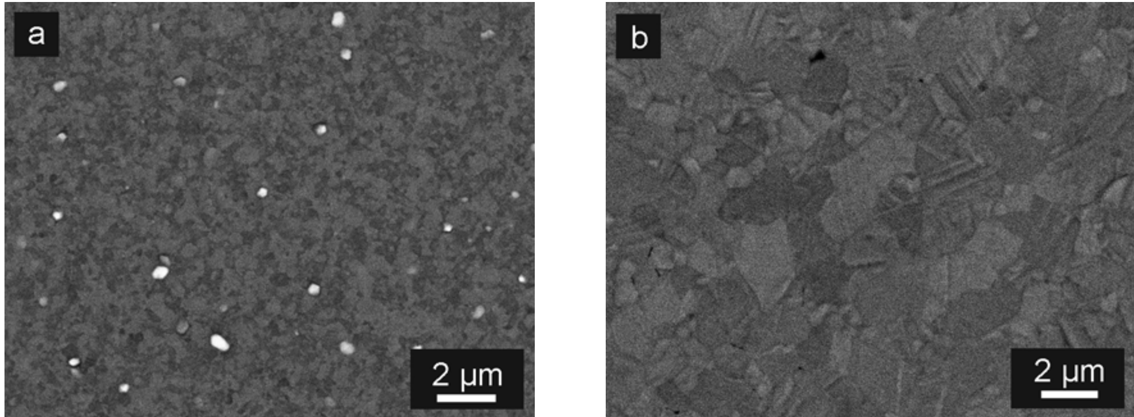

Figure 5.15: SEM micrographs of the 100 nm (a) and 600 nm (b) thick CuSiN/AA films. Hillocks are visible on the surface of the 100 nm thick, annealed Cu film.

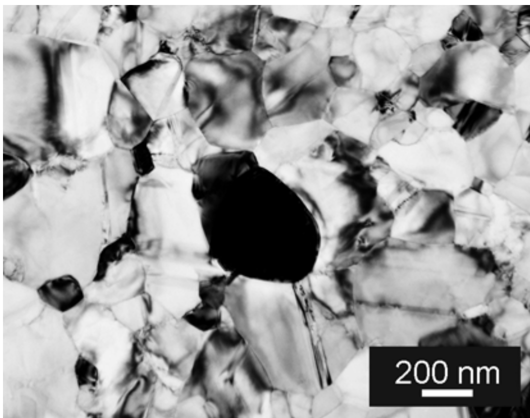

Figure 5.16: TEM image of the 100 nm thick CuSiN/AA film, showing a hillock (black spot) surrounded by Cu grains.

The hillock size is constant over the whole thickness range in which they appear, and varies between 250 and 350 nm in diameter. Their density was quantitatively analyzed and is shown in a power-law plot vs. the film thickness (Figure 5.17). It clearly decreases with increasing film thickness.

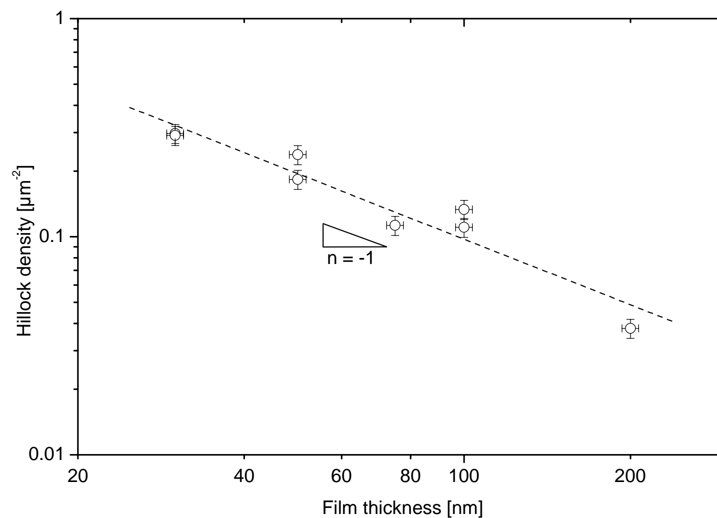

Figure 5.17: Power-law plot of the hillock density vs. film thickness for the CuSiN/AA films. The hillock density decreases with increasing film thickness.

An XPS analysis of the 100 nm thick CuSiN/AA film detected the presence of Cu. This indicates that the passivation layer is likely fractured during hillock growth.

The influence of thermal cycling on the film microstructure was also investigated. No change was observed: both grain size and hillock density remain unchanged after cycling to 500 °C.

5.2.4 Microstructure of the Si_xN_y passivated Cu films of type CuSiN/RR

In this section, we describe the microstructure of the as-deposited non-annealed Cu films passivated after deposition with 10 nm Si_xN_y (type CuSiN/RR). As for the CuSiN/AA films, no distinction will be made between samples of batch 1 and 2 since their microstructure was identical. The film surface was examined with SEM imaging whereas the Cu grain structure was observed with either FIB or TEM imaging.

Figure 5.18 shows SEM images of the as-deposited 100 nm and 2 µm thick CuSiN/RR films. A uniform surface with small regions of about 20 to 100 nm is visible. These "grains" supposedly correspond to the roughness of the film. No pores or hillocks are visible.

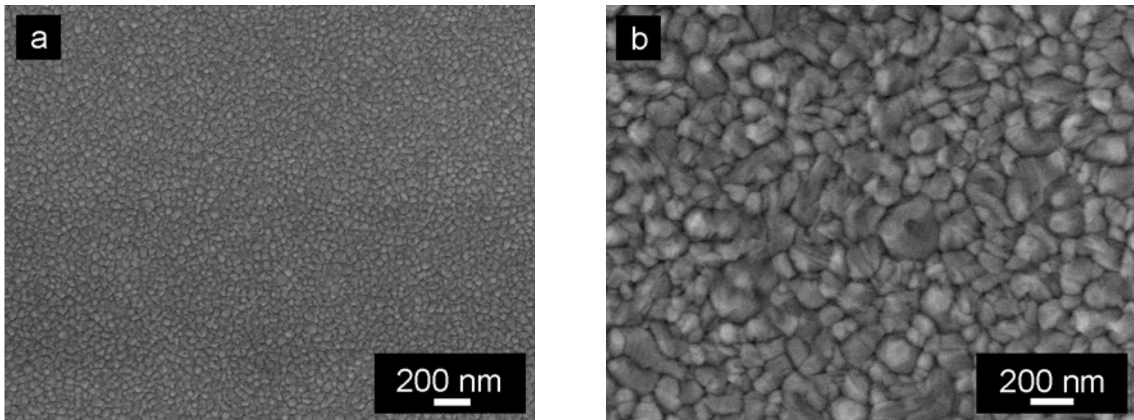

Figure 5.18: Surface morphology of the 100 nm (a) and 2 µm (b) thick as-deposited CuSiN/RR films imaged with SEM. The surface consists of a uniform layer of very small regions.

The size of the surface grains was quantitatively analyzed as a function of film thickness. The grain size distributions are all lognormal, and exhibit an increasing width with increasing film thickness. The obtained median grain size is plotted vs. the film thickness in Figure 5.19, which indicates a dependency between the two parameters.

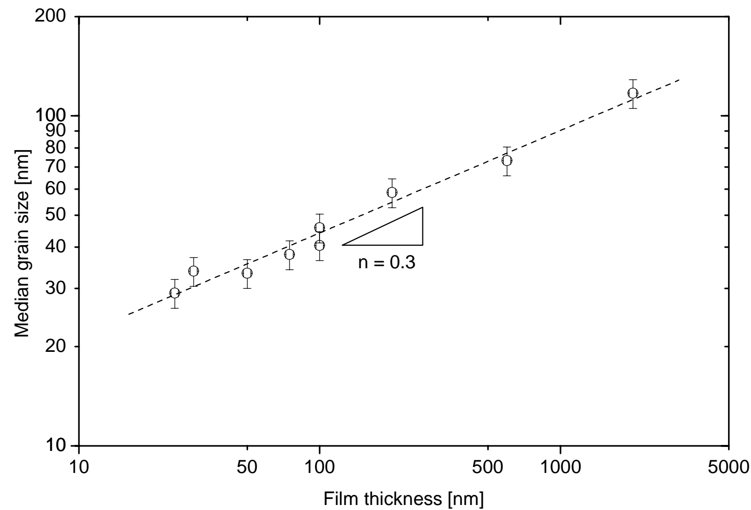

Figure 5.19: Power-law plot representing the median size of the surface grains as a function of the film thickness for the CuSiN/RR films. The median size increases with increasing film thickness.

The Cu grain structure could also be examined with TEM and is shown for the as-deposited 100 nm thick film in Figure 5.20.

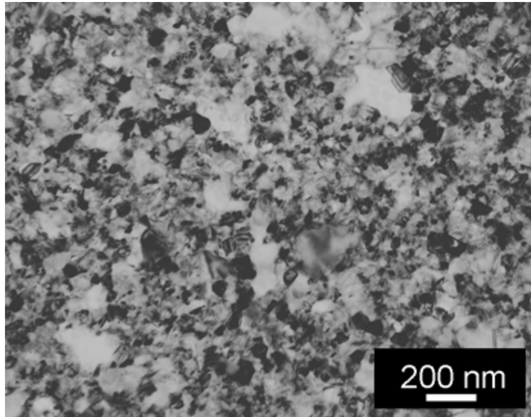

Figure 5.20: Cu grain structure of the as-deposited 100 nm thick CuSiN/RR films. On this TEM image, the grain size distribution appears to be bimodal with a few big grains embedded in a matrix of very small grains.

From a comparison between Figure 5.18(a) and Figure 5.20, it appears that the size of surface morphology corresponds to the size of the smaller Cu grains. However, the distribution of the surface grains is monomodal whereas it is bimodal for the Cu grains. This sustains the idea that the surface grains correspond to the Cu roughness, which is homogeneous over the entire film, and does not depend on the size of the Cu grains.

(111)-pole figures of the as-deposited films were recorded and revealed a strong (111) texture, as shown in Figure 5.21 for the 100 nm thick film.

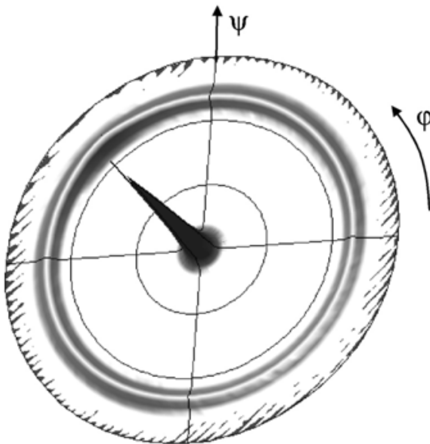

Figure 5.21: (111)-pole figure of the 100 nm thick CuSiN/RR film. The central peak at $\psi = 0°$ and the continuous diffraction ring at $\psi = 70.5°$ are characteristic of a (111) texture.

The continuity of the passivation layer was investigated by XPS for the 25 nm thick film (Figure 5.22). Two spectra were recorded: (1) directly after Cu deposition and (2) after depositing 10 nm Si_xN_y. The film was kept in UHV during the whole preparation and characterization. Detailed spectra of the different peaks are provided in the appendix (section 10.3.3).

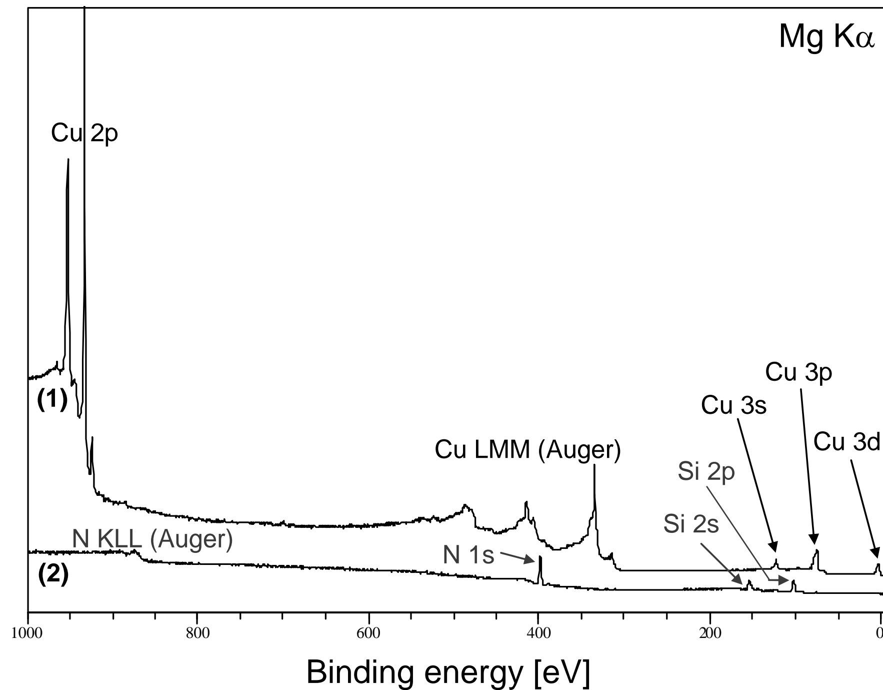

Figure 5.22: XPS spectra of the 25 nm thick CuSiN/RR film, before (1) and after (2) depositing 10 nm Si_xN_y. The Cu peaks detected before passivation are no longer visible afterwards, indicating that the passivation layer completely covers the Cu film.

Before passivating the Cu film, only Cu peaks are detected. These peaks are no longer visible on the spectrum after passivation, which consists of Si and N peaks characteristic of Si_xN_y. Thus, the passivation layer is densely covering the Cu film surface. No O or C peaks are seen, indicating the high purity of the films.

The continuity of the passivation is confirmed by an analysis of the interface between the Cu and the Si_xN_y film with HRTEM. In Figure 5.23, a micrograph of a cross-sectional specimen of the as-deposited 100 nm thick film is presented. Three different materials can be distinguished: crystalline Cu at the bottom, capped with about 10 nm crystalline Si_xN_y, and covered with an amorphous W layer used for the FIB-assisted TEM lamella preparation. The Si_xN_y layer appeared continuous over the entire analyzed interface.

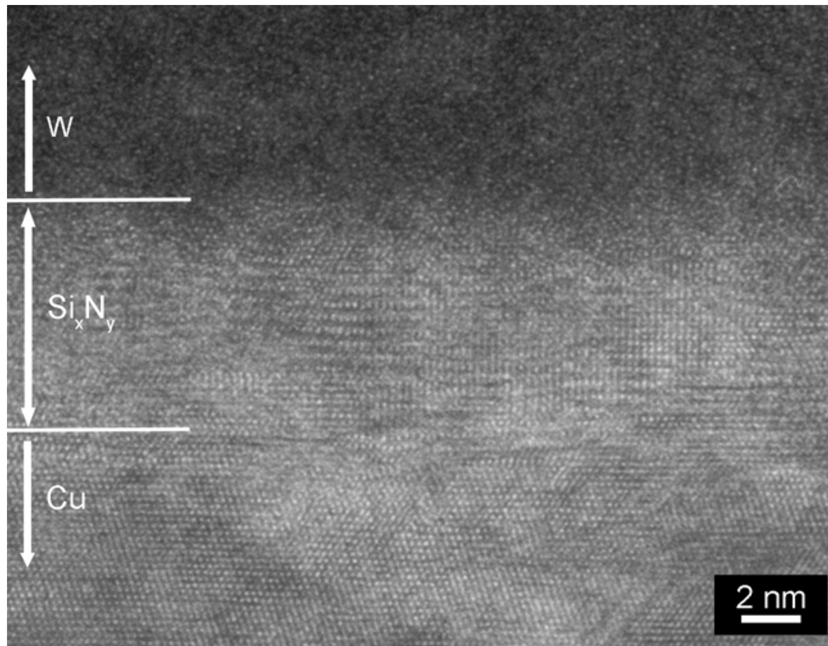

Figure 5.23: HRTEM micrograph of the interface Cu/Si_xN_y shown for the 100 nm thick CuSiN/RR film before thermal cycling.

The thermal stability of the films was evaluated by examining their microstructure after cycling to 500 °C. Both the surface and the Cu grain structure are shown in Figure 5.24 for the 100 nm thick film. The surface morphology does not evolve whereas the Cu grains grow. A few pores form in the Cu film.

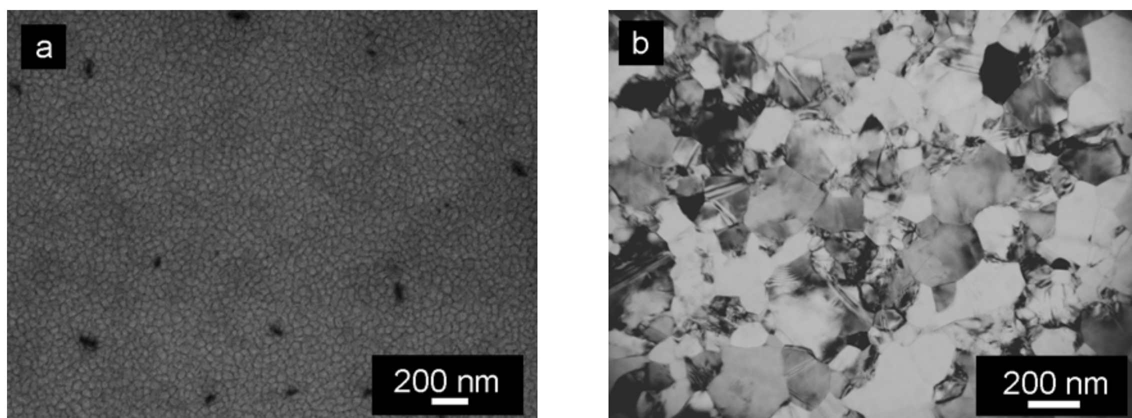

Figure 5.24: Microstructure of the 100 nm thick film after cycling to 500 °C. (a) SEM image of the surface and (b) TEM image of the Cu grain structure. The effect of thermal cycling is visible upon comparing these images with the ones shown in Figure 5.18(a) and Figure 5.20. The black areas on the SEM image correspond to pores which appeared upon thermal cycling.

Cu grain growth upon thermal cycling was also observed *in-situ* in the TEM. A grain size analysis was performed for the 600 nm thick film after thermal cycling. The grain size distribution was monomodal and lognormal with a median grain size of 1400 ± 140 nm.

The passivation layer remains intact after thermal cycling to 500 °C, as proved by XPS. Indeed, a spectrum similar to the spectrum (2) in Figure 5.22 showing no Cu peak was obtained for the 100 nm thick film after thermal cycling.

The Cu grain structure was also studied in cross section, as shown in Figure 5.25 and Figure 5.26 for the 100 and 600 nm thick films, respectively. The as-deposited films exhibit a few columnar grains which are surrounded by small non-columnar grains. Upon heating, the grains grow and become columnar. For both film thicknesses, the film looks thinner after thermal cycling. This is an artifact due to TEM lamella preparation (Figure 5.25) and FIB imaging (Figure 5.26).

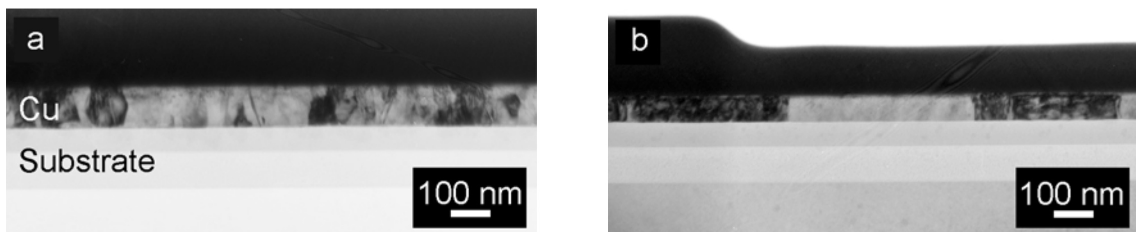

Figure 5.25: TEM cross sectional views of the 100 nm thick CuSiN/RR film before (a) and after (b) thermal cycling to 500 °C. The black contrast on top of the Cu is from the W layer used to protect the Cu film during the FIB-assisted preparation of the TEM lamella. Non-columnar small grains (a) become columnar (b) upon thermal cycling. Note that the apparent smaller film thickness after thermal cycling is not a real effect but can be explained by the TEM lamella being cut out of the wafer edge where the film is locally thinner.

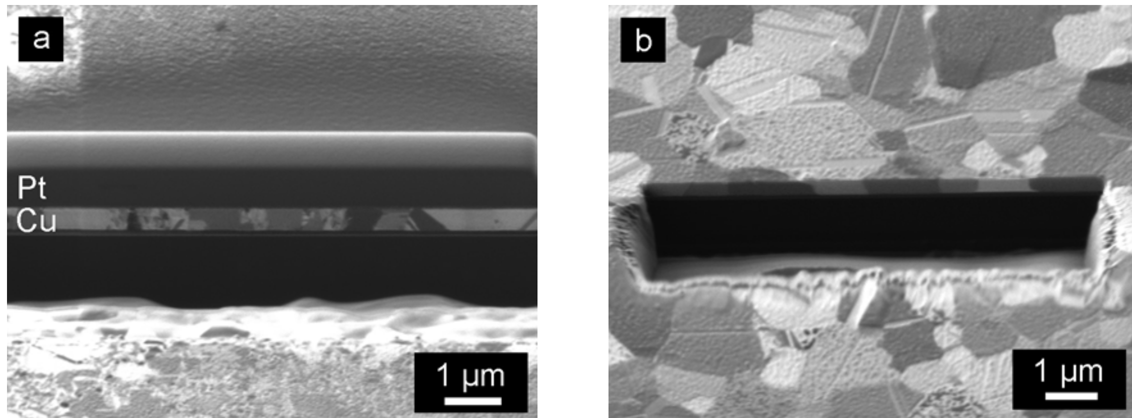

Figure 5.26: FIB cross sectional views of the 600 nm thick CuSiN/RR film before (a) and after (b) thermal cycling to 500 °C. The tilt angles are of 45° for both images. In (a), a Pt layer was deposited on the film to protect it during imaging. Big columnar grains are surrounded with small non-columnar grains. The film shown in (b) looks thinner than the expected 600 nm since the upper side of the film was etched away by the ion beam. Big columnar grains are shown.

5.2.5 Microstructure of unpassivated Cu films (type CuR and CuA)

In order to distinguish between microstructural features typical for sputtered Cu films and microstructural changes due to passivation, the microstructure of unpassivated Cu films was also briefly analyzed. In Figure 5.27, typical Cu grain structures of an as-deposited (type CuR) (a) and annealed (type CuA) (b) 100 nm thick film are presented. The as-deposited film exhibits a bimodal distribution of small grains whereas the grains of the annealed film are bigger and follow a monomodal distribution. The films are perfectly continuous, without pores, grooves, or hillocks.

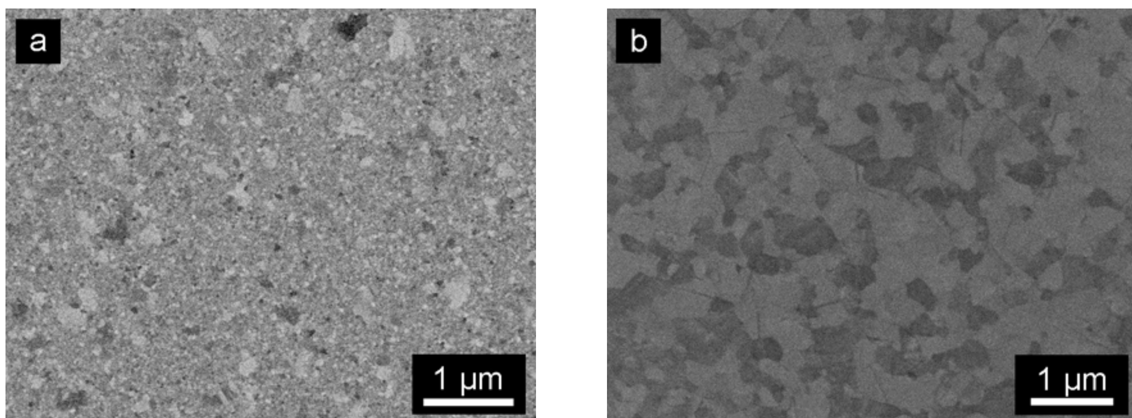

Figure 5.27: SEM images of a 100 nm thick unpassivated Cu film, (a) as-deposited (type CuR) and (b) annealed for 1 hour at 500 °C (type CuA). A bimodal distribution of small grains is characteristic of the as-deposited film whereas the annealed film shows a monomodal distribution of much bigger grains. No pores or hillocks are visible.

5.3 Discussion

The microstructural characterization of the films highlighted different aspects, which will now be discussed. After addressing the grain structure of the Cu films, we will focus on the microstructure of the passivation layers. The film morphology will then be discussed.

5.3.1 UHV-sputtered Cu films

The studied film systems were based both on annealed and as-deposited Cu films, which exhibited different Cu grain structures.

Annealed films

The Cu grain structure is similar for all annealed films, whether passivated or unpassivated, and exhibits common features: a lognormal grain size distribution with a large median grain size scaling with film thickness and a strong and sharp (111) texture. This type of microstructure is typical for annealed Cu films sputtered under UHV conditions and was reported in several studies (e.g. [25,57,59,120]).

The median grain sizes determined for the CuAlO films are compared with data from literature for UHV-sputtered annealed Cu films in Table 5.2.

Table 5.2: Median grain sizes for UHV-sputtered annealed Cu films from this work (type CuAlO) and from the studies of Weiss *et al.* and Balk *et al.*, determined with FIB images.

Film thickness [nm]	Median grain size [nm]		
	Type CuAlO (this work)	Weiss *et al.*[57]	Balk *et al.*[56]
100	251*	-	201*
200	509*	-	337*
400	996	-	888
600	1472	-	-
1000	1729	2400	1614
2000	3033	3700	2544

* determined with TEM images

The grain sizes measured in this study are comparable with the values from literature. It appears that grain growth stagnates at a grain size to film thickness ratio of about 2. A theory by Mullins proposes an explanation for the stagnation of the grain growth at this ratio[121]. Indeed, it was shown that a moving grain boundary gets pinned by a groove on the film surface if a critical grain size of the order of two times the film thickness is reached. The lognormal grain size distributions shown in Figure 5.3 are also consistent with predictions from literature. Thompson indeed observed such distributions in two-dimensional grain growth simulations, based on stagnation of grain size due to grain boundary grooving[122].

A (111) texture is widely observed for UHV-sputtered Cu films[25,59,123] and can be explained with energetic considerations. As described by Thompson and Carel, the driving force for texture evolution in a thin film is the minimization of the surface and interfacial energy[7,124,125]. They proposed following expression for the change in film energy density, $\Delta F_{s/i}$, associated with grain growth-induced texture evolution[125]:

$$\Delta F_{s/i} = \frac{\Delta\gamma_s + \Delta\gamma_i}{h_f} \qquad (5.1)$$

where $\Delta\gamma_s$ and $\Delta\gamma_i$ are the differences in average surface and interfacial energies before and after grain growth, respectively, and h_f is the film thickness. From this relationship, it is visible that the surface and interfacial energies play an increasing role on grain growth with decreasing film thickness. In face-centered cubic metals, the (111)-oriented close packed planes have the lowest surface and interfacial free energies. For example, the surface energy for (111) Cu grains is 1.96 $J \cdot m^{-2}$, to be compared to 2.09 $J \cdot m^{-2}$ for (100) grains[126]. A (111) texture is therefore energetically favored for thin films. A few (100)-oriented grains are also observed in the thicker films. Indeed, the influence of elastic strain energy due to thermal strain, which is minimized for (100)-oriented grains in Cu, increases with film thickness[125,127,128].

As-deposited films

The CuSiN/RR films, which were passivated directly after Cu deposition, without annealing, show a bimodal Cu grain distribution with a few big grains embedded in a

matrix of very small grains. These results agree with those published for as-deposited sputtered Cu films[120,129,130]. A bimodal grain size distribution, with poorly defined small grains and large grains whose size does not exceed a low multiple of film thickness is indeed typical for such films[120]. It results from abnormal grain growth which occurs during deposition[122,125]. Abnormal grain growth, which is the growth of a few grains into a matrix of small stagnant grains, is due to an energy advantage for the abnormally growing grains[131]. The grain size of the smaller grains could be determined experimentally by measuring the roughness of the surface on SEM micrographs. The median grain size varies roughly between 25 nm and 100 nm and is herewith comparable to literature values[120]. The linear increase in median grain size with film thickness can be explained by the grain growth being already active during deposition. Similar microscopic features are predicted by the structure zone model (SZM). It was originally proposed for thick evaporated films by Movchan and Demchishin[132] and modified by Thornton for thick sputtered deposits[133-135]. According to this model, for a film deposited at room temperature, with an homologous temperature T_S/T_M of 0.2 (where T_S and T_M are the substrate temperature during sputtering and the melting temperature of Cu, T_M = 1356 K [15]), two structural morphologies are dominant at high and low sputtering pressures, respectively. Our films, which were deposited at a low argon pressure of $2.5 \cdot 10^{-1}$ Pa, are in zone T (transition zone). In this zone, a dense array of poorly defined fibrous grains with a smooth surface and without voided boundaries is expected, together with a bimodal grain size distribution[129]. Despite the presence of the Si_xN_y capping layer, the small grains in the as-deposited films coarsened upon thermal cycling to 500 °C. The stabilized grain size of the films is comparable with the one measured in annealed films. The initially bimodal distribution became monomodal, as also reported in [120]. However, the film surface observed with SEM was rough even after Cu grain growth. The passivation layer conformally coats the grooved Cu surface and replicates the original Cu microstructure. While post-preparation thermal cycling can change the Cu grain size, it cannot alter the passivation topography replicated in the passivation.

The as-deposited films exhibit a (111) texture. It was shown that texture already develops in the early stages of film growth, during the processes of island nucleation and coalescence[136].

5.3.2 Microstructure of the passivation layers

Aluminum oxide passivation

The Al_xO_y passivation consists of a thin continuous film covered with islands whose height and size depend on the Cu film thickness. The thinner the Cu film, the higher the particles. The continuous film with a thickness of about 5 ± 1 nm is thinner than the expected 10 nm, due to the coalescence of Al into islands. The formation of these islands may have occurred during one of both steps of the passivation preparation: either during Al deposition or during its annealing and oxidizing. Considering the deposition, the lattice mismatch of about 12% between Al and Cu (calculated from the lattice parameters of Cu, a_{Cu} = 3.6146 Å[137] and Al, a_{Al} = 4.0488 Å[79]) might be at the origin of a Stranski-Krastanov film growth of Al on Cu. This would explain the formation of both a continuous film and islands on top of it. During annealing and oxidizing, Al islands of the film may have coalesced for energetical reasons. The layer seems to cover continuously the Cu film, and is thus expected to act as a good diffusion barrier.

Silicon nitride passivation

A HRTEM cross-sectional observation of the Cu/passivation layer interface indicated the crystallinity of the 10 nm thick Si_xN_y layer. This is in contradiction with a previous study in which a 400 nm thick reactively-sputtered Si_xN_y film was found to be amorphous[138]. The difference of crystallinity between the two films may be due to the difference of film thickness or sputtering conditions. The Si_xN_y passivation layer presumably homogeneously covers the Cu film, as indicated by XPS studies. Except for the CuSiN/RR films, in which the passivation layer reproduced the surface topology of the Cu film, it could not be imaged on plan-view microscopic images. However, pores and hillocks arising in some films seem to jeopardize the reliability of the layer as a diffusion barrier.

5.3.3 Pores in the CuSiN/AR/B1 films

Pores were found in the batch 1 CuSiN/AR films. The films prepared in batch 2 under identical conditions were perfectly continuous. This suggests that the morphological variations are linked to the film fabrication process. It is believed that the heating system integrated in the sputtering chamber was not calibrated accurately during the preparation of the films of batch 1. The effective annealing temperature may have been higher than the expected 500 °C, possibly leading to the formation of pores. Pores were exclusively located at grain boundaries, and often at grain boundary triple junctions. This preferential location indicates that diffusive processes control their formation, as confirmed by other studies (e.g. [139,140]). A higher annealing temperature implies higher diffusivities and thus an increased voiding probability.

In addition, pores seem to be strongly affected by the film thickness: thinner films tend to have big pores, whereas thicker films show stronger grain boundary grooving. Two possible factors may contribute to this difference: film stress and diffusion distance. As it will be discussed in chapter 6, thin films exhibit higher stresses than thicker films. Pore formation, which relaxes stresses at high temperatures, is therefore thermodynamically favored in thinner, more highly stressed films. Moreover, diffusion distance increases with film thickness. Thinner films can transport more material relative to their thickness compared to thicker films.

5.3.4 Hillocks in the CuSiN/AA films thinner than 200 nm

The possible formation mechanisms of hillocks have been investigated by a number of researchers. The most accepted model assumes that hillocks form at high temperatures to relax the compressive stress[141] introduced either during deposition[142,143] or subsequently by substrate-induced differential expansion strains[144,145]. The atoms which compose hillocks diffuse out of the film due to the thermally induced compressive stress. The observation of hillocks forming preferentially at grain boundary triple junctions[139] suggests that the mass transport associated to their formation relies both on grain boundary and surface diffusion[146,147]. The presence of a capping layer on a thin film was shown to play a crucial role in hillock growth[148,149]. The encapsulation of a film by a stiff, thick (several hundred nanometers) overlayer is considered to be the

most effective way to suppress hillocking, since the overlayer hinders atomic transportation to the free surface and introduces an energy requirement for fracturing the passivation (e.g. [150-154]). However, the presence of a thinner surface oxide layer is essential for hillock formation. Experimentally, no hillock growth was observed in Al films deposited and subsequently annealed in a UHV system[148]. The application of compressive differential thermal expansion strains caused stress relaxation via surface-diffusion-produced grain boundary grooving rather than hillock formation because of the absence of oxide layer on the surface. After exposure to air, hillocks were observed on the films. This result was interpreted as showing that a capping layer hinders the diffusional creep processes which reduce film stress. The stress is therefore relieved by hillock formation. A similar conclusion was made in a study of Leung *et al.*, which observed hillocks in passivated Au films, but not in bare films[76]. This result is nevertheless in contradiction with a recent work of Sauter *et al.*, which revealed hillock growth in unpassivated non-columnar Au films[88,155].

Hillock growth in capped films may occur following two possible mechanisms[148,149], illustrated in Figure 5.28. On one hand, in the case of a flawless cap, hillocks are expected to nucleate and grow at the interface between the film and the capping layer, preferentially at grain boundaries where out-diffusion is most rapid. This forces the passivation to bulge upwards (a)[156,157]. As the volume of the hillock increases, the stress in the cap may become sufficient to cause the layer to fracture. As a result of the cracking of the cap, the hillock comes out to the free surface (b). On the other hand, hillocks can additionally form on top of a cap with defects by e.g. flowing through a hole (c)[157,158]. Indeed, holes and cracks in the surface layer are regions of low stress and create gradients which drive transport of material. They can act as nucleation and growth sites of hillocks[141,148,158].

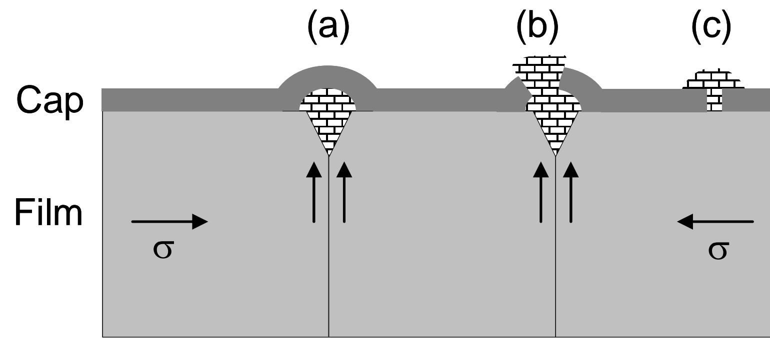

Figure 5.28: Schematic drawing of the possible hillock growth mechanisms in a passivated film. (a) A hillock nucleates and grows at the interface between the film and the capping layer. (b) As the hillock grows, it might break the cap and continue growing on top of it. (c) A hillock is also likely to form at a pore of the passivation layer. Schematic modified after [148] and [149].

In this study, all the films of type CuSiN/AA thinner that 200 nm exhibited hillocks. Two possible formation mechanisms are proposed. First, hillocks may form during annealing at 500 °C, but before passivation. In this case, hillocks should have been observed in annealed unpassivated films at room temperature too, which was not the case. Hillocks in unpassivated films might have formed during annealing and disappeared upon cooling, when the film becomes tensile. The existence of reversible hillock growth in thin films was indeed reported[159]. One can thus speculate that the hillocks that might have formed in the passivated films upon annealing cannot shrink upon cooling, because of the capping layer deposited at 500 °C. The cap, which suppresses surface diffusion, is likely to suppress material flow controlling the disintegration of hillocks upon cooling. Second, another speculation is that hillocks appear after passivation at 500 °C, before cooling. At this temperature, the film is indeed under compressive stress and thus combines all the conditions enumerated above for hillock growth. Nevertheless, this mechanism would predict hillock growth in all the passivated films, and not only in the films passivated at 500 °C. We believe that the Si_xN_y layer sputtered at 500 °C exhibits more defects than if deposited at room temperature, and thus favors hillock growth. Moreover, hillocks were exclusively observed in films thinner than 200 nm and their density was shown to increase with decreasing film thickness. A possible explanation for these observations is that diffusion plays an increasing role for thinner films, as will be discussed in the next chapter. Hillock growth, which relies on diffusion, is therefore likely to be more active in the thinner films.

5.4 Summary

In this chapter, the Cu microstructure in the studied film systems was shown to depend strongly on the preparation route. After thermal cycling, the grain size is identical for all the passivated films and similar to the values obtained by Balk *et al.* for unpassivated annealed Cu films. The passivation layers are continuous, except for a few films presenting microstructural specificities. Films of type CuSiN/AR from batch 1 had pores, whereas films of type CuSiN/AA thinner than 200 nm were covered with hillocks. The main microstructural features are summarized in Table 5.3, which gives an overview over the different types of passivated films.

Table 5.3: Main microstructural features of the different passivated film systems examined in this study.

		Cu film	Passivation layer
CuAlO		(111) texture. Columnar grains. Lognormal grain size distribution. $d \sim 2\ h_f$	For $h_f \leq 400$ nm: continuous film + ~30 nm high particles. For $h_f > 400$ nm: continuous film + flat particles.
CuSiN/AR	B1	Same as CuAlO, with pores.	Interrupted at the pores.
	B2	Same as CuAlO.	Continuous.
CuSiN/AA		Same as CuAlO, with hillocks for $h_f \leq 200$ nm.	Possibly interrupted at the hillocks.
CuSiN/RR		Before thermal cycling: bimodal grain size distribution with big columnar grains surrounded by smaller grains. After thermal cycling: same as CuAlO with a few pores.	Continuous.

CHAPTER 6

EFFECT OF SURFACE PASSIVATION ON THE MECHANICAL BEHAVIOR OF CU THIN FILMS

6.1 Introduction

Passivating the surface of a thin film has dramatic effects on its mechanical properties. Earlier studies found that the film strength at room and at elevated temperatures was increased for passivated films. However, this effect was mainly examined for films thicker than a few hundreds of nanometers. Our study therefore aims at extending the knowledge to thinner films down to a few tens of nanometers. In this thickness regime, where diffusion paths are shorter, different deformation mechanisms are expected and need to be investigated.

This study was conducted with Cu thin films passivated with aluminum oxide (type CuAlO) and with silicon nitride (type CuSiN/AR). Both films underwent a similar thermal treatment during their preparation and thus differ only in the nature of the passivation layer. In order to reveal the effects of the passivation, the mechanical behavior of these films needs to be compared with unpassivated films. For this, the unpassivated annealed films studied by Balk (type CuAB) will be used[56]. There usability in this study will be verified by comparing their stress-temperature behavior with unpassivated annealed films prepared in this work (type CuA). A precise comparison of the stress evolution and the dislocation behavior of all these films will shed new light on the deformation mechanisms and size effects in thin films.

The chapter will be divided into three sections. In the first part, the stress-temperature curves and the flow stress of the Cu films at 50 °C will be described in detail. The second part will be dedicated to the dislocation behavior in the films. Finally, the results will be discussed with a focus on the effect of a passivation layer onto the mechanical properties of thin films.

6.2 Stress measurements

The thermomechanical properties of the films were measured using the wafer curvature method. In this section, the stabilized stress-temperature curves of the different types of Cu films are presented. First thermal cycles are not shown since the thermomechanical response is not yet stable and reproducible. In general, they only differ from the stabilized cycles in that the starting stress is lower than the final stress, which is also the starting stress of the second cycle. This is due to room temperature stress relaxation after film deposition and before stress measurement. The main features of the curves like e.g. the hysteresis between the heating and cooling segments and the biaxial stresses at 50 °C are also reported as a function of film thickness.

6.2.1 Stress-temperature curves for the Al_xO_y passivated Cu films

Two different stress-temperature behaviors were recorded for the CuAlO films, depending on film thickness. The 100 nm thick Cu film represents a transition between these two behaviors. Each category will be illustrated with a few representative examples. As already described in section 3.2.4, except for the 100 nm thick film, the stress in the CuAlO films was measured for the system “Cu film + passivation layer”, since no correction of the passivation layer effect on the stress was realized.

Films with a thickness of 100 nm and thinner (“ultra-thin” films)

Figure 6.1 shows the stabilized stress-temperature curves for the 50 nm thick CuAlO film cycled to 500 °C and to 600 °C. This behavior is representative for all the films thinner than 100 nm.

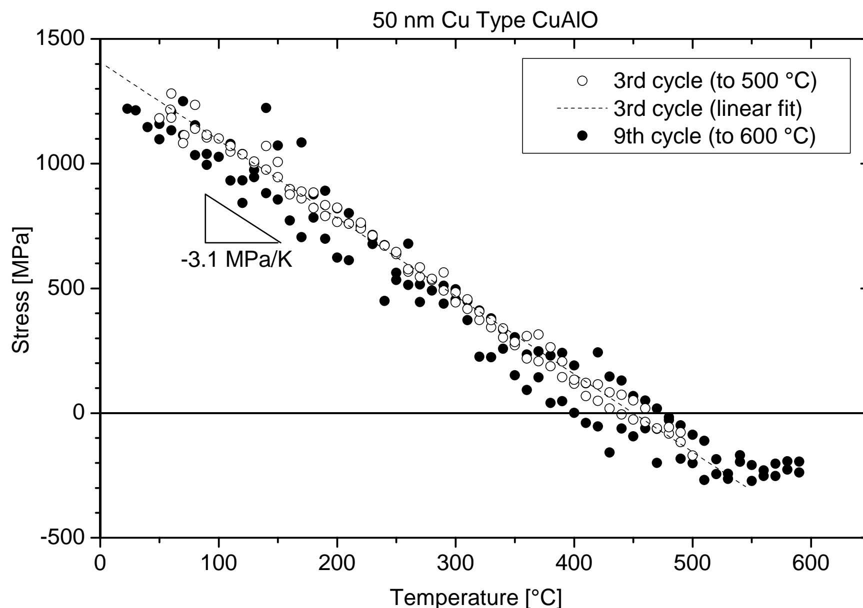

Figure 6.1: Stress-temperature curves of the 50 nm thick CuAlO film obtained from two cycles to 500 °C (open dots) and 600 °C (filled dots), respectively. The dotted line is a linear fit of the cycle to 500 °C. The slope of the curve is indicated under the line.

The film was initially under a biaxial tensile stress of about 1.2 GPa at 50 °C. Upon heating to 500 °C, the stress decreased linearly with a slope of -3.1 MPa/K, since the substrate imposes a constraint to thermal expansion of Cu. It finally reached a compressive stress of -200 MPa at 500 °C. During subsequent cooling, the stress rises

with the same slope until room temperature and reached a final stress identical to the starting stress. The linearity of the curve indicates that the stress is accommodated elastically. A subsequent heating to 600 °C shows a similar behavior until 500 °C. At this temperature, it reached a plateau in compression at about -250 MPa before the maximum temperature of 600 °C was reached. Upon cooling, the stress first stagnated before decreasing linearly between 500 °C and room temperature. It finally reached the same value as at the end of the previous cycles to 500 °C.

The stress evolution in the 100 nm thick CuAlO film is shown in Figure 6.2. The film was first cycled to 500 °C (open dots) before a 10 nm thick Al_xO_y layer was deposited on the back side of the substrate. Thereafter, an additional cycle was carried out (filled dots).

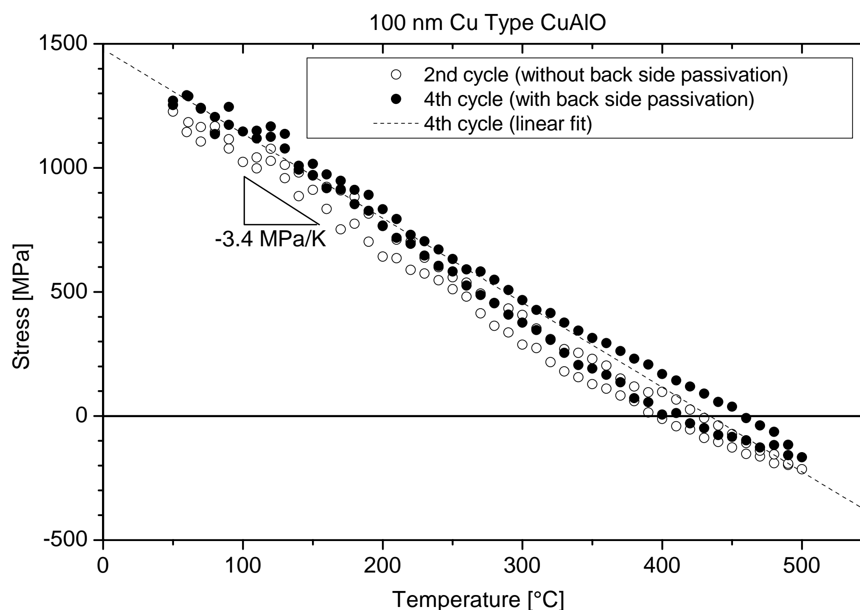

Figure 6.2: Stress-temperature curves of the 100 nm thick CuAlO film before (open dots) and after (filled dots) back side passivation. The curve for the fourth cycle after back side passivation was fitted linearly (dotted line). The slope of this line is also indicated.

The shape of the curves is similar to that of the 50 nm thick film: identical stress values at 50 °C and 500 °C and overall linear evolution of the stress with temperature. However, a small hysteresis is visible for the heating and the cooling segments between 250 °C and 500 °C. Another interesting observation is that both plotted cycles measured before and after passivating the back side of the wafer are very similar both in shapes

and stress values. As for the 50 nm thick film, the maximum temperature of the thermal cycling was increased to 600 °C and to 700 °C. The thermal cycles carried out to these temperatures directly after each other are plotted in Figure 6.3 together with one cycle to 500 °C.

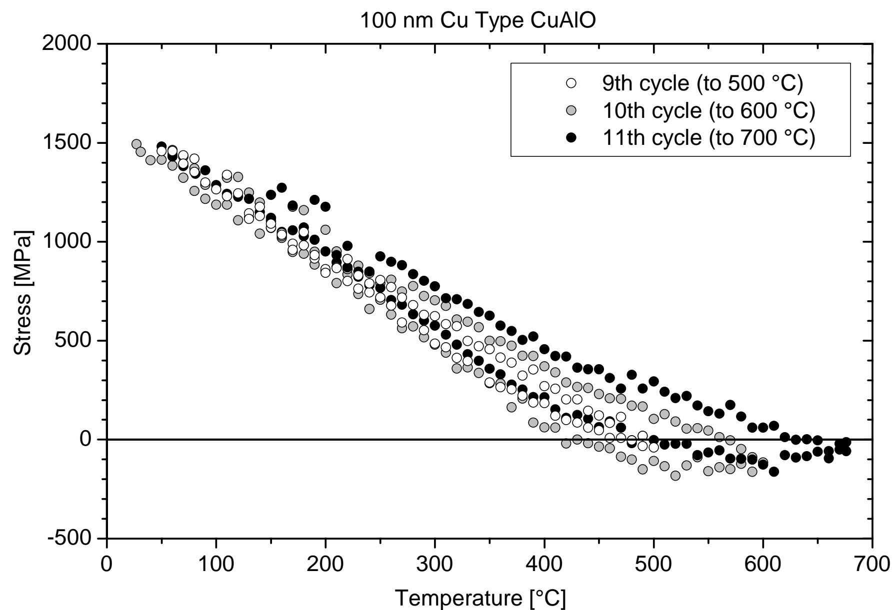

Figure 6.3: Stress-temperature curves of the 100 nm thick CuAlO film obtained from three cycles to 500, 600 and 700 °C.

The curve of the cycle to 500 °C is shifted by about 250 MPa towards higher stress values compared to the cycle shown in Figure 6.2. This is to be explained by an inaccurate positioning of the sample in the wafer curvature apparatus, leading to an offset in the measurement of the absolute stress. However, the shape of the curve is identical. The heating curve to 600 °C is similar until 500 °C, temperature at which the stress stagnated until 600 °C. Upon cooling, the stress increased progressively before reaching its initial value. The stress evolution to 700 °C is analogous, with a compressive stress plateau between 500 and 625 °C. At this temperature, the stress relaxed in compression and dropped towards zero.

Films thicker than 200 nm

The stress-temperature behavior of the 1 µm thick CuAlO film is shown as a representative curve for films thicker than 200 nm. The second cycle to 500 °C for this film is plotted in Figure 6.4. The large hysteresis is in sharp contrast to the linear behavior of the thinner films.

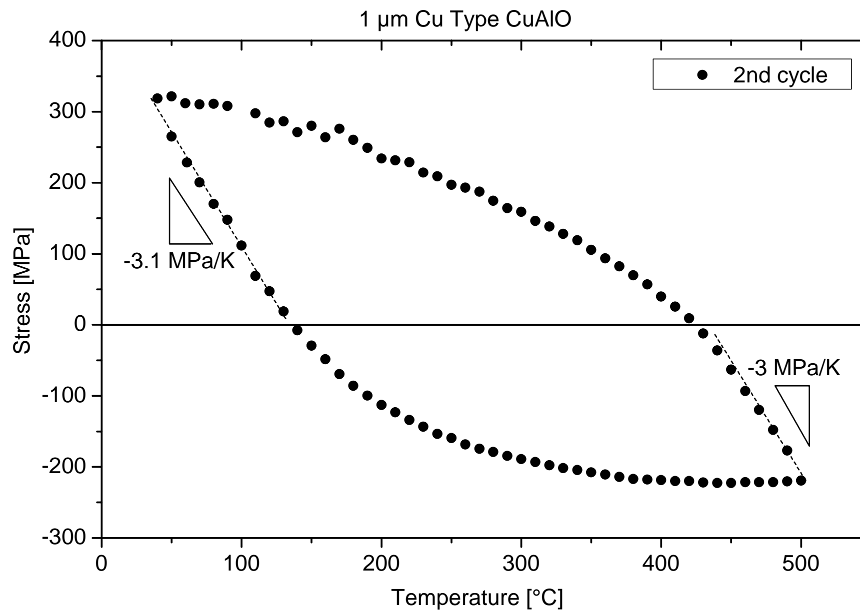

Figure 6.4: Stress-temperature curves of the 1 µm thick CuAlO film for the second cycle to 500 °C. The slopes of the thermoelastic segments are indicated too.

At the beginning of the thermal cycling at 50 °C, the curve exhibits a residual tensile stress of about 300 MPa. A temperature increase made the film stress decrease linearly with a slope of -3.1 MPa/K, consistent with that of the thinner films. In this region, the thermal strain is accommodated elastically. Above 150 °C and under a compressive stress of -50 MPa, the curve deviated from the so-called thermoelastic line, which corresponds to the onset of plastic yielding. Starting at approximately 450 °C, the stress reached a plateau at about -200 MPa. A thermoelastic segment was again observed at the beginning of the cooling regime until plastic yielding occurred in the tensile stress region. Finally, the film reached its initial stress value of 320 MPa at 50 °C.

Very similar behavior is observed for the 2 µm thick film (Figure 6.5), however, both the stresses at room temperature and at 500 °C are lower than in the 1 µm thick film. The slopes of the thermoelastic lines of about -2 MPa/K for the 2 µm thick film are also small compared to the -3 MPa/K measured for the 1 µm thick film.

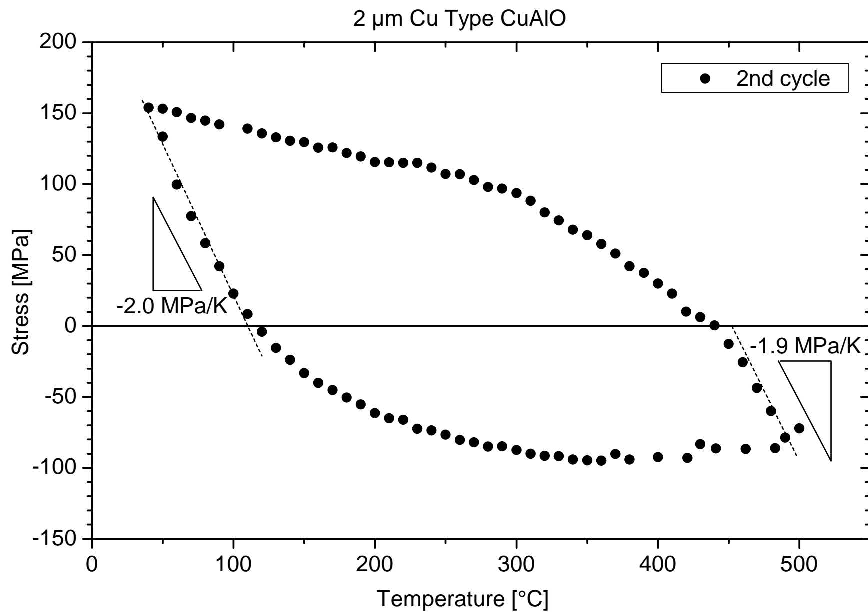

Figure 6.5: Stress-temperature curves of the 2 µm thick CuAlO film for the second cycle to 500 °C. The slopes of the thermoelastic lines are given below the corresponding segments.

Summary

Figure 6.6 presents as a summary the stress-temperature curves of the stabilized response for type CuAlO films with Cu thicknesses between 50 nm and 2 µm.

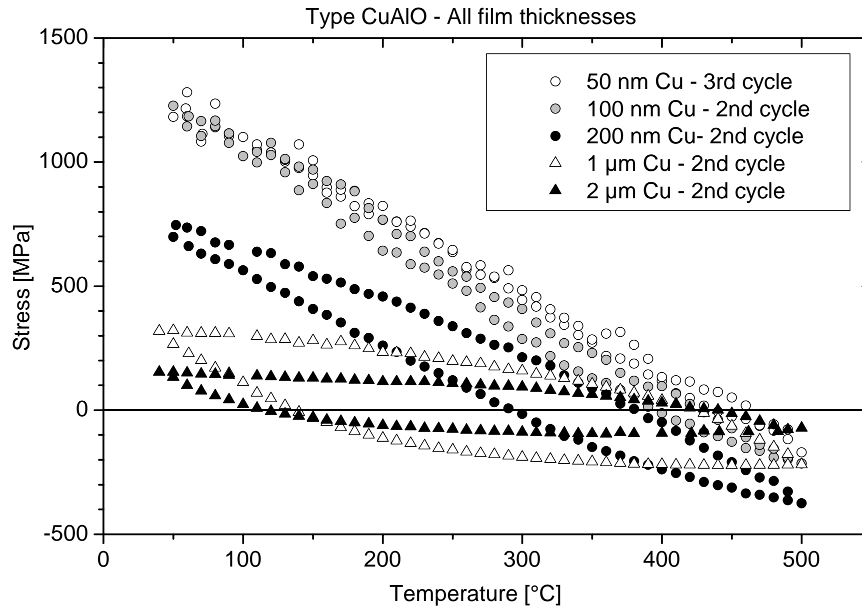

Figure 6.6: Stress-temperature curves for CuAlO films with different thicknesses. The reported curves correspond to the second cycles, except for the 50 nm thick film for which the third cycle is shown. The room temperature stress clearly increases with decreasing film thicknesses for films thicker than 100 nm. The curves for the 50 and 100 nm films lie on top of each other.

For films thicker than 100 nm, the room temperature stress shows a clear size effect: the thinner the film, the higher the stress. The hysteresis also changes with film thickness and will be discussed in details later. However, the room temperature stress and the shape of the curves for the 50 nm and 100 nm films are very close.

6.2.2 Stress-temperature curves for the Si_xN_y passivated Cu films (type CuSiN/AR)

All the films of type CuSiN/AR were back side passivated to subtract out the effect of the passivation layer from the total film stress (see section 3.2.4). Similarly to the CuAlO films, the stress-temperature behavior of these films can be categorized depending on film thickness. However, films with identical nominal thicknesses from different batches yielded different results.

Films with a thickness of 100 nm and thinner ("ultra-thin" films)

Two 50 nm thick films of type CuSiN/AR from two different batches were cycled to 500 °C. The obtained stress-temperature curves are presented in Figure 6.7. It is

surprising that the curves for both samples exhibit different shapes. For the batch 2 film, the film stress of about 1.1 GPa at room temperature decreased linearly with a slope of -3.3 MPa/K and reaches a compressive value of about -400 MPa. The cooling made the film stress increase linearly on the same line. This overall linear stress evolution in the batch 2 film is similar to that of the 50 nm thick CuAlO film. It is however in contrast with the behavior of the batch 1 film. Although the stress in this film decreased linearly at a similar rate for temperatures below 220 °C, it then deviated from the thermoelastic line. Whereas both films exhibit a compressive stress value of about -400 MPa at 500 °C, the room temperature stress of 800 MPa for the batch 1 film is much lower. In addition, the curve of batch 1 film shows a hysteresis between the heating and cooling segments above 220 °C, which is not visible for the batch 2 film.

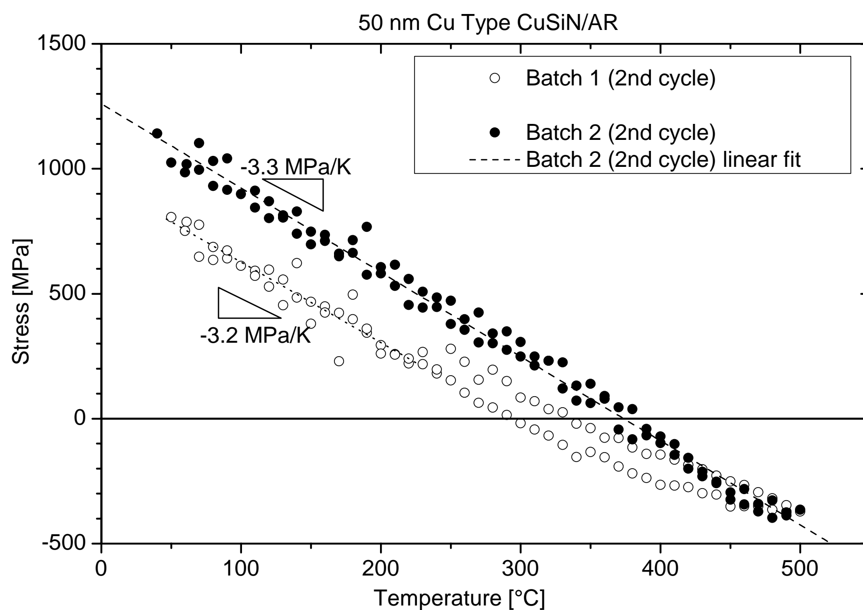

Figure 6.7: Stress-temperature curves of the 50 nm thick CuSiN/AR films of batch 1 and 2 obtained from one cycle to 500 °C. The dotted line is a linear fit of the curve of the batch 2 film, with its average slope indicated under the line. The thermoelastic slope of the batch 1 film is also given.

The 100 nm thick film again represents a transitory behavior between the ultra-thin and the thicker films. Stress-temperature curves for two samples from the two batches are plotted in Figure 6.8. Again, the samples exhibit different behavior with a similar compressive stress at 500 °C but a much higher room temperature stress for the batch 2 film. The overall shape of the curves is alike the 50 nm thick films. However, the curve

of the 100 nm thick batch 2 film shows an hysteresis above 220 °C, which is not observed for the 50 nm thick batch 2 film. The behavior of the 100 nm thick batch 2 film is also similar to that of the 100 nm thick CuAlO film.

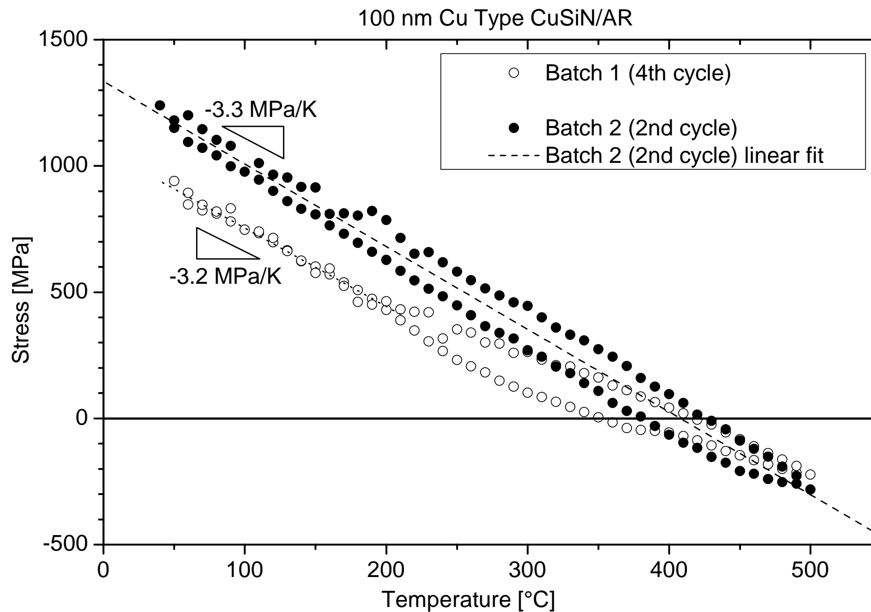

Figure 6.8: Stress-temperature curves of the 100 nm thick CuSiN/AR films of batch 1 and 2 obtained from one cycle to 500 °C. The dotted line is a linear fit of the curve of the batch 2 film, with its average slope indicated under the line. The thermoelastic slope of the batch 1 film is also given.

Films thicker than 200 nm

Finally, the stress in the 600 nm thick CuSiN/AR film from batch 1 was measured and is shown in Figure 6.9. Its behavior is similar to that of the 1 µm thick CuAlO film (Figure 6.4). After deforming elastically with a slope of -3.0 MPa/K, the film started to deform plastically at a temperature of about 200 °C. During the cooling, the stress initially decreased linearly before reaching with a constant rate its initial value of about 500 MPa.

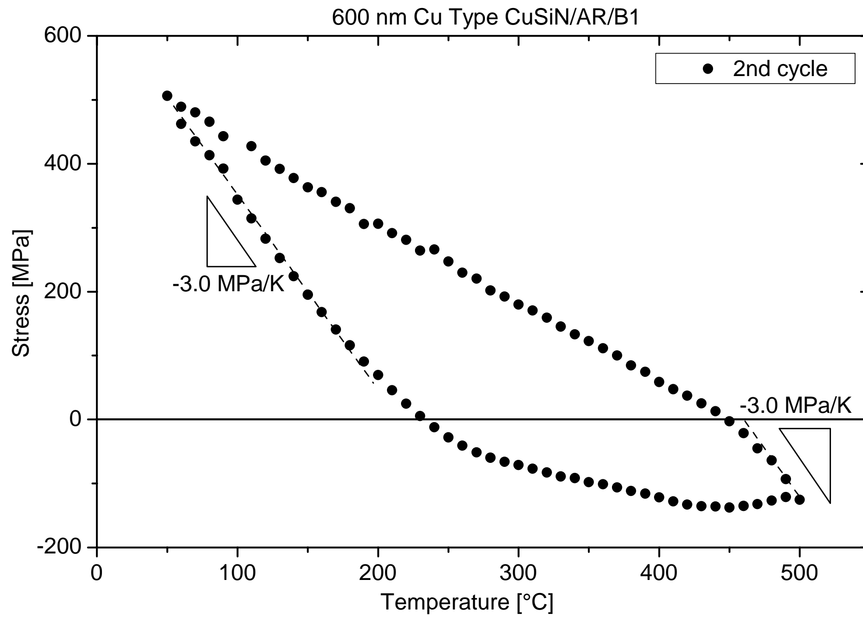

Figure 6.9: Stress-temperature curve of the 600 nm thick CuSiN/AR/B1 film. The thermoelastic slopes are indicated under the corresponding segments.

6.2.3 Stress-temperature curves for the unpassivated annealed Cu films

The stress of the unpassivated annealed Cu films prepared in this study (type CuA) was also measured. The stabilized stress-temperature curves obtained for the 100 and 600 nm thick films are presented in Figure 6.10 (filled dots). Curves obtained for Cu films of the same thicknesses prepared and measured by Balk (type CuAB) are also plotted (continuous line) to serve as a comparison[56]. For the 100 nm film (a), two different regimes can be distinguished: a linear dependency of the stress on temperature between room temperature and 220 °C and a stress loop between 220 °C and 500 °C. The curve for the 600 nm thick film exhibits a classical elastic-plastic shape, as already described for e.g. the 600 nm thick CuSiN/AR film. For both film thicknesses, the obtained results corroborate well the measurements of Balk, as shown by the similarity of the curves.

(a) (b)

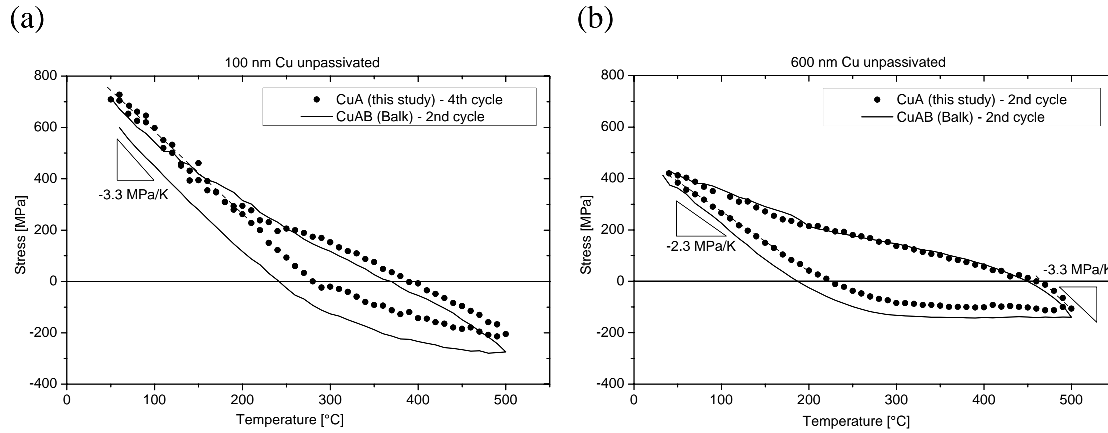

Figure 6.10: Stress-temperature curves of the 100 nm (a) and 600 nm (b) thick CuA films (filled dots). The curves obtained for similarly-prepared and measured films (type CuAB) are also plotted. The thermoelastic slopes are given as well.

6.2.4 Hysteresis of the stress-temperature curves

One of the main characteristics of the measured stress-temperature curves is the observed stress difference between the heating and the cooling segments, the so-called hysteresis. The area of hysteresis during a temperature cycle is typically an indication of the amount of plastic deformation experienced by the film. For the thinnest films, heating and cooling segments lie on top of each other whereas the thicker films exhibit a big difference. It is therefore interesting to quantify this feature and to compare it for different film thicknesses. For this, the stress-temperature curves were first converted to stress-strain curves using the following equation for thermal strain:

$$\varepsilon_{thermal}(T) = \int_{T_0}^{T} \left[(\alpha_f(T') - \alpha_s(T') \right] dT' \cong \Delta\alpha (T - T_0) \qquad (6.1)$$

where α_f and α_s are the linear coefficients of thermal expansion (CTEs) of the Cu film and the Si substrate, $\Delta\alpha$ their difference – $\Delta\alpha = (16.7 - 2.62) \cdot 10^{-6} \approx 14 \cdot 10^{-6}\ K^{-1}$ (from ref. [160]) – and T_0 is the temperature at which the film is free of thermal strain. Since only the relative strain change is relevant for the calculation, and not its absolute value, T_0 is randomly set to 50 °C. The area of the hysteresis was then evaluated between 50 and 500 °C with the trapeze method using the integration function of the program Origin v7.5. This procedure was applied to the stabilized cycles showing no stress relaxation at room temperature before thermal cycling. The standard deviation of the

evaluated area values was calculated based on the reproducibility of the results for different cycles of a single sample and is estimated to be maximum 10%. The results obtained for the CuAlO and the CuSiN/AR films (from both batches) are plotted in Figure 6.11 as a function of film thickness. An increase of the area of the hysteresis with film thickness is clearly visible. For the ultra-thin films, this value is surprisingly different from zero. It can be explained by the scattering of the data in this thickness range which induces error in the area evaluation.

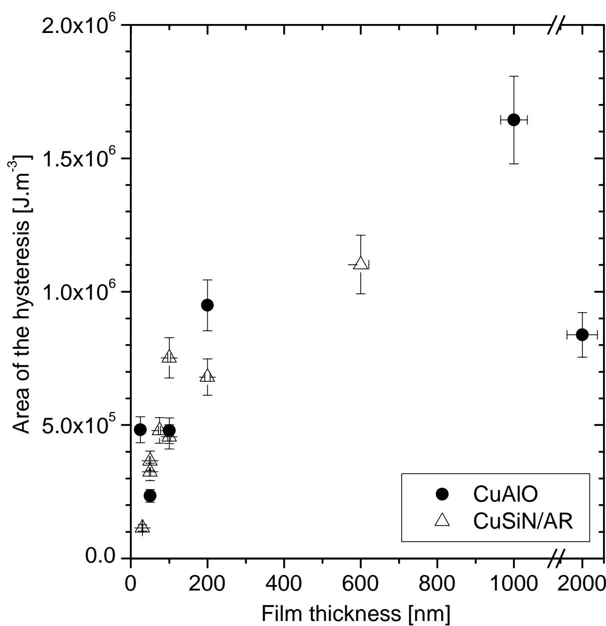

Figure 6.11: Area of the hysteresis under the stress-temperature curves of the CuAlO and CuSiN/AR films (from both batches). Please note that the x-axis is truncated between 1100 and 1900 nm. Except for the 2 µm thick film, the hysteresis area increases with film thickness.

6.2.5 Stress at 50 °C

The stress at 50 °C was determined for each film thickness by averaging the stress values obtained at 50 °C at the end of all the measured stress-temperature cycles. They are plotted as a function of the inverse film thickness for the CuAlO and CuSiN/AR films in Figure 6.12. The exact stress values are given in the appendix (section 10.4). The measurement error differs from sample to sample, since it depends on how uniform the substrate curvature was for the individual substrates, as described in section 4.3.1. Two different stress regimes can be distinguished. For films thicker than 100 nm, the stress depends linearly on the inverse film thickness. It then becomes film-thickness

independent for films thinner than 100 nm. A stress plateau at about 1.2 GPa is observed for the CuAlO films and the CuSiN/AR/B2 films whereas a plateau at about 800 MPa is obtained for the CuSiN/AR/B1 films.

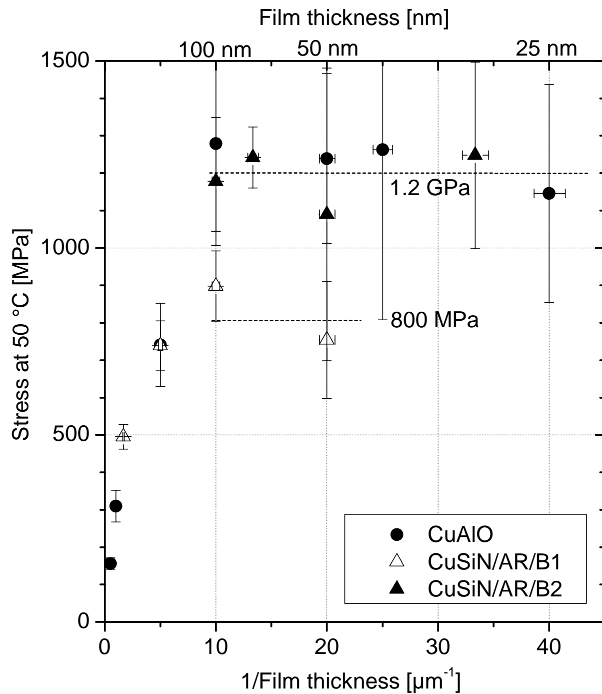

Figure 6.12: The stress at 50 °C vs. the inverse film thickness for the CuAlO and CuSiN/AR films. Two different regimes are visible: a linear increase of the stress with decreasing film thickness for films thicker than 100 nm and a stress plateau for films thinner than 100 nm. The ultra-thin CuSiN/AR films of batch 1 sustain lower stresses than films of batch 2.

6.3 Dislocations

Dislocations were analyzed in the Al_xO_y and Si_xN_y passivated films with TEM. Again, considering the nature of the observed dislocations, the films can be separated into two different categories depending on film thickness; 200 nm being a transition value.

6.3.1 Dislocations in thicker films

A cross-sectional specimen of the 1 µm thick CuAlO film was studied in the TEM. Figure 6.13 presents typical dislocation structures encountered in films of this thickness. In (a), a columnar grain exhibits many threading dislocations. The dislocation density is high close to the film/substrate interface. A threading dislocation is also reaching the

film/passivation layer interface with an almost right angle. In (b), the horizontal grain boundary already visible in Figure 5.6(c) is shown under a different diffraction condition. Two threading dislocations are confined in the grain between the film/substrate interface and the upper grain boundary. Another dislocation in the upper lying grain is also pinned at the horizontal grain boundary.

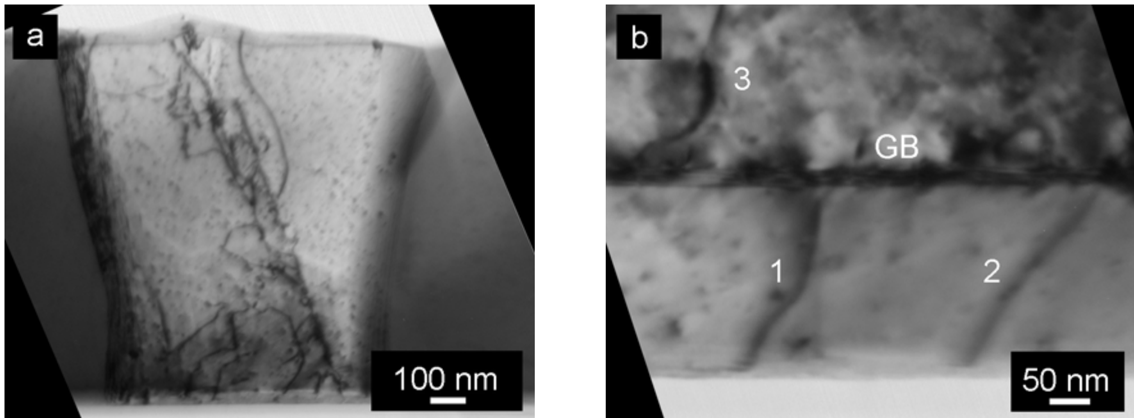

Figure 6.13: Bright-Field (BF) cross-sectional TEM micrographs of the 1 µm thick CuAlO film. (a) A twin boundary crossing the whole grain is surrounded by many threading dislocations. (b) Two threading dislocations (marked 1 and 2) are confined in the film between the substrate and an horizontal grain boundary (marked GB).

In Figure 6.14, an examination of a triple point between a horizontal and a vertical grain boundary reveals the presence of dislocations in the vertical grain boundary.

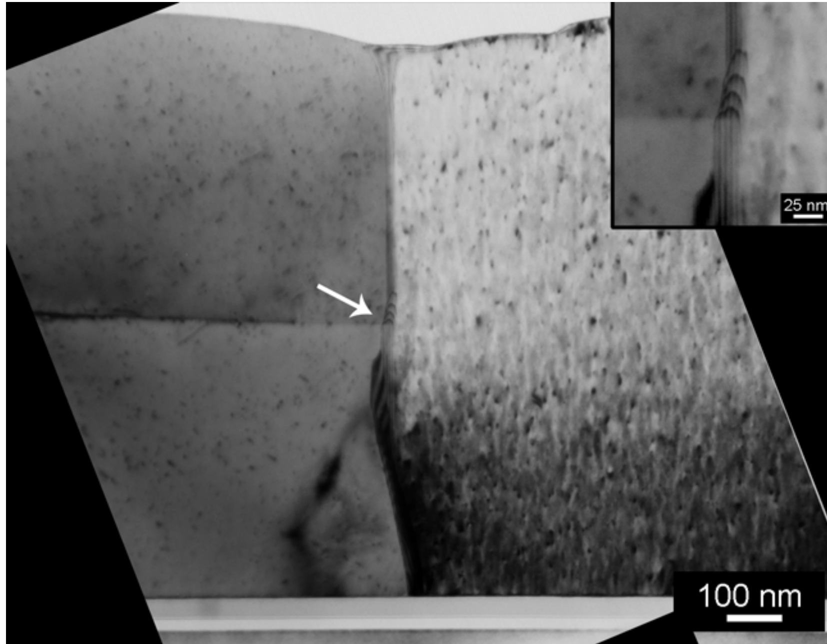

Figure 6.14: BF cross-sectional TEM image of the 1 µm thick CuAlO film. A triple point junction (indicated by the arrow) is visible in the middle of the micrograph. A horizontal grain boundary separates the two grains on the left. In the vertical grain boundary close to the triple point, a series of dislocations are found. The inset presents a zoom of the triple point. The vertical parallel lines are thickness fringes due to the grain boundary, which was not imaged edge-on but instead tilted.

6.3.2 Dislocations in thinner films

The TEM plan-view micrograph in Figure 6.15 shows the presence of parallel glide dislocations[25] in the 100 nm thick CuAlO film. Very few grains show slip traces of threading dislocations and almost exclusively parallel glide dislocations were seen. The 40 nm and 50 nm thick CuAlO films also exhibit these dislocations in a few small grains.

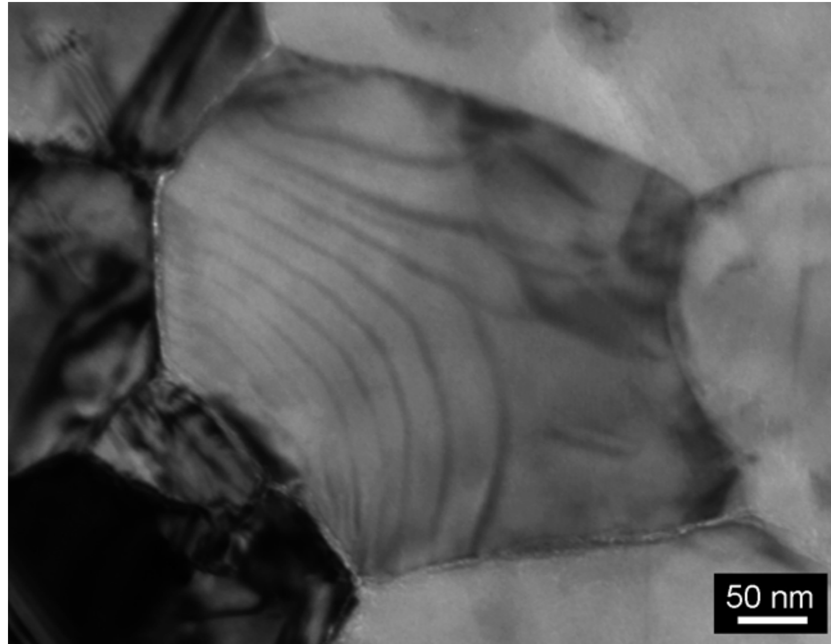

Figure 6.15: BF plan-view TEM micrograph of the 100 nm thick CuAlO film showing parallel glide dislocations bowing out of a grain boundary.

Parallel glide dislocations were also found in the 100 nm thick CuSiN/AR/B1 film, as shown in Figure 6.16. In this film, the parallel glide dislocation density was high: different families of these dislocations are visible in a single grain or in neighboring grains.

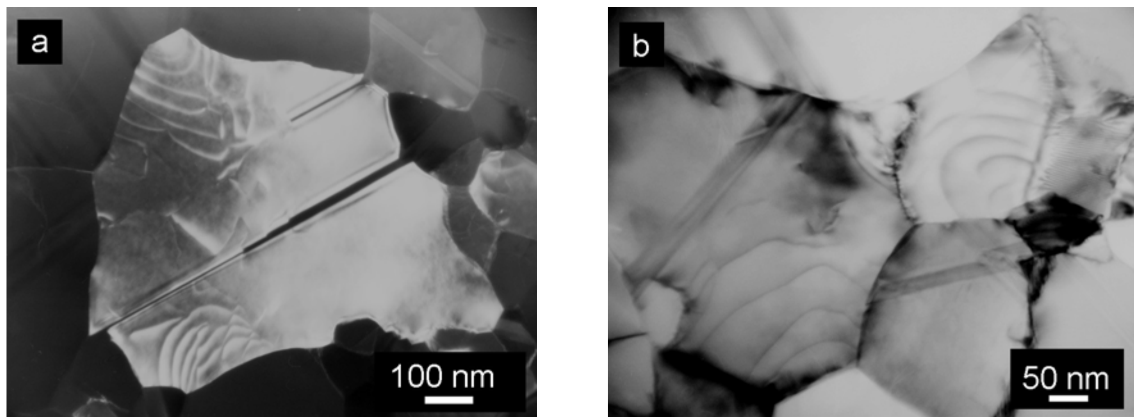

Figure 6.16: Parallel glide dislocations in the 100 nm thick CuSiN/AR/B1 film. (a) Dark-field (DF) plan-view TEM micrograph showing a single grain crossed by a twin boundary with two families of parallel glide dislocations emerging from two grain boundaries. (b) BF plan-view TEM micrograph showing two neighboring grains both containing parallel glide dislocations.

The 200 nm thick CuAlO film represents a transition for the dislocation mechanisms. While parallel glide dislocations are still to be found (Figure 6.17(a)), many grains show exclusively threading dislocations (Figure 6.17(b)): the black parallel lines correspond to slip traces left over by the moving of threading dislocations across the film.

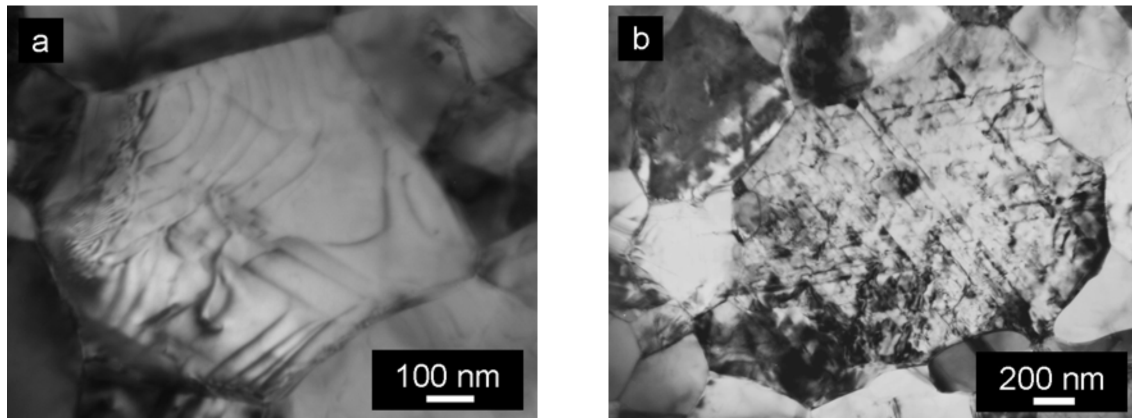

Figure 6.17: BF plan-view TEM micrographs of the 200 nm thick CuAlO film. Parallel glide dislocations are visible (a) as well as slip traces left over by threading dislocations (b).

6.3.3 *In-situ* TEM experiment

In order to characterize the motion of the parallel glide dislocations in passivated films, an *in-situ* thermal cycling experiment was carried out with the 100 nm thick CuAlO film. The series of TEM images in Figure 6.18 present the same grain at different temperatures. Before thermal cycling, many parallel glide dislocations as well as a few slip traces are visible at room temperature (Figures (a) and (b)). During heating to 500 °C, no formation or disappearing of the parallel glide dislocations was noticed. At 500 °C, they are still located at the same places as at the beginning of the experiment (Figures (c) and (d)). Cross slip of dislocations is also apparent. The comparison of the two micrographs at 500 °C, obtained with two different two-beam diffraction conditions, shows an example of interaction between parallel glide dislocations and threading dislocations. The parallel glide dislocations are indeed “cut” by the threading dislocations. After cooling down and reaching again room temperature, the grain did not undergo any visible changes in its defect structure (Figure (e)).

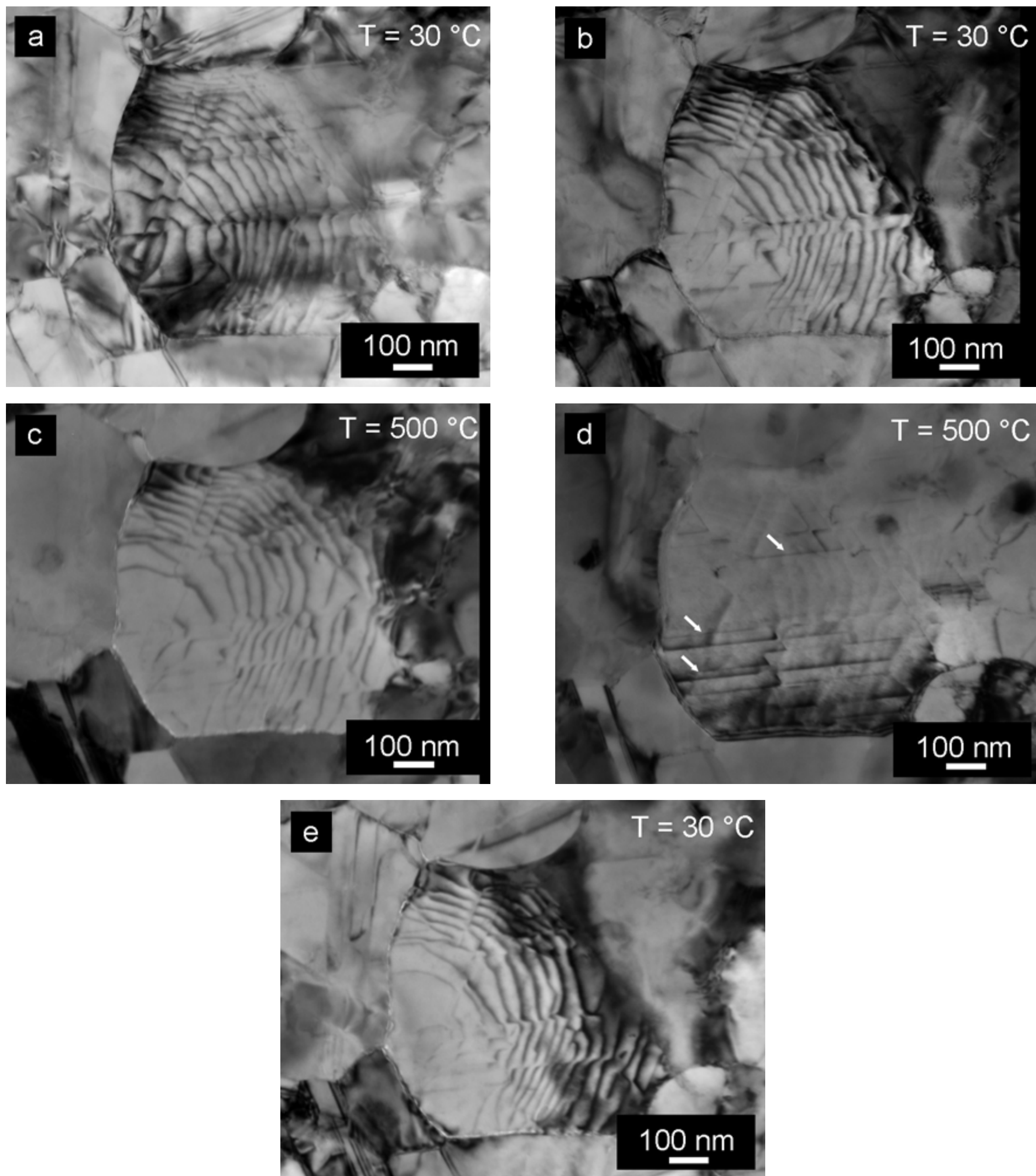

Figure 6.18: TEM micrographs of a single grain cycled to 500 °C in a TEM *in-situ* experiment for the 100 nm CuAlO film. (a) and (b): Grain at room temperature before starting the thermal cycling presented under two different diffraction conditions. Parallel glide dislocations as well as slip traces are visible. (c) and (d): Grain at 500 °C again shown under different diffraction conditions after a thermal cycling time of 30 minutes. Arrows point to a few threading dislocations in (d). (e): Grain at room temperature, after a thermal cycling time of 70 minutes.

6.4 Discussion

6.4.1 Accuracy of the stress measurement

Since the CuSiN/AR films were back side passivated, the stress in the Cu film could be determined directly with an accuracy corresponding to the error of the measurement technique. However, for the CuAlO films, the stress measurements were carried out without subtracting out the influence of the passivation layer from the total film stress. None of the two correction methods listed in the appendix (section 10.2) were applied. Indeed, an accurate measurement of the stress in the pure 10 nm thick Al_xO_y film could not be achieved because the resolution limit of the wafer curvature method was reached and no systematic back side passivation of the wafers was performed. It is nevertheless likely that the absence of correction does not affect the accurate measurement of the Cu film stress: the 100 nm film was indeed cycled before and after being back side passivated and no remarkable stress difference was noticed. The passivation layer is moreover thinner than expected (about 5 nm). For the thinnest measured film of 25 nm, it represents 20% of the total thickness of the Cu film. The possible error due to the absence of correction is therefore diluted in the measurement error.

6.4.2 Elastic properties of the films

In this section, the elastic properties obtained from the stress-temperature measurements are discussed and compared to the theoretical values.

The stress, σ_f, in an elastically-deforming thin film is given by Hooke's law:

$$\sigma_f = M_f \, \varepsilon_{elastic} \tag{6.2}$$

with M_f the biaxial Young's modulus of the film and $\varepsilon_{elastic}$ the elastic strain. In a stress-temperature curve, the elastic strain corresponds to the thermal strain applied in the elastic regime.

The magnitude of the slope q of the initial portion of the heating and cooling stress-temperature curves of the thicker films or of the entire cycle for the ultra-thin films is

given by following expression, obtained by combining Equations (6.1) and (6.2):

$$q = \frac{\Delta\sigma}{\Delta T} = M_f \Delta\alpha \tag{6.3}$$

Both M_f and $\Delta\alpha$ are temperature-dependent. However, it was demonstrated that the temperature dependency of their product is very weak, since $\Delta\alpha$ increases with temperature while M_f decreases[57]. The values for both parameters are thus considered to be constant with temperature and taken at 300 K. The theoretical elastic slope can be calculated using the biaxial Young's modulus for either an isotropic material or a strongly textured material. In the case of an isotropic material, in which the orientation and distribution of single-crystal grains is random, the biaxial Young's modulus, $M_f(iso)$, can be written as a relation between the Young's modulus, E_f, and the Poisson's ratio, ν_f, of the film:

$$M_f(iso) = \frac{E_f}{1-\nu_f} \tag{6.4}$$

For Cu, a value of about 197 GPa is obtained, taking E_{Cu} = 129.8 GPa and ν_{Cu} = 0.34[79]. The elastic slope q is then equal to 2.8 MPa/K. In the case of a (111) fiber-textured material, the expression of the biaxial Young's modulus, $M_f(111)$, is:

$$M_f(111) = \frac{6C_{44}(C_{11} + 2C_{12})}{C_{11} + 2C_{12} + 4C_{44}} \tag{6.5}$$

where C_{ij} are the single crystal elastic stiffness constants (taken from [79]). A value of about 261 GPa is found, which results in an elastic slope q of about 3.7 MPa/K.

For the ultra-thin films deforming purely elastically, the experimental elastic slopes varied between -3.0 and -3.4 MPa/K to be compared to the -3.7 MPa/K expected in (111) textured films. The measured biaxial Young's modulus is herewith smaller than the theoretical value. This effect has already been reported in several studies (e.g. [68,92,161]). Several possible mechanisms have been proposed: the presence of microstructural defects in the films such as voids or microcracks, more compliant grain

boundaries, or small-scale inelasticity. The latter explanation, which relies on an anelastic relaxation process based on grain boundary sliding, is the more accepted to account for the reduced values of the elastic modulus of thin polycrystalline films[161,162]. In the thicker films, similar slopes were obtained for the thermoelastic segments. However, a much lower slope of about -2 MPa/K was measured in the 2 µm thick film. This behavior can be attributed to the presence of (100) oriented grains in this film (see Figure 5.9), which is therefore expected to be closer to that of an isotropic material. However, the experimental elastic modulus lies again far below the theoretical value, possibly for the reasons listed above.

6.4.3 Passivation effects on the thermomechanical behavior

Thin film deformation is controlled by dislocation plasticity and diffusion. The comparison of the stress-temperature behavior of films before and after passivation will shed new light on the dominance of one mechanism at the expense of the other as a function of film thickness. The effect of a surface passivation on the mechanical behavior of the films is described by comparing the shape of the measured stress-temperature curves with the curves obtained for unpassivated films measured by Balk. The validity of such a comparison is first discussed, before presenting and discussing the results for the thinnest and thicker films. Results obtained for both the CuAlO and CuSiN/AR films will be used. The CuSiN/AR/B2 films will serve to illustrate the ultra-thin film behavior, since their stress values were corrected by back side passivating. Due to their atypical stress-temperature behavior, the ultra-thin CuSiN/AR/B1 films will be ignored in this section and discussed later in section 6.4.5. For the thicker films, results of both the CuAlO and CuSiN/AR/B1 types will be employed.

Validity of the comparison with Balk's unpassivated films

To account for the effect of passivation on Cu thin film mechanical properties, it is necessary to compare the stress-temperature behavior of the films before and after passivation. This was achieved using the stress-temperature data collected by Balk for unpassivated films (type CuAB). Here we discuss the validity of this approach. First, these films exhibit a Cu microstructure very close to what is observed for both the

unpassivated films (type CuA) and the passivated films of this study, as already indicated in chapter 5: (111)-texture, big columnar grains and similar grain sizes. In addition, the absolute stress values as well as the stress-temperature hysteresis for the 100 and 600 nm thick films measured by Balk and in this study (Figure 6.10) are similar. The comparison shows good agreement with a maximum deviation of about 100 MPa. The stress values measured at room temperature at the end of the cycles are equal within the measurement accuracy of the wafer curvature method. Considering all these similarities, it appears reasonable to compare the curves obtained for the passivated films of the present study with the ones obtained by Balk for unpassivated films.

Effects of passivation on the behavior of films thinner than 100 nm

In Figure 6.19, the stress-temperature curves obtained for both the 50 and 100 nm films of type CuSiN/AR/B2 are plotted together with the curves measured by Balk for the unpassivated Cu films with the same thicknesses.

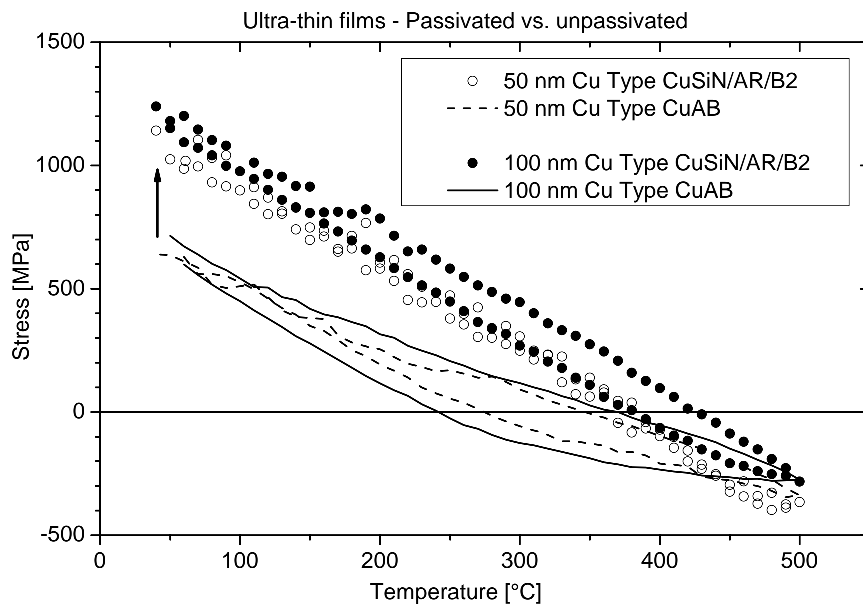

Figure 6.19: Comparison of the stress evolution in passivated (dots) and unpassivated (dashes and line) ultra-thin Cu films. The plotted data corresponds to the CuSiN/AR/B2 passivated films and to the CuAB unpassivated films. The arrow indicates the increase in strength attributed to the passivation.

The passivated films exhibit significantly different thermomechanical behavior from the unpassivated films. While the unpassivated films show elastic-plastic deformation, the passivated films deform only thermoelastically, as indicated by their very linear behavior. At 50 °C, the stress of the passivated films is about twice as high as the stress of the unpassivated film. They are also similar in some respects, however. In particular, the stress values at 500 °C are equal and the thermoelastic slopes are similar. Comparing the 50 and 100 nm curves for each film type reveals that the stresses at 50 and 500 °C are similar. While the film thickness difference does not change the overall shape of the curves, for both passivated and unpassivated films, the 50 nm film exhibits a smaller hysteresis than the 100 nm film.

The purely elastic deformation of the ultra-thin films between room temperature and 500 °C suggests that neither dislocation plasticity nor diffusional creep is active in these films. The absence of dislocation plasticity supported by the area of the hysteresis of the stress-temperature curves being close to zero is confirmed by TEM observations. Most grains are indeed devoid of dislocations. Only a few parallel glide dislocations were observed. This is not specific to passivated Cu films but has also been reported for unpassivated Cu films[22,25]. The dislocation depletion in thinner films can be explained based on dislocation nucleation: the Frank-Read dislocations sources have an increasing difficulty to operate within the confined film thickness, as described by von Blanckenhagen *et al.* [39-42]. Stress relaxation at high temperatures through constrained diffusional creep is prevented in the passivated films, since surface diffusion is shut off by the cap layer. The fact that the suppression of surface diffusion results in an elastic behavior of the films suggests that diffusional creep is the only active permanent deformation mechanism in ultra-thin films. The predominance of diffusion-controlled plasticity for thin films has been reported in numerous studies (e.g. [22,25,76]). However, it is the first time that constrained diffusional creep is proven to be the only deformation mechanism in ultra-thin bare Cu films. One can speculate that this behavior relies on diffusion path length. Indeed, the grain size decreases together with the film thickness, but the aspect ratio of grain size to film thickness remains constant at about 2.5. As a consequence, diffusion paths are shorter and more frequent in an ultra-thin film with fine grains, than in a thicker film with bigger grains. Constrained diffusional creep is thus more efficient for the thinner films. Apparently, the 25 to 500 °C thermal cycling,

which corresponds to a thermal strain of about 0.7%, is not sufficient to induce yielding in ultra-thin films. In order to increase the strain, the temperature range was extended towards higher temperatures with measurements performed to 600 or 700 °C. At these temperatures, the stress stopped decreasing linearly with temperature and stagnated in compression. Below 500 °C, it was again accommodated elastically. This behavior is characteristic of stress relaxation at high temperatures and can generally be attributed to two possible mechanisms: hillock formation or diffusion at the interface Cu film/passivation layer. Since no hillock growth was observed in the films, the second hypothesis appears more realistic. This suggests that, at elevated temperatures, the passivation layer is no longer able to suppress the diffusional flow of material at the Cu film surface. These observations demonstrate that a further heating of the films is not an adequate solution to increase the strain range. The remaining possibility is the cooling of the films, which was realized and is described in chapter 8.

Effects of passivation on the behavior of films in the micrometer range

The effect of passivation on a 2 µm thick film is shown for the CuAlO film in Figure 6.20. The behaviors of the passivated and the unpassivated films are very similar: both show the characteristic linear elastic and plastic regimes with similar stress values and elastic responses. During cooling from 500 °C, the passivation more effectively inhibits high temperature stress relaxation in the roughly 325-450 °C temperature range, as evidenced by the slightly higher slope in this region. This is likely due to the reduction in surface diffusion (or diffusional creep) as a result of the passivation layer. Below 325 °C, where diffusive behavior no longer controls the mechanical response, both curves exhibit similar slopes. This indicates that the passivation layer has little effect on dislocation behavior for the 2 µm thick films.

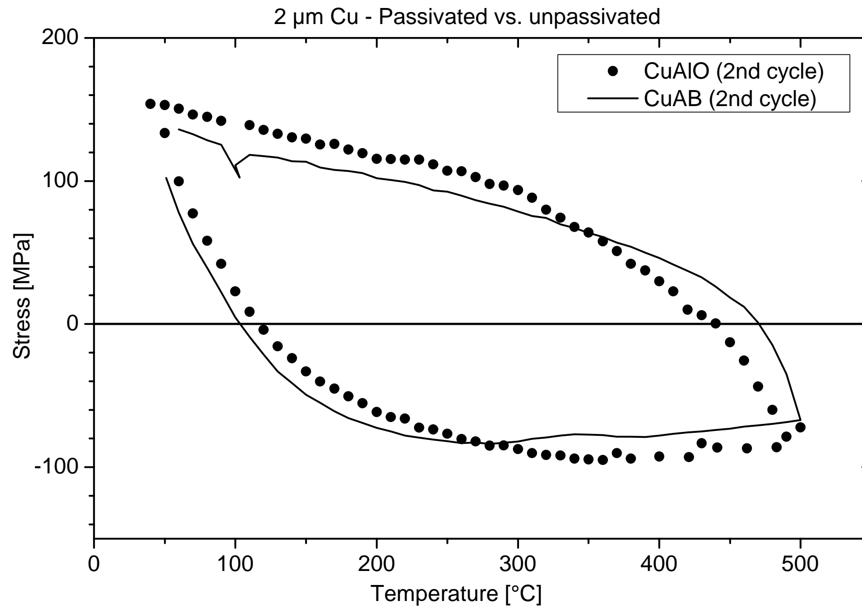

Figure 6.20: Comparison of the stress evolution in passivated (dots) and unpassivated (line) 2 µm thick Cu films. The plotted data is from the CuAlO passivated film and the CuAB unpassivated film.

Thicker films appear to be negligibly strengthened by the passivation layer. This can be possibly explained based on dislocation plasticity, as proposed in the Nix-Freund model[3]. According to the model, a surface passivation would increase the yield stress by constraining dislocations at the film/passivation interface. It can be seen that the hysteresis becomes smaller with decreasing film thickness, implying increasing difficulty of plastic deformation due to the dimensional constraint. However, no observations of specific interactions of dislocations at the Cu film/passivation layer were made. The high dislocation densities observed sustain the predominance of plasticity in thicker films. The greater diffusion distances and lower stresses result in thicker films being relatively unaffected by diffusional relaxation compared to thinner films.

Effects of passivation on the behavior of films in the thickness range 200 - 1 µm

Finally, the behavior of the passivated 600 nm CuSiN/AR/B1 film is now compared with the 600 nm CuAB unpassivated film in Figure 6.21.

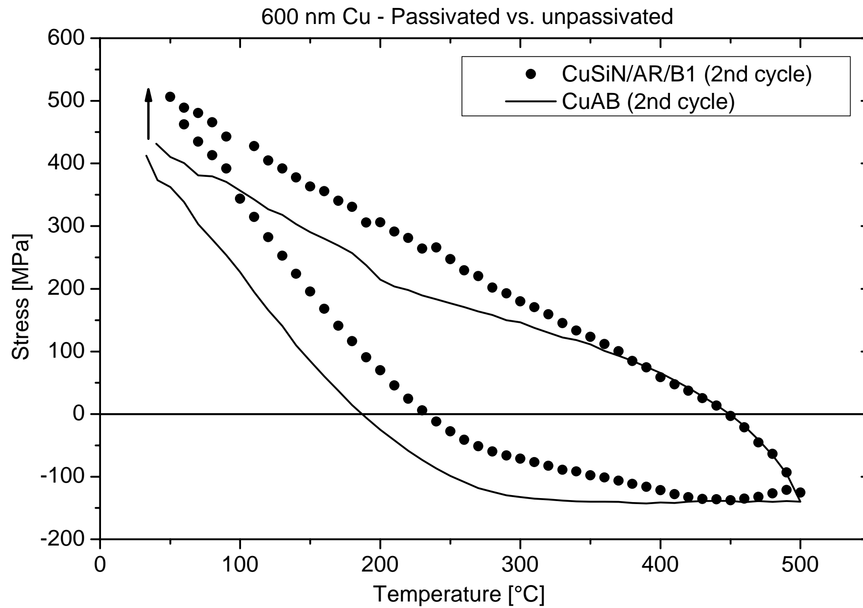

Figure 6.21: Comparison of the stress evolution in passivated (dots) and unpassivated (line) 600 nm thick Cu films. The plotted data is from the CuSiN/AR/B1 passivated film and the CuAB unpassivated film. The arrow marks the strength increase due to the passivation.

Upon heating, both films exhibit similar thermoelastic slopes. At temperatures higher than 300 °C, the unpassivated film settles into a constant compressive stress value, while the passivated film exhibits slight temperature dependent behavior. Both films show very similar compressive stress values. Upon cooling, both films exhibit the same stress profile until about 350 °C. At this temperature, the stress in the passivated film increases at a higher rate than in the unpassivated one, leading to a higher stress at low temperatures. The passivation layer prevents stress relaxation by constrained diffusional creep upon cooling, resulting in a higher stress at room temperature. However, in addition to diffusional relaxation, the large hysteresis of the stress-temperature curve and the important dislocation activity observed in the TEM also indicate dislocation plasticity. Thin films with intermediate thicknesses thus seem to be affected by both dislocation- and diffusion-plasticity.

6.4.4 Simulation of the stress-temperature curves based on dislocation glide

As discussed in the previous section, the film deformation in the micrometer regime is supposedly controlled by dislocation plasticity. The experimental stress-temperature

curve of the 1 µm thick CuAlO film is now compared to the stress-temperature curve simulated with a dislocation-based model.

The shape of the stress-temperature curve is representative of the temperature dependency of the yield stress. This dependency can be calculated and fit to the experimental data based on thermally activated dislocation glide at high stresses in the presence of a regular array of box-shaped obstacles. Frost and Ashby described discrete-obstacle controlled plasticity in bulk material with following equation for the strain rate[15]:

$$\dot{\varepsilon}_{plastic} = \dot{\varepsilon}_0 \exp\left[-\frac{\Delta F}{k_B T}\left(1-\frac{s\sigma}{\hat{\tau}}\right)\right] \qquad (6.6)$$

where $\dot{\varepsilon}_0$ is a constant, which takes into account dislocation density, ΔF is the total free energy required to overcome a single obstacle without aid from external stress, k_B the Boltzmann's constant, s the Schmid factor, and $\hat{\tau}$ the "athermal flow strength", which can be thought of as the flow stress of the material at 0 K. $\hat{\tau}$ corresponds to the critical stress forcing the dislocation through the obstacle with no help from thermal energy and reflects the strength, density and arrangement of the obstacles.

A stress-temperature curve can be calculated by integrating the differential equation[47]:

$$\frac{d\sigma}{dT} + M_f\left(\Delta\alpha + \frac{1}{\dot{T}}\dot{\varepsilon}_{plastic}\right) = 0 \qquad (6.7)$$

where M_f is the biaxial Young's modulus of the film, $\Delta\alpha$ the difference in CTEs between film and substrate, and $\dot{T}$ the experimental heating/cooling rate.

By replacing the strain rate $\dot{\varepsilon}_{plastic}$ with the bulk constitutive equation for thermally activated dislocation glide given in Equation (6.6), we obtain the final differential equation:

$$\frac{d\sigma}{dT} + M_f \Delta\alpha + \frac{M_f}{\dot{T}} \dot{\varepsilon}_0 \exp\left[-\frac{\Delta F}{k_B T}\left(1 - \frac{s\sigma}{\hat{\tau}}\right)\right] = 0 \qquad (6.8)$$

This equation was numerically integrated with the Runge-Kutta routine using Mathematica 5.1 software. The code for the computer simulation was adapted from a code of Weiss[57] and is found in the appendix (section 10.5). The results of the simulations for the 1 µm thick CuAlO film as well as the used constants and fit parameters are given in Figure 6.22.

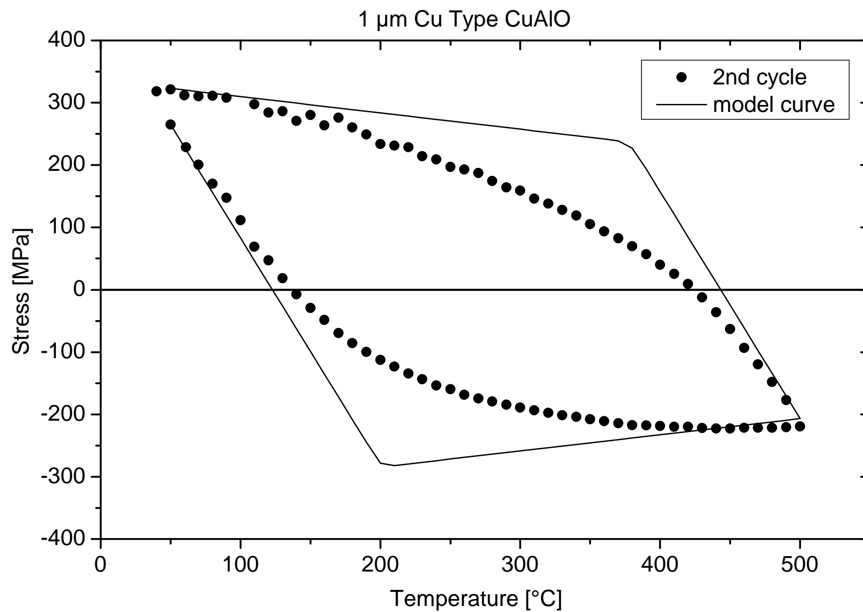

Figure 6.22: Experimental stress-temperature curve of the 1 µm thick CuAlO film and theoretical curve for thermally activated dislocation glide. The model curve is based on Equation (6.8) using the following fit parameters: $\dot{\varepsilon}_0 = 1 \cdot 10^3$ s^{-1}, $\Delta F = 4.4 \cdot 10^{-19}$ J, and $\hat{\tau} = 110$ MPa. Following material constants were used: $\Delta\alpha = 14 \cdot 10^{-6}$ K^{-1} and $M_{Cu} = 2.6 \cdot 10^{11}$ Pa (at 300 K). $s = 0.27$ for (111)-orientation. The heating rate $\dot{T}$ was set to be 0.1 K·s^{-1}. The starting value for the stress at time t = 0 was taken from the experiments (T = 323 K, σ = 265 MPa). The Boltzmann's constant is $k_B = 1.38\ 10^{-23}$ J·K^{-1}.

The simulation fits the stress level at room temperature and at 500 °C. It also succeeds at predicting the temperature at which yielding starts both in compression and in tension. However, it fails to predict the onset of yielding. In the experimental curve, the transition from the elastic to the plastic deformation regime is "smooth", with a constantly changing slope. In the model, this transition happens abruptly. The area of

the hysteresis is also overestimated. These differences are explained by the use of one single value for the parameter $\hat{\tau}$ held constant over the whole cycle, which implicitly excludes work hardening from the model. Moreover, the model was developed for bulk material and thus does not take into account the specificity of thin film geometry. Note that the fit parameters used in the simulation differ from the values prescribed by Frost and Ashby for bulk Cu ($\dot{\varepsilon}_0 = 1 \cdot 10^6$ s^{-1}, $\Delta F = 3.5 \cdot 10^{-19}$ J and $\hat{\tau}$ = 265 MPa[15]). The lower $\hat{\tau}$ and higher ΔF values used indicate that a lower density of obstacles more difficult to overcome had to be considered. One can speculate that the necessity to consider such kind of obstacles may reflect the geometry of thin films.

6.4.5 Pores as fast diffusion paths

The thermomechanical characterization of the CuSiN/AR films revealed a behavior difference between ultra-thin films prepared in batch 1 and batch 2. Figure 6.23 shows that the behavior of the batch 1 film lies between that observed for the batch 2 and unpassivated 100 nm Cu, with identical 500 °C stresses, but different 50 °C stresses.

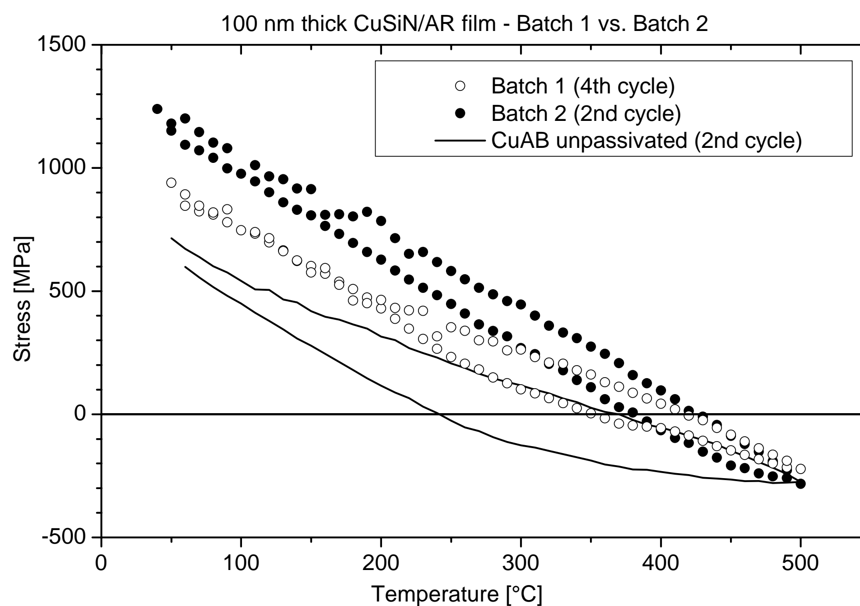

Figure 6.23: Comparison of the stress-temperature curves obtained for the 100 nm thick CuSiN/AR films from batch 1 and batch 2 with an unpassivated 100 nm thick film (type CuAB).

The deformation of ultra-thin films is controlled exclusively by stress relaxation at high temperatures through constrained diffusional creep. The shape of the curve of the batch 1 film indicates a behavior consistent with diffusional relaxation. However, this film sustains higher stresses than the unpassivated film. This suggests a partial blockage of surface diffusion. The difference of behavior between the films from both batches relies on their microstructures. Indeed, pores which interrupt the passivation layer were observed in the films of batch 1. They can act as diffusion paths and enable constrained diffusional creep. The pore density would thus be a measure of the amount of relaxation in the film. However, the weakening of passivated ultra-thin films through pore formation was not analyzed quantitatively. The presence of pores and grain boundary grooves in the thicker films of batch 1 did not visibly influence the stress-temperature behavior. Indeed, in this thickness regime, dislocation plasticity is the dominant deformation mechanism and diffusional creep has a weaker influence.

6.4.6 Comparison of the oxide and nitride passivation layers

The difference between the Al_xO_y and Si_xN_y passivation layers is not significant and not readily observable from the stress-temperature curves. This finding is supported by previous wafer curvature studies of Cu films passivated with different materials[4,45,63]. The shape of the stress curves for different cap layers was reported to be virtually indistinguishable, with minor variation in final stresses. This suggests that the nature of the passivation has no influence on the stress behavior of the Cu film. We will now discuss how models support or undermine this observation.

The contribution of a passivation layer is twofold: it mechanically constrains the film surface, and herewith supposedly the dislocation motion, and inhibits surface diffusion.

Considering the “mechanical” influence of the passivation, a difference of behavior between Al_xO_y and Si_xN_y is intuitively expected, since both materials have different mechanical properties (Table 6.1).

Table 6.1: Mechanical properties of bulk crystalline aluminum oxide and silicon nitride[163].

	Al_xO_y	Si_xN_y
Young's modulus E [GPa]	370	310
Poisson coefficient ν	0.25	0.26
Biaxial Young's modulus M [GPa] [a]	493	419
Shear modulus μ (at 300K) [GPa] [b]	148	123
CTE (between 293 and 1073 K) [10^{-6} K^{-1}]	8.5	3.3

[a]: calculated with $M = \frac{E}{1-\nu}$; [b]: calculated with $\mu = \frac{E}{2(1+\nu)}$

The Nix-Freund model only takes the shear modulus of the passivation layer into account (Equations (2.12) and (2.21)), which is close for both materials. Using identical cut-off radii β_p for both passivations, the model predicts a negligible 1.4 to 2% stress increase for Cu films passivated with Al_xO_y compared to Si_xN_y. The thickness of the passivation layer is also integrated in the model and is expected to have a stronger influence. However, the stress behavior was similar whether the Cu film is passivated with 10 nm or 50 nm of Si_xN_y, as described in the appendix (section 10.6). In addition, in the source model, the predicted stress is insensitive to any property of the capping layer (mechanical properties or thickness). These considerations lead to the conclusion that the influence of a passivation layer is due more to the loss of the free surface than to the particular mechanical properties of the layer itself. This implies that any capping layer which properly inhibits surface diffusion may have the same effect on Cu mechanical behavior. This hypothesis is also supported by the modeling of constrained diffusional creep of Gao *et al.*[52]. According to the model, the absence of free surface due to a passivation is sufficient to inhibit the formation of diffusion wedges, with no condition on the passivation nature or thickness.

However, a study of Gan *et al.*[4] observed that the characterization of stress behavior under thermal cycling test is not sensitive enough to differentiate the effect of different cap layers. Isothermal stress relaxation measurements are more appropriate to reveal the passivation layer effect. They suggested that the kinetics of stress relaxation is controlled by the mass transport at the interface between the Cu film and the passivation layer. The interfacial diffusion is in turn strongly influenced by the chemical bonding at the interface[164]: the better the adhesion and the more reactive the bonds, the slower the

diffusion at the interface. Based on this observation, metallic capping layers are expected to be better diffusion barriers than oxides or nitrides, due to the pure metallic nature of the bonding. One can finally speculate that Al_xO_y and Si_xN_y would both provide similar mass transport at the interface, since the bonding of both layers with Cu is of similar nature.

6.4.7 Stress at 50 °C

Room temperature stress values are often compared to elucidate size effects in thin films. Figure 6.24 shows the stress at 50 °C vs. the inverse film thickness for the passivated CuAlO and CuSiN/AR films together with the stress at 40 °C measured by Balk in the CuAB unpassivated films. The stress values for the CuAB films were published in [25] and corrected after publication by determining the actual film thicknesses with TEM. These latter corrected values, which slightly differ from the values reported in the paper, were used in this study[56]. For the reasons detailed in section 6.4.5, the stress values for the ultra-thin CuSiN/AR films from batch 1 are not represented.

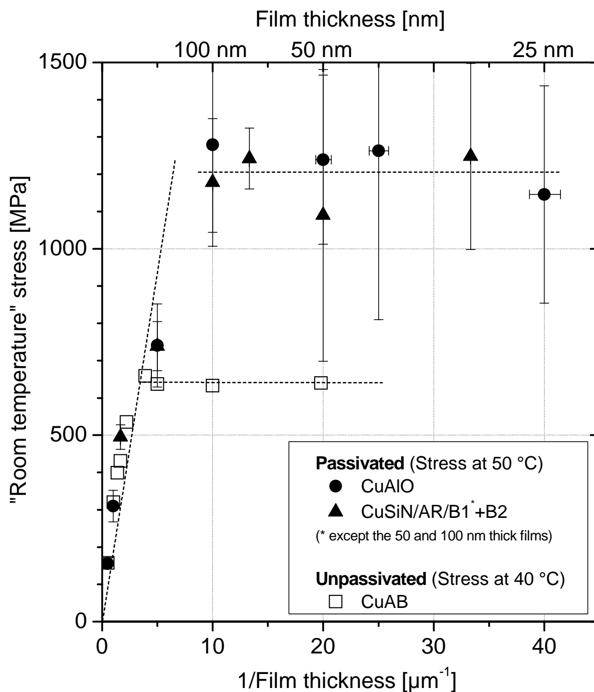

Figure 6.24: Stress at 50 °C for the CuAlO and CuSiN/AR passivated films vs. the inverse film thickness compared with the stress at 40 °C obtained for the unpassivated films CuAB.

Both passivated and unpassivated films exhibit similar behavior and the room temperature stress characterized by two regimes. The stress values first increase linearly with the reciprocal film thickness and then exhibit a plateau. The stress plateau is reached earlier for unpassivated Cu films. We will now discuss the effects accounting for these two different regimes: stress increase with decreasing film thickness and the stress plateau.

Linear increase

The thickness dependence of the film stress at 50 °C for the thicker films is investigated by comparing passivated and unpassivated films. The results are discussed in light of established models of thin film plasticity. The data already presented in Figure 6.24 is re-plotted for film thicknesses down to 100 nm together with the predictions of the most prominent models in Figure 6.25, both in a linear (a) and a logarithmic (b) plot.

In this regime, the film thickness exerts a dramatic effect on the Cu stress at 50 °C, with thinner films exhibiting higher stresses. This size effect has already been reported for unpassivated (e.g. [18,25,45]) as well as for passivated (e.g. [18,45,68]) Cu films. For films thicker than 200 nm, i.e. before the appearance of the plateau for the unpassivated films, the passivated and unpassivated curves are very similar. As visible on the logarithmic plot, the flow stress increase follows a h^n relationship with n values of -0.6 for passivated films and -0.7 for unpassivated films. The difference in slopes, which lies within the error, is however not significant. For passivated films, the area of the hysteresis decreases with decreasing film thickness, suggesting that dislocation plasticity is the main reason for the observed size effect.

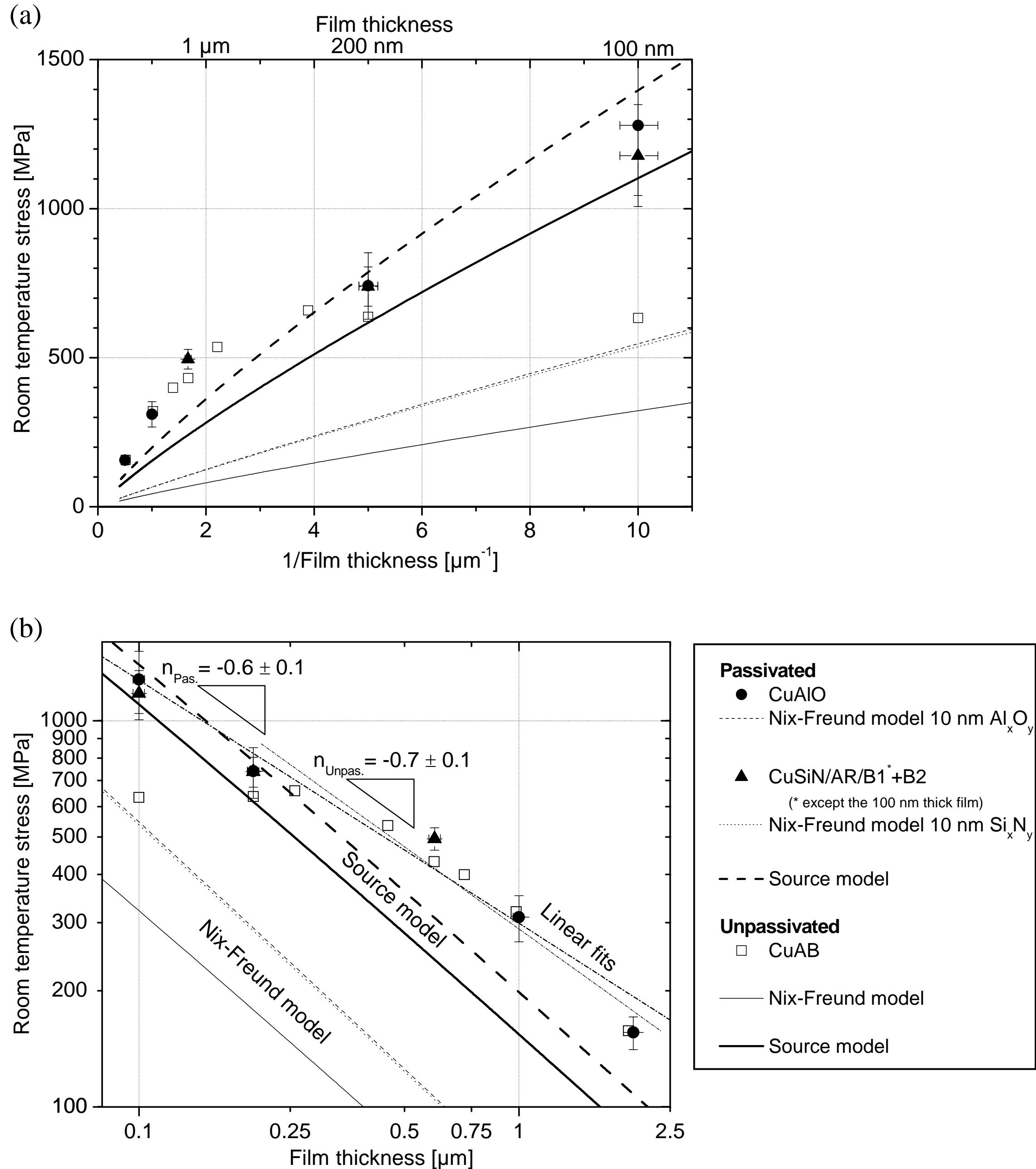

Figure 6.25: "Room temperature" stress measured and calculated with the Nix-Freund and the source models for both the passivated CuAlO and CuSiN/AR films and the unpassivated CuAB films thicker than 100 nm. (a) is a linear plot of the stress vs. the inverse film thickness. (b) is a logarithmic plot of the stress vs. the film thickness. The thin dashed and solid lines represent the stress predicted by the Nix-Freund model for passivated and unpassivated films, respectively. It was calculated with Equations (2.12), (2.13) and (2.21) using the constants already introduced in Figure 2.8 and β_p = 0.85, $\mu_p(Al_xO_y)$ = 148 GPa, $\mu_p(Si_xN_y)$ = 123 GPa and h_p = 10 nm. The thicker lines show the stress predicted by the source model for both passivated (dashed line) and unpassivated (solid line) films calculated with Equations (2.18), (2.19) and (2.22) using the parameters introduced in Figure 2.8. In (b), the additional dotted lines represent the linear fits of the data with weighed errors. For unpassivated films, the slope of the fit is of -0.7 whereas it has a value of -0.6 for passivated films.

The results can be discussed with respect to the Nix-Freund model and the source model. The predictions of the Nix-Freund model were calculated with Equation (2.12) combined with Equations (2.13) and (2.21) for the unpassivated films and for the films passivated with Al_xO_y and Si_xO_y. The Nix-Freund model gives a similar inverse dependency of stress on film thickness, but underestimates the stress values. Several factors may account for the discrepancy. First, the model considers the channeling of an isolated threading dislocation in a single-crystalline film. The films are however likely strengthened by the presence of grain boundaries. Second, an obstacle-free model may not be realistic because of dislocation interactions which occur after the initial stages of yielding as confirmed by our TEM studies. The model also fails at quantifying the effect of passivation. Indeed, it predicts that the presence of a dislocation dipole increases the strength of a single crystal film on a rigid substrate by about a factor of 2 (ref. [31]). The results, however, exhibit a much weaker increase. Experimental TEM observations support this discrepancy: no dislocation dipoles on which the model is based were found in the films.

The source model, also shown in order to evaluate the influence of dislocation nucleation, better fits the data. Again, it predicts a stress increase due to passivation. The estimated absolute stress values are close to the measured ones. This model is based on the activation of dislocation sources. Since no dislocation source was observed in the TEM studies, it is difficult to discuss its ability to describe the size effects in the passivated films of this study.

Following the approach of Venkatraman and Bravman[17] and Keller *et al.*[18], we will now account for the effect of grain size strengthening. The film strength is assumed to be fully described by the sum of a Nix-type dimensional constraint and a Hall-Petch grain-size strengthening. The difference between the stress measured at 50 °C, σ_{50}, and the stress at the same temperature predicted in the Nix-Freund model, σ_{Nix}, can be written as:

$$\sigma_{50} - \sigma_{Nix} = \frac{k_{HP}}{\sqrt{d}} \tag{6.9}$$

where d is the grain size and k_{HP} the Hall-Petch coefficient. The quantity σ_{50} - σ_{Nix} is plotted vs. the inverse square root of the grain size in Figure 6.26 for films thicker than 100 nm.

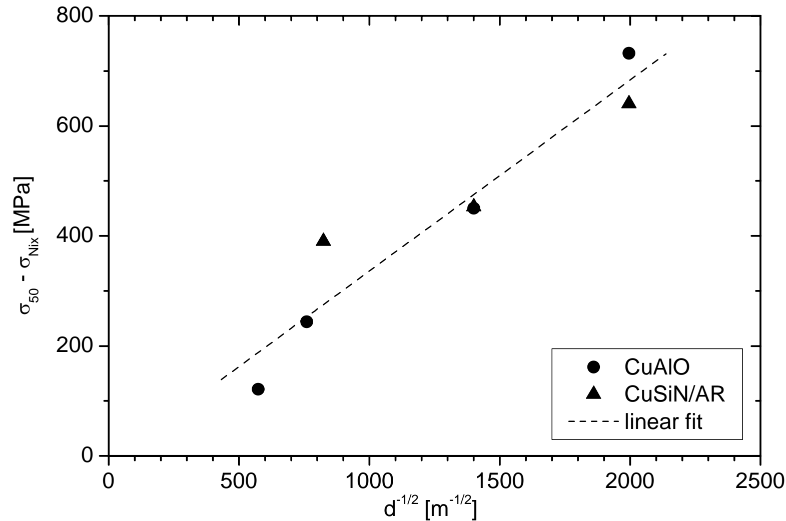

Figure 6.26: The difference between the stress measured at 50 °C and the prediction of Nix-Freund model vs. the inverse square root of the grain size in accordance with a Hall-Petch description of grain-size strengthening for the passivated films (thicker than 100 nm). The Cu grain sizes of the CuSiN/AR films is taken equal to that of the CuAlO films, given in Table 5.1. The dotted line represents the linear fit of the data: σ_{50} - σ_{Nix} = (-10.88 ± 66.42) + (0.347 ± 0.048) $d^{-1/2}$ with R = 0.956.

A straight line fitted to the stress values to determine the Hall-Petch coefficient, k_{HP}, gives a value of 0.347 ± 0.048 $MN \cdot m^{-3/2}$, comparable to the value of 0.344 $MN \cdot m^{-3/2}$ found by Keller *et al.*[18]. However, this value is about three times larger than that of bulk Cu (0.112 $MN \cdot m^{-3/2}$ from ref. [165]). It is not clear whether this increased Hall-Petch coefficient is a real thin film effect or a proof that this approach is inaccurate. If this value is realistic, it is evident from the linear dependence visible in Figure 6.26 that grain size strengthening and a Nix-type dimensional constraint could describe well the stress levels measured in Cu films thicker than 100 nm. Xiang *et al.* measured the yield stress of free-standing electroplated Cu films with the bulge test technique[106]. They found a Hall-Petch coefficient (0.156 $MN \cdot m^{-3/2}$) close to the literature bulk value if the yield stress is defined at a plastic strain of 0.2% and if twin boundaries are taken into account. The higher Hall-Petch coefficient obtained in our study may thus be ascribed to incomplete yielding at smaller plastic strains with the substrate curvature technique.

Stress plateau

Both the Nix-Freund model and the source model predict a steadily increasing stress with decreasing film thickness, as seen in Figure 6.25. Nevertheless, a stress plateau for ultra-thin films is observed for both passivated and unpassivated films. This work reports the first indication of a stress plateau for passivated films. The stress in passivated films stagnates at about 1.2 GPa, which is about twice that of ultra-thin unpassivated films (650 MPa). For unpassivated films, Balk *et al.*[25] attributed the origin of the plateau to parallel glide dislocations. The emergence of this type of dislocations was explained with the constrained diffusional creep model of Gao *et al.*[52]. In the case of passivated films, surface diffusion is hindered and therewith constrained diffusional creep. The effective inhibition of this relaxation mechanism was observed experimentally and already discussed on the basis of the shapes of the stress-temperature curves. If the causal connection between constrained diffusional creep and parallel glide dislocation really exists, the formation of parallel glide dislocations should be prevented in passivated films. Nevertheless, this type of dislocation was unexpectedly observed in the passivated films thinner than 200 nm. This is apparently in contradiction with a previous TEM study of a 200 nm thick self-passivated Cu-1% Al film, in which only threading dislocations were observed[25]. To account for this, the following hypotheses are proposed:

1) One possible explanation is that parallel glide dislocations form in ultra-thin films, even with a capping layer. However, this would contradict Gao's theory. It may be more likely that these dislocations formed during sample preparation. The Cu films were annealed 1 hour at 500 °C prior to the deposition of the passivation layer, which was carried out at room temperature. During the cooling down after annealing and prior to passivation deposition, all the conditions for the appearance of parallel glide dislocations are met. The subsequent passivation of the films may then "imprison" these dislocations in the film. This is actually what was observed experimentally. *In-situ* TEM experiments indeed revealed that these dislocations were immobile during thermal cycling between room temperature and 500 °C. Based on the constrained diffusional creep model, the prerequisite for their displacement is a free surface, which is no longer available after passivation. The presence of the capping layer may have therefore

prevented their glide.

2) An alternative explanation is that the thermal strain applied to the film over the temperature range of the thermal cycling was too low to induce yield in films thinner than 100 nm.

All these aspects raise the question of the true origin of the film thickness-independence of the stress in the ultra-thin films. According to Balk *et al.*, the presence of parallel glide dislocations justifies the existence of a stress plateau in the unpassivated films. It is nevertheless questionable whether the simple presence of these dislocations, artificially introduced during preparation and imprisoned in a passivated film, is enough to account for the plateau observed in passivated films. An examination of the data for the passivated 200 nm CuAlO film contradicts this assumption. This film thickness is critical since its stress lies within the plateau regime for unpassivated films (observed for films thinner than 400 nm) but in the linear increase regime for the passivated films. The presence of parallel glide dislocations in this film can be easily explained on the basis of the previously introduced ideas: they appeared "naturally" in the film upon cooling and before passivation. The origin of the stress plateau seems thus to be different before and after passivation. Considering the type of deformation active in this regime offers a more satisfying explanation. Indeed, the yield stress was not reached in these films and the room temperature value is not a flow stress, but an elastic stress. Comparison with films thick enough that they yield at room temperature is therefore invalid, since one is comparing apples to oranges; flow stresses to elastic stresses. An increase of the applied strain, for example by increasing the temperature range of the wafer curvature method, would give higher stress values and could induce yielding. Additional investigations are therefore needed to see whether the yield stress is truly independent of the film thickness. It remains also unclear how passivated films would behave if parallel glide dislocation formation was suppressed. All these issues will be addressed in chapters 7 and 8.

Comparison with literature

In Figure 6.27, the 50 °C stresses obtained in this study of passivated films are compared to the stresses measured in literature for Ag, Al, Au und Cu thin films already plotted in Figure 2.7.

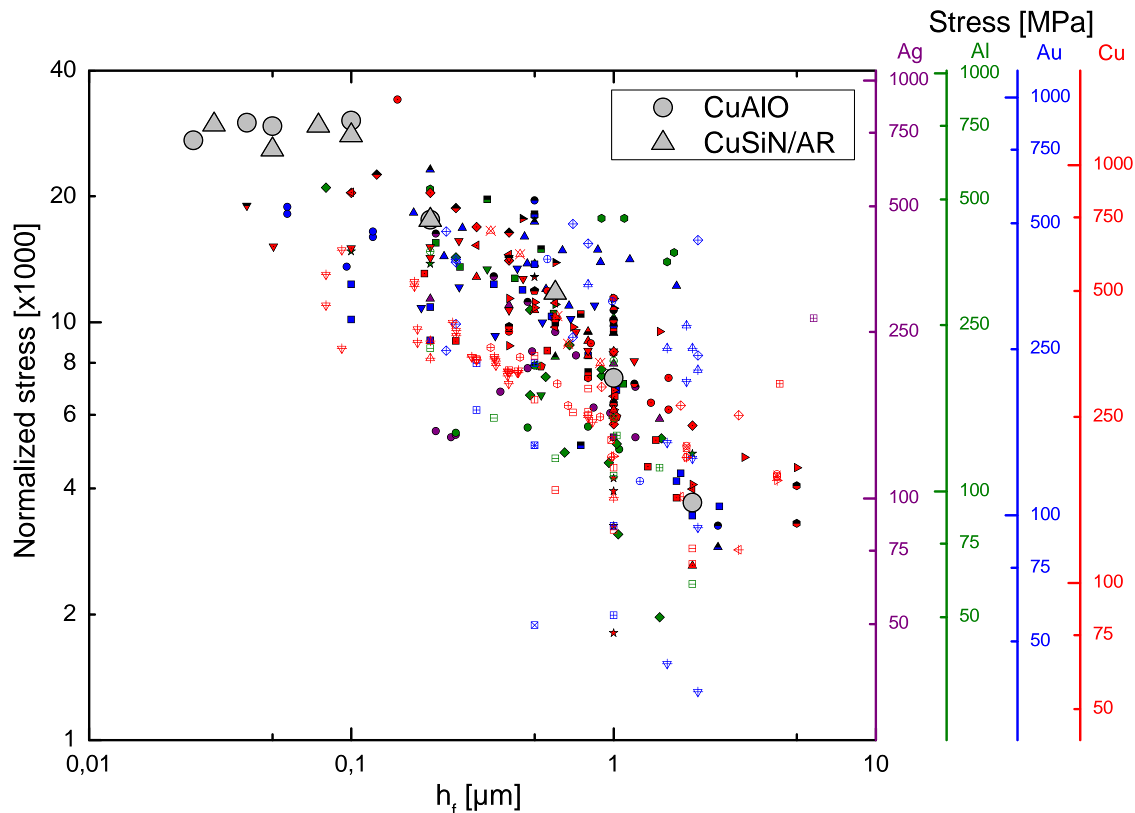

Figure 6.27: Stress at 50 °C measured for the CuAlO and CuSiN/AR passivated films (large symbols) plotted together with the literature data collected in the masterplot. The detailed legend is to be found in Figure 2.7.

This study extended the measurement range of thin films into the ultra-thin film thickness regime, where precious little data exists. It is the first systematic study of passivated films of thicknesses down to 25 nm. The only other study dealing with ultra-thin passivated Cu films was carried out by Shen *et al.*[66,68,69]. They reported stresses reaching 1 GPa in their thinnest films. However, their study was limited to a few isolated film thicknesses with focus on the shape of the stress-temperature curves and not on the size effects. The stresses of our films thicker than 100 nm lie in the linear increase zone, proving that the origin of the size effects is the same for all the films, and

exists whether the film is passivated or not, deposited on a substrate or free-standing, epitaxial or polycrystalline. Another striking feature from the comparison with literature data is that the measured stresses reaching 1.2 GPa are the highest ever reported for thin films. Since this value also represents the strength limit in the ultra-thin films, it is interesting to discuss this value compared to the theoretical strength. As determined in section 2.2, the theoretical strength of Cu amounts 5.2 GPa, i.e. about four times higher than our limiting stress. The stress plateau for passivated films is therefore not an artifact due to the stress in our films reaching the theoretical limit.

6.5 Summary and motivation for chapters 7 and 8

The thermomechanical behavior of passivated Cu thin films with thicknesses ranging from 25 nm to 2 µm was investigated. The Cu films were annealed for 1 hour at 500 °C and then capped at room temperature by either 10 nm of Al_xO_y or Si_xN_y.

Passivating the film surface was shown to exert a dramatic effect on the stress behavior of the films, independent of the passivation material. The dominant stress relaxation mechanism is dependent on film thickness:

- For films thinner than 100 nm, the strain was accommodated purely elastically between room temperature and 500 °C. The elastic deformation and the high stresses can be explained by the switching off of constrained diffusional creep due to the passivation and the absence of dislocation plasticity. Herewith, we demonstrate that the deformation of ultra-thin unpassivated films is exclusively governed by stress relaxation through constrained diffusional creep.

- For films in the micrometer regime, the effects of the passivation were less pronounced, with slightly higher stresses at low and high temperatures. The stress in these thicker films is relaxed mainly through dislocation plasticity.

- Thin films with intermediate thicknesses (between 200 nm and 1 µm) appear to

be significantly affected by both dislocation plasticity and diffusional creep. The influence of diffusional creep, at the expense of dislocation plasticity, increases as film thickness decreases.

In summary, the passivation appears to strengthen the films by inhibiting diffusion rather than by constraining dislocation motion. The microstructure of the ultra-thin films was also shown to play an important role in their deformation, since a few pores in the films interrupted the passivation layer and herewith enabled constrained diffusional creep to occur.

Size effects were investigated by plotting the stress at room temperature after thermal cycling as a function of the inverse film thickness:

- For films in the 200 nm - 2 μm range, the stress at room temperature increases with decreasing film thickness. The size effects in these films could be explained by either the source model, which considers the increasing difficulty of dislocation nucleation with decreasing film thickness, or by a combination of a Nix-Freund type dimensional constraint and a Hall-Petch grain size strengthening.

- The stress of the ultra-thin films stagnates with film thickness at a value of 1.2 GPa. A similar stress plateau observed by Balk *et al.* for unpassivated Cu films was attributed to the presence of parallel glide dislocations in the films that originate in constrained diffusional creep. Parallel glide dislocations were surprisingly found for the first time in passivated films and were immobile during *in-situ* thermal cycling. They have supposedly been introduced during film preparation. Their presence in the film is nevertheless not sufficient to account for the stress plateau, since they were also detected in a 200 nm thick film, lying out of the plateau regime. It is speculated that the plateau is due to the switching off of all the deformation mechanisms, leading to the elasticity of the films.

CHAPTER 7

EFFECT OF PASSIVATION DEPOSITION TEMPERATURE ON THE MECHANICAL BEHAVIOR OF CU THIN FILMS

7.1 Introduction and motivation

In the previous chapter, the presence of parallel glide dislocations in ultra-thin Cu films passivated at room temperature after annealing at 500 °C was reported. This type of dislocations is unexpected in passivated films, however, since their formation should be controlled by a surface diffusion-based mechanism. A plausible explanation could be that they appeared during the cooling step after annealing and before passivation deposition, during which surface diffusion kinetics were favorable. This illustrates the

important role played by processing parameters such as deposition temperature or annealing treatments during sample preparation.

The unexpected presence of parallel glide dislocations complicated the interpretation of a room temperature stress plateau observed for films thinner than 100 nm. To clarify this point, it is therefore necessary to prepare passivated films without parallel glide dislocations by preventing the Cu film from being thermally strained while it still has a free surface. This can be best achieved by either depositing the passivation at room temperature directly after Cu deposition or by depositing the passivation at 500 °C directly after the Cu anneal.

This chapter is based on the study of Cu films passivated with 10 nm of Si_xN_y under different conditions: Cu films deposited and passivated at room temperature without annealing (type CuSiN/RR), Cu films annealed and passivated at 500 °C (type CuSiN/AA), and finally Cu films annealed at 500 °C and passivated at room temperature (type CuSiN/AR). The results of the stress-temperature measurements will be presented first. Then, the role of the thermal history on the arising dislocation mechanisms is investigated. Finally, the influence of the passivation temperature on the thermomechanical behavior of the films will be discussed.

7.2 Stress measurements

7.2.1 Stress-temperature behavior

The stress-temperature behavior of the three film types was investigated with wafer curvature. All films were back side passivated, so that no correction was necessary to measure accurately the Cu film stress. The ultra-thin CuSiN/AR films of batch 1 are not addressed in this study since the passivation in those samples was not continuous (see sections 5.3.3 and 6.4.5). For the CuSiN/RR and CuSiN/AA film types, films of batch 1 and 2 present identical stress-temperatures curves, as shown in the appendix (section 10.7). The first thermal cycle to 500 °C is not shown. Only the reproducible, stabilized

thermomechanical response observed during subsequent cycles is given. For the CuSiN/RR films, which were not annealed during film preparation, grain growth occurred during the first thermal cycle. The stress-temperature behavior is film thickness-dependent and is addressed separately for thick and ultra-thin films.

Thicker films

The thermomechanical behavior of the 600 nm thick films of three types is shown in Figure 7.1. The shape of the curves accounts for an elastic-plastic deformation typical for thicker films. No big difference of behavior is visible between the three film types. The room temperature stress and the elastic slopes of the CuSiN/RR film are, however, slightly smaller than for the other films.

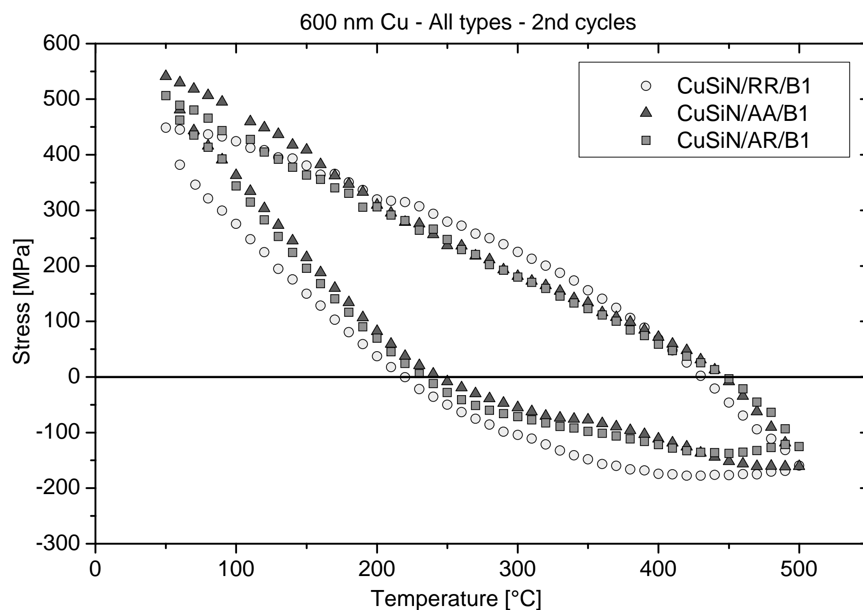

Figure 7.1: Stress-temperature curves of the 600 nm thick films of types CuSiN/RR, CuSiN/AA and CuSiN/AR. The shape of the curves indicates a typical elastic-plastic deformation.

Ultra-thin films

To illustrate the behavior of the ultra-thin 25, 30, 50 and 75 nm thick films, the curves obtained for the 30 nm thick films are presented in Figure 7.2. For all three film types, the stress evolved linear-elastically with temperature and reached similar room temperature and high temperature values.

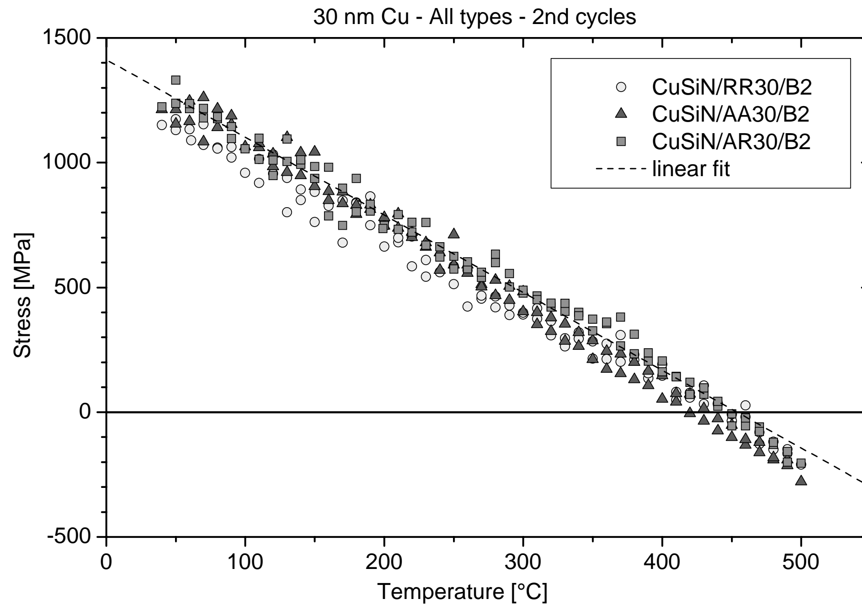

Figure 7.2: Stress-temperature curves of the 30 nm thick films of types CuSiN/RR, CuSiN/AA and CuSiN/AR. The three films deform elastically.

Figure 7.3 summarizes the results obtained for the 100 nm thick films of three types.

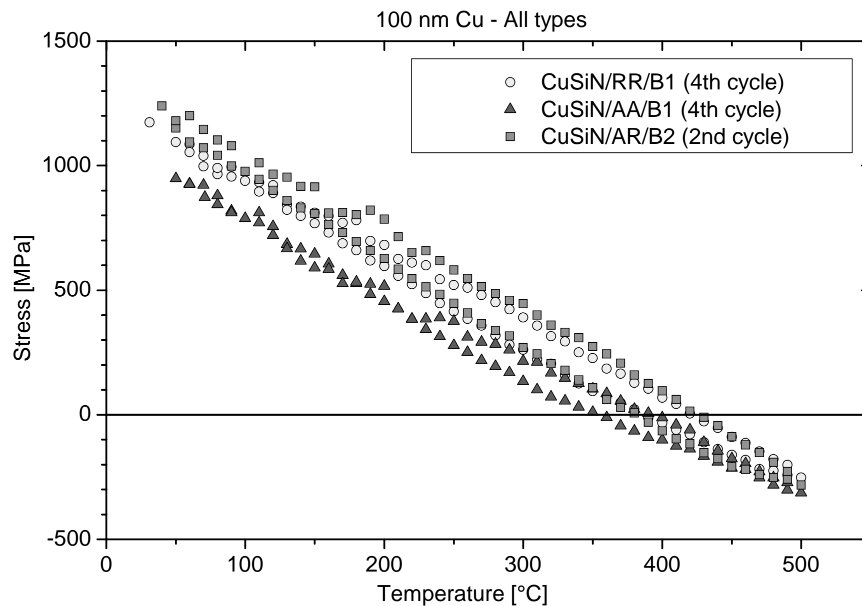

Figure 7.3: Stress-temperature curves of the 100 nm thick films of types CuSiN/RR, CuSiN/AA and CuSiN/AR. The CuSiN/RR and CuSiN/AR films behave very similarly. The CuSiN/AA film reaches a smaller tensile stress at room temperature, but a similar compressive stress at 500 °C.

The shape of the three curves is very similar, with a regime in which cooling and heating segments overlap (between room temperature and 200 °C) and a regime with a small hysteresis (between 200 °C and 500 °C). While the stress in the CuSiN/RR and CuSiN/AR films evolves identically and overall thermoelastically, it reaches a lower value at room temperature for the CuSiN/AA film.

7.2.2 Stress at 40 °C and 50 °C

The stress was determined before and after thermal cycling for the three film types. In Figure 7.4, the stress measured at 40 °C at the beginning of the first thermal cycle is plotted vs. the inverse of the film thickness. The stress values and dependence on film thickness greatly differ among the three film types. The initial stress of the CuSiN/RR films remains roughly constant over the whole thickness range around 0 MPa. The 25 nm film is at the limits of the resolution of the measurement system, as indicated by the large error bars. In contrast, for the CuSiN/AA and CuSiN/AR sample types, the stress increases with decreasing film thickness for films thicker than about 100 nm and then plateaus for thinner films. The stress values are higher for the CuSiN/AA films than for the other two film types over the entire thickness range. Especially for the ultra-thin films, the stress stagnates at about 1.2 GPa for the CuSiN/AA films compared to about 700 MPa for the CuSiN/AR films.

The stress at 50 °C after thermal cycling was also determined by averaging the values obtained after all the measured cycles and is plotted vs. the inverse of the film thickness in Figure 7.5. The three film types follow a similar trend. For films thicker than 100 nm, the stress increases as the film thickness decreases. Below this thickness, the stress no longer depends on film thickness and plateaus at about 1.2 GPa. The transition from the size-dependent to the size-independent regime is less abrupt for the CuSiN/AA films than for the others, with stresses increasing progressively before stagnating below a film thickness of 50 nm.

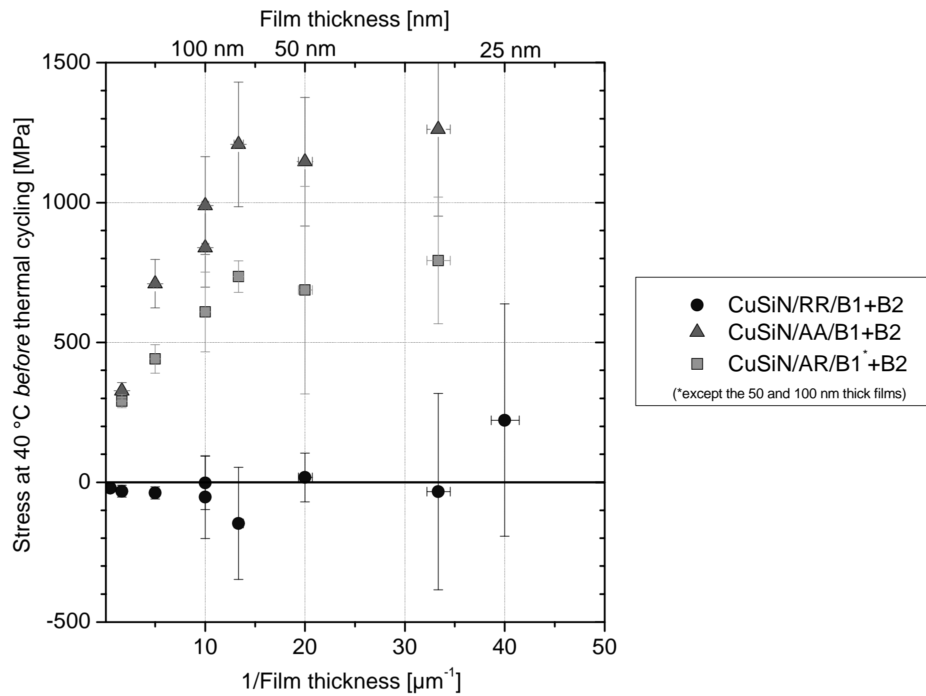

Figure 7.4: Stress at 40 °C *before* thermal cycling vs. the inverse of the film thickness of the three film types. Both the stress dependence on film thickness and the level differ between the three types.

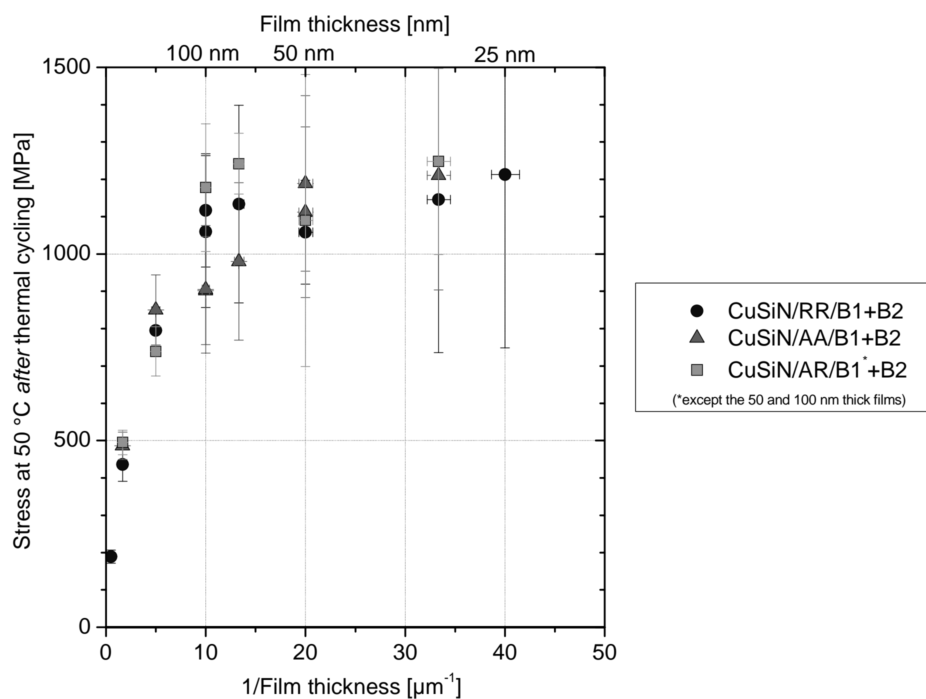

Figure 7.5: Stress at 50 °C *after* thermal cycling vs. the inverse of the film thickness of the three film types. For all the films, two regimes can be distinguished: a linear increase of the stress with decreasing film thickness for films thicker than 100 nm and a stress plateau for thinner films.

7.3 Dislocation behavior

Dislocation mechanisms were examined in the 100 nm thick films of each type by TEM. Before thermal cycling, the 100 nm thick CuSiN/RR film consisted of very small grains (Figure 5.20), in which no dislocations were found. This sample was cycled to 500 °C *in-situ* in the TEM. Grain growth started at about 100 °C and by 500 °C, the grain size had stabilized. Representative stabilized microstructure is shown in Figure 5.24(b). During cooling to room temperature, no dislocation activity was observed. However, after thermal cycling, parallel glide dislocations were observed in a few grains, as illustrated by the micrograph Figure 7.6. Their density is comparable to that observed in the 100 nm thick CuSiN/AR/B1 film (section 6.3.2). In addition, TEM observations of the 100 nm thick CuSiN/AA film also revealed the unexpected presence of parallel glide dislocations in a few grains.

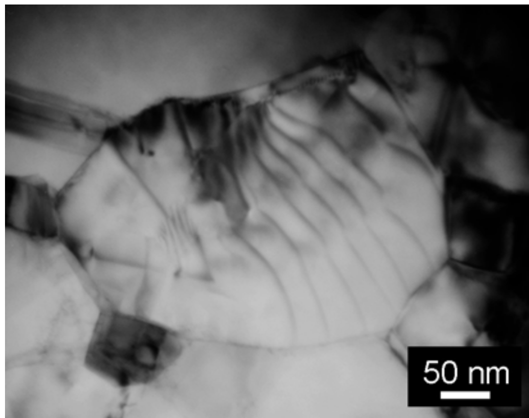

Figure 7.6: Parallel glide dislocations in a grain of the 100 nm CuSiN/RR film at room temperature after thermal cycling to 500 °C.

To summarize, parallel glide dislocations were observed in the 100 nm thick films of the three types despite their different preparation routes.

7.4 Discussion

7.4.1 Stress-temperature behavior

In chapter 5, we demonstrated that the preparation route has a strong influence on the film microstructure. After preparation and before thermal cycling, the CuSiN/RR films exhibit a bimodal distribution of very small grains surrounded by big columnar grains. A monomodal distribution of big columnar grains was reported in the CuSiN/AA and CuSiN/AR films. In addition, hillocks were observed in the CuSiN/AA films thinner than 200 nm whereas pores and grain boundary grooves were found in the CuSiN/AR/B1 films. After thermal cycling, all film types have similar grain sizes. In this section, we will discuss the effects of the preparation route on the thermomechanical behavior of the films.

Despite distinct microstructural features, the stress temperature behavior of the thicker films is close for the three types. This supports the idea that the deformation of thin films is controlled by dislocation mechanisms that are unaffected by the passivation temperature.

A similar trend is observed for the ultra-thin films of the different types, which deform elastically. It was noted in the previous chapter that the stress in bare ultra-thin films can only be relaxed through diffusional creep. Apparently, the mere presence of the passivation layer during thermal cycling, which suppresses surface diffusion, controls the underlying Cu film's deformation. This set of experiments showed that the temperature at which it is deposited did not seem to influence film deformation. The 100 nm thick CuSiN/AA film exhibited a lower 50 °C stress than the other 100 nm thick films. The stress-temperature curve of this film deviates from the linear behavior of the other films and exhibits the characteristic shape of a film in which constrained diffusional creep is active, as already observed and discussed for the CuSiN/AR/B1 thinner films in section 6.4.5. The same behavior is observed in the 75 nm thick film as well. A probable explanation for the weakening of the passivation can be found in the microstructure of the films. Indeed, hillocks were detected at the surface of these films. The observed behavior is consistent with these hillocks having ruptured the passivation

layer and relaxing the film stress at high temperatures. Once these features are present in sufficient density, the film behaves closer to a bare film. Though, it remains unclear why the same behavior is not observed for films thinner than 75 nm, which exhibit a higher hillocks density. Hillocks in these films are maybe not as high as in the thicker films, due to the low film thickness. They would thus grow under the passivation layer without breaking it. However, this is pure speculation since no experimental proof can be given for such a behavior. In summary, no significant effect of the passivation temperature is visible on the stress-temperature behavior of the films.

7.4.2 Stress at 40 °C and 50 °C

The preparation conditions seem to affect strongly the stress measured directly after film preparation at 40 °C, which strongly differs from the stress measured at 50 °C after cooling from 500 °C.

Before thermal cycling, the three film types show completely different trends. In the CuSiN/RR films, which were sputtered and passivated at room temperature, the stress is film thickness-independent and roughly equal to zero, as expected since there is no thermal stress resulting from sample preparation. This result is confirmed by a study of Pletea *et al.*[130], who measured *in-situ* the stress evolution in a 300 nm thick Cu film sputtered on a Si(100) substrate. They discussed the influence of the sputtering pressure on the film stress. At low sputtering pressures, as it is the case in our study, they reported a compressive stress varying between -100 and -200 MPa during film growth. Compression in as-deposited films is believed to be caused by a mechanism known as atomic peening[166]. At low pressures, there are few atomic collisions within the plasma. Sputtered Cu atoms and reflected Ar atoms thus impinge on the film at nearly normal incidence and with high energies. As they strike the film at high energies, incident atoms drive the atoms of the film closer together, imbedding themselves in the film. Pletea *et al.* also characterized stress relaxation after deposition. The stress was shown to decrease towards 0 MPa within 15 hours. They listed as possible reasons for room temperature stress relaxation after deposition dislocation-mediated plasticity, diffusion-mediated plasticity and a possible change of microstructure due to recrystallization. In the CuSiN/AA and CuSiN/AR films, which were both annealed at 500 °C, the residual

stress is different from zero. The stresses created in thin films are commonly due to thermal mismatches. As the film cools down, the difference in CTEs between the film and the substrate leads to stresses in the film. The residual stresses in both film types follow two different regimes: a linear increase with decreasing film thickness above 75 nm and a stress plateau below. The only difference between both film types is that the CuSiN/AR films were cooled from 500 °C with a bare surface whereas it was passivated for the CuSiN/AA films. In the linear regime of the thicker films, the stress in the 600 nm thick film is equal for both film types. This confirms that thicker films, in which dislocation plasticity dominates, are not influenced by the passivation layer, as already discussed in section 6.4.3. The role of diffusion increases with decreasing film thickness. For the 200 nm thick CuSiN/AA film, the passivation layer deposited at 500 °C prevents stress relaxation via diffusional flow during cooling and accounts for the higher stress than in the CuSiN/AR film. In the plateau regime, the same argument is valid to account for the 1.2 GPa stress in the CuSiN/AA films compared to the 700 MPa in the CuSiN/AR films. Note that the plateau for the latter films has a similar stress level as for unpassivated films (type CuAB). This is expected since the film stress could be relaxed at high temperatures as it does in a bare film. The passivation layer deposited after cooling then prevents room temperature diffusional stress relaxation which occurs in unpassivated films, accounting for the stress being slightly higher than in bare films.

The stress at 50 °C after thermal cycling exhibits the same classical dependency on the inverse film thickness for all film types: a linear increase followed by a stress plateau. The onset of the plateau occurs at lower film thicknesses for the CuSiN/AA films, for the reasons evoked in previous section. It is interesting to note that the stress in the ultra-thin CuSiN/AA films is identical before and after thermal cycling. No stress relaxation at room temperature seems to occur in these films, which confirms the total absence of active deformation mechanisms over the thermal cycling temperature range in this thickness regime.

A comparison of the stress before and after thermal cycling reveals the crucial role of high temperature diffusion mechanisms in the formation of the stress plateau. Indeed, before passivation and the associated suppression of diffusional creep, the stress scales differently with film thickness for each preparation route. A unique stress plateau does

not appear until the films are cooled in a passivated state, i.e. after the first thermal cycle for the CuSiN/RR and CuSiN/AR and directly after preparation for the CuSiN/AA films. It is therefore the suppression of constrained diffusional creep at high temperatures which explains the formation of the stress plateau, confirming a hypothesis of the previous chapter.

In addition, parallel glide dislocations were unexpectedly observed in the ultra-thin films of all types. The presence of these dislocations in the CuSiN/AR films was postulated in the previous chapter as follows: during cooling from the annealing temperature to room temperature, the Cu film surface was free and thus diffusional creep active. These conditions enabled parallel glide dislocation formation prior to passivation. It is unclear how they formed in the other film types and call into question current thinking regarding the mechanism of their formation. In the CuSiN/RR films, surface diffusion is shut off during preparation and subsequent thermal cycling, as indicated by the linear shape of the stress-temperature curves. Parallel glide dislocations, which were not observed in the as-deposited film, most likely formed during thermal cycling to 500 °C, even though the passivation layer remained continuous. A similar behavior is encountered in the CuSiN/AA films, which were also cooled to room temperature in a passivated state. For these films, however, one could argue that parallel glide dislocations are expected in the grains neighboring hillocks, where surface diffusion was proven to be active. However, they were found in grains not near hillocks. Three possible explanations for the origin of these dislocations in the films are proposed:

1) First, a straightforward theory is based on the possible existence of cracks at the grain boundaries. Indeed, grain boundary grooves expose the Cu surface and are diffusion paths that can accommodate the dislocation wedges needed for parallel glide dislocation formation. However, no such grain boundary grooves were observed in the CuSiN/RR or CuSiN/AA films after thermal cycling. For this theory to be valid, nanocracks, which cannot be detected in the SEM or TEM, should be present.

2) Second, the choice of Si_xN_y as a diffusion barrier may not have been adequate to suppress their formation mechanism. One can speculate that parallel glide dislocations do not require a perfectly free surface but can also appear if surface diffusion is limited.

The Si_xN_y passivation layer may not completely suppress surface diffusion, which would be sufficient for diffusion wedges to form and parallel glide dislocations to be emitted. This is however in contradiction with the linear stress-temperature behavior of the films, which supports the conclusion that surface diffusion is completely shut off.

3) Third, parallel glide dislocations may be encountered in ultra-thin Cu films irrespective of their surface state. This dislocation mechanism could be a natural response to the increasing geometrical constraint exerted on dislocations in ultra-thin films and already appear during film preparation. Nevertheless, this hypothesis questions the validity of the explanation of the parallel glide dislocations formation by the constrained diffusional creep model. One may advance that their formation occurs during film deposition, while their glide is controlled by diffusional creep.

It appears clear from all these speculations that no satisfactory explanation can be provided for the presence of parallel glide dislocations in these films and that further TEM studies are necessary.

7.5 Summary

The thermomechanical behavior of Cu films passivated with Si_xN_y and fabricated under different conditions was characterized. Three preparation routes were followed. In all the cases, Cu was sputtered at room temperature. It was then either directly passivated with 10 nm Si_xN_y or annealed for 1 hour at 500 °C, after which it was passivated at 500 °C or at room temperature. Despite their distinct microstructures, their stress-temperature behavior was very similar. A 50 °C stress plateau at 1.2 GPa is reported for the ultra-thin films of all types after thermal cycling. Its formation could be explained by the suppression of all the possible stress relaxation mechanisms due to the limited film thickness and the surface passivation.

This study could show that the surface state during the first cooling from 500 °C to room temperature is determining for the stress level at room temperature. Parallel glide

dislocations were unexpectedly found in the ultra-thin films of all types. The tuning of the passivation temperature was thus not successful at preventing their formation. It remains unclear whether they stem from a bad inhibition of surface diffusion or whether they are to be found in ultra-thin films, with or without a free surface.

CHAPTER 8

LOW TEMPERATURE BEHAVIOR OF CU THIN FILMS: THE STRESS PLATEAU AS A MEASUREMENT ARTIFACT?

8.1 Introduction and motivation

Thermal cycling of passivated Cu films, as discussed in previous chapters, revealed a stress plateau for films thinner than 100 nm. Despite a large number of speculations, the exact reason for such a stress plateau at room temperature in passivated films, in which surface diffusion is shut off and constrained diffusional creep therefore not possible, remained unclear. One of the possible explanations was based on the observation that the films in the plateau regime showed a linear elastic behavior between room

temperature and 500 °C. The applied strain over this temperature range was insufficient to plastically deform the film. An increase in the total thermal strain is thus needed to get a better understanding of the deformation in ultra-thin films. An extension to higher temperatures leads to new difficulties, since the passivation layer loses its effectiveness as a diffusion barrier, as described in chapter 6. It is therefore necessary to cool the films to lower temperatures, where the film deformation is expected to be exclusively controlled by dislocation motion since the low temperature deems diffusion-based mechanisms inactive.

In this chapter, the temperature dependency of the stress plateau is studied using Si_xN_y passivated Cu films. Stress measurements were carried out with the substrate curvature method and partially checked with X-ray diffraction. A new experimental setup was developed for the substrate curvature system to enable stress measurements down to -160 °C. X-ray diffraction measurements were performed down to -100 °C. The analysis of the stress evolution in the low temperature regime provides key new information that sheds light on the origin of the stress plateau for polycrystalline passivated films.

8.2 Experimental procedure

The thermomechanical behavior of Cu thin films upon cooling was characterized for different types of films, both unpassivated and passivated. For unpassivated films, a 100 nm thick as deposited Cu film (type CuR) was cooled. For passivated films, the study focused on films of type CuSiN/RR with 4 thicknesses between 25 and 600 nm. A 600 nm thick CuSiN/AA film was also analyzed. The film stress was measured as a function of temperature by either the wafer curvature technique or by X-ray diffraction ($\sin^2\psi$ method), or both. The working principle of both techniques has been extensively detailed in section 4.3. This section aims at describing the setups developed to cool the films.

8.2.1 Wafer curvature cooling experiments

In this study, two different systems that provide different sample environments were employed. The first (named system 1), consisting of a furnace purged with nitrogen (ROSE I), was used for all the stress measurements in the previous chapters. In this system, the films were thermally cycled between room temperature and 500 °C. The cooling and heating rates were controlled by the nitrogen flow and maintained at 6 K/min, except during cooling between 100 and 40 °C where they were of 4 K/min.

The wafer curvature measurements down to -160 °C were carried out in system 2, a unique wafer curvature setup that can run under ultra-high vacuum down to 10^{-7} Pa (ROSE II). In this system it is also possible to control the chamber atmosphere by purging with different gases. A schematic drawing of the apparatus is provided in Figure 8.1. A more detailed description is to be found in [167,168].

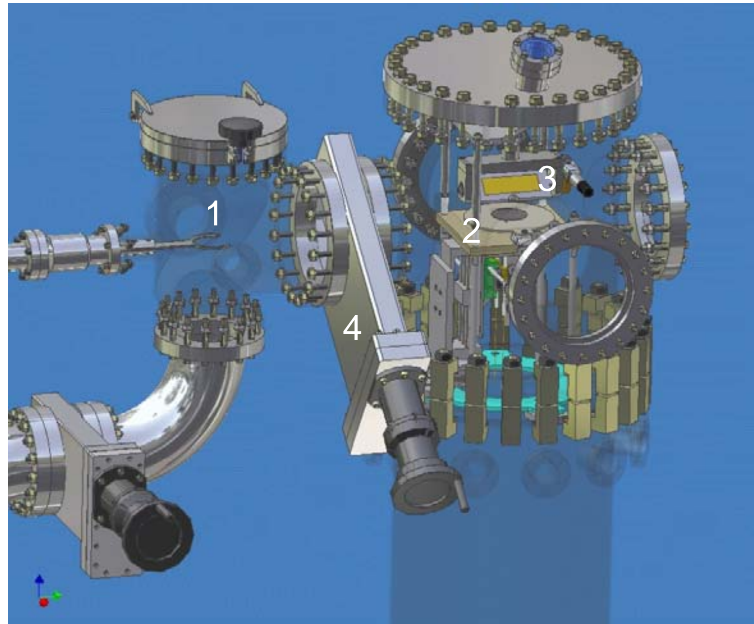

Figure 8.1: Schematic drawing of the UHV capable substrate curvature apparatus, with the main elements: 1 sample transfer, 2 sample holder with heating and cooling system, 3 mirror, 4 gate valve. The laser optical system is not shown.

This system was modified to accommodate temperatures down to -160 °C in order to explore thin film mechanical behavior at low temperatures. A cooling unit consisting of a liquid nitrogen cooled metallic block was mounted in the vacuum chamber. Two

parallel holes were drilled out of a one cm thick Al block and served as liquid nitrogen conduits. A one cm thick Cu block was placed directly on top of this block to assure temperature homogeneity. A ceramic heater above the Cu block was used to heat the measured wafers. The sample was placed onto three movable ceramic pins at a distance of less than 1 mm above the heater. The wafer temperature was measured with 2 Ni-Cr thermocouples located at the extremity of the holding tips. That the thermocouples were in direct contact with the sample guarantees an accurate temperature measurement. A sketch showing the positioning of the sample in the cooling system is provided in Figure 8.2.

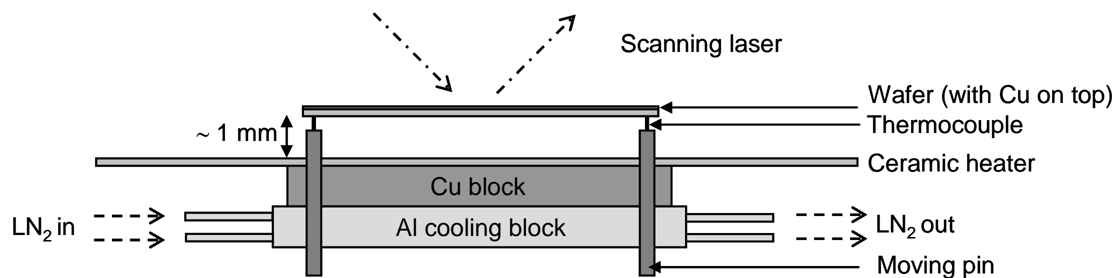

Figure 8.2: Cross-sectional sketch of the sample holder and the cooling and heating systems in the wafer curvature cooling system (system 2). The liquid nitrogen cooled Al block was custom designed for this experiment.

In order to compare the low temperature measurements in system 2 with the thermal cycles in system 1, similar atmospheric conditions were used: the measurement chamber was first evacuated and then purged with nitrogen gas under atmospheric pressure. Since nitrogen gas contains no water vapor, there were no condensation problems during cooling. By maintaining a constant flow of liquid nitrogen at a pressure of $5 \cdot 10^4$ Pa in the conduits, a cooling rate of about 5 K/min could be reached. A temperature plateau at -100 °C could only be overcome by evacuating the chamber. A chamber pressure of about 10 Pa was reached at -160 °C, the lowest reachable temperature. The samples were heated to room temperature at about 2 K/min. All the samples were a) cycled several times between room temperature and 500 °C in system 1, b) moved to system 2, where they were cooled down to -160 °C, heated up to room temperature, and c) moved back to system 1, where they were re-cycled to 500 °C.

At a given temperature, the radius of curvature of a single sample differed by about 20% between system 1 and 2 since the wafer curvature was not uniform and it is not possible to position the sample exactly the same way in the two systems. Thus, the line on which the laser scans the wafer slightly differs, which slightly shifts the position of curve along the y-axis. Since the reference measurements of the bare wafer had all been carried out in system 1, the radius values measured with system 1 were considered as reference values and used to correct the discontinuity in radius evolution. Specifically, the radius measured in system 2 at room temperature after cooling was corrected so as to be identical to the radius measured in system 1 at the same temperature during the following cycle. All the other radii values of system 2 were then corrected proportionally. If not mentioned otherwise, the cooling experiments and the thermal cycles before and after were all carried out on the same day in order to avoid stress relaxation between the measurements that decreases the room temperature stress at the start of the cycle.

8.2.2 X-ray diffraction cooling experiments

An X-ray diffraction setup was used to measure the film stress evolution at low temperatures. The stress calculated with the $\sin^2\psi$ method was determined in the (1x1) cm² substrates deposited along with the wafers, before and after cycling to 500 °C. This thermal cycling was performed in a UHV furnace with the same heating and cooling rates as during a wafer curvature measurement. For *in-situ*, temperature dependent experiments a heating/cooling chamber DCS350 (Anton Paar) was mounted on the Eulerian cradle[169]. With this equipment, *in-situ* experiments were performed at temperatures ranging from -100 °C to room temperature in 25 °C intervals and at pressures in the order of 0.1 Pa. For each temperature step, 2θ scans were performed at two tilt angles, $\psi = 0°$ and $\psi = 70.54°$, which corresponds approximately to 24 minutes for one stress measurement. A delay time of 5 minutes was scheduled for each temperature step in order to guarantee temperature homogenization.

8.3 Results

8.3.1 Low temperature stress evolution in unpassivated films

The stress of a 100 nm thick, unpassivated as-deposited Cu film (type CuR) was measured with XRD between room temperature and -100 °C before and after cycling to 500 °C (Figure 8.3). The first two wafer curvature cycles are shown in the figure as well.

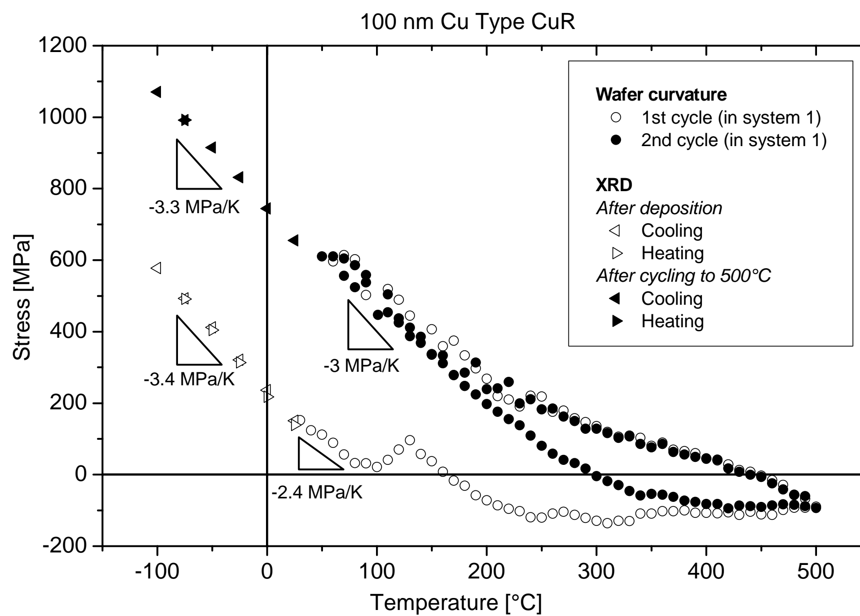

Figure 8.3: Wafer curvature measurements from system 1 and XRD stress-temperature cycles of the 100 nm unpassivated Cu film (type CuR). The film was cycled twice between room temperature and 500 °C in wafer curvature system. In the diffractometer cooling setup, it was cooled down to -100 °C directly after deposition and after one cycle to 500 °C. The slopes of the main segments are given under the curves.

The as-deposited film had an initial tensile stress of about 150 MPa. Upon cooling in the X-ray diffraction system, the stress increased linearly with decreasing temperature with a slope of -3.4 MPa/K and reached 600 MPa at -100 °C. The subsequent heating occurred along the same line. The wafer curvature measurement yielded an identical initial stress value. During the first heating to 500 °C, the stress changes were dominated by microstructural evolution, mainly grain growth, as commonly indicated by the stress drop between 100 and 150 °C. During cooling from 500 °C, the stress

relaxed at a constant rate until 250 °C. Below this temperature, it increased linearly with a slope of -3 MPa/K until room temperature. Another cooling sequence down to -100 °C was achieved in the X-ray system after thermal cycling to 500 °C. The measured cooling segment was perfectly continuous with the previous wafer curvature curve and a further linear stress increase occurred with a similar slope until -100 °C. During re-heating, the stress followed the same line as it did upon cooling.

8.3.2 Low temperature stress evolution in passivated films

CuSiN/RR films

Figure 8.4 shows the stress-temperature curves for the 50 nm thick CuSiN/RR film.

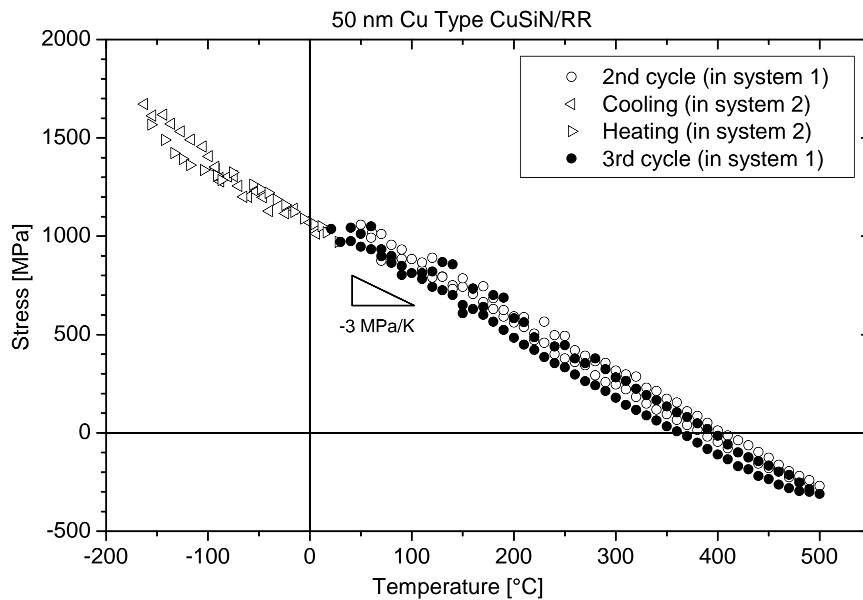

Figure 8.4: Wafer curvature stress-temperature cycles of the 50 nm passivated Cu film. The film was cycled between room temperature and 500 °C in system 1, then cooled down to -160 °C in system 2, and finally cycled again between room temperature and 500 °C in system 1. The slope of the curve is -3 MPa/K.

In system 1, the film started under a tensile stress of about 1.1 GPa at room temperature and deformed purely thermoelastically with a slope of -3 MPa/K up to 500 °C. Upon cooling the stress followed the same line back to room temperature. The sample was then switched to system 2 for liquid nitrogen cooling. The stress continued along the

same line until it reached a very high stress value of about 1.7 GPa at -150 °C. During heating, the stress again followed the same line until room temperature. The wafer was then transferred back to system 1 for a thermal cycle to 500 °C. The curve stabilized at stress levels similar to those exhibited before the cryogenic experiment, showing that the effect of thermal history on the behavior is minimal. In the studied temperature range (-160 °C – 500 °C) over which the total strain reaches 0.9%, the absence of hysteresis in the curves reveals the purely elastic deformation of this film.

Figure 8.5 shows the results for the 100 nm thick CuSiN/RR film. In Figure 8.5(a), the as-deposited film cooled in the XRD setup deformed linear elastically until -100 °C with a slope of -3.5 MPa/K. As for the 100 nm thick CuR film, the agreement between the room temperature stress measured with XRD and wafer curvature is very good. During the first heating to 500 °C in the wafer curvature system 1, the film, which was initially stress-free, went progressively into compression until 500 °C. The deformation upon cooling was elastic with a -3.3 MPa/K slope. Figure 8.5(b) illustrates the stress evolution in the film during the subsequent cycles. The XRD cooling of the previously cycled film again occurred purely elastically. The behavior of the film during the wafer curvature cooling in system 2 exhibits a similar trend. However, the cooling and heating curves between room temperature and -100 °C exhibit a slight hysteresis whereas both segments lie on top of one another between -100 °C and -150 °C. This is believed to be a measurement artifact due to the difference between cooling and heating rates. The film reaches a stress of about 1.7 GPa at -160 °C. Finally, the thermal cycle carried out in system 1 after the cryogenic experiment is similar to the one before.

(a)

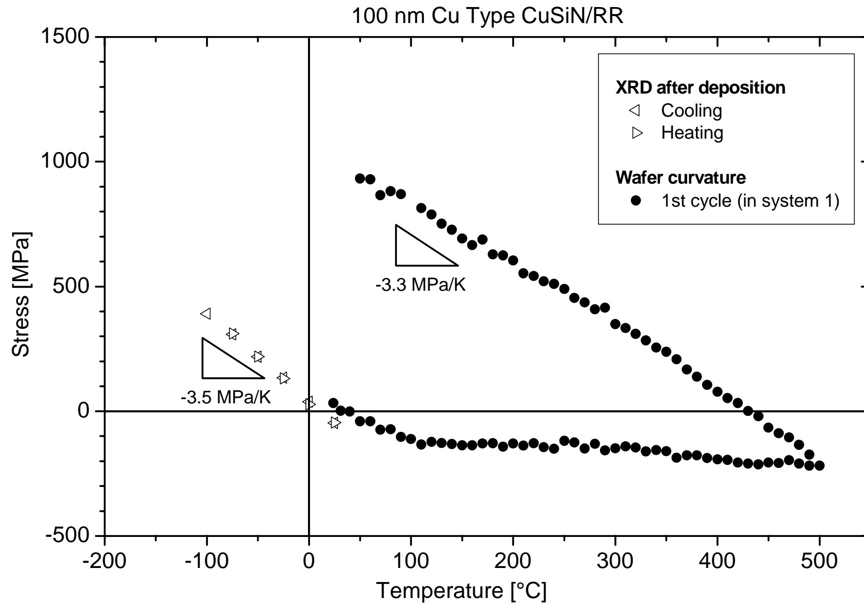

(b)

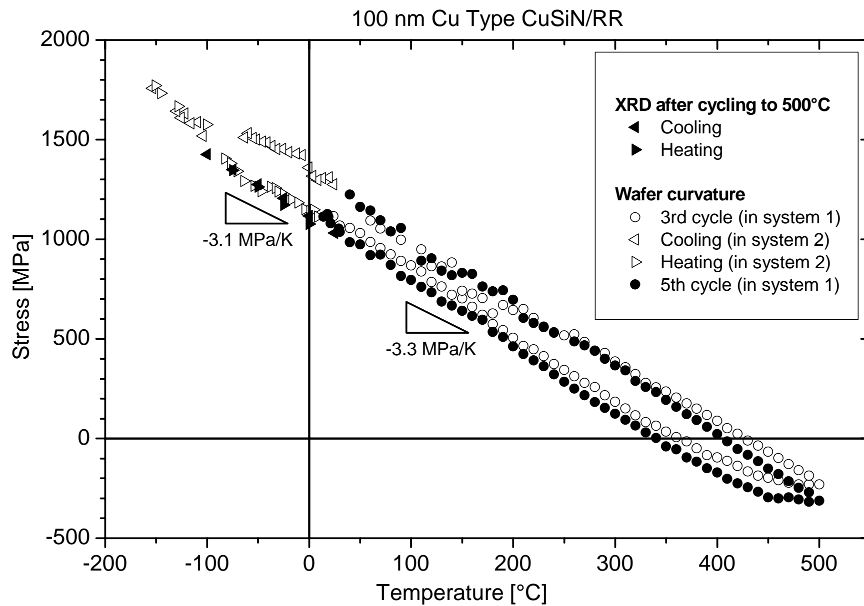

Figure 8.5: Wafer curvature and XRD stress-temperature cycles of the 100 nm passivated Cu film of type CuSiN/RR. (a) XRD cooling of the as-deposited film and first thermal cycle in the wafer curvature apparatus (system 1). (b) Wafer curvature cooling to -160 °C (system 2) and XRD cooling to -100 °C of the film previously cycled to 500 °C. The stabilized thermal cycle and the cycle after the cooling experiment are also shown. The slopes of the main segments are given under the curves.

Figure 8.6 shows the thermomechanical behavior of the 600 nm thick CuSiN/RR film characterized with wafer curvature.

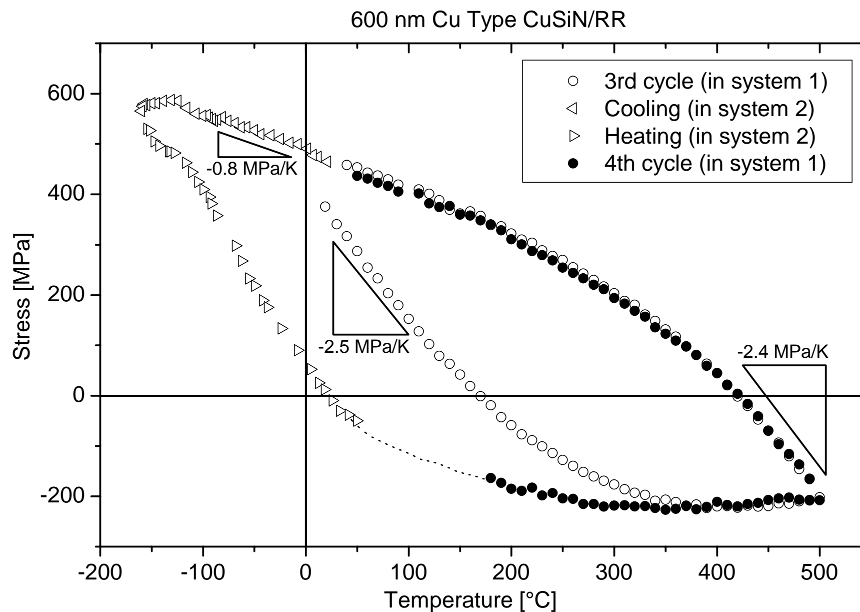

Figure 8.6: Wafer curvature stress-temperature cycles of the 600 nm passivated Cu film. The film was cycled between room temperature and 500 °C in system 1, then cooled down to -160 °C in system 2, and finally cycled again between room temperature and 500 °C in system 1. During the final cycle, stress values between 50 and 170 °C could not be recorded. The slopes of the main segments are given under the curves.

The stabilized cycle between room temperature and 500 °C, measured in system 1 and already described in section 7.2.1, is typical for an elastic-plastic deformation. After thermal cycling, a tensile stress of about 450 MPa is reached at room temperature. During cooling towards liquid nitrogen temperature in system 2, the stress increases continuously with a slope of -0.8 MPa/K, before stabilizing at -130 °C at a plateau value of 580 MPa. Subsequent heating induces a linear elastic drop of the stress. The onset of yielding is at about 20 °C and the final compressive stress of -200 MPa is reached at about 200 °C, i.e. 150 °C earlier than during the previous cycle. Data could not be acquired between 50 and 170 °C and is extrapolated on the plot. The cycle after the cooling experiment corresponds to the stabilized thermomechanical response of the film.

For all films, the values of the biaxial stress at 50 °C, -100 °C and -150 °C are plotted vs. the inverse of the film thickness in Figure 8.7. Each data point is an average of the stress from several cycles with a scatter of less than 5% in each case, except for the values at -100 °C and -150 °C which have been measured only once. For films thinner than 100 nm, the stress does not depend on the film thickness and forms a plateau, whether it is taken at 50, -100 or -150 °C. The plateau occurs at 1.1 GPa at 50 °C, 1.5 GPa at -100 °C and 1.7 GPa at -150 °C.

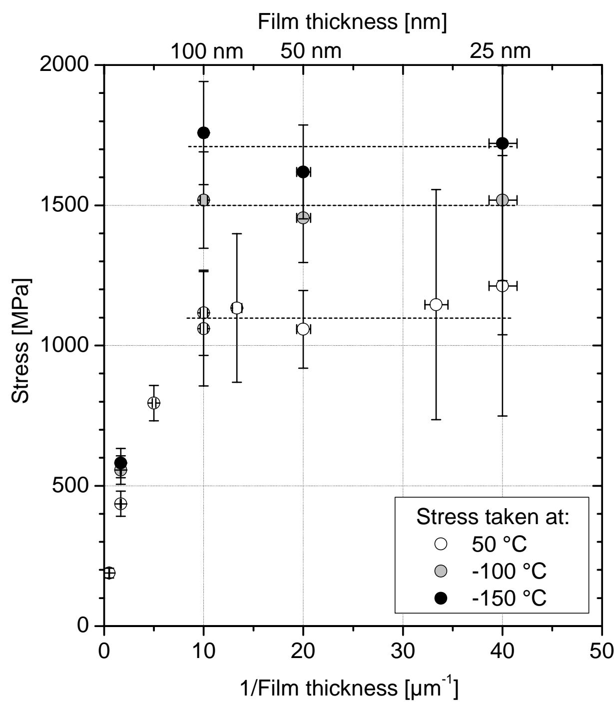

Figure 8.7: Average stress values at 50 °C, -100 °C and -150 °C vs. the inverse of the film thickness for the passivated Cu films of type CuSiN/RR. Film thickness is indicated on the upper scale. The dotted lines are highlighting the stress plateaus at the different temperatures.

CuSiN/AA films

The 600 nm thick CuSiN/AA film was also cooled in the wafer curvature setup. The results are summarized in Figure 8.8.

(a)

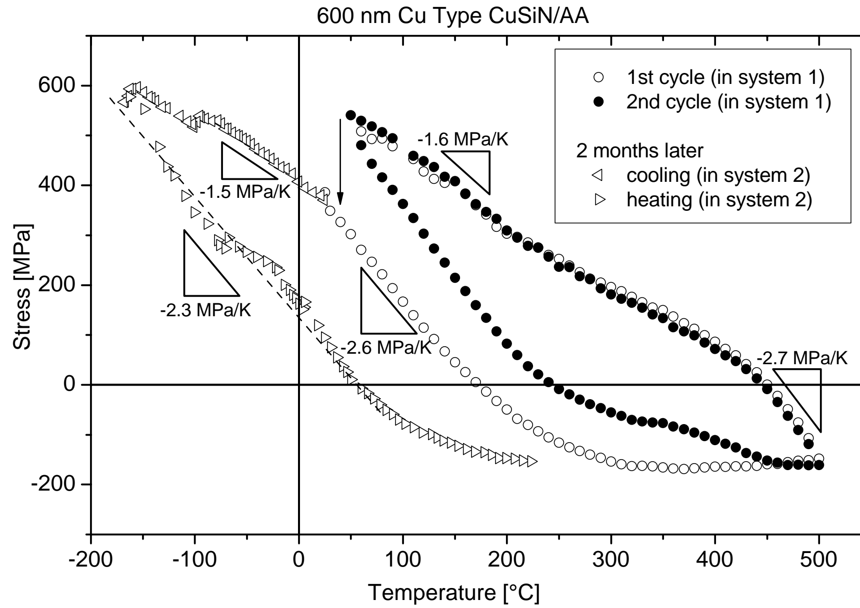

(b)

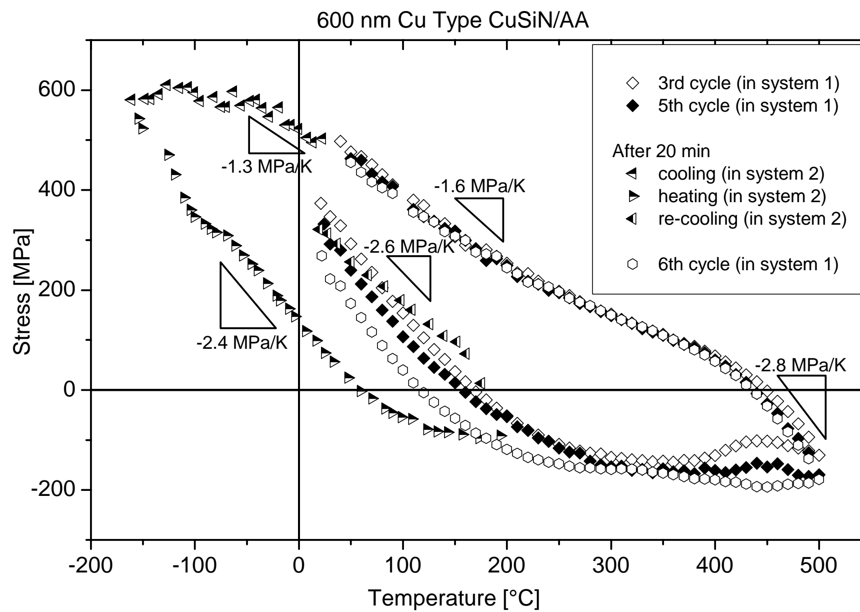

Figure 8.8: Stress-temperature curves of the 600 nm thick CuSiN/AA film. (a) The two first thermal cycles between room temperature and 500 °C in system 1 are shown. A cryogenic experiment was carried out in system 2 two months later, so that room temperature stress relaxation occurred – as marked by the arrow. (b) shows the subsequent thermal cycles. Directly after several cycles were carried out in system 1, the film was transferred to system 2 and cooled to -160 °C. It was then heated up to 200 °C and cooled to room temperature. Finally, a last thermal cycle was realized in system 1.

Two cryogenic experiments were carried out. Before the first cryogenic experiment, shown in Figure 8.8(a), the film was thermally cycled twice in system 1. Two months later, the film was cooled in system 2. In the meantime, room temperature stress relaxation occurred, so that the initial stress of the cryogenic experiment corresponds to the stress after deposition before thermal cycling. Upon cooling to cryogenic temperatures, the stress increased with a slope of -1.5 MPa/K, identical to the slope of the cooling segment between 200 °C and room temperature. At -160 °C, it reached a value of about 600 MPa. The stress then decreased linearly with a slope of about -2.3 MPa/K during re-heating. Plastic yielding occurred at 100 °C and the maximum compressive stress of -170 MPa was reached at 200 °C. Subsequent cooling to room temperature was not recorded. To summarize, the cryogenic response of the film can be described as a lateral shift of about 200 °C towards negative temperatures from the stabilized curve between 50 °C and 500 °C. Afterwards, the film was moved from system 2 to system 1 where it was cycled several times between room temperature and 500 °C (Figure 8.8(b)). These cycles differ from the cycles before the cryogenic excursion, in that they show a “tail” shape between 400 °C and 500 °C, characterized by a compressive stress drop followed by a compressive stress increase. This effect seems to attenuate after several cycles. Moreover, the room temperature stress after thermal cycling of about 500 MPa was lower than before the cryogenic experiment. Directly after a thermal cycle in system 1, the film was transferred back to system 2 for another cooling sequence down to -160 °C. No room temperature stress relaxation was observed. After an initial linear increase, the stress stagnated between -50 and -160 °C at about 600 MPa. During subsequent heating, it decreased linearly before yielding at 50 °C and reaching a compressive stress of -100 MPa at 200 °C. At this temperature, the film was cooled down and exhibits a final stress of 300 MPa, identical to the relaxed stress before thermal cycling. Finally, an additional thermal cycle in system 1 showed a response similar to that observed before the second cryogenic experiment, but with an attenuated “tail”.

8.3.3 Thermal expansion coefficient at low temperatures

The thermal expansion coefficient (CTE) of Cu, α_{Cu}, was calculated from the XRD data by plotting the (111) interplanar spacing $d_{(111)}$ determined from the diffraction angle as a

function of temperature. α_{Cu} is related to the slope of the obtained line with following equation:

$$\alpha_{Cu} = \frac{\Delta d_{(111)}}{\Delta T} \cdot \frac{1}{d^0_{(111)}} = \frac{\Delta d_{(111)}}{\Delta T} \cdot \frac{\sqrt{3}}{a} \tag{8.1}$$

with $d^0_{(111)}$ the strain-free (111) interplanar spacing and a the lattice parameter ($a_{Cu} = 3.6146$ Å). The values obtained for the 100 nm thick film, as-deposited and cycled to 500 °C, unpassivated (type CuR) and passivated (type CuSiN/RR) are reported in Table 8.1.

Table 8.1: CTEs of Cu in a 100 nm thick film as-deposited and cycled to 500 °C, unpassivated and passivated, determined with XRD during cooling from 25 °C to -100 °C.

	Unpassivated	Passivated
As-deposited	$17.3 \cdot 10^{-6}$ K^{-1}	$17.3 \cdot 10^{-6}$ K^{-1}
Cycled to 500 °C	$16.1 \cdot 10^{-6}$ K^{-1}	$15.5 \cdot 10^{-6}$ K^{-1}

8.4 Discussion

8.4.1 Wafer curvature vs. XRD

It is first of interest to discuss the consistency of the data since it was collected with three different setups. After correction, the wafer curvature measurements from system 2 are consistent with those from system 1, as revealed by the similar elastic slopes found with both systems. In addition, the slopes and absolute stress values from the *in-situ* X-ray diffraction measurements were similar to those from the wafer curvature measurements. The agreement between a macroscopic method, based on the change in curvature of a wafer and an atomic-resolved method, based on the lattice spacing change is very good. Hence our approach to deposit a passivation layer on the back side of the wafer to compensate for the additional effect on the curvature exerted by the passivation layer was a sound one which yielded good data.

8.4.2 Effect of passivation and annealing on the film properties

The XRD cooling experiments carried out with a 100 nm thick Cu film before and after thermal cycling to 500 °C, unpassivated and passivated, are summarized in Figure 8.9.

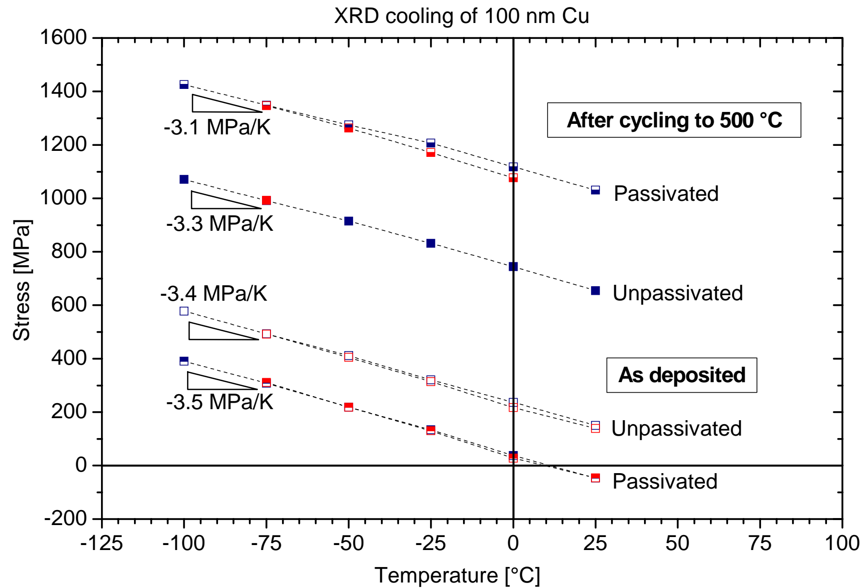

Figure 8.9: Summary of the XRD cooling experiments performed on the 100 nm thick Cu film before and after cycling to 500 °C, unpassivated and passivated. The slopes of the lines are indicated.

A comparison between the elastic slopes before and after passivation indicates no noticeable change, proving that a 10 nm thick passivation layer does not influence the elastic properties of thin films. However, the slope becomes slightly smaller upon cycling to 500 °C for both unpassivated and passivated films, which corresponds to a decrease of the biaxial Young's modulus. The only difference between as-deposited and annealed films likely to account for this effect is the grain size. In all the theories that explain the lower values of Young's modulus in thin films, grain boundaries play an important role. For the grain sliding model[161] discussed in section 6.4.2, the smaller the grain size, the smaller the expected Young's modulus. However, this theory is in contradiction with our results. The same effect of annealing was reported by Xiang *et al.* for free-standing Cu films, but no satisfactory explanation could be provided[106].

It is also worth commenting on the values obtained for the CTE of Cu presented in Table 8.1. The as-deposited ($17.3 \cdot 10^{-6}$ K^{-1}) and annealed ($16.1 \cdot 10^{-6}$ K^{-1} and

$15.5 \cdot 10^{-6}$ K^{-1}) values for the CTE bracket the bulk value of $16.7 \cdot 10^{-6}$ K^{-1}. Here again, grain growth seems to play an important role in the change of the thermal expansion coefficient with annealing. This effect can be explained based on atomistic considerations. Kiguchi and co-workers[170] studied Cu and Ni thin films and could demonstrate that, for "surface atoms", bonds are both softer and more anharmonic than for "bulk atoms". Thus, a lower bonding energy of these atoms is expected. As a result, the same amount of thermal energy will cause a larger expansion of a metal with a higher fraction of such atoms than of bulk metal. This will directly lead to a larger CTE. Now, supposing that the bonding state of grain boundary atoms is similar to that of surface atoms, a material with many grain boundary atoms should also have a larger CTE than if consisting of only bulk atoms. When grain size increases, the fraction of grain boundary atoms decreases, which can cause a decrease of the average CTE of the sample.

8.4.3 Stress behavior at low temperatures

Stress-temperature curves

The stress evolution of the films upon cooling will now be discussed. The behavior of the thicker films is illustrated by the 600 nm thick passivated film, whose deformation was already shown to be mainly controlled by dislocation plasticity. As expected, cooling the film to -160 °C resulted in a flow stress increase, as commonly observed for fcc metals. Nevertheless, the stress stagnated with decreasing temperature when it reached a value of about 600 MPa for both the CuSiN/RR and the CuSiN/AA films and did not depend upon the initial stress before cooling. This value therefore appears to be the maximal stress the film can sustain in tension. It is therefore proposed that this stress level corresponds to the ultimate tensile stress (UTS) of a 600 nm thick passivated film. This is supported by the fact that the shape of the cooling curve, with its constantly decreasing slope, clearly indicates strain hardening. However, this is apparently in contradiction with the fact that the cycles after the cooling experiments were identical to the ones before. Indeed, for a bulk material, a further increase of the strain beyond the ultimate strength leads to necking. A thin film may exhibit irreversible voiding, which was nevertheless not observed experimentally.

The high temperature tail observed for the 600 nm thick CuSiN/AA film remains unexplained. A similar feature was observed in several studies, but was always explained by the exposure of the Cu surface to oxygen before passivation[64,67,70-72], which is not the case in our study.

Since dislocation plasticity is the predominant low temperature deformation mechanism for a 600 nm thick film, it is interesting to compare the experimental curves with the stress predicted by thermally activated dislocation glide. To this extent, the stress evolution in the 600 nm thick CuSiN/RR film was simulated with this model between -160 °C and 500 °C, following the same approach as in section 6.4.4. The obtained curves are presented in Figure 8.10.

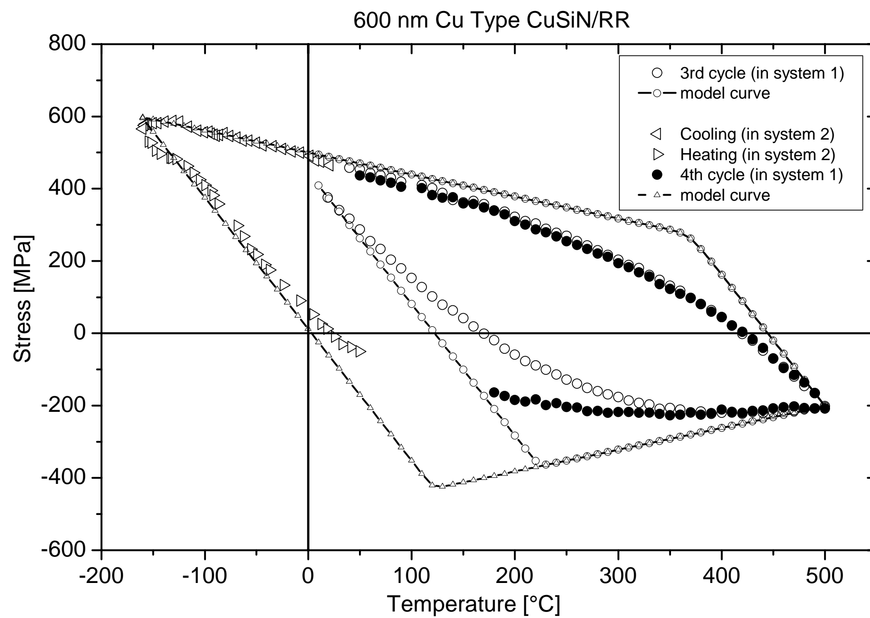

Figure 8.10: Experimental stress-temperature curves of the 600 nm thick CuSiN/RR film and theoretical curve for thermally activated dislocation glide. The model curve is based on Equation (6.8) using the following fit parameters: $\dot{\varepsilon}_0 = 1 \cdot 10^5$ s^{-1}, $\Delta F = 3.8 \cdot 10^{-19}$ J, and $\hat{\tau} = 180$ MPa. The constants used include: $\Delta\alpha = 14 \cdot 10^{-6}$ K^{-1}, $M_{Cu} = 2.6 \cdot 10^{11}$ Pa (at 300 K), and $s = 0.27$ for (111)-orientation. The heating rate was set to be 0.1 K·s^{-1}. The line with dots represents the simulation of the cycle between room temperature, 500 °C, and -160 °C with following boundary condition: $T = 292$ K, $\sigma = 376$ MPa. The line with triangles is the simulation of the cycle between -160 °C, 500 °C and room temperature calculated with this starting value: $T = 113$ K, $\sigma = 595$ MPa.

As in section 6.4.4, the model fails to predict the stress level reached at the onset of plasticity since other diffusional processes, which obviously play a role in deformation in this temperature regime, are not considered. However, despite this weakness, it gives a good estimate of the stress evolution at low temperatures, where diffusional processes are shut off. Both the slopes and the stress values are reproduced well. Also the reproducibility of the cycles after the cryogenic excursion is shown.

The cooling behavior of the films thinner than 100 nm is completely different than that of the thicker samples. The thinner films deform purely elastically across the entire temperature range tested. The further extension of the thermal strain through cooling to -160 °C was insufficient to induce plastic deformation in these films.

Size effects as a function of temperature

For films thicker than 100 nm, the flow stresses determined at -100 °C or at -150 °C depend strongly on the film thickness with thinner films exhibiting higher stresses. An analysis of the exponential dependency of the stress on the film thickness yields a power-law exponent of 0.6. This value does not change significantly with the temperature at which the stress is considered. Arguments accounting for the size effects in this regime were already discussed earlier in section 6.4.7.

The stress plateau, which appears if the stress is plotted vs. the inverse film thickness, is of greater interest. A stress plateau for films thinner than 100 nm is found not only at 50 °C, but also at -100 °C and -150 °C. This size independent behavior is explained by the purely linear elastic deformation of the thinnest films over the entire temperature range measured. This interpretation is supported by the calculation of the expected stress increase during the cryogenic experiment considering a purely thermoelastic behavior, given by Equations (6.1) and (6.2). The predicted stress increase between 50 °C and -150 °C of 560 MPa is very similar to that measured (500 MPa). The stresses at -150 °C of about 1.7 GPa measured in this dissertation are the highest ever reported for Cu thin films. However, they lie below the theoretical strength of Cu of 5.2 GPa. These results are supported by a recent *in-situ* XRD study of Al thin films between -100 and 350 °C[171]. Eiper *et al.* also found a stress plateau for films thinner than 400 nm, independent of the temperature at which the stress was measured.

The results of the cryogenic experiments carried out in this dissertation definitively prove that the stress plateau results from the elastic behavior of the ultra-thin passivated films, since all possible deformation mechanisms are suppressed. The strain applied with both the wafer curvature method and the X-ray cooling setup is insufficient to induce plastic deformation in films thinner than 100 nm. This work clearly shows the limitations of the standard methods relying on thermal loading of the films.

Microtensile testing is a powerful method capable of inducing much larger strains in thin films. Recently, Gruber also studied size effects in passivated Cu films[172]. In his work, Cu was deposited onto a thin polyimide foil, previously coated with a thin Ta layer, and passivated with Ta. The stress was shown to depend overall linearly on the inverse film thickness with two different slopes: the dependency which is strong for films thicker than 100 nm becomes very weak for the ultra-thin films. For the 20 nm thick film – the thinnest measured – plastic yielding started at a strain of about 1.5% under a stress of about 1.3 GPa. At higher strains, cracks appeared in the films. For comparison, the maximum strain induced in the low temperature substrate curvature experiments carried out in this dissertation is 0.9%.

Finally, the cooling experiments not only elucidate the origin of the stress plateau for passivated Cu films but also shed new light on the origin of the stress plateau for unpassivated Cu films. The shape of the stress-temperature curve for the 100 nm thick unpassivated film reveals its deformation behavior. Above approximately 200 °C, during both heating and cooling, the film yields by diffusional creep. Cooling below about 250 °C reveals a slope change and the onset of a linear segment with a slope consistent with the thermoelastic slope of Cu. That this behavior continues until -100 °C indicates that there are no active deformation mechanisms in this temperature range. Thus, the room temperature stress is not a flow stress. This suggests that the room temperature stress plateau for unpassivated films is due to the fact that the maximum stress applied to the samples using thermomechanical loading was insufficient to activate low temperature plasticity mechanisms. Thus, the lack of size effect in ultra-thin unpassivated films supposedly originates from stress relaxation at high temperatures through constrained diffusional creep. Dislocation plasticity, and most especially the parallel glide dislocation mechanism, may not contribute to the stress

plateau but just be active as a result of diffusional creep. It remains however unclear why the amount of stress relaxed at high temperatures would be the same for all the ultra-thin films. One could speculate that this is due to the constant grain size to film thickness ratio of the films. Until now, most studies assume that the room temperature stress is equivalent to the yield stress. This work demonstrates that this is not a valid assumption for ultra-thin films.

8.5 Summary

The mechanical behavior of passivated Cu thin films was characterized at low temperatures. The main advances of this study can be summarized in following points.

- For the first time, the stress evolution of thin films could be monitored *in-situ* down to a temperature of -160 °C with the substrate curvature method thanks to a specifically designed setup. X-ray diffraction stress measurements down to -100 °C yielded very similar results, which supports the validity of this data.
- The dominant low temperature deformation mechanism of thicker films is dislocation plasticity. A maximum stress of about 600 MPa was measured in a 600 nm thick film.
- The stress plateau reported for the passivated Cu films thinner than 100 nm is due to the limitation in the applied strain of the measurement methods. These ultra-thin films deformed purely elastically between -160 °C and 500 °C, which corresponds to a total strain of about 0.9%.
- A stress value of 1.7 GPa measured at -150 °C in films thinner than 100 nm is the highest ever reported for thin films. However, it remains far below the theoretical strength of Cu and a lower limit for the actual flow stress.

- A 100 nm thick unpassivated Cu film was shown to deform purely elastically below 200 °C, shedding new light on the origin of the plateau for unpassivated Cu films.

- These observations reveal the limitations of measurement techniques based on thermal straining for flow stress determination.

CHAPTER 9

SUMMARY AND CONCLUSIONS

The effect of a passivation layer on the thermomechanical behavior of Cu thin films was examined in this dissertation. A literature review revealed experimental and theoretical evidence for dislocation plasticity and surface diffusion as controlling mechanisms for thin film deformation. However, their respective contribution to thin film plasticity as a function of film thickness is not yet well understood. Passivated Cu films, for which surface diffusion is suppressed, thus provide an ideal system to investigate the role of diffusion in thin film deformation. Moreover, as shown in a study of Balk *et al.*, a creep mechanism relying on surface diffusion, named constrained diffusional creep, was purported to account for the formation of a new type of dislocations that glide parallel to the film/substrate interface in Cu films thinner than 400 nm, the so-called parallel glide dislocations. The presence of these dislocations in unpassivated ultra-thin Cu films was used to explain a film-thickness independent stress plateau. In this context, this study of

passivated films provides the chance to clarify the interplay among the experimental observation of a stress plateau for ultra-thin films, TEM observations of parallel glide dislocations, and the theory of constrained diffusional creep.

This work provides the first extensive study of passivated films covering a broad film thickness range that includes ultra-thin films. Specifically, Cu films with thicknesses varying between 25 nm and 2 μm were magnetron-sputtered onto Si_xN_y-coated (111)-oriented Si wafers and passivated with either 10 nm Al_xO_y or Si_xN_y following different heat treatments:

1) Cu films were passivated directly after deposition (type CuSiN/RR),
2) Cu films were annealed and passivated at 500 °C (type CuSiN/AA) or
3) Cu films were annealed at 500 °C and passivated at room temperature (types CuSiN/AR and CuAlO).

After thermal cycling, the microstructure of the Cu films was similar for all types with a strong (111) texture and grain sizes about twice the film thickness. Hillocks were observed in the CuSiN/AA films thinner than 200 nm, whereas the films of type CuSiN/AR from batch 1 had pores and grain boundary grooves. Although the Al_xO_y layer coalesced into particles spread on the surface, a thin continuous passivation layer was confirmed to cover the Cu surface by TEM. With the exception of the CuSiN/AR samples from batch 1, a continuous Si_xN_y passivation layer covered the Cu films.

The thermomechanical behavior of these films was characterized using the substrate curvature method. The nature of the passivation layer and the processing parameters had no significant influence on the stress-temperature behavior of the films. The film thickness is critical, however, as films behaved completely differently depending upon their thickness.

Films in the micrometer and sub-micrometer regime exhibited elastic-plastic deformation, which was simulated by thermally activated dislocation glide. Films thinner than 100 nm deformed purely elastically between -160 °C and 500 °C. In this temperature range, the thermal strain reached 0.9%, which is much larger than the typically observed yield strain for bulk Cu. The passivation layer suppressed

constrained diffusional creep at high temperatures and thereby prevented stress relaxation. The absence of plasticity in the ultra-thin films suggests that diffusional creep is the only deformation mechanism available in this thickness regime. This can be explained by the fact that, as grain size and film thickness decrease, diffusion paths become shorter, dislocation nucleation harder, and the percentage of grain boundary area increases. As expected, films with intermediate thicknesses appear to be significantly affected by both dislocation plasticity and diffusional creep.

In addition, the presence of hillocks and pores was shown to complicate the study of strengthening mechanisms in thin films. They indeed weakened the passivation layer and enabled diffusional stress relaxation.

Size effects were investigated by plotting the stress at room temperature as a function of the inverse film thickness. Two regimes were distinguished: a linear increase with decreasing film thickness for films thicker than 100 nm and a stress plateau at 1.2 GPa for films less than 100 nm thick. The size effect in the sub-micrometer regime is thought to have its origin in the increased difficulty of dislocation nucleation with decreasing film thickness. The magnitude of the stress plateau, whose origin was explained by the presence of parallel glide dislocations in unpassivated films, was higher for passivated films. Although parallel glide dislocations were surprisingly observed for the first time in the passivated films, they were immobile upon thermal cycling, probably due to the suppression of diffusional flow at the film surface. The stress plateau therefore appears to be a consequence of the elastic deformation of the ultra-thin films: the applied thermal strain was insufficient to induce plastic deformation. Thus, this work identified the limitations of the substrate curvature method for the thermomechanical analysis of ultra-thin films. Stress values up to 1.7 GPa measured for these ultra-thin films – the highest ever reported – still lie well below the theoretical strength of Cu.

These revelations also bring us to reconsider the explanations which currently account for the plateau in unpassivated films. Ultra-thin unpassivated films indeed also behave purely elastically at lower temperatures. The stress plateau may therefore be a measurement artifact as well, due to limitations in applied strain.

Finally, the findings of this study are relevant from a technological point of view. Indeed, this work shows that passivated ultra-thin films, which will continue to be used as metal interconnects in the coming years, undergo no plastic deformation over a broad temperature range and can sustain huge stresses that stagnate with decreasing film thickness under the normal operating temperature range.

CHAPTER 10

APPENDIX

10.1 List of the literature data plotted in the masterplot

Table 10.1: Values of the flow stress, σ_y, of Ag thin films for different film thicknesses, h_f, and grain sizes, d.

Name	Preparation conditions	Measurement conditions	h_f [µm]	d [µm]	σ_y [MPa]	Ref.
Ag96 Thouless	E-beam evaporated Ag films on oxidized Si(100) previously coated with 10 nm Cr adhesion layer.	Substrate curvature; obtained at ~ 20 °C after cooling from 400 °C; values read from plot.	1		~ 140	46
Ag96P Thouless	Same as above but coated with 10 nm Cr and passivated with 100 nm thick SiO_x.		1		~ 190	46
Ag98 Kobrinsky	UHV e-beam deposited Ag films on oxidized Si(100).	Substrate curvature; data obtained at 23 °C after cooling from 500 °C; values read from plots.	0.21		~ 145	73
			0.24		~ 140	
			0.25		~ 142	
			0.37		~ 180	
			0.47		~ 205	
			0.49		~ 225	
			0.60		~ 250	
			0.72		~ 220	
			0.84		~ 165	
			0.97		~ 160	
			1.21		~ 140	
Ag98P Kobrinsky	Same as above, but passivated with 50-70 nm thick SiO_x layer.		0.21		~ 430	73
			0.35		~ 340	
			0.47		~ 295	
			1.21		~ 185	
Ag00F Huang	E-beam deposited free-standing thin film of 99.99% pure Ag with strong (111) texture.	Microtensile test at ~ 20 °C at strain rate of $1.1 \cdot 10^{-5}$ s^{-1}; 0.2% offset yield strength; values read from plot.	5.8		~ 270	92
Ag03 Schwaiger	Pure Ag films magnetron-sputtered in UHV on micromachined SiO_2 cantilever beams 2.83 µm thick.	Microbeam deflection tests at ~ 20 °C with a nanoindenter tip; exact values.	0.2	0.92	300	80
			0.4	0.93	290	
			0.6	0.84	270	
			0.8	0.91	250	
			1.0	0.98	210	
			1.5	1.01	155	

Table 10.2: Values of the flow stress, σ_y, of Al thin films for different film thicknesses, h_f, and grain sizes, d.

Name	Preparation conditions	Measurement conditions	h_f [µm]	d [µm]	σ_y [MPa]	Ref.
Al86 Doerner	Magnetron-sputtered 99.999% pure Al films on SiO_x-coated Si(100).	Substrate curvature; data obtained at room temperature after cooling from 450 °C; values taken from [83].	0.21	0.3	393	82,83
			0.26	-	344	
			0.42	-	323	
			0.59	-	266	
			1.09	1.4	181	
Al89 Korhonen	E-beam deposited Al films on oxidized Si(100).	X-ray diffraction; residual stress after annealing 1 hour at 450 °C; rounded values.	0.25		~ 138	84
			0.47		~ 142	
			0.8		~ 143	
			1.05		~ 126	
Al90 Venkatraman	Sputtered Al-0.5% Cu films on oxidized Si(100).	Substrate curvature; data obtained at 50 °C after cooling from 450 °C; grain size given after annealing; values read from plots.	0.5	0.55	~ 350	85
			1	0.4	~ 260	
Al91 Paszkiet	E-beam evaporated Al films on oxidized Si(100).	X-ray diffraction; stress after annealing; values read from plot.	0.33		~ 340	81
			0.53		~ 170	
Al91P Paszkiet	Same as above but passivated with 0.3 µm Si_xN_y.		0.33		~ 500	81
			0.53		~ 380	
Al92 Venkatraman	Pure Al films on oxidized Si(100); successive etching of film to vary h_f with a constant d.	Substrate curvature; data gathered at 60 °C after cooling from 460 °C; values taken from [83].	0.48	>10	170	17,83
			0.65		124	
			1.04		79	
			1.5		50	
			0.25	1.9	363	
			0.55		188	
			0.96		117	
			1.03-1.52		130-134	
			0.08	0.9	533	
			0.48		272	
			0.68		224	
			0.90		189-196	

Al96 Thouless	Magnetron sputtered 99.999% pure Al films on oxidized Si(100).	Substrate curvature; obtained at ~ 20 °C after cooling from 400-550 °C; values read from plot.	0.5		~ 200	46
			1		~ 150	
Al96P Thouless	Same as above but passivated with 100 nm thick SiO_x.		0.5		~ 200	46
Al97 Jawarani	Sputtered Al-1 wt %Cu on Si coated with 0.6 µm boro-phospho-silicate glass.	Substrate curvature; data at room temperature after cooling from 400 °C; values read from plot.	0.6	1.8	~ 280	78
Al97P Jawarani	Same as above with 0.4 µm phospho-silicate-glass and 0.7 µm Si_3N_4 as passivation.		0.6	5.8	~ 210	78
Al99 Macionczyk	Magnetron sputtered Al-0.5 wt % Cu film on 13 µm thick polyimide.	Microtensile test; plastic strain ~ 0.2%; values taken from [83].	0.2	0.14	529	83,86
			0.5	0.2	457	
			0.9-1.1	0.3	450	
			1.6-1.7	0.5	354-373	
Al01E Dehm	Epitaxial Al films magnetron sputtered in UHV on (0001) α-Al_2O_3.	Substrate curvature; measured at 40 °C at the end of the first cycle after cooling from 400 °C; exact values.	0.2		220	20-22
			0.35		150	
			0.6		120	
			1		109	
			2		60	
Al01 Dehm	(111) textured Al films magnetron sputtered in UHV on oxidized Si(001).	Same as above.	0.1		375	21,22, 87
			0.2		350	
			0.4		360	
			0.6		300	
			1		217	
			2		123	
Al03F Son	Magnetron-sputtered free-standing Al beams with a width of 20 µm.	Microcantilever-beam test; exact values.	0.51	0.89	200	93
			1.03	1.03	136	
			1.50	1.18	114	
Al04F Espinosa	E-beam evaporated free-standing Al films; membrane width varies between 5 and 20 µm.	Membrane deflection; obtained from stress-strain curves; exact values.	0.2		375*	95
			1		150-205	

*: failure stress

Table 10.3: Values of the flow stress, σ_y, of Au thin films for different film thicknesses, h_f, and grain sizes, d.

Name	Preparation conditions	Measurement conditions	h_f [µm]	d [µm]	σ_y [MPa]	Ref.
Au00 Leung	E-beam evaporated Au films on nitride-coated Si(100) with a 10 nm W or Ti adhesion layer.	Substrate curvature; data obtained at room temperature after cooling from 600 °C; values read from plot.	0.1		~ 280-340	75,76
			0.2		~ 250-300	
			0.35		~ 340	
			0.45		~ 330	
			0.5		~ 380	
			0.58		~ 285	
			0.8		~ 230	
			1.025		~ 190	
			1.74		~ 115	
			1.8		~ 120	
			2		~ 95	
			2.53		~ 100	
Au00P Leung1	Same films as above with a 50 nm thick Si_3N_4 passivation.		0.5		~ 500	75
			0.75		~ 140	
Au00P Leung2	Same films as above with a 10 nm thick W passivation.		0.5		~ 540	74
			1		~ 270	
			2.5		~ 90	
Au00P Leung3	Same films as above with either a 10 nm thick W or Ti passivation or a 50 nm thick Si_3N_4 passivation.		0.2		~ 640	76
			0.5		~ 480	
			1		~ 260	
			2.5		~ 80	
Au02F Espinosa	E-beam evaporated free-standing Au films fabricated on Si(100) membranes; membrane width varies between 2.5 and 20 µm.	Membrane deflection; obtained from stress-strain curves; exact values.	0.3		170-220	95,97-99
			0.5		140-220	
			1.0		55-90	
Au02FP Espinosa	Same as above with a SiO_2 passivation on both sides of the free-standing film.		0.5		52-140	98
Au03F Son	Magnetron-sputtered free-standing Au beams with a width of 20 µm.	Microcantilever-beam test; exact values.	0.56	0.09	391	93
			0.99	0.16	310	
			1.26	1.61	115	

Au03F Emery1	E-beam or thermal evaporated free-standing Au films; coarse grained; films as deposited.	Microtensile test; yield stress was defined as the stress at which the slope of the stress-strain curve is reduced to a value of $E_{Au}/10$; exact values.	0.8	1.59	340	100
			1.6	1.61	239	
			1.9	1.73	271	
			2.0	2.04	239	
			2.1	2.69	212	
Au03F Emery2	Same as above but annealed 1 min at 800 °C.		1.6	2.05	142	100
			1.6	28.4	42	
			1.9	1.99	199	
			2.0	2.65	130	
			2.1	4.21	89	
			2.1	25.81	36	
Au03F Emery3	Same as above but fine-grained as deposited.	Strain rate varies between $1 \cdot 10^{-6}$ and $6 \cdot 10^{-4}$ s^{-1}.	0.23	0.205	236-455	103
			0.25	0.245	273-390	
			0.25	0.550	384	
			0.7	0.320	254-474	
			0.8	0.360	426	
			2.1	0.400	230-434	
Au06 Sauter1	Au films UHV magnetron-sputtered at room temperature on oxide and nitride-coated (100) Si; fine grained columnar films.	Substrate curvature; data obtained at 50 °C after cooling from 500 °C; exact values.	0.057	~1.2 h_f	521	88
			0.057		501	
			0.096		375	
			0.121		441	
			0.121		455	
Au06 Sauter2	Same films as above but non columnar.		0.173	width: 98 to 181 nm; height: 105 to 300 nm	504	88
			0.226		397	
			0.265		464	
			0.458		442	
			0.469		381	
			0.552		331	
			0.640		410	
			0.676		302	
			0.870		411	
			0.893		384	
			1.154		390	
			1.738		337	

Au06 Sauter3	Same films as above but sputtered at 300 °C; coarse grained and columnar.		0.185	~1.2 h_f	299	[88]
			0.258		335	
			0.354		256	
			0.430		371	
			0.536		276	
			0.688		281	
			0.847		303	

Table 10.4: Values of the flow stress, σ_y, of Cu thin films for different film thicknesses, h_f, and grain sizes, d.

Name	Preparation conditions	Measurement conditions	h_f [µm]	d [µm]	σ_y [MPa]	Ref.
Cu91 Flinn	Sputtered Cu films on SiO_x-coated Si.	Substrate curvature; obtained at ~ 20 °C after cooling from 600 °C; values read from plot.	1		~ 420	90
Cu93 Thouless	Magnetron sputtered Cu films on oxidized Si(100).	Substrate curvature; obtained at ~ 20 °C after cooling from 450 °C; values read from plot.	1		~ 270	44
Cu93 Vinci	Magnetron sputtered Cu films on oxidized Si(100) with barrier layers of 50 nm thick W, Ta, TiN or Si_xN_y.	Substrate curvature; data obtained at room temperature after cooling from 460 °C; values read from plot.	0.8		~ 350-380	62
Cu93P Vinci	Same as above passivated with 10 nm thick Al over 10 nm Ta.		0.8		~ 320	62
Cu95 Vinci	Magnetron sputtered Cu films on oxidized Si(100), with a Ta barrier layer.	X-ray diffraction; data obtained at room temperature after cooling from 400 °C; values read from plot.	0.2 0.4 0.8 1.2		~ 600 ~ 450 ~ 360 ~ 340	45
Cu95P Vinci	Same as above with a 200 nm thick Si_3N_4 passivation.		0.4 1.2		~ 400 ~ 300	45
Cu96 Thouless	E-beam evaporated Cu films on oxidized Si(100) previously coated with 10 nm Cr adhesion layer.	Substrate curvature; obtained at ~ 20 °C after cooling from 400-550 °C; values read from plot.	1		~ 240	46
Cu96P Thouless	Same as above but coated with 10 nm Cr and passivated with 100 nm thick SiO_x.		1		~ 270-300	46
Cu98P Shen	E-beam deposited Cu films on SiO_2, passivated with SiO_x, whose thickness is 20% of the Cu thickness. 10 nm Cr interlayer.	Substrate curvature; obtained at room temperature after cooling from 450 °C; values read from plot.	0.04 0.4		~ 800 ~ 600	66

Cu03P Shen1	Same as above with 15 nm Cr interlayer.		0.125		~ 950	[68,69]
			0.25		~ 790	
			0.4		~ 690	
Cu03P Shen2	Sputtered Cu films on oxidized Si substrates, passivated with 50 nm SiO_x. 50 nm W interlayer.		1		~ 300	[68,69]
Cu98 Keller	Magnetron-sputtered Cu films on SiO_x- and Si_xN_y-coated Si substrates.	Substrate curvature; obtained at room temperature after cooling from 600 °C; exact values.	0.6	1.02	410	[18,47]
			1.0	1.31	280	
Cu98P Keller	Same as above, but with 50 nm Si_3N_4 passivation.		0.45	0.35	745	[18]
			0.60	0.83	585	
			1.0	1.3	455	
Cu99 Hommel	Cu films sputtered on 125 µm thick polyimide at ~ 20 °C; without or with a 50 nm thick Si_3N_4 or a 3 µm thick polyimide interlayer; annealed or not.	Microtensile tests; flow stress at 0.5% plastic strain; values read from plot.	0.4		~ 370-480	[89]
			0.5		~ 470	
			0.6		~ 430	
			0.7		~ 410	
			1.0		~ 260-480	
			1.5		~ 400	
			3.15		~ 200	
			5.0		189	
Cu99P Hommel	Same as above passivated with 50 nm Si_3N_4.	Flow stress at 0.1% plastic strain; exact values.	0.4		411	[89]
			1.0		426	
			5.0		139-171	
Cu01 Hommel1	Same as above; (111) texture component.	Same as above; exact values taken from [83].	1.0	0.18	481	[83,91]
				0.6	320-355	
				1.0	268-306	
				1.2	268	
Cu01 Hommel2	Same as above; (100) texture component.		1.0	0.6	166-178	[83,91]
				1.0	137	
				1.2	76	
Cu00F Huang	Free-standing thin film of 99.99% pure Cu with strong (111) texture.	Microtensile test at ~ 20 °C at strain rate of $1.1 \cdot 10^{-5}$ s^{-1}; 0.2% offset yield strength; values read from plot.	4.3		~ 300	[92]
Cu00 Weihnacht	Magnetron sputtered Cu films on oxidized Si.	Substrate curvature; data obtained at room temperature after cooling from 500 °C; values read from plot.	0.53		~ 330	[94]
			1.03		~ 250	

Cu00 Spolenak1	1.8 µm thick electroplated Cu film on Si previously coated with a 500 nm thick TEOS film, a 50 nm thick Ta diffusion barrier, and a 50 nm thick sputtered Cu seed; film thinned down by CMP.	Substrate curvature; stress obtained at 30 °C after cooling from 400 °C; values read from plot.	0.19 0.25 0.56 1.01 1.35 1.45 1.74		~ 550 ~ 380 ~ 360 ~ 280 ~ 190 ~ 220 ~ 160	96
Cu00 Spolenak2	1.8 µm thick sputtered Cu film on Si previously coated with 180 nm Si_xN_y and 50 nm Ta; film thinned down by CMP.	Same as above.	0.15 0.56 0.82 1.39 1.62		~ 1436 ~ 500 ~ 375 ~ 270 ~ 260-310	96
Cu00 Weiss	UHV magnetron sputtered Cu films on SiO_x- and Si_xN_y-coated Si(100).	Substrate curvature; data at 40 °C after cooling from 500 °C; values read from plot.	0.3 0.5 1 2	 1.4 2.4-2.5 3.7	~ 540 ~ 450 ~ 260-300 ~ 110	57,59
Cu00P Weiss	Cu-1% Al films UHV magnetron sputtered on SiO_x- and Si_xN_y-coated Si(100), annealed and oxidized between 400 and 600 °C.	Same as above.	0.5 1	 2.4	~ 540 ~ 250-310	57,59
Cu02P Shu	UHV magnetron sputtered Cu films on Si_xN_y-coated Si(100), passivated with 50 nm thick Si_xN_y.	Substrate curvature; data obtained at room temperature after cooling from 500 °C; values read from plot.	0.5		~ 500	71
Cu03P Shu	HV magnetron sputtered Cu films on Si_xN_y-coated Si(100), passivated with a 100 nm thick AlN_x layer.	Substrate curvature; data at room temperature after cooling from 400 °C; values read from plot.	0.6 0.75 1		~ 420 ~ 440 ~ 310-400	72
Cu02P Vinci	Magnetron sputtered Cu films on Si(100) coated with a 100 nm thick Si_3N_4 or a 50 nm thick Ta diffusion barrier, passivated with a 100 nm thick Si_3N_4 layer.	Substrate curvature; data obtained at room temperature after cooling from 400 °C; values read from plot.	1		~ 450	70

Cu03 Balk	UHV magnetron sputtered Cu films on SiO_x- and Si_xN_y-coated Si(100).	Substrate curvature; obtained at 40 °C after cooling from 500 °C; exact values.	0.0505		640	[25,56]
			0.1		633	
			0.2		637	
			0.257		659	
			0.452		535	
			0.598		431	
			0.719		399	
			0.983		320	
			1.943		157	
Cu04F Xiang	Electroplated free-standing Cu films deposited on nitride-coated Si(100) with a 20 nm thick TaN adhesion layer.	Bulge testing; flow stress at 0.35% residual strain; values read from plot.	0.98	Const d	~ 200	[104]
			1.9		~ 200	
			4.2		~ 180	
Cu04FP Xiang	Same as above with a 20 nm thick Ti passivation on one side.		0.98	Const d	~ 220	[104]
			1.9		~ 210	
			4.2		~ 180	
Cu04 Schmidt1	UHV magnetron-sputtered Cu films on Si(100) coated with SiO_x and Si_xN_y. 10 nm thick Ag interlayer.	Substrate curvature; data obtained at room temperature after cooling from 500 °C; exact values.	0.1		858	[101,102]
			0.2	0.6	859	
			0.3		711	
			0.4	0.96	592	
			0.6		426	
			1	1.87	358	
			2		238	
Cu04 Schmidt2	Same as above with 10 nm thick Ta interlayer.		0.1		860	[101,102]
			0.2	0.64	762	
			0.3		643	
			0.4	0.89	611	
			0.6		468	
			1	1.98	309	
			2		168	
Cu04E Edongué	Magnetron-sputtered or MBE-evaporated epitaxial Cu films on (0001) Al_2O_3.	Substrate curvature; obtained at 40 °C after cooling from 500 °C; exact values.	0.4		323-403	[23]
			0.5		350	
			0.6		167	
			0.7		256	
			0.8		257-292	
			1		134-245	
			2		111-121	

Cu04EP Edongué	Same as above but epitaxial co-sputtered Cu-1 at.% Al films.		0.3		343	23
			0.5		275	
			1		189	
Cu04 Edongué	Same as above but polycrystalline Cu films.		0.5		456	23
			0.6		433	
			1		245-289	
			2		172	
Cu04F Espinosa	E-beam evaporated free-standing Cu films prepared on Si(100); membrane width varies between 5 and 20 µm.	Membrane deflection; yield stress obtained from stress-strain curves; exact values.	0.2		345-380	95
			1		160	
Cu05F Onuseit	Free-standing Cu films	Bulge testing; yield stress taken at 0.05% strain; exact values.	0.08		462-547*	105
			0.092		364-626*	
			0.174		513-526*	
			0.179		376-405	
			0.244		420	
			0.251		391-402	
			0.288		347-348	
			0.300		341-343	
			0.352		344-348	
			0.356		332-340	
			0.394		313-321	
			0.398		300-320	
			0.43		319	
			0.433		319-323	
			0.801		249-252	
			0.831		243	
Cu06F Xiang1	Free-standing electroplated Cu films; as-deposited.	Bulge testing; yield stress at 0.2% offset strain; exact values.	0.9	1.82	295	106
			1.8	1.91	266	
			3.0	1.95	252	
Cu06F Xiang2	Same as above but annealed.		0.9	2.99	-	106
			1.8	3.00	161	
			3.0	6.13	120	
Cu06F Xiang3	Free-standing electroplated Cu films with constant microstructure obtained by thinning a 5.4 µm thick film by CMP.	Bulge testing; yield stress at 0.2% offset strain; exact values.	1.0	1.5	201	107
			1.9	1.51	200	
			4.2	1.5	176	

Cu06FP Xiang1	Same as above passivated with 20 nm Ti on both surfaces.		1.0	1.5	251	107
			1.9	1.51	213	
			4.2	1.5	182	
Cu06F Xiang4	Free-standing sputter-deposited Cu films with variable grain size.	Bulge testing; yield stress at 0.2% offset strain; exact values.	0.34	0.33	366	107
			0.44	0.39	347	
			0.61	0.54	300	
			0.67	0.46	266	
			0.89	0.46	250	
Cu06FP Xiang2	Same as above with one surface passivated with 80 nm Si_3N_4 and 20 nm Ta.		0.34	0.33	696	107
			0.44	0.39	612	
			0.61	0.54	435	
			0.67	0.46	374	
			0.89	0.46	336	
Cu06 Gan	Electroplated Cu films on Si(100) coated by a 100 nm thick SiO_x etch stop layer, 450 nm carbon-doped oxide and 18 nm TaN/Ta diffusion barrier.	Substrate curvature; data obtained at room temperature after cooling from 400 °C; values read from plot.	0.8		~ 310	4
Cu06P Gan	Same as above but passivated with either 100 nm SiN, SiC, or SiCN or with 10-20 nm Co followed by 100 nm SiN.		0.8		~ 400	4

*: fracture stress

Table 10.5: Values of the flow stress of nanocrystalline Cu as a function of the grain size.

Preparation conditions	Measurement conditions	d [µm]	σ_y [MPa]	Ref.
Nanocrystalline Cu; different preparation routes.	Different measurement techniques; values read from plot in a review paper.	0.011	230	[108]
		0.017	301	
		0.021	175	
		0.023	360	
		0.026	185	
		0.026	190	
		0.027	365	
		0.028	420	
		0.028	460	
		0.037	115	
		0.041	400	
		0.041	400	
		0.045	170	
		0.051	165	
		0.051	345	
		0.057	100	
		0.057	140	
		0.058	390	
		0.058	305	
		0.063	475	
		0.085	120	
		0.115	300	
		0.18	575	
		0.18	400	
		0.18	250	
		0.23	400	
		0.32	415	
		1.3	260	
		1.6	270	
		10.5	55	
		10.5	340	

Table 10.6: Values of the flow stress of Cu whiskers as a function of the whisker diameter.

Preparation conditions	Measurement conditions	d [µm]	σ_y [MPa]	Ref.
Cu whiskers.	Tensile test; values read from plot.	1.2	2960	[109]
		2.1	2205	
		2.1	1548	
		2.3	2078	
		2.7	2283	
		3.3	1333	
		3.35	1558	
		3.5	1421	
		4.8	892	
		5.1	1911	
		5.3	882	
		5.3	617	
		5.6	1000	
		6.3	921	
		6.5	833	
		6.5	1725	
		6.6	921	
		6.7	1137	
		6.8	1049	
		6.95	804	
		7.15	1519	
		7.15	598	
		7.7	510	
		8.1	1343	
		8.6	960	
		9.05	1098	
		10	794	
		10.5	323	
		10.55	441	
		10.65	1009	
		11.6	255	
		12.25	1147	
		15.35	402	

10.2 Correction of stresses measured with substrate curvature in passivated films

In the substrate curvature method, the film stress is calculated with Stoney's equation (Equation (4.1)), as described in 4.3.1. Among other parameters, it depends on the net substrate curvature, which corresponds to the difference of curvature between the bare substrate and the substrate coated with the thin film. In the case of multilayered films and most especially for the studied passivated films, the change in curvature due to the films deposited onto the substrate is due to both the Cu film and the passivation layer. Moreover, in Stoney's equation, the stress also depends on the total film thickness h_f, which includes in this study both the Cu film and the passivation layer thickness. Without any correction work, it is the stress of the system "Cu film and passivation layer" which would be measured. In order to determine the biaxial stress in the Cu film, σ_{Cu}, two different approaches are possible.

(1) The first approach consists to measure the stress-temperature evolution of a thin film composed solely of the pure passivation layer deposited onto a substrate, σ_p, and to subtract it from the total measured biaxial film stress, σ_f, considering the force equilibrium in the thin film structure:

$$\sigma_f h_f = \sigma_{Cu} h_{Cu} + \sigma_p h_p \qquad (10.1)$$

with h_f, h_{Cu} and h_p the known thicknesses of the entire film system, the Cu film and the passivation layer, respectively.

(2) The biaxial film stress in the passivation layer can also be balanced by depositing an identical layer on the back side of the substrate. With this method, no calculation is necessary and the wafer curvature measurement provides directly the value for the biaxial stress in the Cu film.

The last approach was privileged in this work for its simplicity, since it does not require any additional calculation. It is however necessary to discuss its validity. To do this,

both previously mentioned approaches are combined and compared. After measuring the total stress, σ_f, of a passivated film system and the stress in the pure passivation layer, σ_p, the stress in the Cu film, σ_{Cu}, can be calculated with Equation (10.1) and compared with the values obtained in a straight forward manner with a back side passivated sample.

Due to the experimental error inherent to a wafer curvature measurement, it was not possible to measure accurately enough the absolute stress values in pure 10 nm thick Al_xO_y and Si_xN_y films. Only the stress evolution with temperature could be recorded. It was therefore necessary to carry out the verification experiments on films with a thicker passivation layer. A precise measurement of the absolute stress in a 50 nm thick Si_xN_y film deposited at room temperature was realizable. This film was thermally cycled several times between room temperature and 500 °C. Figure 10.1 shows the stabilized biaxial stress evolution in this film, which exhibits a compressive stress of about -450 MPa and a weak temperature dependency. The stress-temperature data was fitted using a linear regression, whose equation is also given.

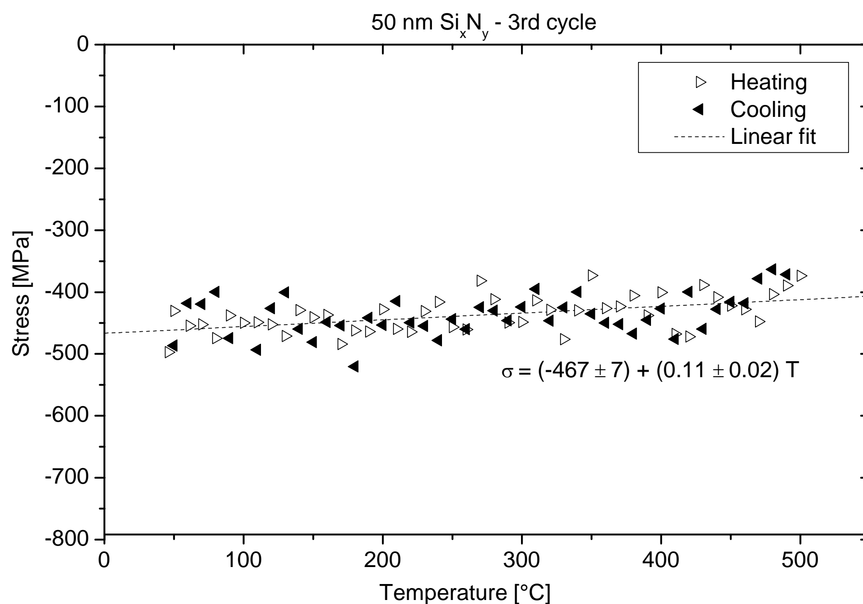

Figure 10.1: Stress-temperature evolution in a 50 nm thick Si_xN_y film. The biaxial stress data shown for the third cycle was fitted linearly. The function of the fitted line is used in Equation (10.1) to calculate the biaxial stress in the Cu film without the stress influence of the passivation layer.

In addition, the stress-temperature behavior of a 100 nm thick Cu film passivated with 50 nm Si_xN_y (type CuSiN/RR) without back side passivation was characterized. The stress-temperature curve obtained for this film system is shown in Figure 10.2 (open dots). The measured stress values – for the whole film system, σ_f – and the corresponding stress values for the pure passivation layer, σ_p – calculated with the linear regression equation of Figure 10.1 for all temperatures – were implemented into Equation (10.1) to determine the actual stress-temperature evolution within the 100 nm Cu film (black line in Figure 10.2).

Another 100 nm thick Cu film passivated with 50 nm Si_xN_y was prepared and additionally back side passivated with 50 nm Si_xN_y. The measured stress-temperature curve is also presented in Figure 10.2 (filled dots).

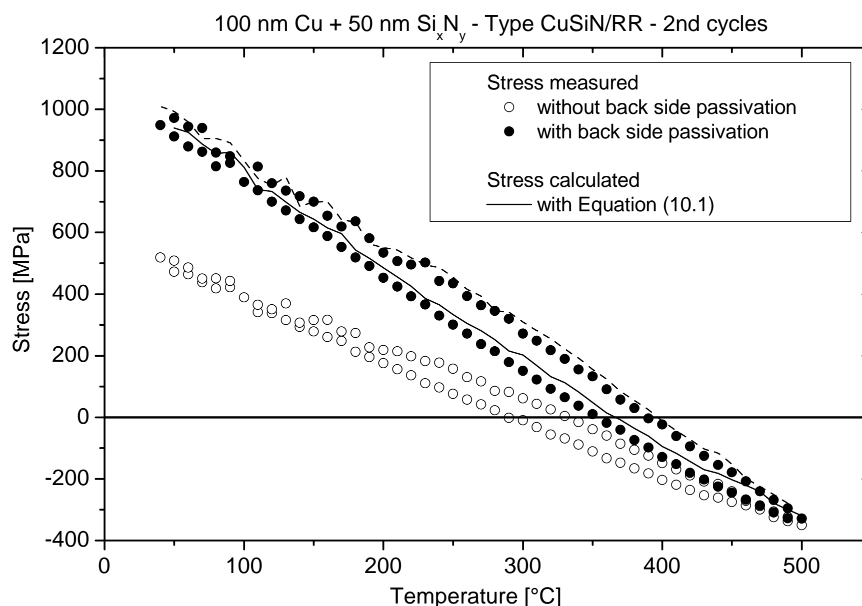

Figure 10.2: Stress-temperature curves of a 100 nm Cu film passivated with 50 nm Si_xN_y (type CuSiN/RR). Measured stress values for a sample without back side passivation (open dots) are compared with stress values for a sample with back side passivation (filled dots). The black line represents the stress calculated with Equation (10.1) out of the stress in the film without back side passivation (open dots) and the stress of the pure 50 nm Si_xN_y layer calculated with the linear regression equation in Figure 10.1.

Both correction methods yield very similar absolute stress values and evolutions with temperature. Although these experiments were achieved with a 50 nm thick passivation layer, it is believed that this correction method also works for a thinner passivation.

Considering the significant difference in slope and in room temperature stress between the uncorrected and the corrected measurements, it appears critical to correct the stress in the case of a 50 nm thick passivation layer. However, this effect is thought to be less important with a 10 nm thick passivation layer. To verify this hypothesis, the stress in a 100 nm Cu passivated with 10 nm Si_xN_y (type CuSiN/RR) was measured before and after passivating the back side of the substrate. The obtained results are presented in Figure 10.3.

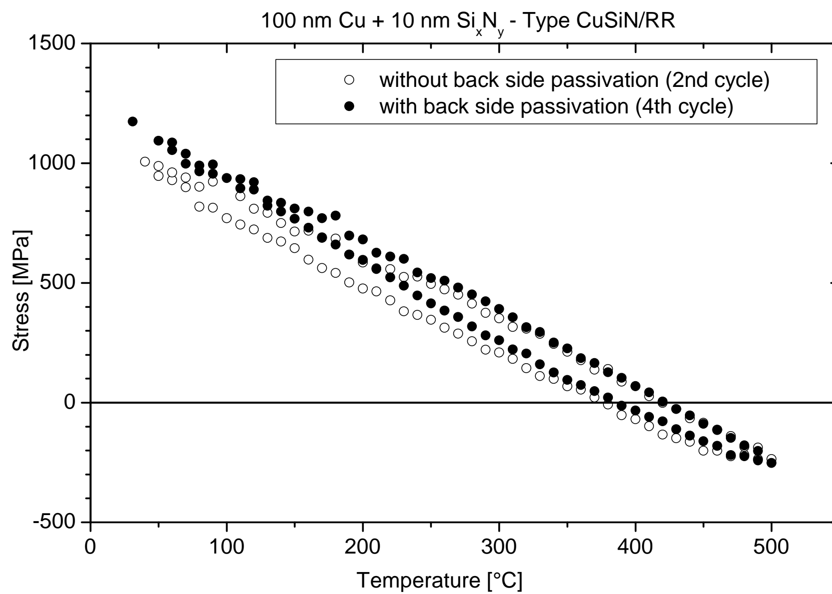

Figure 10.3: Stress-temperature cycles of a 100 nm thick Cu film passivated with 10 nm Si_xN_y (type CuSiN/RR) before (open dots) and after (filled dots) depositing the passivation layer on the back side of the substrate.

The stress at room temperature is about 100 MPa higher after correcting the stress with back side passivation. This difference is nevertheless not as big as for the films passivated with 50 nm Si_xN_y and lies within the measurement error.

Finally, from all these experiments, back side passivating the substrates appears to be a good and simple method to determine accurately the stress in the Cu film.

10.3 XPS analysis of the films

10.3.1 XPS spectra of a 10 nm thick Si_xN_y layer

A pure 10 nm thick Si_xN_y layer was analyzed with XPS. The spectra collected for the different detected elements are presented in Figure 10.4. The main detected elements are Si and N. The peak positions are characteristic of Si and N bound in Si_3N_4. A small peak of pure Si is also found, indicating that the Si may have not entirely reacted with N to form Si_3N_4. Traces of O likely bound to Si in SiO_2 are also visible.

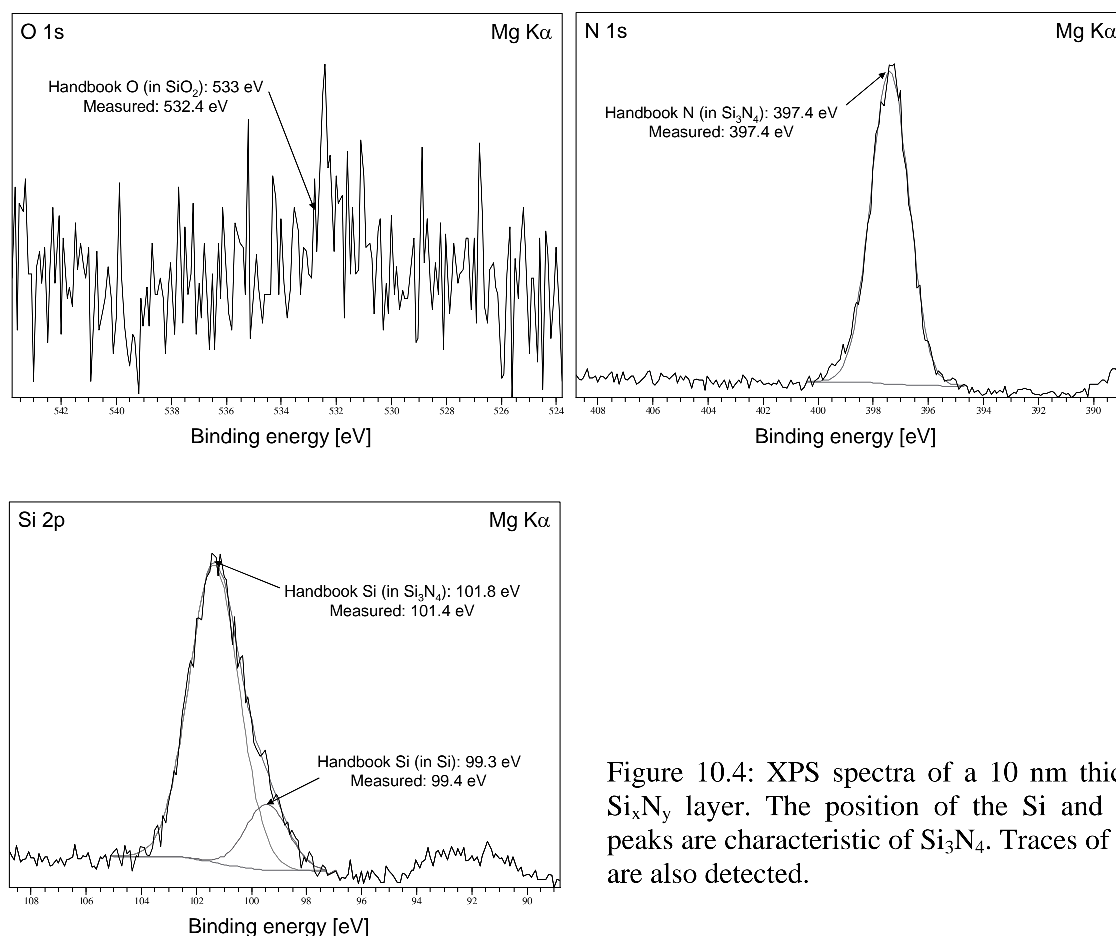

Figure 10.4: XPS spectra of a 10 nm thick Si_xN_y layer. The position of the Si and N peaks are characteristic of Si_3N_4. Traces of O are also detected.

10.3.2 XPS spectra of the 100 nm thick CuSiN/AR/B1 film

A XPS analysis of the 100 nm thick CuSiN/AR film from batch 1 was carried out. The overview spectrum is shown in Figure 5.13. The detailed spectra zooming on the different detected elements are presented in Figure 10.5.

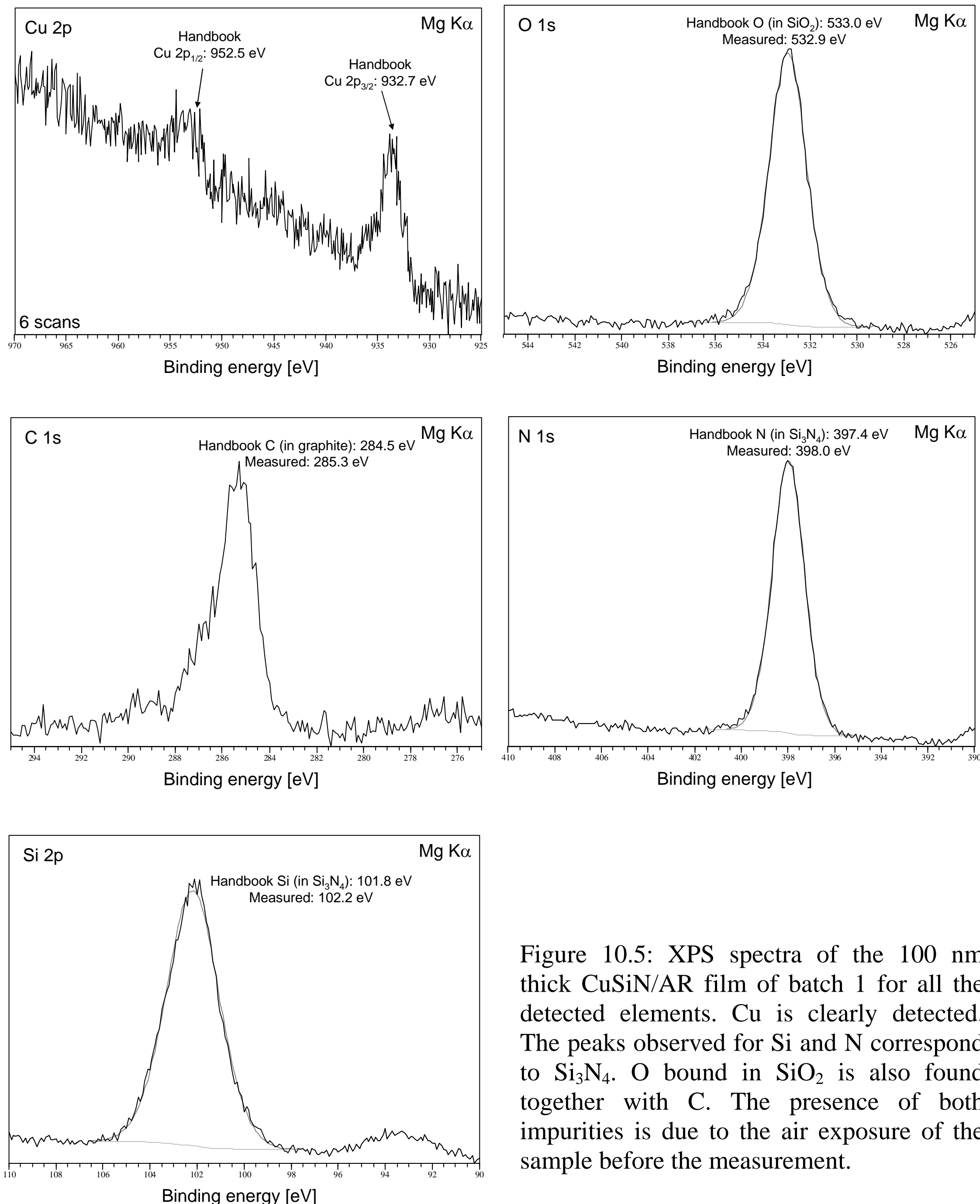

Figure 10.5: XPS spectra of the 100 nm thick CuSiN/AR film of batch 1 for all the detected elements. Cu is clearly detected. The peaks observed for Si and N correspond to Si_3N_4. O bound in SiO_2 is also found together with C. The presence of both impurities is due to the air exposure of the sample before the measurement.

Cu is clearly detected. Peaks corresponding to Si and N bound in Si_3N_4 are observed too. Both O (bound in SiO_2) and C are present due to the air exposure of the sample before the measurement.

10.3.3 XPS spectra of the 25 nm thick CuSiN/RR film

The detailed spectra of the 25 nm thick CuSiN/RR film before (1) and after (2) depositing a 10 nm thick Si_xN_y layer are presented in Figure 10.6. The overview spectrum is shown in Figure 5.22. Before passivation, only Cu peaks are visible. After passivation, these peaks are no longer observed. Only Si and N bound in Si_3N_4 is detected. There are no traces of O or C.

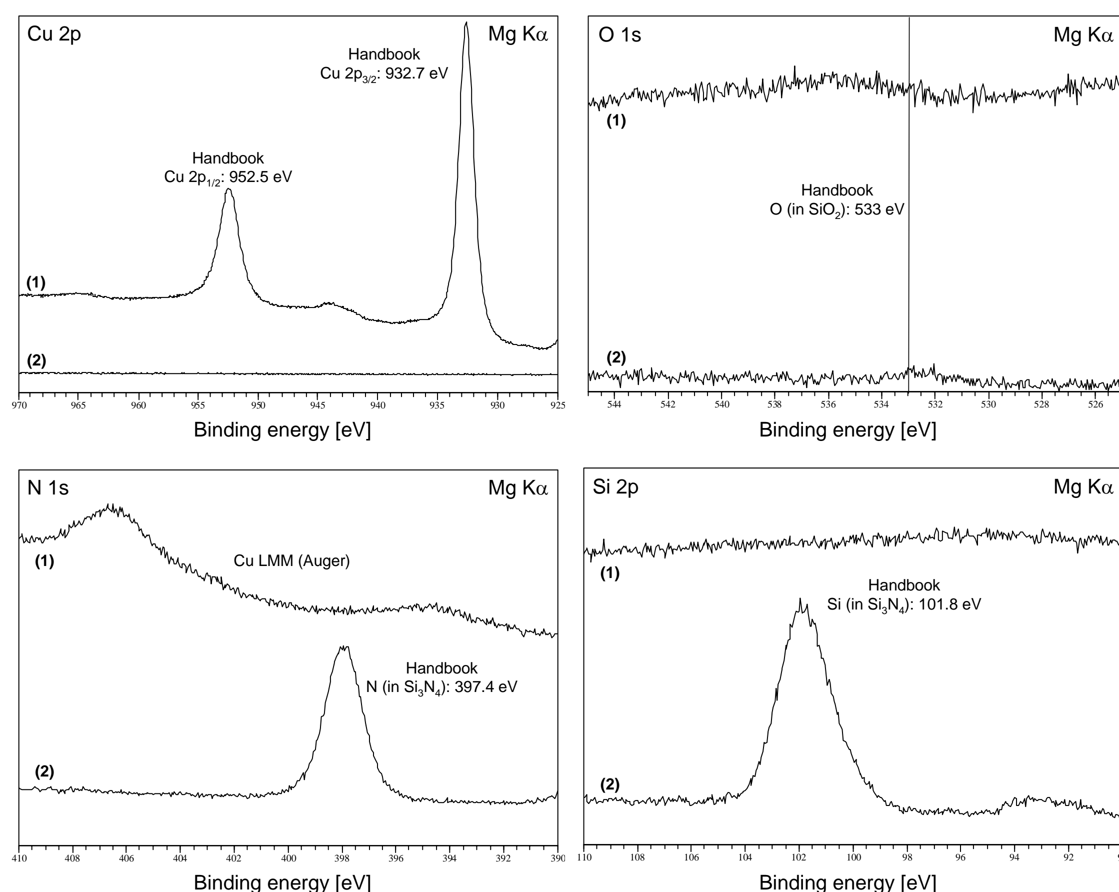

Figure 10.6: Detailed XPS spectra of the 25 nm thick CuSiN/RR film, shown for different peaks, before (1) and after (2) depositing a 10 nm thick Si_xN_y layer on the Cu film. The Cu peaks visible before passivation are no longer visible afterwards. Then, only Si and N peaks are detected. No O or C is detected.

10.4 Plotted stress values

Table 10.7: Stress of the passivated films in this study given at 50 °C, -100 °C and -150 °C as a function of film thickness, h_f, for the different batches. The stress value is taken after cooling from 500 °C and averaged over all the cycles.

Film type	h_f [nm]	Stress at 50 °C		Stress at -100 °C		Stress at -150 °C	
		B1	B2	B1	B2	B1	B2
CuAlO	25	1146					
	40	1263					
	50	1239					
	100	1279					
	200	741					
	400						
	600						
	1000	310					
	2000	156					
CuSiN/AR	30		1248				
	50	754	1090				
	75		1242				
	100	898	1178			1348	
	200	739					
	600	495					
CuSiN/RR	25	1213		1518		1721	
	30		1146				
	50	1058		1455		1619	
	75		1134				
	100	1117	1060	1519		1758	
	200	795					
	600	436		556		581	
	2000	189					
CuSiN/AA	30		1211				
	50	1112	1189			1621	
	75		980				
	100	902	905			1351	
	200	850					
	600	486				589	

10.5 Code for the simulation of thermally activated dislocation glide

This section provides the reproduction of the Mathematica 5.0 code used for the simulation of a stress-temperature curve under the control of thermally activated dislocation glide.

```
(* simulation of stress-temperature curve with thermally activated dislocation glide *)

(* experimental parameters *)
Tstart = 313;              (* starting temperature of simulation *)
Tmax = 773;                (* ending temperature of simulation *)
Tref = 313;                (* boundary condition - initial temperature *)
sigref = 154*10^6          (* boundary condition - initial stress *)

(* used constants *)
M = 2.6*10^11;                (* biaxial modulus (111)-textured Cu *)
deltaalpha = 1.4*10^-5;       (* difference in CTEs *)
Tdot = 0.1;                   (* heating rate *)
s = 0.27;                     (* Schmid factor for (111) oriented grain *)
k = 1.38*10^-23;              (* Boltzmann constant *)

(* discrete obstacle-controlled plasticity after Frost and Ashby *)
epsdot0 = 1*10^6;
DeltaF = 3.5*10^-19;
taubar = 240*10^6;

(* solve differential equation, heating cycle *)
epsdot[sig_, T_]:= Sign[sig]*epsdot0*Exp[-DeltaF/(k*T)*(1-s*Abs[sig]/taubar)];
NDSolve[{sig'[T] ==-M*deltaalpha-1/Tdot*M*epsdot[sig[T], T], sig[Tref] == sigref}, sig, {T, Tstart,
Tmax}, Method == Automatic];
heatstress[T_]:= Evaluate[sig[T]/%];

(* solve differential equation, cooling cycle *)
epsdot[sig_, T_]:= epsdot0*Exp[-DeltaF/(k*T)*(1-s*sig/taubar)];
NDSolve[{-sig'[T] == M*deltaalpha-1/Tdot*M*epsdot[sig[T], T], sig[Tmax] ==
Part[heatstress[Tmax], 1]}, sig, {T, Tmax, Tstart}, Method == Automatic];
coolstress[T_]:= Evaluate[sig[T]/%];

(* plot cycle *)
Plot[ {heatstress[T], coolstress[T]}, {T, Tstart, Tmax}];

(* create table *)
Export["D:\Results\CuAl1mu", Table[{T-273, Part[heatstress[T], 1]/10^6, Part[coolstress[T],
1]/10^6},{T, Tstart, Tmax, 10}]];
```

10.6 Influence of the passivation layer thickness

The influence of the passivation layer thickness was studied by comparing the stress-temperature behavior of a 100 nm thick film passivated with either 10 nm or 50 nm Si_xN_y. The obtained curves are shown in Figure 10.7 for films of type CuSiN/RR (a) and CuSiN/AA (b). In these two examples, it is clearly visible that the shape and the stress values of the curves are identical, proving that the thickness of the passivation layer has no influence on the film deformation mechanism.

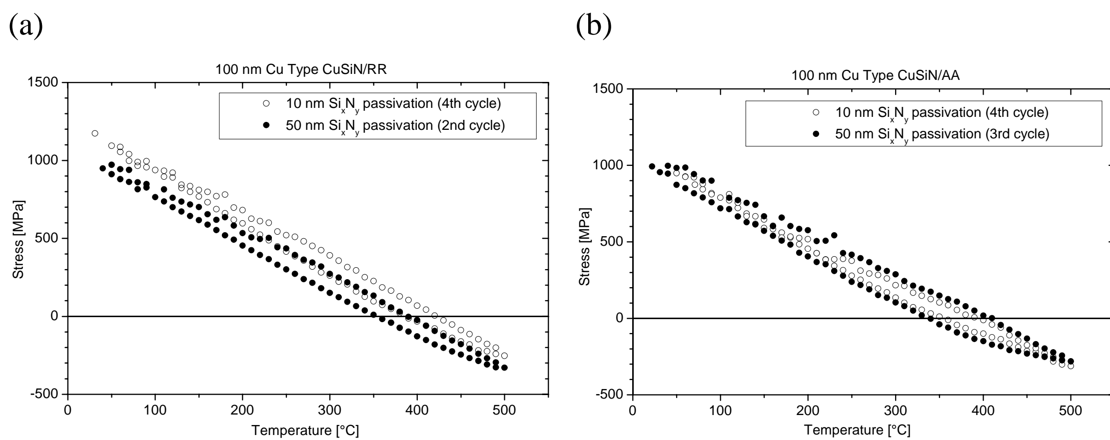

Figure 10.7: Influence of the passivation layer thickness on the mechanical behavior of a 100 nm thick film of type CuSiN/RR (a) and type CuSiN/AA (b). For each film, the stress-temperature curves of a film passivated with 10 nm Si_xN_y is compared with the curves of a film passivated with 50 nm Si_xN_y. All the films were back side passivated. The difference in absolute stress values between the two curves visible in (a) are due to an error in the measurement of the uncoated wafer (the “reference” measurement) with the wafer curvature method.

10.7 Stress-temperature curves reproducibility for films of different batches

In this section, the stabilized stress-temperature curves of films of type CuSiN/RR and CuSiN/AA with identical thicknesses and prepared in the two different batches B1 and B2 are shown (Figure 10.8). A comparison of both curves for each thickness clearly shows that the results are highly reproducible.

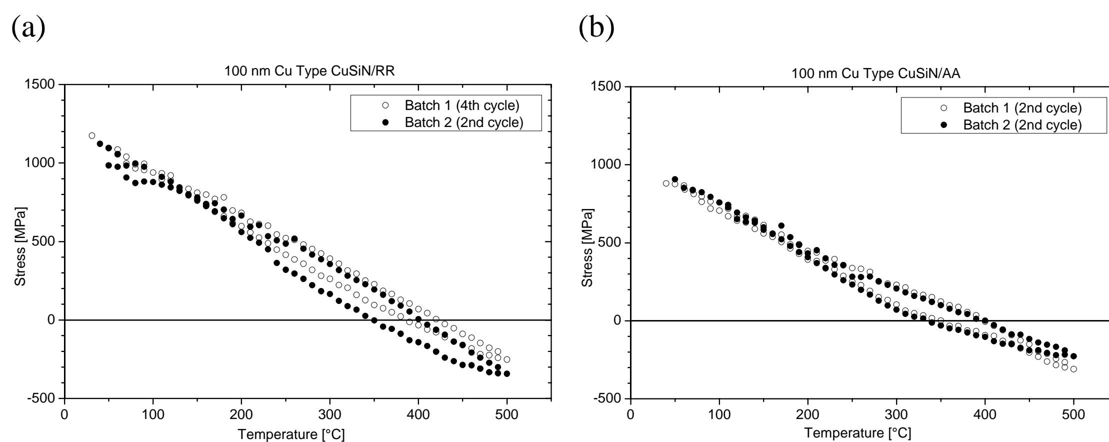

Figure 10.8: Batch 1 vs. batch 2 for a 100 nm thick film of type CuSiN/RR (a) and type CuSiN/AA (b). The stress-temperature behavior of the films is highly reproducible.

10.8 Contribution of this study to the field

The contribution of this study to thin film mechanics can be evaluated by plotting all the measured data together with the literature data collected in section 2.5 (Figure 10.9).

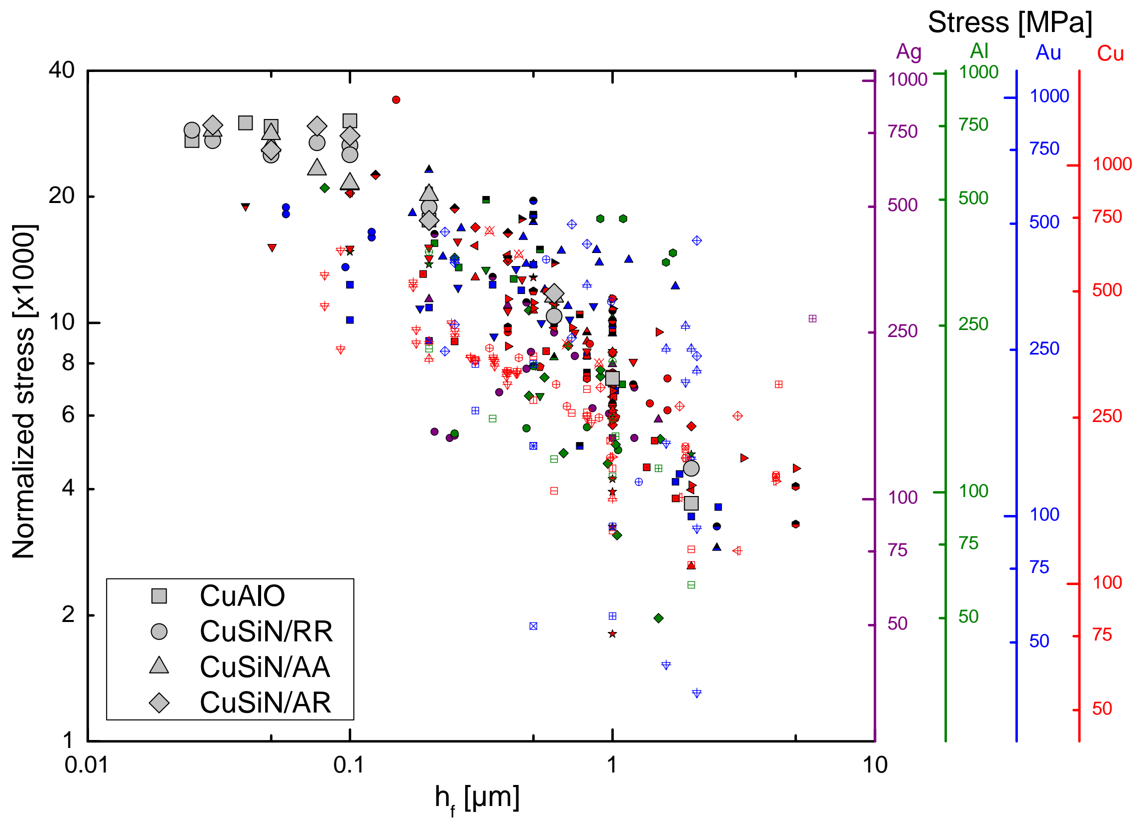

Figure 10.9: Data measured in this work for passivated films (large symbols) plotted together with literature data collected in the masterplot. The legend of the literature data is to be found in Figure 2.7.

CHAPTER 11

DEUTSCHE ZUSAMMENFASSUNG

11.1 Einleitung

Ein verbessertes Verständnis der mechanischen Eigenschaften von ultra-dünnen Metallschichten ist zwingend erforderlich, um die Leistung und Zuverlässigkeit von mikro-elektro-mechanischen Systemen (MEMS) und elektronischen Geräten gewährleisten zu können. Aufgrund der unterschiedlichen thermischen Ausdehnungskoeffizienten der einzelnen in diesen Geräten verwendeten Materialien können sehr hohe thermische Spannungen in den Metallschichten auftreten und somit zum Versagen führen. Aus Sicht der Grundlagenforschung ist die Untersuchung der Veränderungen der Materialeigenschaften durch die Geometrie der dünnen Schichten von besonderem Interesse. Insbesondere bewirken die sehr kleinen Dimensionen, dass

die Fließspannung von dünnen Metallschichten die des Massivmaterials um ein Vielfaches überschreitet und mit abnehmender Schichtdicke weiter ansteigt[5]. Die Ursachen dafür sind jedoch unklar und müssen weiter erforscht werden.

In dieser Arbeit wurde der Effekt einer Passivierungsschicht auf das thermomechanische Verhalten dünner Kupferschichten (Cu) untersucht. Im Literaturüberblick *(Kapitel 2)* wurden experimentelle und theoretische Beweise für zwei kontrollierende Verformungsmechanismen in dünnen Schichten erläutert: die Behinderung der Versetzungsbewegung durch die Grenzflächen sowie Diffusionsmechanismen an der Oberfläche. Jedoch ist ihr jeweiliger Beitrag zur Dünnschichtplastizität in Abhängigkeit der Schichtdicke noch nicht gut verstanden. Passivierte Cu-Schichten, in denen Oberflächendiffusion unterbunden sein sollte, eignen sich somit als Modellsystem, um die Rolle von Oberflächendiffusion bei der Dünnschichtverformung zu untersuchen.

Nach einer Studie von Balk *et al.* tritt in unpassivierten Cu-Schichten dünner als 400 nm ein neuer Typ von Versetzungen auf, die parallel zur Schicht/Substrat-Grenzfläche gleiten: die so genannten parallelen Gleitversetzungen[25]. Die Bildung dieser Versetzungen ist vermutlich auf einen Kriechmechanismus zurückzuführen, der auf Oberflächendiffusion beruht, nämlich eingeengtes Diffusionskriechen[52]. Das Auftreten eines schichtdickenunabhängigen Spannungsplateaus in unpassivierten ultra-dünnen Cu-Schichten konnte durch diese Versetzungen erklärt werden. Die Untersuchung von passivierten Schichten bietet in diesem Kontext die Möglichkeit, das Zusammenspiel zwischen Auftreten des Spannungsplateaus für ultra-dünne Schichten, Beobachtung von parallelen Gleitversetzungen im TEM und der Theorie des eingeengten Diffusionskriechen zu verstehen.

11.2 Experimente

Diese Arbeit ist die erste ausführliche Studie passivierter Dünnschichten über einen breiten Schichtdickenbereich, der auch ultra-dünne Schichten beinhaltet. Dazu wurden

Cu-Schichten mit Schichtdicken zwischen 25 nm und 2 µm hergestellt *(Kapitel 3)*. Die Schichten wurden mittels Hochleistungskathodenzerstäuben (Magnetron-Sputtern) im Ultrahochvakuum auf mit amorphem Siliziumnitrid beschichteten (111) Silizium-Substraten abgeschieden. Ohne Unterbrechung des Vakuums wurden die Schichten mit einer 10 nm dicken Aluminiumoxid- oder Siliziumnitrid-Passivierungschicht bedeckt, wobei unterschiedliche Wärmebehandlungen erfolgten:

1) Cu-Schichten wurden direkt nach der Cu-Abscheidung bei Raumtemperatur passiviert (Typ CuSiN/RR)

2) Cu-Schichten wurden bei 500 °C ausgelagert und bei 500 °C passiviert (Typ CuSiN/AA), oder

3) Cu-Schichten wurden bei 500 °C ausgelagert und anschließend bei Raumtemperatur passiviert (Typen CuSiN/AR and CuAlO).

Als Vergleich dienten von Balk gemessene unpassivierte Cu-Schichten (Typ CuAB)[56].

Zur Charakterisierung der Mikrostruktur der Schichten wurden fokussierte Ionenstrahl- (FIB), Rasterelektronen- (REM) und Transmissionselektronenmikroskopie (TEM) verwendet *(Kapitel 4)*. Die Untersuchung der Textur der Schichten erfolgte mittels Röntgenbeugungsexperimenten (XRD). Die Entwicklung von thermischen Spannungen in den Cu-Schichten wurde hauptsächlich mittels der Substrat-Krümmungsmethode untersucht. Zusätzlich wurden ausgewählte Schichten *in-situ* im TEM thermisch zykliert, um die Versetzungsaktivität während des Temperaturzyklus zu untersuchen.

11.3 Ergebnisse und Diskussion

Die Mikrostruktur der untersuchten Schichtsysteme wurde ausführlich charakterisiert *(Kapitel 5)*. Nach thermischer Zyklierung wiesen alle Schichtsystemtypen eine ähnliche Mikrostruktur auf, gekennzeichnet durch eine starke (111) Textur und Korngrößen jeweils im Bereich der zweifachen Schichtdicke. Hügel wurden nur in den CuSiN/AA Schichten dünner als 200 nm beobachtet. Eine der beiden Probensätze des Typs CuSiN/AR wies Poren und Korngrenzenfurchen auf. Mit TEM konnte nachgewiesen

werden, dass die Passivierungsschicht die Cu-Oberfläche durchgehend bedeckt, obwohl Aluminiumoxid hauptsächlich als Inseln auf der Oberfläche vorliegt. Ausnahmen mit einer nicht geschlossenen Passivierungsschicht bilden die porenhaltigen Schichten vom Typ CuSiN/AR.

In *Kapiteln 6* und *7* wurde gezeigt, dass die Natur der Passivierungsschicht und ihre Abscheidungstemperatur keinen signifikanten Einfluss auf das Spannungs-Temperatur-Verhalten der Schichten haben. Im Gegensatz dazu ist die Dicke der Cu-Schicht eine beeinflussende Größe. Dies wird in Abbildung 11.1 illustriert. Der Effekt der Passivierung wird beim Vergleich der Spannungs-Temperatur-Kurven passivierter und unpassivierter Schichten für ultra-dünne Schichten (a) und eine 2 µm dicke Schicht (b) deutlich.

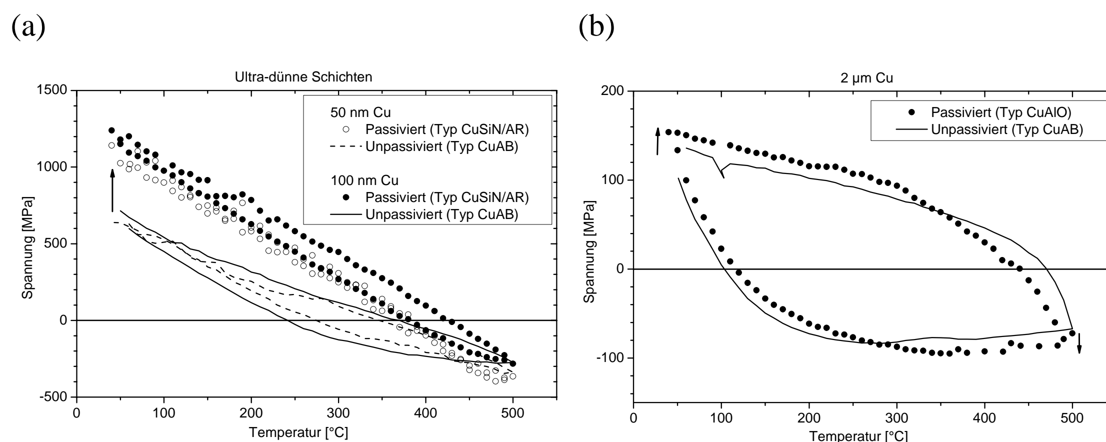

Abbildung 11.1: Effekt einer Passivierung auf das Verhalten von Cu-Schichten, gezeigt anhand Spannungs-Temperatur-Zyklen ultra-dünner (a) und dickerer (b) Schichten.

Schichten im Mikrometer- oder Submikrometer-Regime weisen eine elastisch-plastische Verformung auf, die mit thermisch aktiviertem Versetzungsgleiten simuliert werden konnte.

Passivierte Schichten mit einer Schichtdicke kleiner als 100 nm verformten sich rein elastisch zwischen Raumtemperatur und 500 °C. Durch die Passivierungsschicht wurde eingeengtes Diffusionskriechen bei hohen Temperaturen und damit Spannungsrelaxation unterdrückt. Der Mangel an Plastizität in ultra-dünnen Schichten legt nahe, dass Diffusionskriechen der einzige zur Verfügung stehende

Verformungsmechanismus in diesem Schichtdickenbereich ist. Dies kann durch folgende Gründe erklärt werden: mit abnehmender Korngröße und Schichtdicke verkürzen sich zum einen die Diffusionswege und Versetzungsnukleation wird schwieriger, zum anderen steigt der Anteil an Korngrenzenflächen.

Wie erwartet werden Schichten mit dazwischenliegenden Dicken sowohl von Versetzungsplastizität als auch von Diffusionskriechen beeinflusst.

Größeneffekte wurden durch Darstellung der Spannung bei Raumtemperatur nach thermischer Zyklierung in Abhängigkeit von der reziproken Schichtdicke hervorgehoben (Abbildung 11.2).

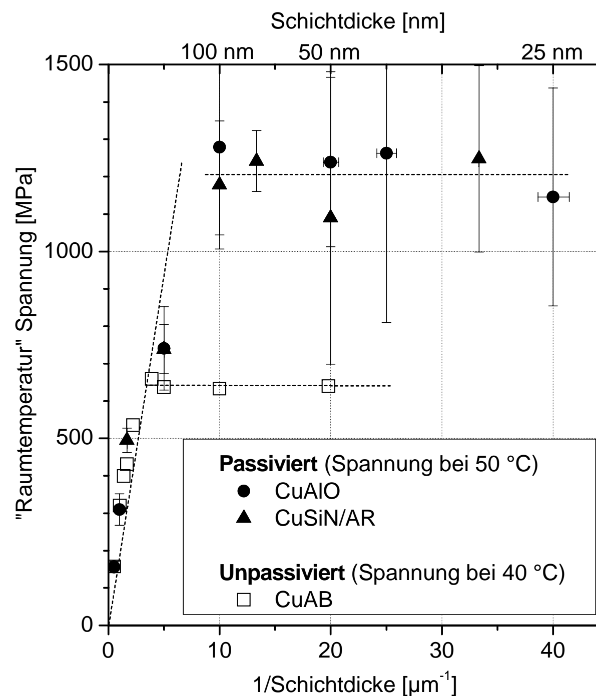

Abbildung 11.2: Die Spannungen der passivierten (Typ CuAlO und CuSiN/AR) und unpassivierten (Typ CuAB) Schichten bei Raumtemperatur nach thermischer Zyklierung in Abhängigkeit von der reziproken Schichtdicke.

Zwei Regime konnten unterschieden werden: ein lineares Ansteigen der Spannung mit abnehmender Schichtdicke für Schichten dicker als 100 nm und ein Spannungsplateau bei 1.2 GPa für Schichten dünner als 100 nm. Der Größeneffekt im Mikrometer- und Submikrometer-Bereich findet seine Herkunft vermutlich in der steigenden Schwierigkeit, Versetzungen mit abnehmender Schichtdicke zu erzeugen. Das

Spannungsplateau für die passivierten Schichten weist einen höheren Wert auf als das für die unpassivierten Cu-Schichten, welches durch die Präsenz von parallelen Gleitversetzungen erklärt worden ist. Obwohl parallele Gleitversetzungen erstaunlicherweise und für das erste Mal auch in passivierten Schichten beobachtet worden sind, haben sie sich während *in-situ* thermischer Zyklierung im TEM nicht bewegt, was wahrscheinlich auf die Ausschaltung der Oberflächendiffusion durch die Passivierungsschicht zurückzuführen ist.

Um die genaue Herkunft des Spannungsplateaus zu klären, sollte die angelegte Dehnung erhöht werden. Dies ist durch eine Erweiterung des Messtemperaturbereichs möglich und konnte durch Kühlen der Schichten mit flüssigem Stickstoff erreicht werden *(Kapitel 8)*. Für die Durchführung dieser Kühlversuche wurde eine Substrats-Krümmungsanlage speziell umgebaut. Die Spannungen in den Schichten konnten somit in einem Temperaturbereich zwischen -160 °C und 500 °C untersucht werden, was einer Gesamtdehnung von ungefähr 0.9% entspricht. Das Verhalten der Schichten wird anhand von zwei Beispielen in Abbildung 11.3 illustriert.

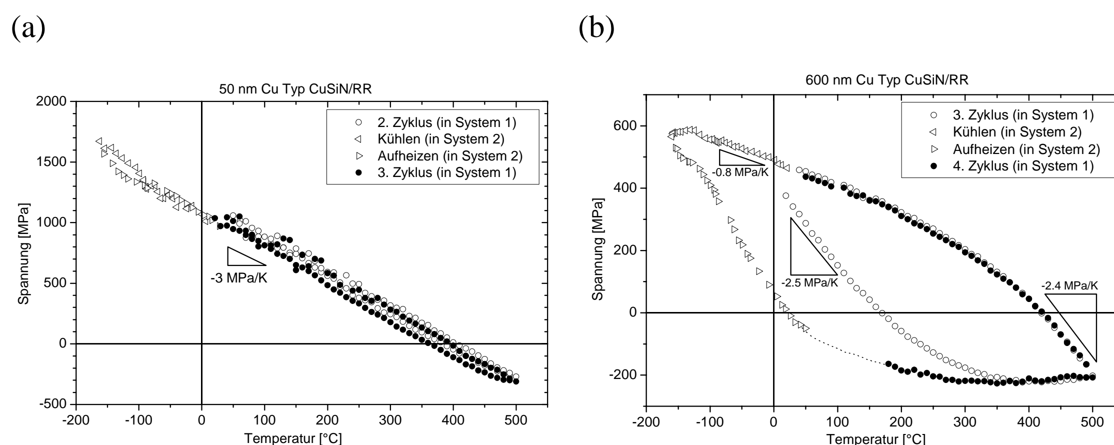

Abbildung 11.3: Spannungs-Temperatur-Zyklen einer 50 nm (a) und 600 nm (b) dicken passivierten Schicht (Typ CuSiN/RR).

Im Tieftemperaturbereich verformen sich die ultra-dünnen Schichten weiterhin elastisch, während die dickeren ein klassisches elastisch-plastisches Verhalten aufweisen. Aufgrund dieser Erkenntnisse erscheint die Herkunft des Spannungsplateaus unter einem anderen Licht. Sie ist die Konsequenz von der elastischen Verformung der

ultra-dünnen Schichten. Die angelegte thermische Dehnung ist zu klein, um plastisches Fliessen zu erzeugen. Hiermit zeigt diese Arbeit die Grenzen der Substrat-Krümmungsmethode für die Untersuchung des thermomechanischen Verhaltens ultra-dünner Schichten. Außerdem liegen die in den dünnsten Schichten gemessenen Spannungswerte von 1.7 GPa, was den höchsten je berichteten Werten für Cu entspricht, immer noch weit unter der theoretischen Festigkeitsgrenze von Cu.

Diese Überlegungen führen auch dazu, das Auftreten des Plateaus für unpassivierte Schichten unter einem kritischen Blick neu zu betrachten. Ultra-dünne unpassivierte Schichten verhalten sich bei niedrigen Temperaturen ebenfalls rein elastisch. Das beobachtete Spannungsplateau könnte daher ein Messartefakt sein, bedingt durch nicht ausreichende Dehnung der Schichten.

Die Ergebnisse dieser Arbeit sind relevant in Anbetracht der technologischen Anwendungen in der Mikroelektronik. Es wurde gezeigt, dass passivierte ultra-dünne Schichten, die auch in den kommenden Jahren weiter als Metallische Leiterbahnen in Chips Einsatz finden werden, über einen breiten Temperaturbereich keine plastische Verformung aufweisen. Im normalen Temperatur-Einsatzbereich können diese ultra-dünnen Schichten gewaltige Spannungen ertragen, die mit abnehmender Schichtdicke stagnieren.

CHAPTER 12

REFERENCES

[1] R. F. Tylecote, A History of Metallurgy, 2nd Edition, The Institute Of Materials (1992).

[2] P. Bai, C. Auth, S. Balakrishnan, M. Bost *et al.*, 2004 International Electron Devices Meeting IEEE, pp. 657-60. Piscataway, NJ, USA.

[3] W. D. Nix, *Metallurgical Transactions A* **20A**, 2217 (1989).

[4] D. Gan, P. S. Ho, Y. Pang, R. Huang, J. Leu, J. Maiz, and T. Scherban, *Journal of Materials Research* **21**, 1512 (2006).

[5] E. Arzt, *Acta Materialia* **46**, 5611 (1998).

[6] C. V. Thompson, *Journal of Materials Research* **8**, 237 (1993).

[7] C. V. Thompson, *Scripta Metallurgica Et Materialia* **28**, 167 (1993).

[8] J. Frenkel, *Zeitschrift für Physik* **37**, 572 (1926).

[9] E. Orowan, *Proceedings of the Physical Society* **52**, 8 (1940).

[10] J. K. Mackenzie, Dissertation, University of Bristol (1949).

[11] A. Seeger, Landolt-Börnstein, Handbuch der Physik, VII. Band, 2. Teil, edited by S. Flügge (Springer Verlag, 1958), pp. 7.

[12] W. L. Bragg and W. M. Lomer, *Proceedings of the Royal Society* **A196**, 171 (1949).

[13] W. M. Lomer, *Proceedings of the Royal Society* **A196**, 182 (1949).

[14] N. H. Macmillan, *Journal of Materials Science* **7**, 239 (1972).

[15] H. J. Frost and M. F. Ashby, Deformation-mechanism maps, Pergamon Press Oxford (1982).

[16] Landolt-Börnstein, Handbuch der Physik, IV. Band Technik, 2. Teil, Bandteil b, 6. Auflage, Springer Verlag (1964).

[17] R. Venkatraman and J. C. Bravman, *Journal of Materials Research* **7**, 2040 (1992).

[18] R.-M. Keller, S. P. Baker, and E. Arzt, *Journal of Materials Research* **13**, 1307 (1998).

[19] L. B. Freund, *Journal of Applied Mechanics* **54**, 553 (1987).

[20] G. Dehm, B. J. Inkson, T. J. Balk, T. Wagner, and E. Arzt, Dislocations and Deformation Mechanisms in Thin Films and Small Structures (Material Research Society Symposium Proceedings Vol.673) . Mater. Res. Soc. 2001, pp. P2.6.1-12. Warrendale, PA, USA.

[21] G. Dehm, T. Wagner, T. J. Balk, E. Arzt, and B. J. Inkson, *Journal of Materials Science & Technology* **18**, 113 (2002).

[22] G. Dehm, T. J. Balk, H. Edongué, and E. Arzt, *Microelectronic Engineering* **70**, 412 (2003).

[23] H. Edongué, Dissertation, Dünnschichtplastizität und Wechselwirkung von Gitterversetzungen mit der Film/Substrat Grenzfläche, Universität Stuttgart (2004).

[24] B. J. Inkson, G. Dehm, and T. Wagner, *Acta Materialia* **50**, 5033 (2002).

[25] T. J. Balk, G. Dehm, and E. Arzt, *Acta Materialia* **51**, 4471 (2003).

[26] G. Dehm and E. Arzt, *Applied Physics Letters* **77**, 1126 (2000).

[27] G. Dehm, D. Weiss, and E. Arzt, *Materials Science & Engineering A* **309-310**, 468 (2001).

[28] M. Legros, K. J. Hemker, A. Gouldstone, S. Suresh, R. M. Keller-Flaig, and E. Arzt, *Acta Materialia* **50**, 3435 (2002).

[29] E. O. Hall, *Proceedings of the Physical Society B* **64**, 747 (1951).

[30] N. J. Petch, *Journal of the Iron and Steel Institute* **174**, 25 (1953).

[31] W. D. Nix, *Scripta Materialia* **39**, 545 (1998).

[32] K. W. Schwarz and J. Tersoff, *Applied Physics Letters* **69**, 1220 (1996).

[33] P. Pant, K. W. Schwarz, and S. P. Baker, Dislocations and Deformation Mechanisms in Thin Films and Small Structures (Material Research Society Symposium Proceedings Vol.673) . Mater. Res. Soc. 2001, pp. P2.2.1-6. Warrendale, PA, USA.

[34] P. Pant, K. W. Schwarz, and S. P. Baker, *Acta Materialia* **51**, 3243 (2003).

[35] L. Nicola, E. van der Giessen, and A. Needleman, *Materials Science & Engineering A* **309-310**, 274 (2001).

[36] L. Nicola, E. van der Giessen, and A. Needleman, *Journal of Applied Physics* **93**, 5920 (2003).

[37] L. Nicola, E. van der Giessen, and A. Needleman, *Thin Solid Films* **479**, 329 (2005).

[38] Y. Xiang, X. Chen, and J. J. Vlassak, Thin Films: Stresses and Mechanical Properties IX (Materials Research Society Symposium Proceedings Vol.695). Mater. Res. Soc. 2002, pp. 189-94. Warrendale, PA, USA.

[39] B. von Blanckenhagen, P. Gumbsch, and E. Arzt, *Modelling and Simulation in Materials Science and Engineering* **9**, 157 (2001).

[40] B. von Blanckenhagen, Dissertation, Versetzungen in dünnen Metallschichten, Institut für Metallkunde, Universität Stuttgart (2002).

[41] B. von Blanckenhagen, P. Gumbsch, and E. Arzt, *Philosophical Magazine Letters* **83**, 1 (2003).

[42] B. von Blanckenhagen, E. Arzt, and P. Gumbsch, *Acta Materialia* **52**, 773 (2004).

[43] G. Dehm, T. J. Balk, B. von Blanckenhagen, P. Gumbsch, and E. Arzt, *Zeitschrift fur Metallkunde* **93**, 383 (2002).

[44] M. D. Thouless, J. Gupta, and J. M. E. Harper, *Journal of Materials Research* **8**, 1845 (1993).

[45] R. P. Vinci, E. M. Zielinski, and J. C. Bravman, *Thin Solid Films* **262**, 142 (1995).

[46] M. D. Thouless, K. P. Rodbell, and C. Cabral, Jr., *Journal of Vacuum Science & Technology A* **14**, 2454 (1996).

[47] R.-M. Keller, S. P. Baker, and E. Arzt, *Acta Materialia* **47**, 415 (1999).

[48] R. L. Coble, *Journal of Applied Physics* **34**, 1679 (1963).

[49] G. B. Gibbs, *Philosophical Magazine* **13**, 589 (1966).

[50] M. S. Jackson and Li Che-Yu, *Acta Metallurgica* **30**, 1993 (1982).

[51] M. D. Thouless, *Acta Metallurgica et Materialia* **41**, 1057 (1993).

[52] H. Gao, L. Zhang, W. D. Nix, C. V. Thompson, and E. Arzt, *Acta Materialia* **47**, 2865 (1999).

[53] T. J. Balk, G. Dehm, and E. Arzt, Dislocations and Deformation Mechanisms in Thin Films and Small Structures (Material Research Society Symposium Proceedings Vol.673) . Mater. Res. Soc. 2001, pp. P2.7.1-6. Warrendale, PA, USA.

[54] T. J. Balk, G. Dehm, and E. Arzt, Thin Films: Stresses and Mechanical Properties IX (Materials Research Society Symposium Proceedings Vol.695). Mater. Res. Soc. 2002, pp. 53-8. Warrendale, PA, USA.

[55] T. J. Balk, G. Dehm, and E. Arzt, Multiscale Phenomena in Materials - Experiments and Modeling Related to Mechanical Behavior. Symposium (Mater. Res. Soc. Symposium Proceedings Vol.779). Mater. Res. Soc. 2003, pp. 87-96. Warrendale, PA, USA.

[56] T. J. Balk, Personal communication (2004).

[57] D. Weiss, Dissertation, Deformation Mechanisms in Pure and Alloyed Copper Films, Universität Stuttgart (2000).

[58] D. Weiss, H. Gao, and E. Arzt, Dislocations and Deformation Mechanisms in Thin Films and Small Structures (Material Research Society Symposium Proceedings Vol.673) . Mater. Res. Soc. 2001, pp. P1.2.1-6. Warrendale, PA, USA.

[59] D. Weiss, H. Gao, and E. Arzt, *Acta Materialia* **49**, 2395 (2001).

[60] M. J. Buehler, A. Hartmaier, and Gao Huajian, Nanoscale Materials and Modeling-Relations Among Processing, Microstructure and Mechanical Properties (Materials Research Society Symposium Proceedings Vol.821). Materials Res. Soc. 2004, pp. 221-32. Warrendale, PA, USA.

[61] Y. C. Joo, P. Mullner, S. P. Baker, and E. Arzt, Materials Reliability in Microelectronics VII. Symposium. Mater. Res. Soc. 1997, pp. 409-14. Pittsburgh, PA, USA.

[62] R. P. Vinci and J. C. Bravman, Materials Reliability in Microelectronics III Symposium. Mater. Res. Soc. 1993, pp. 269-73. Pittsburgh, PA, USA.

[63] R. P. Vinci, Dissertation, Thermal strains and stresses in copper thin films and microelectronic interconnect structures, Department of Materials Science and Engineering, Stanford University (1994).

[64] R.-M. Keller, S. Bader, R. P. Vinci, and E. Arzt, Thin Films: Stresses and Mechanical Properties V. Symposium . Mater. Res. Soc. 1995, pp. 453-8. Pittsburgh, PA, USA.

[65] R.-M. Keller, Thermomechanisches Verhalten und Mikrostruktur dünner, polycrystalliner Kupferschichten, Institut für Metallkunde, Universität Stuttgart (1996).

[66] Y. L. Shen, S. Suresh, M. Y. He, A. Bagchi, O. Kienzle, M. Ruhle, and A. G. Evans, *Journal of Materials Research* **13**, 1928 (1998).

[67] S. P. Baker, R. -M. Keller-Flaig, and J. B. Shu, *Acta Materialia* **51**, 3019 (2003).

[68] Y. L. Shen and U. Ramamurty, *Journal of Applied Physics* **93**, 1806 (2003).

[69] Y. L. Shen and U. Ramamurty, *Journal of Vacuum Science & Technology B* **21**, 1258 (2003).

[70] R. P. Vinci, S. A. Forrest, and J. C. Bravman, *Journal of Materials Research* **17**, 1863 (2002).

[71] J. B. Shu and S. P. Baker, Thin Films: Stresses and Mechanical Properties IX (Materials Research Society Symposium Proceedings Vol.695). Mater. Res. Soc. 2002, pp. 15-20. Warrendale, PA, USA.

[72] J. B. Shu, B. Clyburn, T. E. Mates, and S. P. Baker, *Journal of Materials Research* **18**, 2122 (2003).

[73] M. J. Kobrinsky and C. V. Thompson, *Applied Physics Letters* **73**, 2429 (1998).

[74] O. S. Leung and W. D. Nix, Thin Films - Stresses and Mechanical Properties VIII. Symposium (Materials Research Society Symposium Proceedings Vol.594). Mater. Res. Soc. 2000, pp. 51-6. Warrendale, PA, USA.

[75] O. S. Leung, A. Munkholm, S. Brennan, and W. D. Nix, *Journal of Applied Physics* **88**, 1389 (2000).

[76] O. S. Leung, Dissertation, Studies in the strengthening mechanisms of thin polycrystalline gold films, Department of Materials Science and Engineering, Stanford University (2001).

[77] P. A. Flinn, D. S. Gardner, and W. D. Nix, *IEEE Transactions on Electron Devices* **ED-34**, 689 (1987).

[78] D. Jawarani, H. Kawasaki, I. S. Yeo, L. Rabenberg, J. P. Stark, and P. S. Ho, *Journal of Applied Physics* **82**, 171 (1997).

[79] Smithells Metals Reference Book (8th Edition), W. F. Gale & T. C. Totemeier, Elsevier

[80] R. Schwaiger and O. Kraft, *Acta Materialia* **51**, 195 (2003).

[81] C. A. Paszkiet, M. A. Korhonen, and Li Che-Yu, Materials Reliability Issues in Microelectronics Symposium . Mater. Res. Soc. 1991, pp. 161-6. Pittsburgh, PA, USA.

[82] M. F. Doerner, D. S. Gardner, and W. D. Nix, *Journal of Materials Research* **1**, 845 (1986).

[83] L. B. Freund and S. Suresh, (Cambridge University Press, 2003), pp. 528.

[84] M. A. Korhonen and C. A. Paszkiet, *Scripta Metallurgica* **23**, 1449 (1989).

[85] R. Venkatraman, J. C. Bravman, W. D. Nix, P. W. Davies, P. A. Flinn, and D. B. Fraser, *Journal of Electronic Materials* **19**, 1231 (1990).

[86] F. Macionczyk and W. Bruckner, *Journal of Applied Physics* **86**, 4922 (1999).

[87] G. Dehm, Personal communication (2005).

[88] L. Sauter, Dissertation, Microstructural and Film thickness effects on the thermomechanical behavior of Thin Au films, Universität Stuttgart (2006).

[89] M. Hommel, Dissertation, Röntgenographische Untersuchung des monotonen und zyklischen Verformungsverhaltens dünner Metallschichten auf Substraten, Universität Stuttgart (1999).

[90] P. A. Flinn, *Journal of Materials Research* **6**, 1498 (1991).

[91] M. Hommel and O. Kraft, *Acta Materialia* **49**, 3935 (2001).

[92] H. Huang and F. Spaepen, *Acta Materialia* **48**, 3261 (2000).

[93] D. Son, J. H. Jeong, and D. Kwon, *Thin Solid Films* **437**, 182 (2003).

[94] V. Weihnacht and W. Brockner, Thin Films - Stresses and Mechanical Properties VIII. Symposium (Materials Research Society Symposium Proceedings Vol.594). Mater. Res. Soc. 2000, pp. 87-92. Warrendale, PA, USA.

[95] H. D. Espinosa, B. C. Prorok, and B. Peng, *Journal of the Mechanics and Physics of Solids* **52**, 667 (2004).

[96] R. Spolenak, C. A. Volkert, K. Takahashi, S. Fiorillo, J. Miner, and W. L. Brown, Thin Films - Stresses and Mechanical Properties VIII. Symposium (Materials Research Society Symposium Proceedings Vol.594). Mater. Res. Soc. 2000, pp. 63-8. Warrendale, PA, USA.

[97] H. D. Espinosa and B. C. Prorok, Thin Films: Stresses and Mechanical Properties IX (Materials Research Society Symposium Proceedings Vol.695). Mater. Res. Soc. 2002, pp. 349-54. Warrendale, PA, USA.

[98] B. C. Prorok and H. D. Espinosa, *Journal of Nanoscience and Nanotechnology* **2**, 427 (2002).

[99] H. D. Espinosa and B. C. Prorok, *Journal of Materials Science* **38**, 4125 (2003).

[100] R. D. Emery and G. L. Povirk, *Acta Materialia* **51**, 2067 (2003).

[101] T. K. Schmidt, T. J. Balk, G. Dehm, and E. Arzt, *Scripta Materialia* **50**, 733 (2004).

[102] T. K. Schmidt, Personal communication (2006).

[103] R. D. Emery and G. L. Povirk, *Acta Materialia* **51**, 2079 (2003).

[104] Y. Xiang, J. J. Vlassak, M. T. Perez-Prado, T. Y. Tsui, and A. J. McKerrow, Thin Films - Stresses and Mechanical Properties X (Mater. Res. Soc. Symposium Proceedings Vol.795). Mater. Res. Soc. 2004, pp. 417-22. Warrendale, PA, USA.

[105] F. Onuseit, Diploma thesis, "Bulge-Test" an freistehenden Kupferschichten, Universität Stuttgart (2005).

[106] Y. Xiang, T. Y. Tsui, and J. J. Vlassak, *Journal of Materials Research* **21**, 1607 (2006).

[107] Y. Xiang and J. J. Vlassak, *Acta Materialia* **54**, 5449 (2006).

[108] K. S. Siow, A. A. O. Tay, and P. Oruganti, *Materials Science and Technology* **20**, 285 (2004).

[109] S. S. Brenner, *Journal of Applied Physics* **27**, 1484 (1956).

[110] T. Serikawa and A. Okamoto, *Journal of the Electrochemical Society* **131**, 2928 (1984).

[111] A. Strecker, U. Salzberger, and J. Mayer, *Prakt. Metallogr., Carl Hanser Verlag, München* **30**, 482 (1993).

[112] R. Spolenak, B. Heiland, C. Witt, R. Keller, P. Mullner, and E. Arzt, *Praktische Metallographie* **37**, 90 (2000).

[113] G. Dehm, F. Ernst, J. Mayer, G. Moebus *et al.*, *Zeitschrift fur Metallkunde* **87**, 898 (1996).

[114] G. G. Stoney, *Proceedings of the Royal Society*, 172 (1909).

[115] M. Wohlschlögel, T. U. Schülli, and U. Welzel, *In preparation*, (2007).

[116] U. Welzel, J. Ligot, P. Lamparter, A. C. Vermeulen, and E. J. Mittemeijer, *Journal of Applied Crystallography* **38**, 1 (2005).

[117] Profit for User's Guide, Philips Analytical X-ray, Holland (1996).

[118] V. Hauk, Structural and Residual Stress Analysis by Nondestructive Methods Evaluation, Application, Assessment, Elsevier Holland (1997).

[119] D. B. Williams and C. B. Carter, Transmission electron microscopy: a textbook for materials science, Plenum Press New York (1996).

[120] D. B. Knorr and D. P. Tracy, *Materials Chemistry and Physics* **41**, 206 (1995).

[121] W. W. Mullins, *Acta Metallurgica* **6**, 414 (1958).

[122] C. V. Thompson, *Annual Review of Materials Science* **20**, 245 (1990).

[123] W. M. Kuschke, A. Kretschmann, R. M. Keller, R. P. Vinci, C. Kaufmann, and E. Arzt, *Journal of Materials Research* **13**, 2962 (1998).

[124] C. V. Thompson and R. Carel, *Materials Science & Engineering B* **32**, 211 (1995).

[125] C. V. Thompson and R. Carel, *Journal of the Mechanics and Physics of Solids* **44**, 657 (1996).

[126] H. L. Skriver and N. M. Rosengaard, *Physical Review B (Condensed Matter)* **46**, 7157 (1992).

[127] C. V. Thompson, *Annual Review of Materials Science* **30**, 159 (2000).

[128] P. Sonnweber-Ribic, P. Gruber, G. Dehm, and E. Arzt, *Acta Materialia* **54**, 3863 (2006).

[129] S. Craig and G. L. Harding, *Journal of Vacuum Science and Technology* **19**, 205 (1981).

[130] M. Pletea, W. Bruckner, H. Wendrock, and R. Kaltofen, *Journal of Applied Physics* **97**, 54908 (2005).

[131] V. Weihnacht and W. Bruckner, *Thin Solid Films* **418**, 136 (2002).

[132] B. A. Movchan and A. V. Demchishin, *Physics of Metals and Metallography - USSR* **28**, 83 (1969).

[133] J. A. Thornton, *Journal of Vacuum Science and Technology* **11**, 666 (1974).

[134] J. A. Thornton, *Journal of Vacuum Science & Technology* **12**, 830 (1975).

[135] J. A. Thornton, *Annual Review of Materials Science* **7**, 239 (1977).

[136] M. Ohring, The materials science of thin films, Academic Press, Inc. London (1992).

[137] P. Villars, (ASM International, Materials Park, OK, 1997), Vol. 1-2.

[138] M. Vila, D. Caceres, and C. Prieto, *Journal of Applied Physics* **94**, 7868 (2003).

[139] F. Y. Genin, *Acta Metallurgica et Materialia* **43**, 4289 (1995).

[140] D. Weiss, O. Kraft, and E. Arzt, *Journal of Materials Research* **17**, 1363 (2002).

[141] R. W. Vook, *Materials Chemistry and Physics* **36**, 199 (1994).

[142] R. Abermann, *Thin Solid Films* **186**, 233 (1990).

[143] C. Y. Chang and R. W. Vook, *Journal of Vacuum Science & Technology A* **9**, 559 (1991).

[144] R. W. Vook and F. Witt, *Journal of Applied Physics* **36**, 2169 (1965).

[145] F. Witt and R. W. Vook, *Journal of Applied Physics* **39**, 2773 (1968).

[146] P. Chaudhari, *Journal of Applied Physics* **45**, 4339 (1974).

[147] M. Murakami and T. S. Kuan, *Thin Solid Films* **66**, 381 (1980).

[148] C. Y. Chang and R. W. Vook, *Thin Solid Films* **228**, 205 (1993).

[149] E. Iwamura, K. Takagi, and T. Ohnishi, *Thin Solid Films* **349**, 191 (1999).

[150] M. Rocke and M. Schneegans, *Journal of Vacuum Science & Technology B* **6**, 1113 (1988).

[151] C. J. Santoro, *Journal of the Electrochemical Society* **116**, 361 (1969).

[152] C. J. Dell'oca and A. J. Learn, *Thin Solid Films* **8**, R47 (1971).

[153] D. S. Herman, M. A. Schuster, and R. M. Gerber, *Journal of Vacuum Science and Technology* **9**, 515 (1972).

[154] T. J. Faith, *Journal of Applied Physics* **52**, 4630 (1981).

[155] L. Sauter, T. J. Balk, G. Dehm, J. A. Nucci, and E. Arzt, Thin Films-Stresses and Mechanical Properties XI. Symposium (Materials Research Society Symposium Proceedings Vol.875). Materials Research Society. 2005, pp. 177-82. Warrendale, PA, USA.

[156] N. Kristensen, F. Ericson, J. A. Schweitz, and U. Smith, *Thin Solid Films* **197**, 67 (1991).

[157] F. Ericson, N. Kristensen, J. A. Schweitz, and U. Smith, *Journal of Vacuum Science & Technology B* **9**, 58 (1991).

[158] P. Chaudhari, *Ibm Journal of Research and Development* **13**, 197 (1969).

[159] S. K. Lahiri and O. C. Wells, *Applied Physics Letters* **15**, 234 (1969).

[160] J. H. Adams, Properties and Selection: Nonferrous Alloys and Special-Purpose Materials. Metals Handbook, Vol. 2, ASM International (1990).

[161] A. J. Kalkman, A. H. Verbruggen, and G. C. A. M. Janssen, *Applied Physics Letters* **78**, 2673 (2001).

[162] S. P. Baker, R. P. Vinci, and T. Arias, *MRS Bulletin* **27**, 26 (2002).

[163] Metall, 45. Jahrgang, Heft 3 (1991), p. 232.

[164] M. W. Lane, E. G. Liniger, and J. R. Lloyd, *Journal of Applied Physics* **93**, 1417 (2003).

[165] T. H. Courtney, edited by McGraw-Hill (New York, 1990), p. 171.

[166] D. W. Hoffman and J. A. Thornton, *Thin Solid Films* **40**, 355 (1977).

[167] T. Wubben, G. Dehm, and E. Arzt, Thin Films-Stresses and Mechanical Properties XI. Symposium (Materials Research Society Symposium Proceedings Vol.875). Materials Research Society. 2005, pp. 201-6. Warrendale, PA, USA.

[168] T. Wubben, G. Dehm, and E. Arzt, *AIP Conference Proceedings*, 98 (2006).

[169] M. Wohlschlögel, U. Welzel, G. Maier, and E. J. Mittemeijer, *Journal of Applied Crystallography* **39**, 194 (2006).

[170] M. Kiguchi, T. Yokoyama, D. Matsumura, H. Kondoh, O. Endo, and T. Ohta, *Physical Review B (Condensed Matter)* **61**, 14020 (2000).

[171] E. Eiper, J. Keckes, K. J. Martinschitz, I. Zizak, M. Cabie, and G. Dehm, *Acta Materialia* **55**, 1941 (2007).

[172] P. Gruber, Dissertation (in preparation), Universität Stuttgart (2007).